

Inhibition Studies of Glu Ligase TTL7 and Peptidoglycan Peptidase Csd4

by

YANJIE LIU

A THESIS SUBMITTED IN PARTIAL FULFILLMENT OF THE
REQUIREMENTS FOR THE DEGREE OF

DOCTOR OF PHILOSOPHY

in

The Faculty of Graduate and Postdoctoral Studies

(Chemistry)

THE UNIVERSITY OF BRITISH COLUMBIA

(Vancouver)

July 2015

© YANJIE LIU, 2015

Abstract

Microtubules are one of the major components of the cytoskeleton, and are comprised of two kinds of tubulin proteins (α/β). The presence of diverse post-translational modifications provides microtubules with multiple biological functions, including both structural and physiological roles. Polyglutamylation is one of the widespread post-translational modifications and is catalyzed by the tubulin tyrosine ligase-like (TTL) enzymes. The reaction adds multiple glutamates to the γ glutamate side chain near the tubulin C-terminus to form a polyglutamate chain of various lengths. Such a side chain can be recognized by microtubule-associated proteins (MAPs) as a regulation signal. Our work focuses on the inhibition studies of the enzyme TTL7. Three inhibitors (Inhibitor 1 – 3) targeting different stages of polyglutamylation were designed and synthesized. The inhibitors were then tested in our collaborator Dr. Roll-Mecak's Lab, and we found Inhibitor 2, that targets an α -elongation process, had the highest potency with an IC_{50} of approximately 150 μ M.

Peptidoglycan is a key component of the bacterial cell wall and plays an essential role in determining bacterial cell morphology. The cell shape determining genes were recently discovered in *Helicobacter pylori*, which encode different DD-, DL- or endo-, carboxypeptidases. These peptidases hydrolyze the peptide bond in either crosslinked or uncrosslinked muropeptides in order to alter bacterial cell shape. Our study focuses on the enzyme Csd4, a carboxypeptidase that cleaves the PG tripeptides PG-L-Ala-iso-D-Glu-meso-Dap to the dipeptide PG-L-Ala-iso-D-Glu. Its homolog Pgp1 in *Campylobacter jejuni* was also identified recently. We synthesized a simple tripeptide Ac-L-Ala-iso-D-Glu-meso-Dap as a substrate for Csd4, which was successfully co-crystallized with the enzyme. We also measured the activity of Csd4 with this substrate. The Michaelis constant (K_M) and catalytic rate constant (k_{cat}) are 112 μ M and 0.044 s^{-1} , respectively. Based on a mechanistic analysis, we designed and synthesized a pseudodipeptidyl phosphinate as a Csd4 inhibitor. The inhibitor was tested and gave a K_I of 3.3 μ M. The crystal structure of Csd4-inhibitor proved the supported mechanism involving ligation of the oxyanion tetrahedral intermediate by the zinc ion. *In vivo* studies with the inhibitor showed it induced significant cell straightening in *H. pylori* and acapsular *C. jejuni* at millimolar concentration.

Preface

A version of Chapter 2 has been published and some figures are reproduced with permission from: Liu, Y.; Garnham, C. P.; Roll-Mecak, A.; Tanner, M. E. *Bioorganic & Medicinal Chemistry Letters* **2013**, 23, 4408 – 4412 (© 2013 Elsevier Ltd). The purification of the TTLL7 enzyme and testing of inhibitors **1**, **2** and **3** with TTLL7 were performed by Christopher P. Garnham at the National Institutes of Health (NIH) under the supervision of Principal Investigator Antonina Roll-Mecak. The synthesis of the compounds was completed by the author of this thesis, under the supervision of Principal Investigator Martin E. Tanner.

A portion of Chapter 3 has been published and some figures are reproduced with permission from: Chan, A. C. K.; Blair, K. M.; Liu, Y.; Frirdrich, E.; Gaynor, E. C.; Tanner, M. E.; Salama, N. R.; Murphy, M. E. P. *Journal of Biological Chemistry* **2015**, 290, 3622-3638 (© 2015 American Society for Biochemistry and Molecular Biology). The plasmid was provided by Principal Investigator Nina R. Salama, and all *in vivo* mutation studies of Csd4 variants were carried out by Kris M. Blair under supervision of Principal Investigator Nina R. Salama. A crystallographic studies of Csd4, including multiple sequence alignments, were accomplished by Dr. Anson C. K. Chan under supervision of Michael E. P. Murphy. The mutagenesis and *in vitro* assays with Csd4, Csd4-Q46H, Csd4-Q46E and Csd4-Q46A were also performed by Dr. Anson C. K. Chan. The synthesis of the tripeptide substrate and Csd4 inhibitor, as well as the *in vitro* activity and inhibition assays were performed by the author of this thesis, under the supervision of Principal Investigator Martin E. Tanner.

Table of Contents

Abstract	ii
Preface	iii
Table of Contents	iv
List of Tables	viii
List of Figures	ix
List of Symbols and Abbreviations	xvi
Acknowledgements	xxii
Dedication	xxiii
1. Introduction	1
1.1 Tubulin and Microtubules	1
1.1.1 Microtubules overview	1
1.1.2 Anti-cancer drugs and cell division	7
1.1.3 The post-translational modifications of MTs.....	8
1.1.3.1 Single molecule PTMs (mono-PTMs)	9
1.1.3.2 Multiple molecule PTMs	11
1.1.4 Polyglutamylation and TLL enzymes.....	11
1.1.4.1 Enzymes and catalysis.....	11
1.1.4.2 Characteristics and cellular functions of polyglutamylation.....	13
1.2 Peptidoglycan and Its Modifying Enzymes	16
1.2.1 Peptidoglycan and the bacterial cell wall	16
1.2.2 Peptidoglycan biosynthesis	18
1.2.2.1 The peptidoglycan biosynthetic pathway	19
1.2.2.2 Inhibitors targeting the PG biosynthetic pathway	27
1.2.3 Peptidoglycan modifications and the cell shape determinant genes.....	29
1.2.3.1 PG modifications and their <i>in vivo</i> functions	29
1.2.3.2 Cell shape determinant (Csd) genes in <i>Helicobacter pylori</i>	30
1.2.3.3 Mechanism of the zinc-dependent carboxypeptidases	32
1.3 Phosphinate Based Inhibitor System and Design	34
1.4 Project Goals	39
1.4.1 Inhibition studies of the tubulin polyglutamylase TLL7 (Tubulin Tyrosine Ligase-Like 7).....	39

1.4.2	Inhibition and structural studies on the peptidoglycan modifying carboxypeptidase Csd4 from <i>Helicobacter pylori</i>	41
2.	Substrate and Inhibitor Design for the Enzyme TTLL7.....	42
2.1	Previous Advances at Assaying TTLL7 activity	43
2.2	Design and Synthesis of Phosphinate Inhibitors	45
2.2.1	Synthesis of initiation inhibitor 1 and elongation inhibitor 3	46
2.2.2	Synthesis of elongation inhibitor 2	49
2.3	Testing Inhibitors with TTLL7	51
2.4	Discussion	54
2.5	Summary	55
2.6	Future Directions.....	56
2.7	Experimental.....	57
2.7.1	Materials and general procedures.....	57
2.7.2	Synthesis of inhibitor 1	57
2.7.2.1	Compound 8	57
2.7.2.2	Compound 10	58
2.7.2.3	Inhibitor 1	59
2.7.3	Synthesis of inhibitor 2	59
2.7.3.1	Compound 19	59
2.7.3.2	Compound 20	60
2.7.3.3	Compound 21	60
2.7.3.4	Compound 22	61
2.7.3.5	Inhibitor 2	61
2.7.4	Synthesis of inhibitor 3	62
2.7.4.1	Compound 11	62
2.7.4.2	Inhibitor 3	62
2.7.5	Peptide synthesis.....	63
2.7.6	Inhibition assay.....	63
3.	Inhibition and Structural Studies on the Peptidoglycan-Modifying Carboxypeptidase Csd4 from <i>Helicobacter pylori</i>.....	65
3.1	Previous Characterization of Csd4 from <i>H. pylori</i>	66
3.1.1	Deletion of the <i>csd4</i> gene leads to lack of helical shape in <i>H. pylori</i> mutants	66
3.1.2	Csd4 is a DL-carboxypeptidase that hydrolyzes uncrosslinked tripeptides.....	67

3.1.3	Muropeptide composition analysis and genetic mutation results indicate two distinct PG modification pathways control the helical rod shape	69
3.1.4	Csd4 mutant shows weaker gastric stomach colonization but normal PG integrity	70
3.1.5	Reduced motility with shape-dependent phenotypes were observed in gel-like media	70
3.1.6	Csd4 homologue Pgp1 determines the helical cell shape of <i>C. jejuni</i>	70
3.2	Design and Synthesis of the Ac-L-Ala-<i>iso</i>-D-Glu-<i>m</i>-Dap Tripeptide	72
3.3	Kinetic Studies of Csd4 with the Tripeptide Substrate.....	73
3.4	Structural Studies of <i>H. pylori</i> Csd4 with the Tripeptide Substrate	76
3.4.1	Crystallization conditions of Apo-Csd4, zinc bound-Csd4 and tripeptide bound-Csd4	76
3.4.2	Csd4 domain structure	76
3.4.3	Zinc and the tripeptide binding Site	78
3.5	Mutation Studies of <i>H. pylori</i> Csd4.....	82
3.5.1	Q46 is required for full Csd4 activity	82
3.5.2	Csd4 suggests a new family of CPases.....	84
3.6	Design and Synthesis of a Pseudodipeptyl Phosphinate Inhibitor.....	85
3.7	Kinetic Studies with Inhibitor 8	88
3.8	Structural Studies of <i>H. pylori</i> Csd4 with the Phosphinate Inhibitor 8.....	90
3.9	<i>In vivo</i> Assays of Inhibitor 8 with <i>H. pylori</i> and <i>C. jejuni</i>	94
3.9.1	Assay with <i>C. jejuni</i>	94
3.9.2	Assay with <i>H. pylori</i>	102
3.10	Summary	105
3.11	Future Directions.....	106
3.11.1	Develop more potent inhibitors of Csd4	106
3.11.2	Inhibition studies of Csd4 with the new inhibitors	108
3.11.3	Crystal structure of Csd4-Inhibitor complexes	108
3.11.4	Morphological effects of inhibitor on cell shape and colonization potential	109
3.12	Experimental.....	109
3.12.1	Synthesis of tripeptide substrate	109
3.12.1.1	Ac-L-Ala-D-Glu(OtBu)-OH (Compound 23).....	110
3.12.1.2	Compound 25	110
3.12.1.3	Compound 26	110
3.12.1.4	Ac-L-Ala- <i>iso</i> -D-Glu(OH)- <i>meso</i> -Dap-OH (Tripeptide Substrate).	111
3.12.2	Bacterial strains and growth conditions.....	111
3.12.3	Cloning and recombinant expression of Csd4	111

3.12.4	Crystallization and structure determination	112
3.12.4.1	Csd4-Zn and Csd4-Tripeptide.....	112
3.12.4.2	Csd4-Inhibitor	113
3.12.5	Sequence alignments	114
3.12.6	Stopped kinetic assays	114
3.12.7	Synthesis of inhibitor 8	114
3.12.7.1	Compound 31	115
3.12.7.2	Compound 34	115
3.12.7.3	Compound 35	116
3.12.7.4	Inhibitor 8 (Csd4 Inhibitor).....	117
3.12.8	Testing of Csd4 activity using a continuous coupled assay	117
3.12.9	<i>In vivo</i> assays of inhibitor 8 with <i>C. jejuni</i> and <i>H. pylori</i>	118
	References	120
	Appendix	133
	NMR Spectra of Selected Compound	133

List of Tables

Table 3.1. Muropeptide composition of PG in mutant strains.....	69
Table 3.2. Summary of muropeptide percentage composition of <i>C. jejuni</i> strains.....	71
Table 3.3. Kinetic constants for the Csd4 catalyzed reaction.....	76
Table 3.4. Zinc ligand bond lengths (Å) in the crystal structures.	84
Table 3.5. The inhibitory constant and the α value of the inhibitor 8	90
Table 3.6. Summary of microscopic observations of cellular morphology (<i>C. jejuni</i>).	96
Table 3.7. Summary of microscopic observations of cellular morphology (<i>H. pylori</i>).	102

List of Figures

Figure 1.1. Left: The cytoskeleton in a eukaryotic cell (http://www.nat.vu.nl/~fcm/images/resear1.jpg). Right: microtubule distribution in an interphase cell.	1
Figure 1.2. Microtubule structures. (http://www.mikeblaber.org/oldwine/BCH4053/Lecture30/Lecture30.htm).	2
Figure 1.3. Microtubules assembly and dynamic instability (http://www.pha.jhu.edu/~ghzheng/old/webct/note2_6.files/F19-11.jpg).	3
Figure 1.4. Dynein and kinesin are the major MT motor proteins.	4
Figure 1.5. Organelles including centrosome and centrioles are constituted by MTs. (http://fig.cox.miami.edu/~cmallery/150/cells/c7x22centrosome.jpg).	5
Figure 1.6. Microtubules (blue strings) in axons and dendrites in a neuronal cell.	5
Figure 1.7. Microbutules in cilia and flagella. (http://micro.magnet.fsu.edu/cells/ciliaandflagella/ciliaandflagella.html).	6
Figure 1.8. Mitotic spindles in cell mitosis (http://www.nature.com/scitable/content/types-of-microtubules-involved-in-mitosis-14752887).	6
Figure 1.9. Anticancer medicines: vincristine/vinblastine (left) and paclitaxel (right).	7
Figure 1.10. Post-translational modifications of MTs.	8
Figure 1.11. Enzymes involved in tubulin PTMs. C- terminal tyrosine is presented as dark blue cube (bigger); C-terminal glutamic acid is blue cube; side chain glutamic acid is colored orange (branch point) and red (extended); side chain glycine is light green cube (branch point) and green cube(extended); side chain amine is white cube and phosphate is pink cube.	10
Figure 1.12. Chemistry of polygutamylation/deglutamylation.	12
Figure 1.13. Mechanism of TTLL glutamylation.	13
Figure 1.14. The bacterial cell envelope (http://kdhellner.tripod.com/id15.html).	16
Figure 1.15. General repeating structure of peptidoglycan showing GlcNAc-MurNAc disaccharide and crosslinked pentapeptide.	17
Figure 1.16. The cell wall structures of the Gram-positive (left) and the Gram-negative (right) bacteria (http://biology-forums.com/gallery/33_15_07_11_12_13_35.jpeg).	18
Figure 1.17. Overview of the peptidoglycan biosynthesis pathway.	19
Figure 1.18. Biosynthesis of UDP-MurNAc.	20

Figure 1.19. Biosynthesis of UDP-MurNAc-L-Ala-D-Glu- <i>m</i> -Dap-D-Ala-D-Ala.	21
Figure 1.20. Synthesis of Lipid I and Lipid II.....	22
Figure 1.21. Glycan chain polymerization.	23
Figure 1.22. The LMM TPase trimming reactions.....	24
Figure 1.23. Mechanism of the transpeptidation reaction.	26
Figure 1.24. The different crosslinkage patterns in Gram-positive (A) and Gram-negative (B) bacteria (http://www.studyblue.com/notes/note/n/ch-4-lecture-3/deck/2692055).	27
Figure 1.25. Structures of fosfomycin, cycloserine and vancomycin.	28
Figure 1.26. The four main categories of β -Lactams.....	28
Figure 1.27. The peptidoglycan modifications of <i>O</i> -acetylation (left) and <i>N</i> -deacetylation (right).	29
Figure 1.28. The phenotype of wild-type <i>H. pylori</i> (left) and the Δ <i>csd6</i> mutant (right) (http://www.fhcrc.org/en/news/spotlight/imports/using-flow-cytometry-to-find-rare-cell-shape-changes-in-helicoba.html).	30
Figure 1.29. Potential Csd1 – 3 modifications of PG.	31
Figure 1.30. PG trimming by Csd6 and Csd4.	32
Figure 1.31. The mechanism of carboxypeptidase A.	33
Figure 1.32. Tetrahedral intermediate formation in ligase and carboxypeptidase catalysis.....	34
Figure 1.33. The structure of a tetrahedral intermediate and a phosphinic pseudo-peptide.....	35
Figure 1.34. The potent inhibitors of various ligases and peptidases.....	35
Figure 1.35. Partial structure of the active site of astacin.	36
Figure 1.36. Left: The phosphorylation of the phosphinate inhibitor. Right: The active site of the D-Ala-D-Ala ligase, with phosphorylated inhibitor and ADP bound to the Mg^{2+}	37
Figure 1.37. A(top): The phosphinate and hydroxamate inhibitor of MMP-2. B(bottom): The MMP-9 phosphinate inhibitor RXP03.....	38
Figure 1.38. The clinical drug fosinopril, <i>N</i> -domain inhibitor RXP407, and <i>C</i> -domain inhibitor RXPA380.	39
Figure 1.39. Top: the tetrahedral intermediates formed during tubulin initiation and elongation (α - and γ -). Bottom: the designed phosphinate inhibitors mimicking these intermediates.....	40
Figure 1.40. The sequence of linear peptide1 and peptide2.	40
Figure 1.41. Left: the natural substrate of Csd4. Right: the tripeptide substrate and phosphinate inhibitor of Csd4.	41

Figure 2.1. MALDI of CTT peptides of newborn β II Tubulin (Top) and those peptides after incubation with TTLL7 (Bottom).....	43
Figure 2.2. Tandem mass spectrometry of CTT peptide with 3E incorporated after TTLL7 incubation.....	44
Figure 2.3. Inhibitory efficiency of class III and class IV β tubulin C-terminal peptides (10 mM). 44	
Figure 2.4. The structure of the potential TTLL7 intermediates (top) and the structure of the corresponding inhibitors (bottom).....	46
Figure 2.5. Synthesis of inhibitor 1 and 3	47
Figure 2.6. Mechanism of the reaction to synthesize <i>mono</i> -alkylphosphinic acid 6	48
Figure 2.7 The mechanism of the coupling reaction to synthesize compound 7	49
Figure 2.8. A – B) The normal Michael addition reactions are unsuccessful for preparing α -amino phosphinic acid inhibitor. C) Georgiadis’s strategy is using a phosphinic acid with phenyl group to complete the coupling reaction first, and followed by oxidation of the phenyl to a carboxylic acid.	50
Figure 2.9. Synthesis of inhibitor 2	51
Figure 2.10. Structure of the β IVb-tubulin CTT peptide.....	52
Figure 2.11. A series of mass spectra monitoring changes in the mass of The CTT peptide after enzymatic incubations in the presence of varying amounts of inhibitor 2	53
Figure 2.12. A plot of normalized activity versus the concentration of inhibitor 2 for the inhibition of tubulin C-terminal peptide (100 μ M) glutamylation by TTLL7.	53
Figure 2.13. MurD inhibitors showed different potency depending on the presence of the sugar and UDP group.	55
Figure 2.14. Peptide inhibitor synthesis.	56
Figure 3.1. A, C) Wild-type and Δ <i>csd4</i> mutant phase contrast images. B, D) Wild-type and Δ <i>csd4</i> mutant transmission electron microscopy images.	67
Figure 3.2. The trimming process of single strand muropentapeptide in <i>H. pylori</i>	68
Figure 3.3. Negatively stained TEM images of <i>C. jejuni</i> strains. A) 81-176, the wild-type. B) Δ <i>pgp1</i> , the deletion mutant.....	71
Figure 3.4. The natural substrate muropentapeptide (left) of Csd4 and the designed tripeptide substrate (right).....	72
Figure 3.5. The synthetic scheme for the tripeptide substrate.....	73
Figure 3.6. The continuous enzyme-coupled assay used in the kinetic analysis.....	74
Figure 3.7. Left: the structures of NADP ⁺ /NADPH. Right: the absorbance of NADP ⁺ and NADPH. 74	

Figure 3.8. Absorbance versus time plot as monitored by UV spectroscopy. The initial slope of the curve represents the initial velocity of Csd4.....	74
Figure 3.9. Plots of initial velocity vs. substrate concentration for Csd4 catalysis.....	75
Figure 3.10. A) The overall monomeric structure of Csd4 with Zn (II) and <i>m</i> -Dap bound. Domains 1 (CPase domain), 2 and 3 are displayed in color blue, gray and green. B) Overall electrostatic surface potential of Csd4 (Contoured at $\pm 3 k_bT/e_c$).	77
Figure 3.11. 1000X phase contrast images of wild-type and <i>csd4</i> mutant <i>H. pylori</i> strains.	78
Figure 3.12. Left: the zinc binding pocket with key ligands and a density map for the density of the bound <i>m</i> -Dap molecule (contoured at 3σ). Right: two-dimensional interaction map between Csd4, zinc and <i>m</i> -Dap in Csd4 active site.	78
Figure 3.13. Tripeptide binding in Csd4 active site. A) Zinc (purple) and substrate (yellow) interactions with Csd4. Zinc ligands are colored gray; tripeptide ligands are colored cyan; catalytic water and its ligands are red and orange. B) Structural alignments between Csd4-Zn and Csd4-Tripeptide. View is of the active site in panel A with a 30° rotation about the X-axis. .	80
Figure 3.14. Two-dimensional Csd4-Tripeptide interaction map. Tripeptide substrate is highlighted in grey; H ₂ O molecules are colored cyan; zinc and its ligands are not shown.	81
Figure 3.15. Activity tests for wild-type Csd4 and its active site mutants Q46H, Q46A and Q46E. A) Activity difference between wild-type Csd4 and its mutants in two buffer systems: Bis-tris and phosphate. The enzyme activity is continuously coupled with <i>m</i> -Dap dehydrogenase and monitored. B) pH-based differences between wild-type Csd4 and its mutants. The assay was examined by measuring the amount of product after 20 min reaction.	82
Figure 3.16. Three-dimensional Csd4-Q46H interaction map in the active site with zinc bound. Zinc and binding ligands are colored grey and white; Phosphate and binding ligands are colored orange and blue; <i>m</i> -Dap is colored yellow.....	83
Figure 3.17. 1000X phase contrast images of wild-type and <i>csd4</i> variants <i>H. pylori</i> . (1H) is <i>csd4-Q46H</i> ; (1A) is <i>csd4-Q46A</i> ; (2Q) is <i>csd4-WT, rdxA:: csd4-WT</i> ; (2H) is <i>csd4-Q46H, rdxA:: csd4-Q46H</i> ; (1Q, 1H) is <i>csd4-WT, rdxA:: Csd4-Q46H</i>	84
Figure 3.18. Comparison between tripeptide substrate (left), tetrahedral intermediate (middle) and dipeptidyl phosphinate inhibitor (right). The scissile peptide bond is colored to blue.	86
Figure 3.19. Synthesis of the inhibitor 8	87
Figure 3.20. Stepwise reactions from compound 27 to compound 28	88
Figure 3.21. Proposed formation of compound 31	88
Figure 3.22. Dixon plot for determination of competitive inhibitor kinetic constants.	89
Figure 3.23. Electron density map of inhibitor 8 in the Csd4-Inhibitor complex. The observed electron density of the Csd4 bound inhibitor in A) The initial F_o-F_c map contoured at 3.5σ and B) the refined $2F_o-F_c$ map contoured at 1.5σ . The (S) configuration of the inhibitor stereocenter	

that is closed to the phosphinate is shown. Carbon atoms are colored blue, oxygen atoms red, and phosphorus atoms orange.	91
Figure 3.24. Comparison of the active sites of (A) Csd4-Inhibitor complex and (B) Csd4-Tripeptide complex. Zinc ion is colored to grey in both structures. The catalytic water is shown as a red sphere. Interacting amino acid residues are shown in CPK coloring with carbon in cyan, grey and orange. Carbon atoms in the inhibitor and the tripeptide substrate are colored light blue and yellow, respectively. Oxygen, nitrogen and phosphorus atoms are shown in red, blue and orange, respectively.	92
Figure 3.25. Structural alignment of the active site of the Csd4-Inhibitor and the Csd4-Tripeptide complex. The Zn (II) binding motif Glu49, His128 and Gln46 are shown with carbons in grey. The zinc ion is colored as grey sphere for Csd4-Tripeptide and as a blue sphere for Csd4-Inhibitor, respectively. Carbon atoms of the tripeptide are colored yellow, and those of the inhibitor are blue. Oxygen, nitrogen and phosphorus atoms are shown in red, blue and orange respectively.	92
Figure 3.26. Proposed mechanism of Csd4 catalyzed hydrolysis of the tripeptide substrate.	93
Figure 3.27. DIC microscopy images of the <i>C. jejuni</i> wild-type (left) (natural growth, control) and <i>C. jejuni</i> wild-type treated with 2.3 mM inhibitor (right) for 24h.	95
Figure 3.28. DIC microscopy images of the <i>C. jejuni</i> $\Delta kpsM$ (left) (natural growth, control) and <i>C. jejuni</i> $\Delta kpsM$ treated with 2.3 mM inhibitor (right) for 24h.	95
Figure 3.29. Strain shape distribution of <i>C. jejuni</i> wild-type (natural growth) and wild-type treated with 2.3 mM inhibitor for 24h.	98
Figure 3.30. Strain shape distribution of <i>C. jejuni</i> $\Delta kpsM$ (natural growth) and $\Delta kpsM$ treated with 2.3 mM inhibitor for 24h.	99
Figure 3.31. Histogram displaying population density of <i>C. jejuni</i> wild-type (natural growth, control) and <i>C. jejuni</i> wild-type treated with 2.3 mM inhibitor for 24h.	100
Figure 3.32. Histogram displaying population density of <i>C. jejuni</i> $\Delta kpsM$ (natural growth, control) and <i>C. jejuni</i> $\Delta kpsM$ treated with 2.3 mM inhibitor for 24h.	101
Figure 3.33. DIC microscopy images of the <i>H. pylori</i> wild-type (left) (natural growth, control) and wild-type treated with 2.5 mM inhibitor (right) for 24h.	103
Figure 3.34. Histogram displaying population density of <i>H. pylori</i> _WT (natural growth, control) and that treated with 2.5 mM inhibitor for 24h. Horizontal axis indicates the actual side curvature of the cell.	103
Figure 3.35. Strain shape distribution of wild-type <i>H. pylori</i> (natural growth) and that treated with 2.5 mM inhibitor for 24h. The horizontal and vertical axis show the actual length and side curvature of <i>H. pylori</i> cells.	104
Figure 3.36. Inhibitor design using phosphorus-containing pseudopeptides.	107

Figure 3.37. Synthetic strategy for Csd4 inhibitor 9	108
Figure A. 1. ^1H NMR (400 MHz, CDCl_3) spectrum of compound 8	134
Figure A. 2. ^{31}P (1H) NMR (400 MHz, CDCl_3) spectrum of compound 8	135
Figure A. 3. ^1H NMR (400 MHz, CDCl_3) spectrum of compound 10	136
Figure A. 4. ^{31}P (1H) NMR (400 MHz, CDCl_3) spectrum of compound 10	137
Figure A. 5. ^1H NMR (400 MHz, MeOH) spectrum of inhibitor 1	138
Figure A. 6. ^{31}P (1H) NMR (400 MHz, MeOH) spectrum of inhibitor 1	139
Figure A. 7. ^1H NMR (400 MHz, CDCl_3) spectrum of compound 19	140
Figure A. 8. ^{31}P (1H) NMR (400 MHz, CDCl_3) spectrum of compound 19	141
Figure A. 9. ^1H NMR (400 MHz, CDCl_3) spectrum of compound 20	142
Figure A. 10. ^{31}P (1H) NMR (400 MHz, CDCl_3) spectrum of compound 20	143
Figure A. 11. ^1H NMR (400 MHz, CDCl_3) spectrum of compound 21	144
Figure A. 12. ^{31}P (1H) NMR (400 MHz, CDCl_3) spectrum of compound 21	145
Figure A. 13. ^1H NMR (400 MHz, CDCl_3) spectrum of compound 22	146
Figure A. 14. ^{31}P (1H) NMR (400 MHz, CDCl_3) spectrum of compound 22	147
Figure A. 15. ^1H NMR (400 MHz, MeOH) spectrum of inhibitor 2	148
Figure A. 16. ^{31}P (1H) NMR (400 MHz, MeOH) spectrum of inhibitor 2	149
Figure A. 17. ^1H NMR (400 MHz, CDCl_3) spectrum of compound 11	150
Figure A. 18. ^{31}P (1H) NMR (400 MHz, CDCl_3) spectrum of compound 11	151
Figure A. 19. ^1H NMR (400 MHz, MeOH) spectrum of inhibitor 3	152
Figure A. 20. ^{31}P (1H) NMR (400 MHz, MeOH) spectrum of inhibitor 3	153
Figure A. 21. ^1H NMR (400 MHz, CDCl_3) spectrum of compound 23	154
Figure A. 22. ^1H NMR (400 MHz, CDCl_3) spectrum of compound 25	155
Figure A. 23. ^1H NMR (400 MHz, CDCl_3) spectrum of compound 26	156
Figure A. 24. ^1H NMR (400 MHz, MeOH) spectrum of tripeptide substrate.	157
Figure A. 25. ^1H NMR (400 MHz, CDCl_3) spectrum of compound 31	158
Figure A. 26. ^1H NMR (400 MHz, CDCl_3) spectrum of compound 34	159
Figure A. 27. ^{31}P (1H) NMR (400 MHz, CDCl_3) spectrum of compound 34	160
Figure A. 28 ^1H NMR (400 MHz, CDCl_3) spectrum of compound 35	161

Figure A. 29. ^{31}P (1H) NMR (400 MHz, CDCl_3) spectrum of compound 35	162
Figure A. 30. ^1H NMR (400 MHz, MeOH) spectrum of inhibitor 8	163
Figure A. 31. ^{31}P (1H) NMR (400 MHz, MeOH) spectrum of inhibitor 8	164

List of Symbols and Abbreviations

+TIP	plus-end tracking protein
δ	chemical shift (ppm)
λ	wavelength
Å	angstrom
[E]	enzyme concentration
[S]	substrate concentration
[I]	inhibitor concentration
Ac	acetyl
Ac ₂ O	acetic anhydride
AcOH	acetic acid
ACE	angiotensin-converting enzyme
ADP	adenosine diphosphate
AMP	adenosine monophosphate
ATP	adenosine triphosphate
Bn	benzyl
BOC	<i>tert</i> -butylcarbonyl
Bu	butyl
<i>C. jejuni</i>	<i>Campylobacter jejuni</i>
CAP-Gly	cytoskeleton-associated protein glycine rich
CAZy	carbohydrate-active enzyme
Cbz	benzyloxycarbonyl

CCP	cytosolic carboxypeptidase
CPA	carboxypeptidase A
CTT	C-terminal tail
DAP	diaminopimelic acid
DAPDH	diaminopimelic acid dehydrogenase
DCC	N, N'-dicyclohexylcarbodiimide
DCM	dichloromethane
DMF	dimethylformamide
<i>E. coli</i>	<i>Escherichia coli</i>
EDTA	ethylenediaminetetraacetic acid
ESI-MS	electrospray ionization mass spectrometry
EtOAc	ethyl acetate
EtOH	ethanol
Fmoc	fluorenylmethyloxycarbonyl
GDP	guanosine diphosphate
GlcNAc	N-acetyl glucosamine
GTP	guanosine triphosphate
<i>H. pylori</i>	<i>Helicobacter pylori</i>
HBTU	N, N, N', N'-tetramethyl-O-(1H-benzotriazol-1-yl)-uronium hexafluorophosphate
HMDS	hexamethylphosphoramide
HOBt	hydroxybenzotriazole
HPLC	high performance liquid chromatography

IC ₅₀	half maximal inhibitory concentration
IPTG	isopropyl β-D-galactopyranoside
<i>J</i>	coupling constant
<i>k_{cat}</i>	catalytic rate constant
<i>m</i>	meso
<i>m/z</i>	mass to charge ratio (mass spectrometry)
K _d	dissociation constant
kDa	kilodalton
K _I	inhibition constant
K _M	Michaelis constant
M	molar
MAP	microtubule associated protein
MCAK	mitotic centromere associated kinesin
Me	methyl
MeOD	deuterated methanol
MeOH	methanol
MHz	megahertz
MS	mass spectrometry
MT	microtubule
MTOC	microtubule organizing center
Mur	muramic acid
MurNAc	N-acetylmuramic acid

MW	molecular weight
NAD ⁺	nicotinamide adenine dinucleotide, oxidized form
NADH	nicotinamide adenine dinucleotide, reduced form
NADP ⁺	nicotinamide adenine dinucleotide phosphate, oxidized form
NADPH	nicotinamide adenine dinucleotide phosphate, reduced form
NMR	nuclear magnetic resonance
PBP	penicillin binding protein
PG	peptidoglycan
Pgp	peptidoglycan peptidase
Ph	phenyl
ppm	parts per million
PTM	post-translational modification
rt	room temperature
<i>S. aureus</i>	<i>Staphylococcus aureus</i>
SD	standard deviation
SDS-PAGE	sodium dodecyl sulfate-solyacrylamide gel electrophoresis
TACE	tumor necrosis factor- α -converting enzyme
TCP	tubulin carboxypeptidase
TEA	triethylamine
TEM	transmission electron microscopy
THF	tetrahydrofuran
TLC	thin layer chromatography

Tris	tris(hydroxymethyl)aminomethane
TTL	tubulin tyrosine ligase
TTLL	tubulin tyrosine ligase- <i>like</i>
TMS	trimethylsilyl
UDP	uridine 5'-diphosphate
UPP	undecaprenyl diphosphate
UV-Vis	ultraviolet-visible
WT	wild-type

Common Amino Acid Abbreviations

A	Ala	Alanine
C	Cys	Cysteine
D	Asp	Aspartate
E	Glu	Glutamate
F	Phe	Phenylalanine
G	Gly	Glycine
H	His	Histidine
I	Ile	Isoleucine
K	Lys	Lysine
L	Leu	Leucine
M	Met	Methionine

N	Asn	Asparagine
P	Pro	Proline
Q	Gln	Glutamine
R	Arg	Arginine
S	Ser	Serine
T	Thr	Threonine
V	Val	Valine
W	Trp	Tryptophan
Y	Tyr	Tyrosine

Acknowledgements

First and foremost, I would like to show my deepest gratitude to my supervisor, Dr. Martin Tanner, a respectable, responsible and resourceful scholar, who has provided me with valuable guidance in every stage of my Ph. D. program. Without his enlightening instruction, impressive kindness and patience, I could not have completed my thesis. His keen and vigorous academic observation enlightens me not only in this thesis but also in my future study.

I shall extend my thanks to Dr. Michael Murphy and Dr. Anson Chan, for all their kindness and help. I would also like to thank Dr. Timin Hadi and Mrs Xu Li, who have helped me to develop the fundamental and essential academic competence. My sincere appreciation also goes to all my colleagues in Tanner Lab and Dr. Jessie Chen in Biology Service, who provided great academic and technical support for my research.

Last but not least, I would like to thank my parents, family and friends, especially Miss Siduo Zhang, for her encouragement and support.

Dedication

*To my parents, from whom I have got unconditional love and support
and inherited the great curiosity and passion for knowledge.*

1. Introduction

In this chapter, an introduction to two different topics involving amino acid ligation and peptide hydrolysis is presented. The first concerns a glutamic acid ligation enzyme that acts on tubulin (the protein component of microtubules). This is the subject of Chapter 2, where an inhibitor is synthesized and tested by *in vitro* assay. The second is a peptidoglycan protease that controls cell shape morphology in helical bacteria. This is the subject of Chapter 3 where the synthesis and testing of a substrate and a phosphinic acid inhibitor is presented.

1.1 Tubulin and Microtubules

1.1.1 Microtubules overview

The cytoplasm of eukaryotic cells contains not only the cytosol and organelles, but also an inner framework structure called the “cytoskeleton”. The cytoskeleton determines and maintains the physical shape of a cell, and consist of three types of fibrous protein: microfilaments, intermediate filaments, and microtubules (1) (Figure 1.1, Left). Intermediate filaments (Figure 1.1, Left: purple strings) are normally localized around the nucleus to restrict its movement. Microfilaments (Figure 1.1, Left: red strings) are short, thin contractile proteins linked to the cytoplasmic membrane. By comparison, microtubules (MTs) (Figure 1.1, green strings) are large, thick and long tubules structures spreading all over the cell (Figure 1.1, Right) (2).

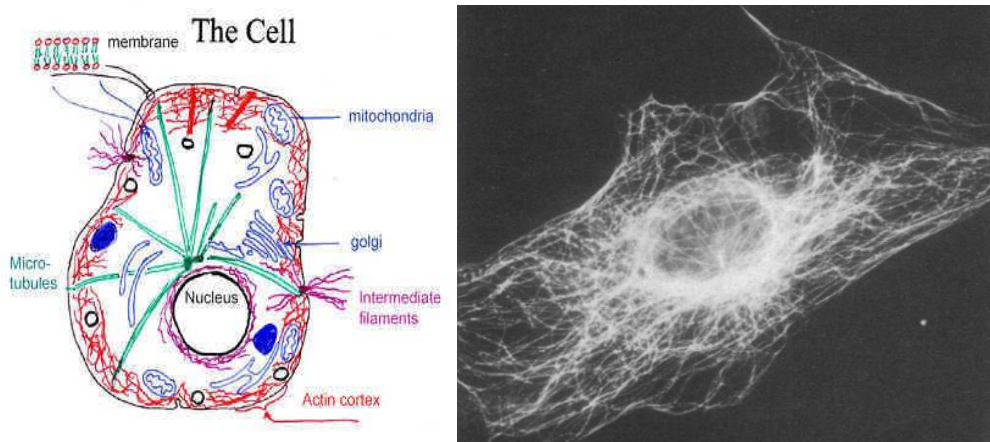


Figure 1.1. Left: The cytoskeleton in a eukaryotic cell (<http://www.nat.vu.nl/~fcm/images/resear1.jpg>).

Right: microtubule distribution in an interphase cell.

Tubulin is the basic protein building block of MT construction. Although tubulin isotypes are greatly diversified in different organisms, only four fundamental tubulin types are found. α and β tubulin are the most abundant, whereas γ tubulin is a minor form and is in the centrosome. δ tubulin is a very rare tubulin species, only found in the triplet MT structure of centrioles (3).

Stable MTs contain thirteen protofilaments, and the inner/outer diameters are 14/25 nm (Figure 1.2). α tubulin and β tubulin are highly conserved proteins of very similar structure (4,5). These two tubulin monomers first form a heterodimer by non-covalent interactions. The polarity of the monomers makes the assembly arrange in a head-to-tail pattern (6). α and β Tubulin bind tightly at their non-polar interface, leaving polar interfaces on the top of a β tubulin and the bottom of an α tubulin for binding with neighboring tubulin dimers. The linear protofilament structure elongates as the head-to-tail binding keeps extending. Finally, the linear filamentous structures assemble laterally to produce the cylindrical MT lattice.

MTs are continuously polymerizing and depolymerizing; polymerization occurs at the plus (+) end, and depolymerization occurs at the minus (-) end (1) (Figure 1.3). During MT assembly, each α and β tubulin has a GTP molecule associated with its binding interface. The GTP-tubulin drives polymerization and the growth of MTs at their plus end. Thus, the polymerizing side is called a GTP-cap. On the other hand, MT depolymerization involves the GTP on β tubulin hydrolyzing to GDP at the minus end of the MT. As the GDP-associated tubulin is less stabilized by electrostatic interactions than the GTP-associated species, depolymerization occurs at the minus end. The continuous assembly/deassembly processes is called dynamic instability, which is essential for the fast remodeling of MTs in cells (7).

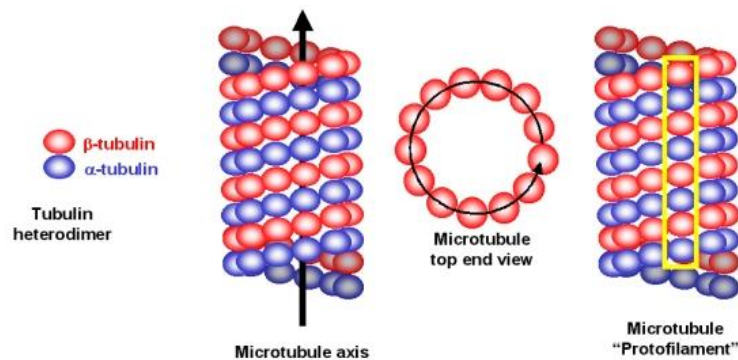


Figure 1.2. Microtubule structures.

(<http://www.mikeblaber.org/oldwine/BCH4053/Lecture30/Lecture30.htm>).

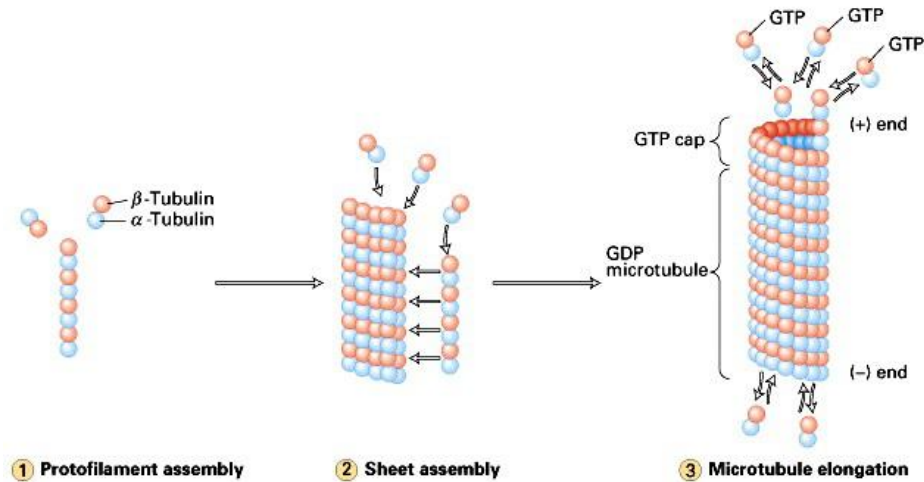


Figure 1.3. Microtubules assembly and dynamic instability

(http://www.pha.jhu.edu/~ghzheng/old/webct/note2_6.files/F19-11.jpg).

As a major component of the cytoskeleton, MTs sustain the physical rigidity and the shape of a cell. MTs also provide tracks for intracellular transport of cargo molecules and movement of organelles. MTs also provide signaling patterns to MT associated proteins (MAPs). MAPs are proteins which interact with MTs, and include MT motor proteins and non-motor regulator proteins. Kinesins (8) and dyneins (9) represent two main MT motor protein families, and they move to opposite directions along MTs (Figure 1.4) (10). Kinesin is the motor protein that moves towards the plus end of MTs. Kinesin is usually dimerized and contains two light chains and two heavy chains. The heavy chain has a coiled coil structure with a bulky globular head motor domain. Kinesin proceeds along the MT with its head domain binding to both MT and ATP. The binding to ATP is essential in the movement mechanism, as ATP binding strongly increases the affinity of kinesin for MTs (11). Additionally, ATP hydrolysis provides the energy required for this movement. Dynein is the first identified MT motor protein and it moves towards the negative end of MT. Compared to kinesin, the structure of dynein is more complex as it contains two or three heavy chains and a varying number of light chains. The movement mechanism of dynein is similar to that of kinesin and also involves ATP binding. The non-motor MAPs comprise proteins that control MT polymerization/ depolymerization. For instance, MAP1, MAP2 as well as Tau from neurons are MAPs that stabilize MTs (12,13). Alternatively, spastin and katanin are MAPs that sever MTs (13,14). The plus-end tracking proteins (+TIPs) are MAPs that regulate MT interaction with cell membranes and organelles (15,16).

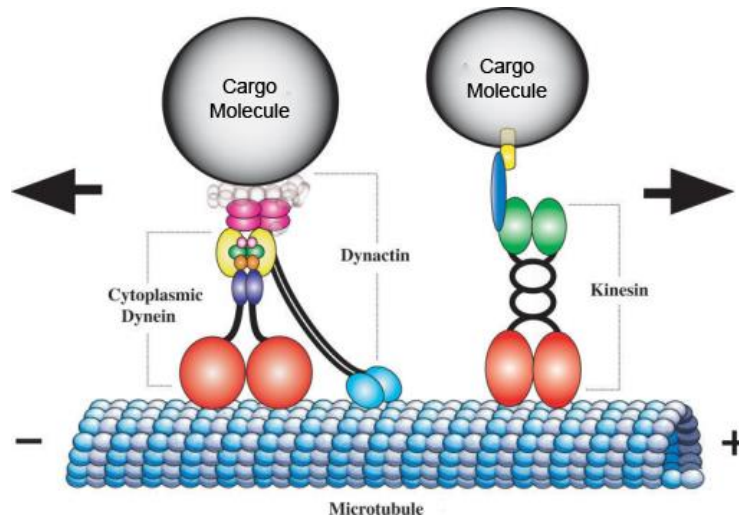


Figure 1.4. Dynein and kinesin are the major MT motor proteins.

In most eukaryotic cells, organelles including the centrosome, centrioles and mitotic spindles are intimately involved in cell division. All these organelles contain MTs as their core components. The centrosome is the organelle located nearby the nucleus, where all cytoplasmic MTs start growth. MTs have their negative end anchored in a structure called the MT organization center (MTOC). In most animal cells, the centrosome is the primary MTOC, and contains a pair of centrioles located inside (Figure 1.5). The centriole is an organelle with a straight rod shape. It forms a tubular structure of nine MT triplets, and a γ tubulin complex filling in the inner chamber of the centriole. The γ tubulin complex is thought to be essential for core nucleation of the MT minus end and fast growth of MTs.

For neuronal cells, the MTs located in dendrites and axons are called neurotubules, which is a special type of MT that is extremely elongated (length up to 1 m) (Figure 1.6) (17). The neurotubule serves in the trafficking of signal molecules during synaptic transmission (18). Moreover, for eukaryotic cells with flagella and cilia, a key component is an organelle called the axoneme. The outer layer of the axoneme is covered by the plasma membrane, and the inner layer has a ring structure consisting of nine MT-based units (19) (Figure 1.7). Each unit contains a complete MT (with two dyneins bound) and an incomplete MT to form a microtubule doublet. The core part is formed by two complete MTs in a parallel manner, which is surrounded by the nine MT doublets.

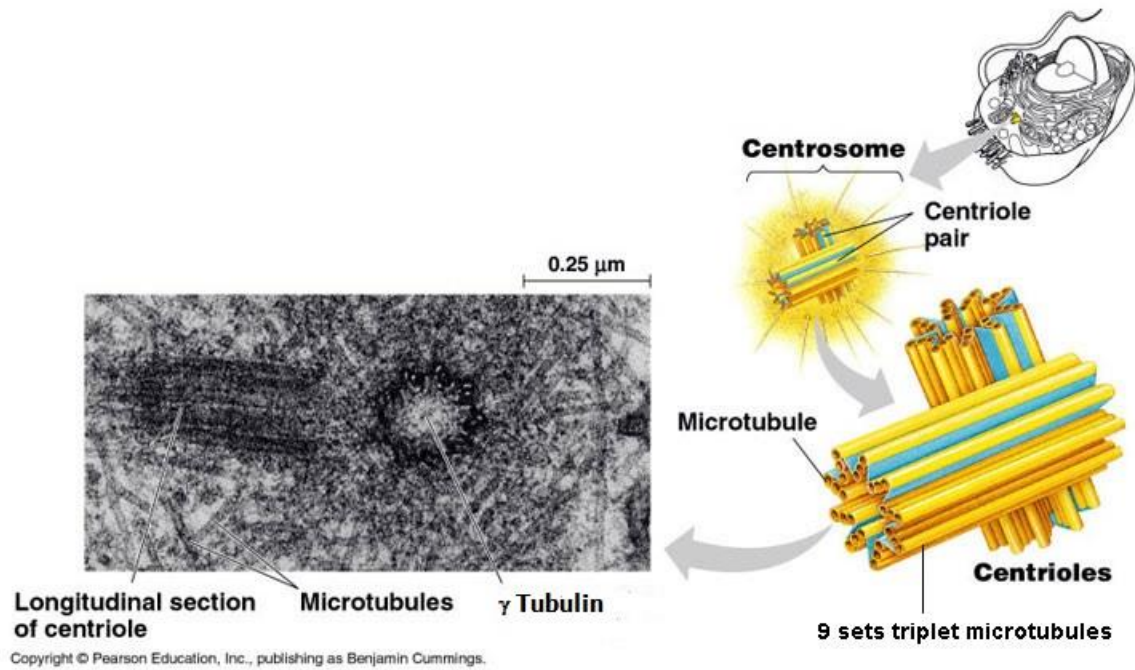


Figure 1.5. Organelles including centrosome and centrioles are constituted by MTs.
 (<http://fig.cox.miami.edu/~cmallery/150/cells/c7x22centrosome.jpg>).

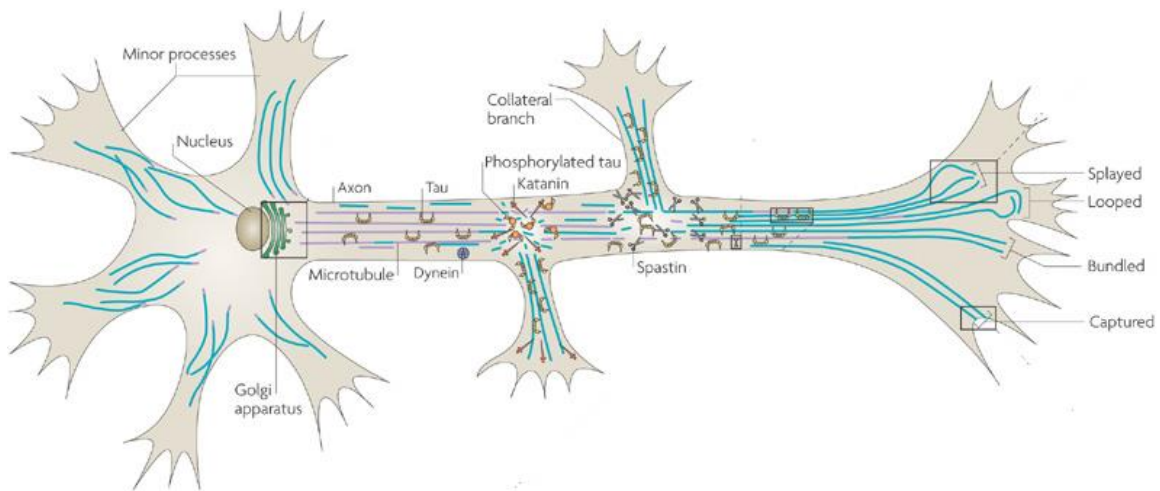


Figure 1.6. Microtubules (blue strings) in axons and dendrites in a neuronal cell.

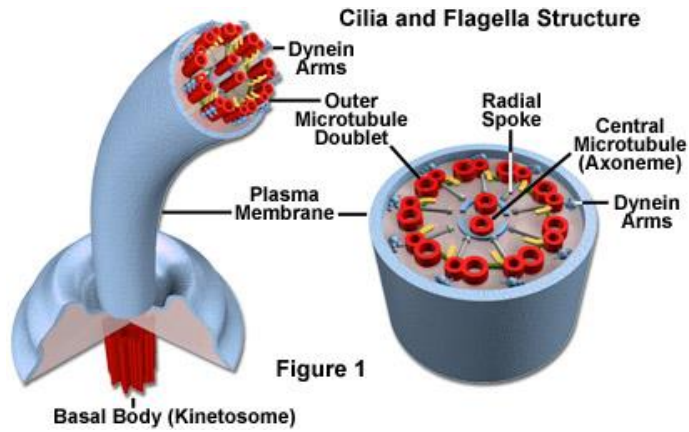


Figure 1.7. Microtubules in cilia and flagella.

(<http://micro.magnet.fsu.edu/cells/ciliaandflagella/ciliaandflagella.html>).

During mitosis, centrioles migrate in opposite directions to form the poles. Mitotic spindles emerge from the centrosome and will ultimately be linked to the chromosome. Driven by the motor MAPs, movement of the spindles along the longitudinal axis segregates the chromosome during metaphase (20) (Figure 1.8).

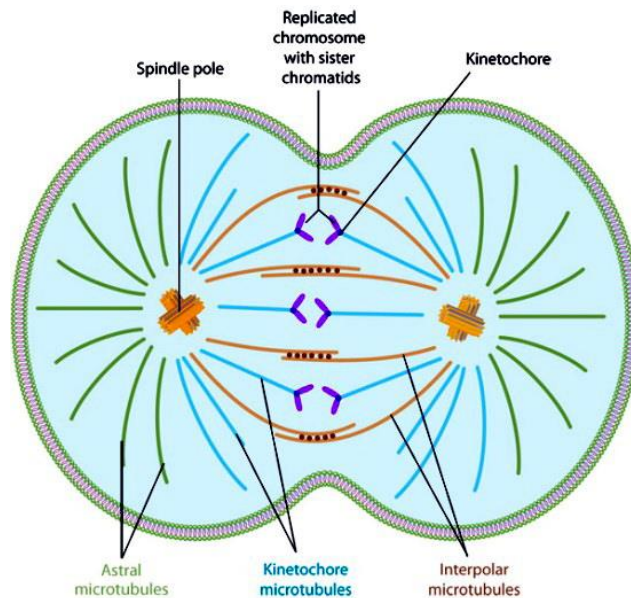


Figure 1.8. Mitotic spindles in cell mitosis (<http://www.nature.com/scitable/content/types-of-microtubules-involved-in-mitosis-14752887>).

1.1.2 Anti-cancer drugs and cell division

Due to the high assembly/disassembly rates of MTs required during mitosis, interference of MT dynamic instability becomes an important drug target. As division of tumor cells occurs much more frequently than with normal cells, cancer cells are more sensitive to anti-microtubule drugs or mitotic inhibitors. Representative anticancer medicines in this area are vinblastine/vincristine which interfere with MT assembly (21) (Figure 1.9, Left), and paclitaxel (taxol) which interferes MT disassembly (Figure 1.9, Right).

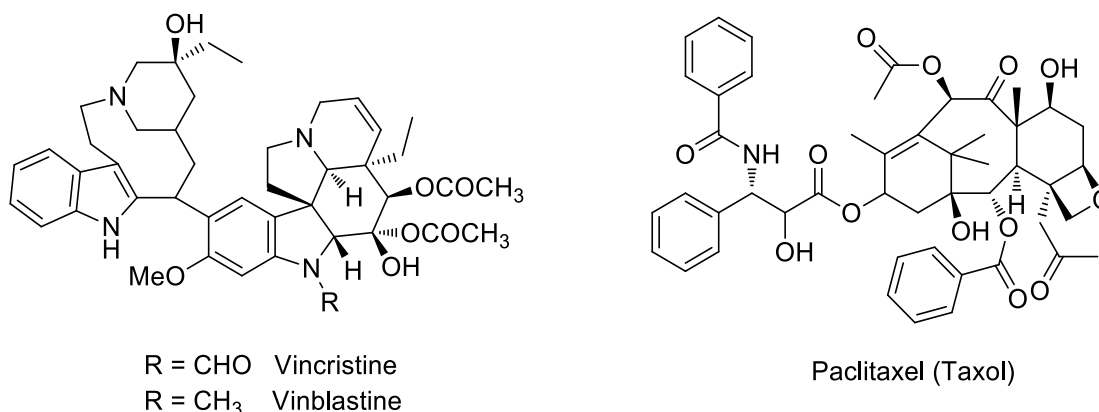


Figure 1.9. Anticancer medicines: vincristine/vinblastine (left) and paclitaxel (right).

Vincristine and vinblastine are alkaloids that originate from a Madagascar Periwinkle *Catharanthus roseus*. In the clinic, they are used to treat several kinds of cancer, including lung cancer, breast cancer and testicular cancer. At low concentrations, vinblastine/vincristine function through inhibition of the $\alpha\beta$ tubulin dimer assembly, so the polymerizing MT cannot elongate and mitosis is interrupted. At high concentrations, these drugs can stimulate the minus end to depolymerize, thus also disrupting the cell division process.

Paclitaxel (taxol) is another mitotic inhibitor. Unlike vinblastine or vincristine, taxol functions to stabilize the MT from depolymerization (22). It is widely used to treat lung, ovarian and breast cancers. Paclitaxel is originated from the bark of the pacific yew, *Taxus brevifolia*. Its mechanism involves stabilizing the lateral interaction between protofilaments, thus preventing MTs generated during metaphase from deassembly. Through this mechanism, paclitaxel also pauses mitosis at a intermediate stage and leads to cell apoptosis.

1.1.3 The post-translational modifications of MTs

For many genetically encoded proteins, the “prototype” formed after translation needs to be altered to reach the fully functional form. This process is referred as a post-translational modification (PTM). PTMs involve either the incorporation of different functional moieties (such as phosphate, saccharide, amino acid residue, peptide linker or lipid group) or proteolysis at specific sites. These modifications may help proteins fold/function properly, mediate interactions with other biomolecules or insert a signal sequence to tell the carrier where to deliver the protein (23-26).

PTMs of microtubules are thought to be an important factor in allowing for their diverse functions (Figure 1.10). For instance, modified MTs are thought to serve as recognition sites for Microtubule Associated Proteins (MAPs). Single molecule modifications, including deetyrosination/tyrosination, acetylation/deacetylation and phosphorylation, could serve as an ON/OFF switch signal for regulator proteins. Multiple molecular modifications, including polyglutamylolation and polyglycylation, could provide multi-level signals or codes to implement more complex regulations (23). Moreover, palmitoylation (27,28) and ubiquitination (29,30) of tubulin have also been reported.

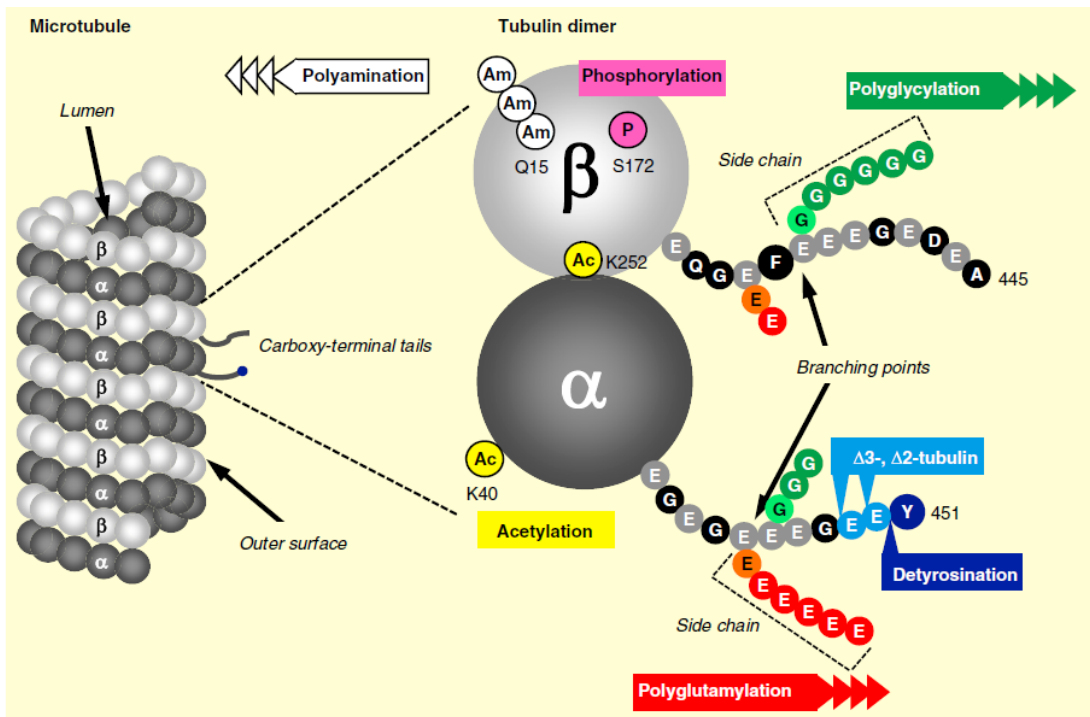


Figure 1.10. Post-translational modifications of MTs.

1.1.3.1 Single molecule PTMs (mono-PTMs)

Naturally encoded α tubulin contains a tyrosine at its C-terminal position. Tubulin detyrosination/tyrosination is a cyclic process that removes/adds this C-terminus Tyr (Figure 1.10, Blue Tag).

The tubulin detyrosinase enzyme that removes the tyrosine has not been characterized thus far (31). The enzyme tubulin tyrosine ligase (TTL) accounts for the tyrosination (32,33), and is the first discovered tubulin modifying enzyme. This cycle is closely related to the MTs dynamic instability. Most stable MTs have been found to be highly detyrosinated, and TTL is most active on depolymerized tubulin. The detyrosinated tubulin (detyr-tubulin) has a glutamate exposed in the C-terminal position, which can be removed by enzymes called cytosolic carboxypeptidases (CCPs) (34). The resulted tubulin (called $\Delta 2$ -tubulin) is irreversibly modified and cannot be converted back to detyr-tubulin (35). The CCP enzymes also act as the deglutamylases in the MT polyglutamylation/ deglutamylation cycle.

The tyrosination/detyrosination cycle has a significant impact on many cellular functions. Genomic analysis has found there is only one TTL enzyme coded in the genome. Further studies showed that TTL knockout mice died soon after birth, most probably due to the mislocation of a MT plus end tracking protein (+TIP) CLIP170 (36,37). Moreover, the MTs in neurons were highly detyrosinated, which is very likely involved in synaptic vesicle transport driven by kinesin-1 (38).

Few phosphorylation studies have been published so far (Figure 1.10, Pink Tag). The only site identified to be phosphorylated is the S172 residue in β tubulin. Two enzymes have been reported to be the phosphorylases: Cyclin-dependent kinase 1 (CDK1) (39) and tyrosine kinase (Syk) (40). CDK 1 is responsible for the S172 phosphorylation (Figure 1.11, Last Entry), and Syk may phosphorylate a residue in the C-terminal tail (CTT) region (site unspecified).

Acetylation is one of the unique PTMs, as it is found on the luminal surface of MTs (Figure 1.10, Yellow Tag). Positions that have been reported to be acetylated are K40 of α tubulin, and K252 of β tubulin. Of particular importance is K252 as it is positioned at the boundary surface between the $\alpha\beta$ tubulin dimer. It may affect the dynamic assembly/deassembly of MTs. The cellular function of this PTM still remain unclear. Mutagenesis studies on K40 in several organisms did not influence either the phenotype or survival rate. Other studies showed that the kinesin-1 protein has higher binding affinity to MTs with higher acetylation levels. Antibody stain results found that flagellar, ciliary and neuronal cells are the most highly acetylated regions. Two

acetyltransferases α TAT/ Mec-17 and Atat-2 have been discovered to function in MT acetylation (K40 site) (Figure 1.11, 1st Entry) (41,42). Two other enzymes HDAC6 and SIRT2 have been reported to remove the acetyl group from MTs (K40 site) (43).

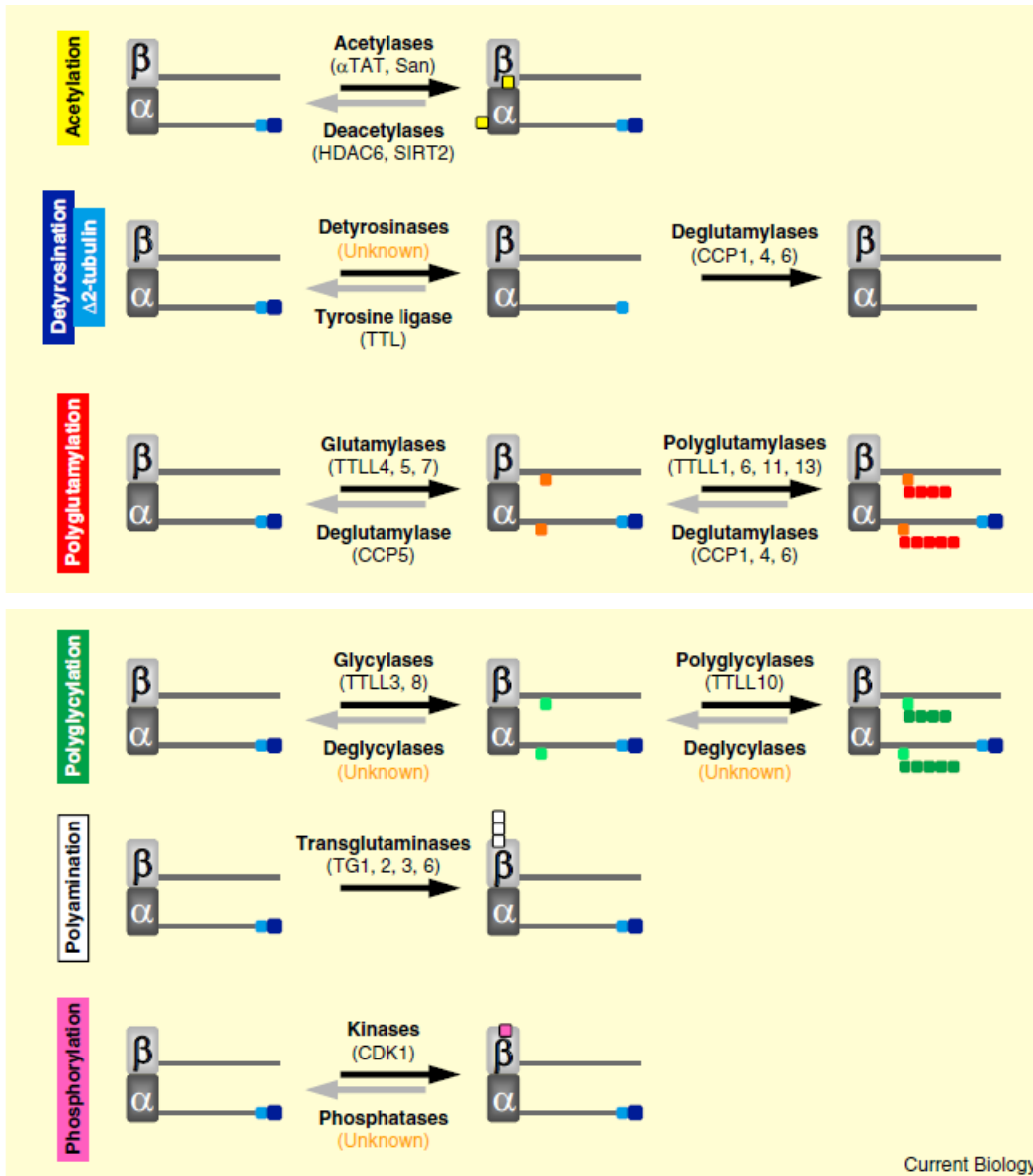


Figure 1.11. Enzymes involved in tubulin PTMs. C- terminal tyrosine is presented as dark blue cube (bigger); C-terminal glutamic acid is blue cube; side chain glutamic acid is colored orange (branch point) and red (extended); side chain glycine is light green cube (branch point) and green cube(extended); side chain amine is white cube and phosphate is pink cube.

1.1.3.2 Multiple molecule PTMs

Polyglutamylation (Figure 1.10, Red Tag) and polyglycylation (Figure 1.10, Green Tag) are processes that add multiple glutamates or glycines to glutamate residues in the CTT region of both α and β tubulin (44). Since the CTT region is displayed outward from the surface of an intact MT, these modifications greatly change the surface properties of the MT. The enzymes responsible for these reactions were discovered to bear sequence similarity to members of the TTL enzyme family, so they were given the name tubulin tyrosine ligase *like* enzymes (TTLLs). In the TTLL enzyme family, TTLL3, 8 and 10 are polyglycylation enzymes (Figure 1.11, 4th Entry) (45,46), and TTLL1, 4, 5, 6, 7, 11 and 13 are polyglutamylases (Figure 1.11, 3rd Entry) (33). Both glutamylation and glycylation are reversible PTMs. Although the deglycylation enzymes are still unknown, six deglutamylation enzymes of the cytosolic carboxypeptidase family have been identified. Interestingly, with either modification, each TTLL enzyme has a substrate preference for either α or β tubulin. Moreover, each of the TTLL family members also has preference to implement initiation (addition of the 1st Glu or Gly) or elongation (addition of the subsequent residues), although some members have been proposed to do both.

To date, polyglycylation has only been found in the MTs of the axoneme, the core component of cilium and flagellum, suggesting it is likely related to cell motility (47). Other studies showed that the lack of specific glycylation enzymes in mouse sperm results in complete depolymerization. The cellular function of polyglycylation is not fully understood. Details about the mechanism and function of polyglutamylation/deglutamylation will be discussed in Section 1.1.4.

Several other modifications have been discovered in recent years, such as polyamination (Figure 1.10, White Tag), palmitoylation, ubiquitination, methylation and glycosylation. Their cellular functions still remain unclear and need further examination. Initial studies have suggested polyamination could be related to MTs' dynamic instability; palmitoylation is involved in the interactions between MT and cell membrane proteins; and ubiquitination may be related to the degradation of misfolded MTs.

1.1.4 Polyglutamylation and TTLL enzymes

1.1.4.1 Enzymes and catalysis

Polyglutamylation involves the incorporation of several glutamic acid residues onto a glutamate side chain in the C-terminal tail (CTT) of tubulin (Figure 1.12). This process has been observed in

both free tubulin and assembled MTs. The normal length of the side chain is 1 – 6 glutamates, however the longest chain could be up to 20 glutamates (48). The incorporation of the 1st Glu only occurs at the γ - carboxylate position of the tubulin Glu, and is referred to as initiation. The incorporation of all subsequent Glu residues could potentially occur at either the α - or γ - position of the previous Glu, and are referred to as elongation. The linkage structure (α - vs γ -) has not been well studied and remains a question in this field.

Seven enzymes in the TTLL family have been identified as glutamylases, but no structural information on any TTLL is available. As it is difficult to overexpress and purify these enzymes, their catalytic function as initiators or elongases are not conclusive. Generally, TTLL4 and 5 are thought to be initiases, and TTLL1, 6, 11, 13 are considered to be elongases. It is noteworthy that different homologues of the same enzyme clade could have different catalytic preferences. For instance, mice TTLL6 is α tubulin specific enzyme, while its homologue TTLL6a from *Tetrahymena thermophile* is a β tubulin specific enzyme (49). TTLL7 is the only enzyme that has been overexpressed in *Escherichia coli* and purified to homogeneity. Previous studies showed that it prefers β tubulin, and catalyzes both initiation and elongation (50). Additionally, TTLL7 was observed to be inhibited by C- terminal peptides of β III or IV tubulin with ~20 amino acids at mM concentrations (50), suggesting the C-terminal peptide potentially serves as substrate. The enzymes that catalyze the reverse reaction belongs to the cytosolic carboxypeptidase (CCP) family. Six CCP enzymes have been identified recently and CCP5 was reported to remove the first-added Glu (the branch point Glu).

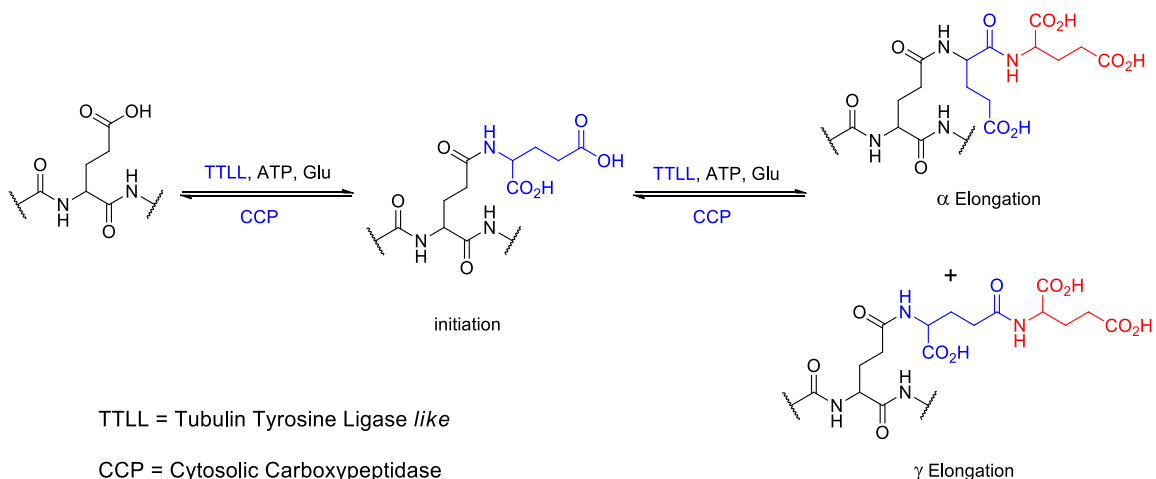


Figure 1.12. Chemistry of polyglutamylation/deglutamylation.

The conserved catalytic domain implicates the TTLs as members of a large enzyme superfamily of ADP forming ligases (51). By analogy to the well-studied enzyme D-Ala-D-Ala ligase of this superfamily (52), the mechanism of TTL glutamylation is thought to include three major steps (Figure 1.13). In the first step is activation by ATP. The γ -glutamate side chain in the tubulin C-terminus is phosphorylated by ATP. Next, the active phosphoryl ester species undergoes a nucleophilic attack from the amino group of free glutamate. This forms a tetrahedral intermediate and is the rate limiting step of catalysis. The final step involves collapse of the intermediate in which the phosphoryl leaving group departs and a Glu-Glu peptide bond is formed.

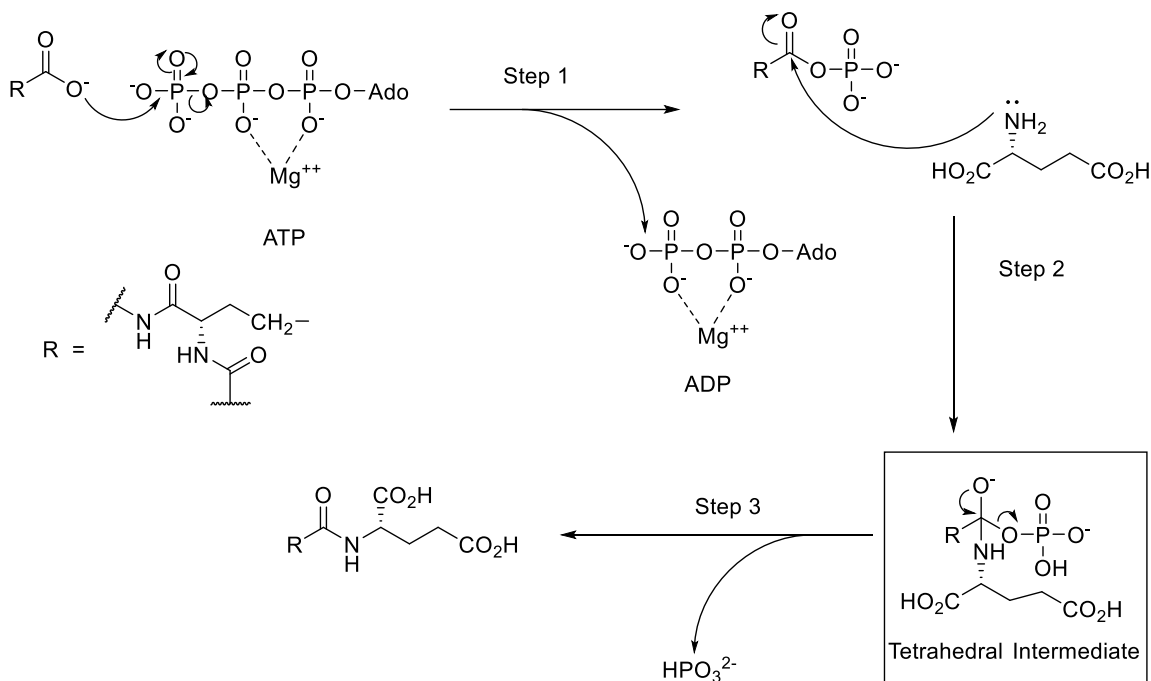


Figure 1.13. Mechanism of TTL glutamylation.

1.1.4.2 Characteristics and cellular functions of polyglutamylation

Compared to other PTMs, polyglutamylation has several unique characteristics. Firstly, polyglutamylation has more potential sites than mono-PTMs as the modification sites for single molecule addition are restricted. For instance, acetylation occurs specifically at K40 of α tubulin and K252 of β tubulin. Tyrosination/detyrosination only occurs at the C-terminal Tyr position of α tubulin. In contrast, many more glutamylation sites are possible because of the sequence

diversity of CTTs in different tubulin isotypes as well as in different organisms. The variety of sites and chain lengths gives glutamylation the possibility to code for more complex functions.

Secondly, polyglutamylation is more prevalent than polyglycylation. Polyglycylation is specifically observed in axonemes, therefore only cells containing cilia and flagella have polyglycylated MTs. Glutamylation is mainly found in centrioles and axonemes, however neuronal cells are also found to be highly glutamylated. Moreover, the TLL family has more members than any of the other PTM enzyme families. The polyglutamylation/deglutamylation cycle involves seven TLL enzymes and six CCP enzymes in total, which outnumbers any other tubulin PTM enzyme family. Even enzymes with similar catalytic function may play distinct physiological roles. A recent publication reported that both CCP1 and CCP5 have dual functions in the removal of both the side chain glutamates and the branch point glutamate (53-55). However, this functional redundancy did not compensate for the loss of CCP5 activity in *Zebrafish* (53). The CCP5 knockout species showed a markedly different phenotype from the wild-type in the early growth stage.

Known cellular functions of polyglutamylation include two aspects: regulation of MT dynamic instability and regulation of MT associated motors. The regulation of MT dynamic instability involves two types of non-motor MAPs: MT Stabilizing proteins (e.g. Tau, MAP1 and MAP2) and MT severing proteins (e.g. spastin and katanin). Overexpression of TLL6 in HeLa cells resulted in a diminished size of the MTs, but in contrast, overexpression of TLL4 in the same cell line gave no such effect (56). As TLL6 usually forms a long polyglutamate side chain, and TLL4 generates a relative short side chain. This suggests that the extent of polyglutamylation could serve as a regulation signal that controls MTs-spastin interactions. In neuronal cells where MTs are also highly polyglutamylated, the interaction between MTs and Tau protects MTs from severing. Moreover, the axial extension of the MT towards the axon is essential for intracellular cargo transport.

The regulation of MT motors is critical for cell motility. Early *in vivo* studies with mice showed that the depletion of a TLL1 subunit caused reduced glutamylation levels declining in neuronal cells. Similar to polyglycylation, two recently studies in the organisms *Chlamydomonas reinhardtii* and *Tetrahymena thermophila* demonstrated that diminished polyglutamylation affects cilia motility. Moreover, the observation that some kinesin motors recognize specific MT tracks for the transport of cargo molecules in neuronal cells also suggested the existence of a signal-reading system. Because the MTs in neuronal cells are highly glutamylated and

polyglutamylation could be used to produce and adjust multi-level signals, it is considered to be a potential signal generator.

As studies on TTLL polyglutamylation have progressed, the interest in the relationship between PTMs and tumorigenesis keeps rising (21,57). One reason to account for the interest is the diversity of potential polyglutamylation substrates. Several non-tubulin proteins, including nucleosome assembly proteins (NAP1 and NAP2) and nucleocytoplasmic shuttling proteins (such as EB1, ANP32, and NF45) have been observed to undergo polyglutamylation in HeLa cells (58). This discovery also suggested a close relationship between TTLL regulation and nucleosome activities. Moreover, several different proteins could be activated or induced by polyglutamylation, thus TTLLs may regulate pathways not immediately related to tubulins. For instance, TTLL4 upregulation has been reported in pancreatic ductal adenocarcinoma, and interestingly it raised the polyglutamylation level of a non-tubulin substrate (57). The abundance of another TTLL family member, TTLL12 was observed in epithelial cells of prostate cancer patients (59). The MT severing protein spastin was found to be upregulated in glioblastomas, and another study reported spastin could be activated by high levels of tubulin polyglutamylation (60). The potential regulation relationship remains to be addressed.

The demonstration of a wide range of substrates for TTLL enzymes opened a door for understanding the generality of polyglutamylation in cells. These studies also reported that many other protein substrates contain glutamate-rich sequences, which are similar to the glutamate-rich CTTs in tubulin (58). As the CTT is the location of most PTM processes and is positioned on the outer surface of MTs, it is very likely that a peptide bearing the C-terminal sequence could act as a TTLL substrate. A preliminary study from *Weber et al* found that the shortest effective peptide sequence only contains 14 amino acids, and needs at least one glutamate near its C-terminus (61). The latest research on deglutamylase CCP5 has demonstrated this CCP family enzyme is also able to remove side chain glutamates from peptides (54). The fact that peptides serve as substrates for these enzymes demonstrate that full length tubulin is not required for activity. This suggests that small molecule inhibitors may also bind to these enzyme and serve to regulate activity. The design and testing of such compounds will be the focus of Chapter 2.

1.2 Peptidoglycan and Its Modifying Enzymes

The second half of this thesis will also deal with peptide formation and hydrolysis, but in a bacterial system. In the subsequent sections, background information on peptidoglycan and the bacterial cell wall will be provided.

1.2.1 Peptidoglycan and the bacterial cell wall

In most bacteria, the cytoplasm and nucleoid are encapsulated by the cell envelope structure (Figure 1.14), which is comprised of the cell wall and the cytoplasmic membrane (Gram-negative bacteria have an additional outer membrane) (62,63). The main component of the bacterial cell wall is the peptidoglycan (PG or murein) sacculus that is a three-dimensional network encompassing the cytoplasmic membrane. PG is composed of a linear disaccharide chain of alternating *N*-acetylglucosamine (NAG or GlcNAc) and *N*-acetylmuramic acid (NAM or MurNAc) residues linked in a β -1, 4 fashion. These carbohydrate chains are crosslinked by peptide chains which are appended to the lactate moiety of the MurNAc residues (Figure 1.15). The three-dimensional shape of PG produces structural rigidity, which maintains the cellular integrity and protects the organism against osmotic pressure and lysis. As PG is exclusively formed as a cell wall component of bacteria, it becomes an excellent target for pharmaceutical research (62). The enzymes involved in PG biosynthesis are unique, and do not have any mammalian homologues (64). The developments of inhibitors against enzymes involved in several steps of PG metabolism have achieved great success, which include examples such as penicillin, cycloserine, and vancomycin.

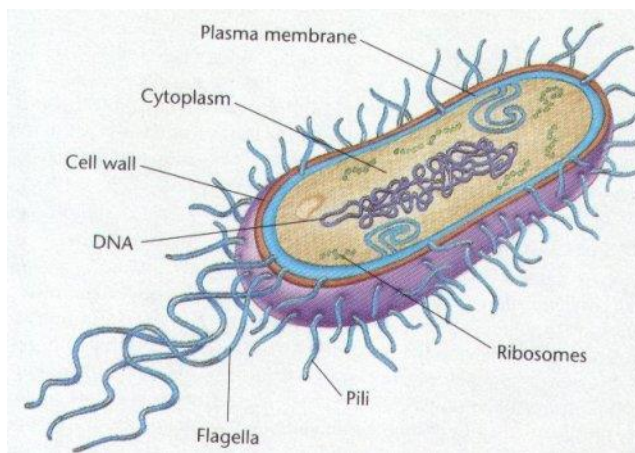


Figure 1.14. The bacterial cell envelope (<http://kdhellner.tripod.com/id15.html>).

Based on the structure of the cell wall, most bacteria species fall into two major categories: the Gram-positive bacteria and the Gram-negative bacteria. The PG membrane is the outermost layer for Gram-positive bacteria, and it is much thicker (Figure 1.16). The PG layer in Gram-negative bacteria is a thin layer located in the periplasmic space between the cytoplasmic membrane and the outer phospholipid membrane (Figure 1.16) (62,65). Unlike the templated synthesis of proteins (based on the mRNA sequences), the biosynthesis of PG does not follow any template thus it does not have a definite end point and an accurate molecular mass. In fact, glycan polymerization and peptide crosslinking is continuously proceeded throughout the bacteria's life cycle.

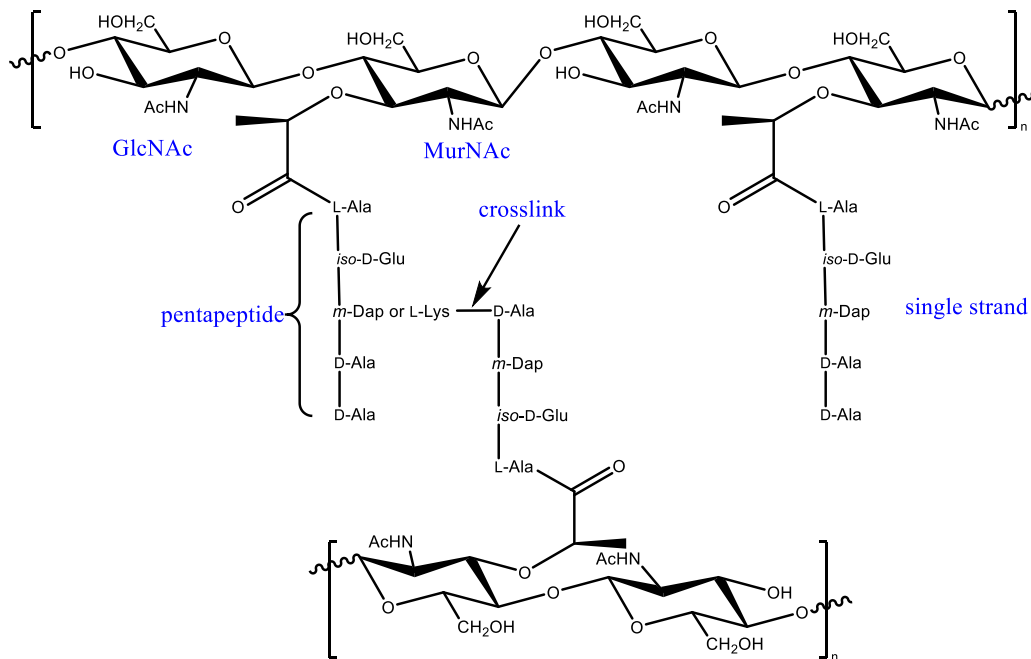


Figure 1.15. General repeating structure of peptidoglycan showing GlcNAc-MurNAc disaccharide and crosslinked pentapeptide.

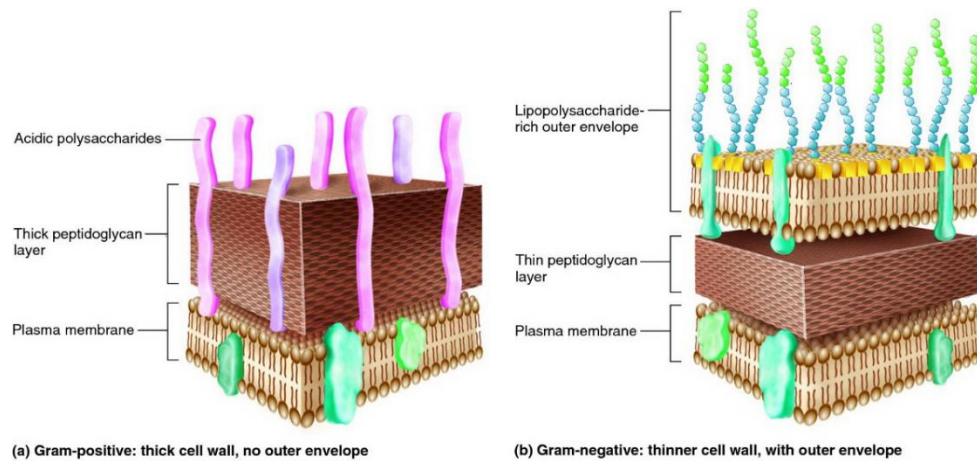


Figure 1.16. The cell wall structures of the Gram-positive (left) and the Gram-negative (right) bacteria (http://biology-forums.com/gallery/33_15_07_11_12_13_35.jpeg).

1.2.2 Peptidoglycan biosynthesis

The biosynthesis of PG includes three main stages (Figure 1.17) (66). The first stage is the synthesis of the MurNAc monosaccharide linked to a tetra- or pentapeptide, which takes place in the bacterial cytoplasm. In the second stage, the synthesized PG monomer is transported to the inner surface of the cytoplasmic membrane, in which the MurNAc precursor is first linked to a lipid phosphate (Lipid I) and then combined with GlcNAc (Lipid II). The final and the most important stage occurs in the extracellular periplasm, involving disaccharide chain polymerization as well as neighboring peptide strand crosslinking to obtain the three-dimensional network structure (63).

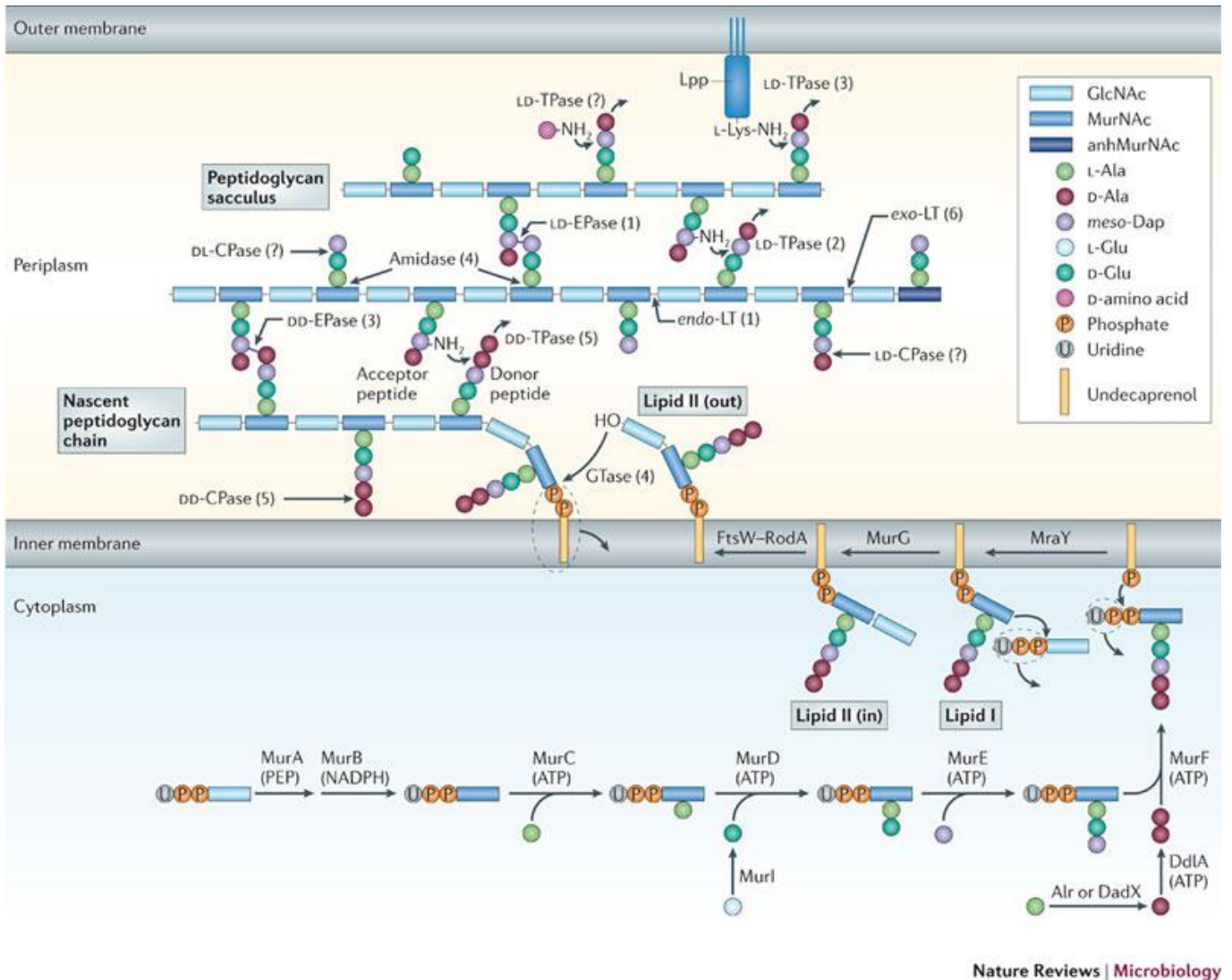


Figure 1.17. Overview of the peptidoglycan biosynthesis pathway.

1.2.2.1 The peptidoglycan biosynthetic pathway

The starting point of the PG biosynthetic pathway involves uridine diphosphate *N*-acetylglucosamine (UDP-GlcNAc) (Figure 1.18). The conversion of UDP-GlcNAc to UDP-MurNAc is catalyzed by the enzymes MurA and MurB. MurA is an enolpyruvyl transferase that adds the enolpyruvyl group from phosphoenolpyruvate (PEP) to the C-3 position of UDP-GlcNAc and forms enolpyruvyl UDP-GlcNAc (67-69). The next step is catalyzed by MurB, a NADPH-dependent reductase, which converts enolpyruvyl UDP-GlcNAc to UDP-MurNAc (70-72).

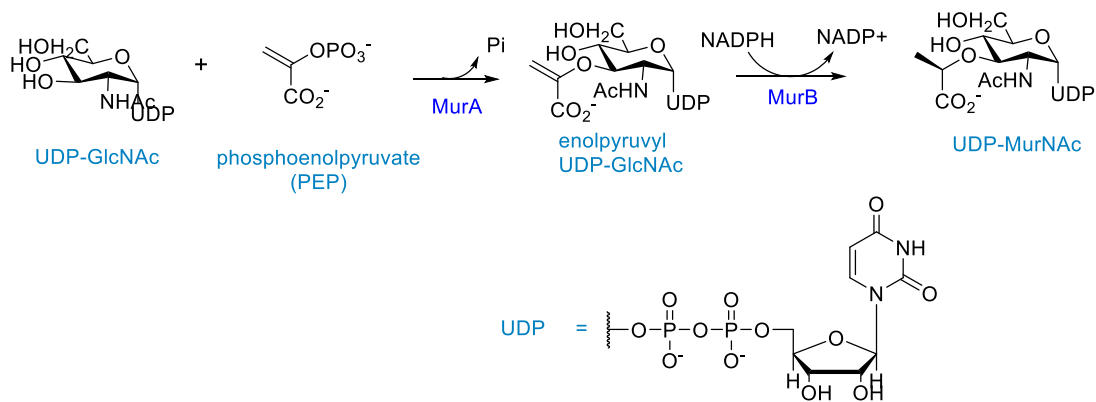


Figure 1.18. Biosynthesis of UDP-MurNAc.

The second part of this stage involves peptide chain elongation, and is catalyzed by the enzymes MurC – MurF. Each of these four enzymes adds one specific amino acid or dipeptide moiety to UDP-MurNAc, and all of them are highly conserved ATP-dependent ligases (73,74) (Figure 1.19).

MurC catalyzes the addition of an L-alanine to UDP-MurNAc, and MurD adds the subsequent D-glutamic acid, to generate UDP-MurNAc-L-Ala-D-Glu. These enzymes share high sequence similarity and utilize the same binding order for ATP, the UDP-MurNAc substrate and the amino acid substrate (the mechanism of ATP-dependent ligases is discussed in Section 1.1.3) (75).

MurE catalyzes the addition of the third amino acid: *meso*-diaminopimelic acid (*meso*-Dap) for all Gram-negative bacteria (e.g. *Helicobacter pylori* and *E. coli*) and a few strains of Gram-positive bacteria, or L-lysine for most Gram-positive bacteria (e.g. *Staphylococcus aureus*). These amino acids are added to the γ -carboxylate of the D-Glu to form an *iso*-Glu linkage. Structural studies demonstrated that the key site responsible for *meso*-Dap recognition in Gram-negative is Arg416 (*E. coli* numbering) which binds to the terminal carboxylic acid of *meso*-Dap. This Arg is replaced by an Ala or Asn in the Gram-positive homologue of *S. aureus* (76,77).

While MurC – MurE adds a single amino acid to their UDP-MurNAc (peptide) precursor, MurF adds a D-Ala-D-Ala dipeptide (Figure 1.19). Initially, L-Ala is converted to D-Ala by alanine racemase in the bacteria cytoplasm (Figure 1.19, panel). Then the D-Ala-D-Ala dipeptide is made by D-Ala-D-Ala ligase (52). Finally the dipeptidyl moiety is added to the main tripeptide chain to finish the synthesis of UDP-MurNAc-pentapeptide.

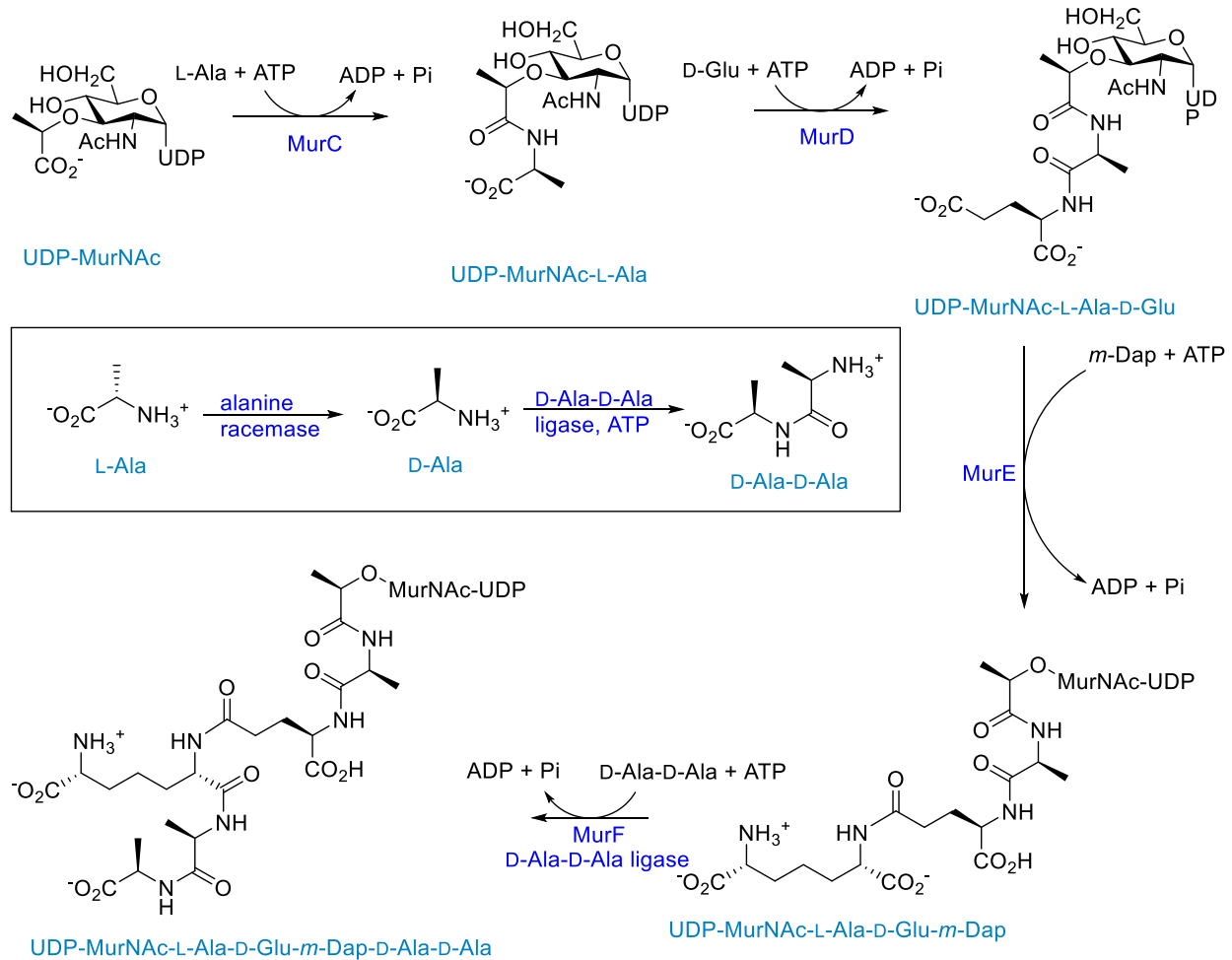


Figure 1.19. Biosynthesis of UDP-MurNac-L-Ala-D-Glu-*m*-Dap-D-Ala-D-Ala.

The UDP-MurNac-pentapeptide is translocated to the surface of the cytoplasmic membrane before the next reaction. The hydrophobic carrier undecaprenyl phosphate (UP) is then incorporated by *MraY* for the transport across the membrane (Figure 1.20) (78). The lipidic product of this prenyl transfer is commonly referred to as Lipid I.

The next step is formation of the final disaccharide that will ultimately undergo polymerization. This is catalyzed by the glycosyl transferase (GT) *MurG* which adds UDP-GlcNAc to Lipid I (Figure 1.20). The lipidic disaccharide product is similarly referred to as Lipid II. Structural results show that *MurG* contains two substrate binding domains. The one for UDP-GlcNAc binding is shared with many other members of the glycosyl transferase GT₂₈ CAZy family, but

the one for Lipid I binding is more characteristic of PG biosynthetic enzymes, in which several hydrophobic residues are located to accommodate the lipid moiety.

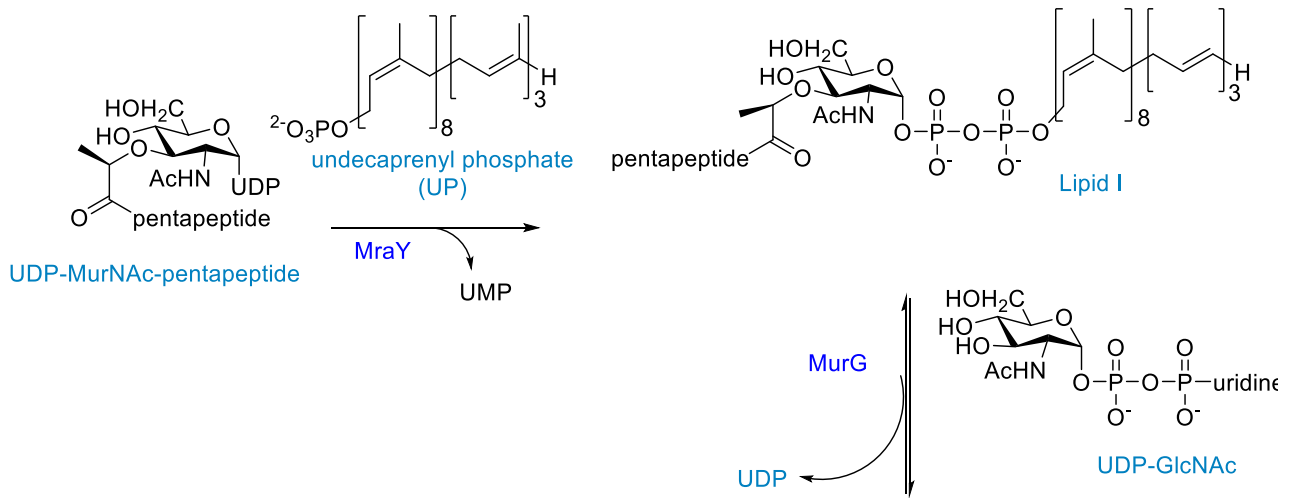


Figure 1.20. Synthesis of Lipid I and Lipid II.

The transfer of Lipid II from the inner surface of the cytoplasmic membrane to the periplasmic space has been studied for decades, since it was discovered that the translocation is not an energetically-favored process. The membrane carrier protein is known as a flippase. The initial flippase candidate was protein FtsW, but this assignment was brought into question as it also exists in cell wall deficient bacterial species. A recent major advance is the observation of FtsW transport activities *in vitro* (79). A Lipid II analog was used as guest and FtsW catalyzed flipping across a vesicle membrane was monitored, providing the first direct evidence that FtsW is a flippase (Figure 1.17).

Once Lipid II is transferred across membrane onto its outer surface, the stage is set for GlcNAc-MurNAc disaccharide polymerization and transpeptidation (TP) crosslinking. The linear glycan

chain extension involves the glycosyl transfer peptidoglycan polymerization (GT_{PGP}) reaction. The GT_{PGP} enzymes are integral membrane proteins and are historically named as penicillin-binding proteins (PBPs) (80). Some PBP members are monofunctional containing only a GT_{PGP} domain, whereas the other PBPs are bifunctional containing a GT_{PGP} domain as well as a TP domain.

The glycan chain polymerization starts with an initiation, in which two Lipid II molecules are linked (to form Lipid IV) and an undecaprenyl diphosphate (UPP) is released (Figure 1.21). Subsequent elongations add additional Lipid II groups to the main chain. The byproduct undecaprenyl pyrophosphate (UPP) is recycled by dephosphorylation to undecaprenyl phosphate (UP). Then UP is transferred back into cytoplasm and used to regenerate Lipid I/II pool. In fact, the dephosphorylation step is essential for bacteria as the UPP : UP ratio not only regulates the PG biosynthesis pathway but also involves several other pathways utilizing prenyl materials. Thus, the UPP dephosphorylase family is studied extensively as an important pharmacological target.

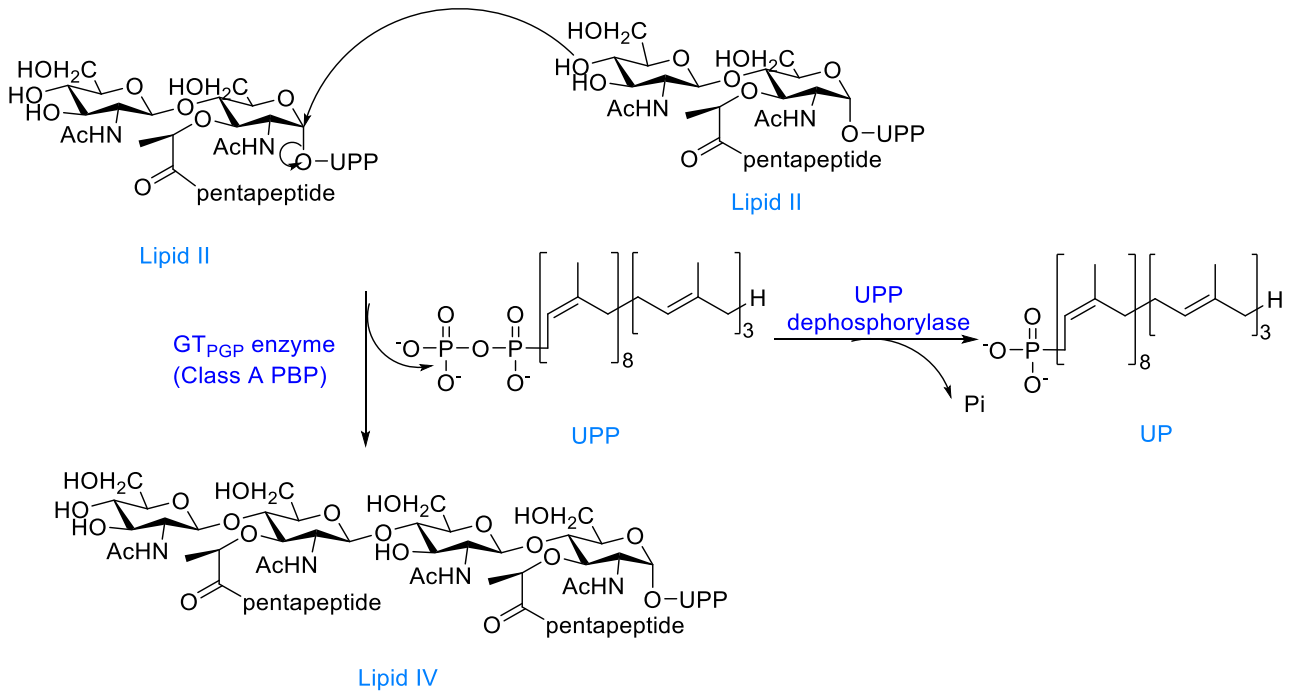


Figure 1.21. Glycan chain polymerization.

The crosslinking of adjacent pentapeptides after glycan polymerization involves transpeptidation reactions. The transpeptidase (TPase) superfamily includes two main categories: the high molecular mass (HMM) TPases and low molecular mass (LMM) TPases. The HMM TPases can be further divided into two different classes: A and B. Class A HMM family members are the bifunctional TPases, containing a *N*-terminal GT_{PGP} domain and a C-terminal TP domain. Class B HMM family members also have the C-terminal TP domain, but their *N*-terminal domain is not involved in PG biosynthesis. The LMM TPase family members are usually muropeptide modifying enzymes that catalyze carboxypeptidase trimming reactions (Figure 1.22). The trimming reactions involve hydrolysis of the terminal peptide bond and release of the amino acid at the terminal position. The trimmed muropeptide strand can only act as a donor rather than an acceptor in crosslinking transpeptidation, thus the LMM TPases regulates the degrees of PG crosslinking by this means.

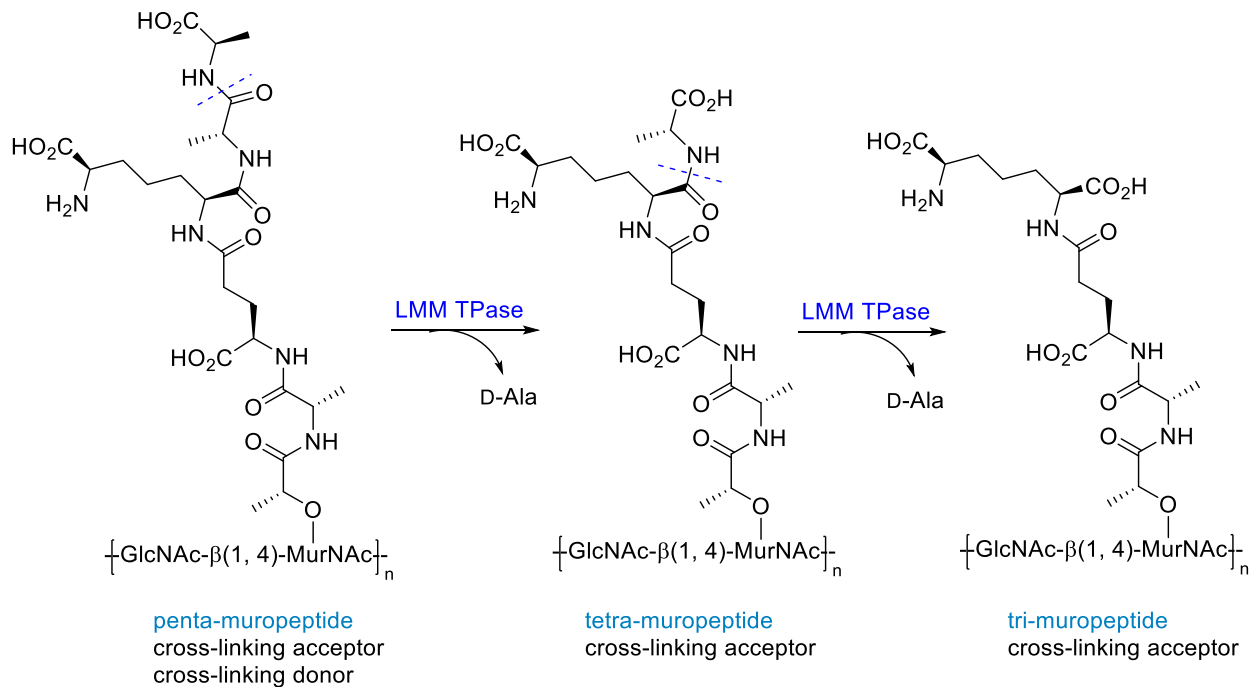


Figure 1.22. The LMM TPase trimming reactions.

The TP reaction mechanism begins with the donor peptide strand binding to the active site (Figure 1.23). Next a serine in the active site nucleophilically attacks the D-Ala-D-Ala peptide bond, and forms an acyl-enzyme intermediate. A subsequent substitution by a free amino group from the

neighboring acceptor chain then generates the crosslinkage. The source of the acceptor amino group differs in bacterial species. In most Gram-negative bacteria (e.g. *H. pylori* and *E. coli*), the free amine of *meso*-Dap attacks the intermediate (Figure 1.23 and Figure 1.24.B), while in Gram-positive bacteria, the nucleophilic amine could come from L-Lys (e.g. *Streptococcus pneumoniae*) or a pentaglycine peptide linker (e.g. *S. aureus*) (Figure 1.24.A). After the crosslinkage formed, the trimming TPases will remove the terminal D-Ala-D-Ala from the acceptor strand. These reactions follow a similar mechanism except that water serves as the nucleophile that attacks the acyl-enzyme intermediate instead of an amino group.

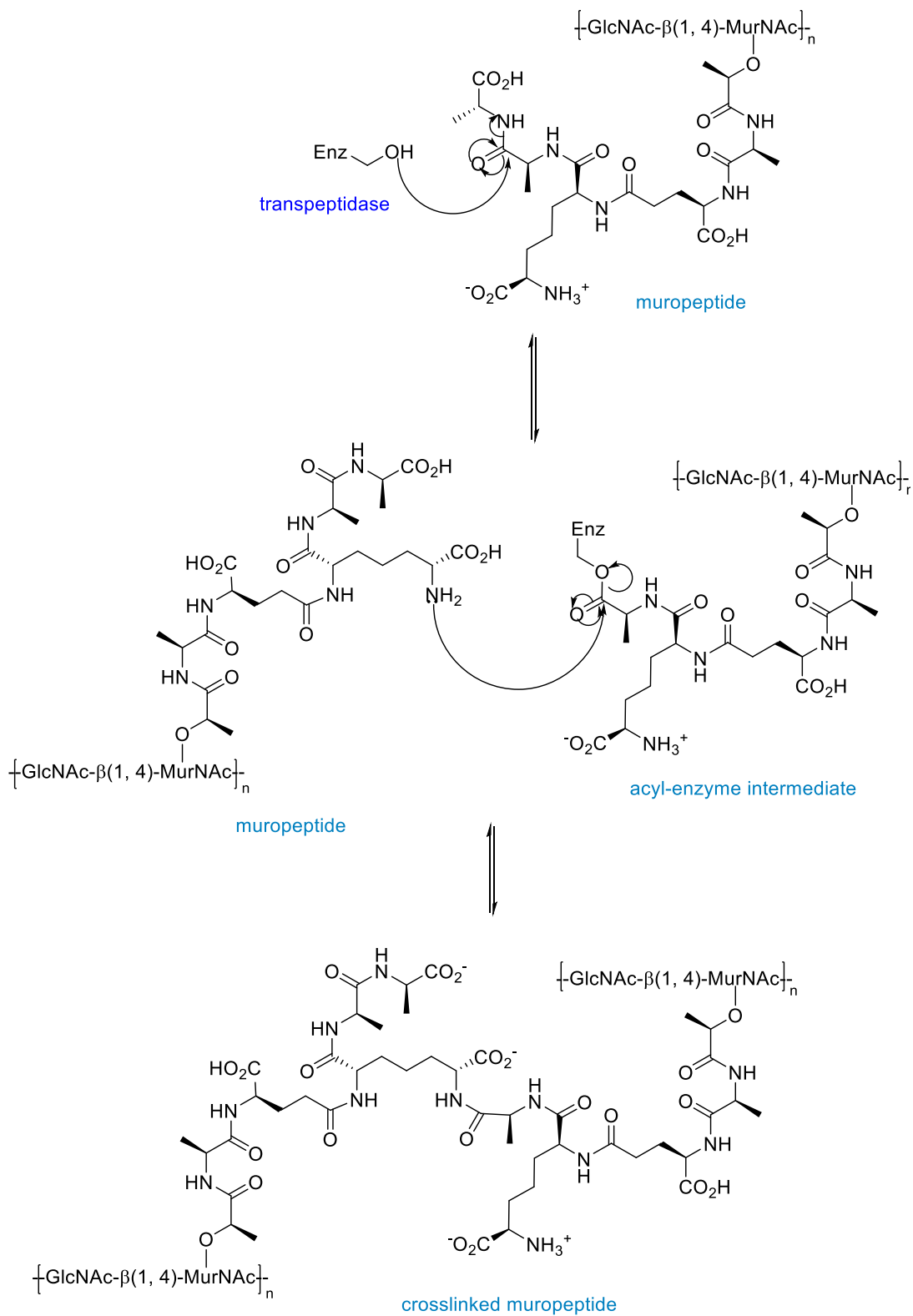


Figure 1.23. Mechanism of the transpeptidation reaction.

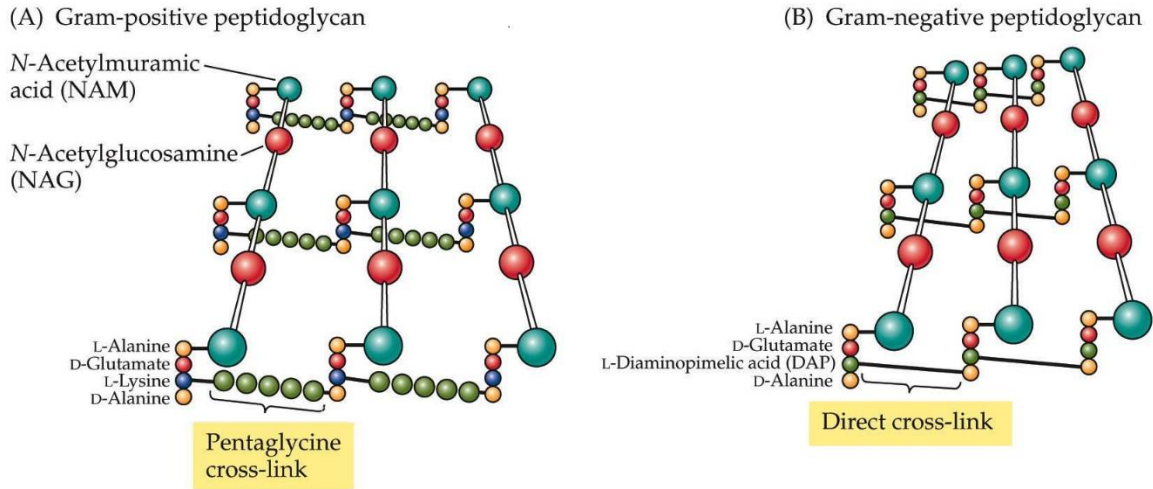


Figure 1.24. The different crosslinkage patterns in Gram-positive (A) and Gram-negative (B) bacteria (<http://www.studyblue.com/notes/note/n/ch-4-lecture-3/deck/2692055>).

1.2.2.2 Inhibitors targeting the PG biosynthetic pathway

Fosfomycin is a natural product antibiotic produced by the *Streptomyces* species (Figure 1.25, Left Top) (81). It is a PEP analogue that inactivates MurA by irreversibly forming a covalent C-S bond with the key residue Cys115. Fosfomycin is effective against Gram-negative bacteria, as these species contain glycerophosphate transporters that can ferry fosfomycin into the cell. However, for Gram-positive bacteria, that lack such transporters, fosfomycin does not perform very well in treating infections. Fosmidomycin and terreic acid are two other commonly used MurA inhibitors.

D-cycloserine is a D-Ala structural analogue, and has inhibitory effects on both alanine racemase as well as the D-Ala-D-Ala ligase (Figure 1.25, Left Bottom). Like fosfomycin, the D-cycloserine inactivation mechanism of alanine racemase also involves irreversible covalent bond formation (82,83). Vancomycin is a well-known inhibitor that blocks PG glycan chain growth and crosslinking (Figure 1.25, Right). It is a sequester that can tightly bind to the D-Ala-D-Ala moiety of the MurNAc pentapeptide, thus impeding interactions with PBPs (52). Bacteria with vancomycin-resistance mutate their D-Ala-D-Ala moiety to various structures (e.g. D-Ala-D-Lac)

to decrease the chelating affinity (84). In clinical trials, combinations of cycloserine and vancomycin have been used to treat multidrug resistant bacterial infections.

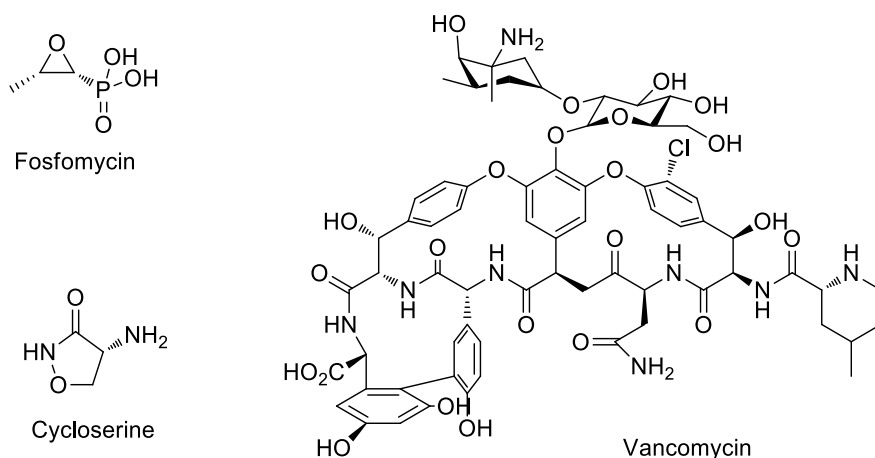


Figure 1.25. Structures of fosfomicin, cycloserine and vancomycin.

The β -lactam antibiotics are the most widely prescribed clinical antibiotic drugs. This drug family has been developed into four main categories: penicillins, cephalosporins, monobactams and carbapenems (Figure 1.26) (62). Although the structural variants of the β -lactams have been extensively expanded in the past decades, they all share a core four-member ring lactam structure that mimics the D-Ala-D-Ala moiety. This highly strained lactam is easily attacked by the serine residue from TPase during the PG crosslinking step, and the resulting acyl enzyme intermediate is a dead-end complex that inactivates TPase. Bacteria with impaired cell wall crosslinking are vulnerable to osmotic swelling and autolysis, which results in cell death. Generally the β -lactams have higher activity with Gram-positive bacteria than with Gram-negative ones, since the PG layer in Gram-positive bacteria is the outmost shell and the periplasmic space is less accessible in Gram-negative bacteria.

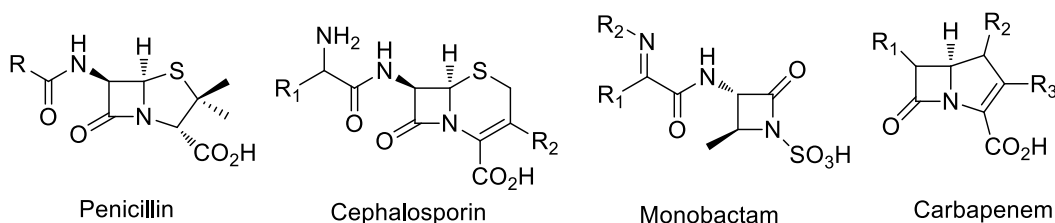


Figure 1.26. The four main categories of β -Lactams.

1.2.3 Peptidoglycan modifications and the cell shape determinant genes

1.2.3.1 PG modifications and their *in vivo* functions

When the bacterial infection (usually occurring in the mucous membrane) is detected by the host immune system, an immune response is initiated by the secretion of antimicrobials from the epithelium cell. The secretion is a complex mixture of antibacterial enzymes and peptides. One of most the abundant enzymes is lysozyme, which targets the PG network and hydrolyzes the β -1, 4 glycosidic bond between GlcNAc and MurNAc. The hydrolysis releases PG fragments into the extracellular environment, and then triggers the host signaling cascades that request more immune cells to help in clearing the pathogens (85,86).

To avoid triggering the host immune response and to resist the hydrolysis from lysozymes, many pathogenic bacteria species have evolved modified PG backbone structures. Compared to Gram-negative organisms, lysis-resistance is very essential to Gram-positive bacteria as their PG layer is exposed to the secreted antibacterials. The *N*-deacetylation of GlcNAc was the earliest observed modification in *Streptococcus pneumoniae* (Figure 1.27, Right) (87). It was later also observed in a lysozyme-resistant *Bacillus anthracis* strain, and restoration of the *N*-acetylation by acetic anhydride treatment increased the lysozyme sensitivity. This was the first evidence of a relationship between PG modification and bacterial infection. The first enzyme responsible for *N*-deacetylation was identified from *S. pneumoniae*, and is encoded by the gene *pgdA* (peptidoglycan deacetylase A). Several *pgdA* homologues in other organisms (e.g. *H. pylori* and *E. coli*) have subsequently been identified. Another prevailing modification in bacteria is *O*-acetylation at the MurNAc C6 position (Figure 1.27, Left) (88). This modification was first observed in the Gram-negative species *Neisseria gonorrhoeae*, and later in other pathogenic species. The first identified *O*-acetylase was encoded by the gene *oatA* (*O*-acetyltransferase A) from *S. aureus*, and like *pgdA*, the *oatA* gene is widely conserved in many organisms.

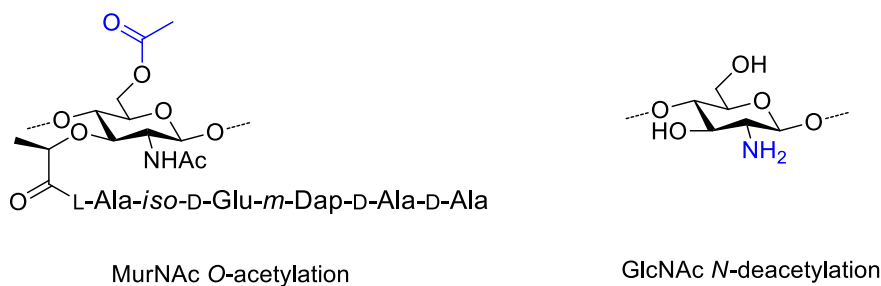


Figure 1.27. The peptidoglycan modifications of *O*-acetylation (left) and *N*-deacetylation (right).

1.2.3.2 Cell shape determinant (Csd) genes in *Helicobacter pylori*

Helicobacter pylori is a helical-shaped Gram-negative microaerobic bacterium that colonizes in the human stomach and duodenum (Figure 1.28, Left Panel). *H. pylori* infection is the main cause of several gastric diseases, including chronic gastritis and peptic ulcers. The former can lead to gastric cancer if not treated properly (89). Previous studies have found that the helical shape of *H. pylori* is a key factor that assists colonization (90). Through a cork-screwing mechanism, the bacterium drills into the mucosal epithelium, where it is protected from exposure to the highly acidic gastric secretions. Very little of the relationship between bacterial morphology and PG modification was known until recent years. Several advances have been made in studies of bacterial species with common shape models, including rod species (e.g. *E. coli* and *Bacillus subtilis*) and coccoid species (e.g. *S. aureus*) (91,92). However, the mechanism for the determination of helical bacteria morphology is still poorly understood.

Analysis of the PG biosynthetic pathway in *H. pylori* revealed one class A HMM PBP (PBP1) and two class B HMM PBPs (PBP2 and PBP3) (63). The class A PBP1 is a bifunctional glycosyl transferase as well as TPase, while the class B PBP2 and PBP3 are monofunctional TPases that specifically catalyze the crosslinking between neighboring muramyl pentapeptide chains. It is usually thought that those uncrosslinked or terminal crosslinked peptide will be truncated by DD, DL-endopeptidases or carboxypeptidases. However, no LMM PBPs (that normally function as trimming enzymes) have been identified, suggesting non-PBP peptidases may participate in this modification process.

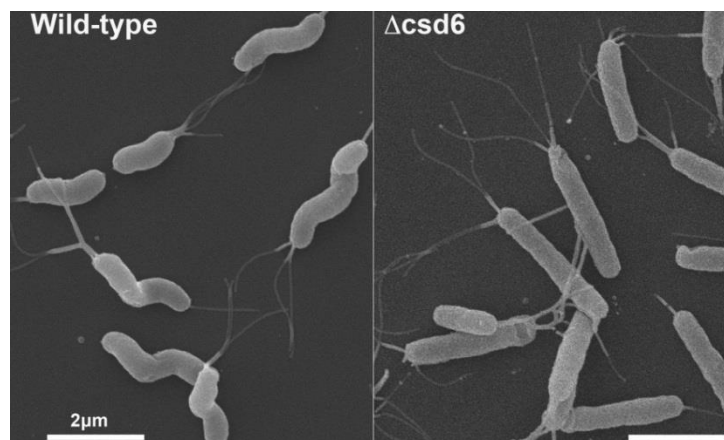


Figure 1.28. The phenotype of wild-type *H. pylori* (left) and the $\Delta csd6$ mutant (right) (<http://www.fhcr.org/en/news/spotlight/imports/using-flow-cytometry-to-find-rare-cell-shape-changes-in-helicoba.html>).

By employing flow cytometry with fluorescent-activated cell sorting (FACS), Sycuro *et al* have identified a series of genes responsible for maintaining *H. pylori*'s helical shape and named them as cell shape determinants (*csds*) (93). *Csd1 – 3* and *ccmA* were the first identified genes, and *Csd1 – 3* shared homology with the known LytM peptidases from *S. aureus*. The term *ccmA* refers to curved cell morphology A, which was first identified in *Proteus mirabilis* and is known to determine its curved rod shape. Mutants with a deletion of *csd1*, *csd2* or *ccmA* display the slightly curved rod morphology, while deletion of *csd3* leads to a heavily curved shape (letter “C” shape). The conserved LytM domain indicated that *Csd1 – 3* are peptidases. It has not been determined whether they are DD- or DL- proteases (cleaving the peptide bond between two D-AAs or one D-AA and one L-AA), or whether they are endo or exopeptidases. A comparison of the muropeptide composition between *csd1 – 3* knockout mutants and the wild-type strains revealed an enhancement of crosslinked peptides and a decrease of monomeric peptides. These results suggested that the *Csd1 – 3* enzymes are probably endo or carboxypeptidases that trim crosslinked muropeptides (Figure 1.29).

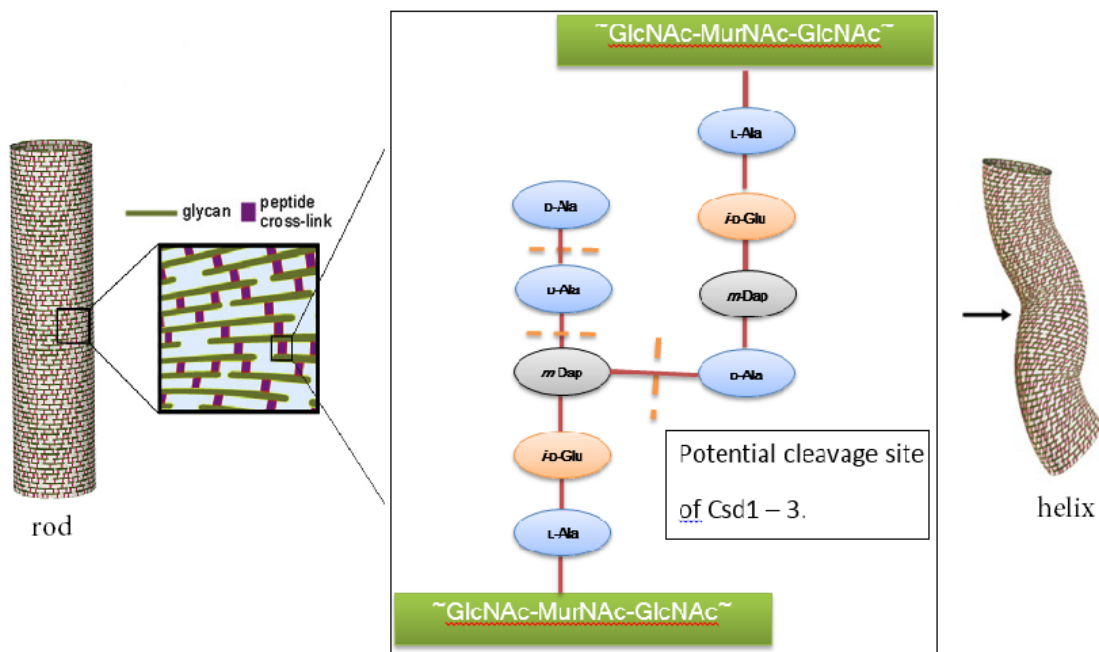


Figure 1.29. Potential *Csd1 – 3* modifications of PG.

In recent years, two additional genes *csd4* and *csd6* have been identified and mutants that lack either of them display a straight rod phenotype (Figure 1.28, Right Panel) (94,95). Further

exploration revealed that Csd4 and Csd6 are a DL-carboxypeptidase and a DD-carboxypeptidase, respectively. Csd6 catalyzes the hydrolysis of the last peptide bond in an uncrosslinked strand sequence (GlcNAc-MurNAc-)L-Ala-*iso*-D-Glu-*m*-Dap-D-Ala, and Csd4 trims the resulting tripeptide to the dipeptide by hydrolysis of *iso*-D-Glu-*m*-Dap peptide bond (Figure 1.30). Moreover, the *in vivo* assay of these rod shape mutants in mice stomach showed significant attenuation of colonization compared to the wild-type species, although their motility and sensitivity to the acidic stomach environment were not obviously affected. In further studies, it was found that Csd4 mutants show impaired motility in gel-like media. This likely impairs their ability to penetrate the mucus layer of the stomach and leads to a decrease of virulence.

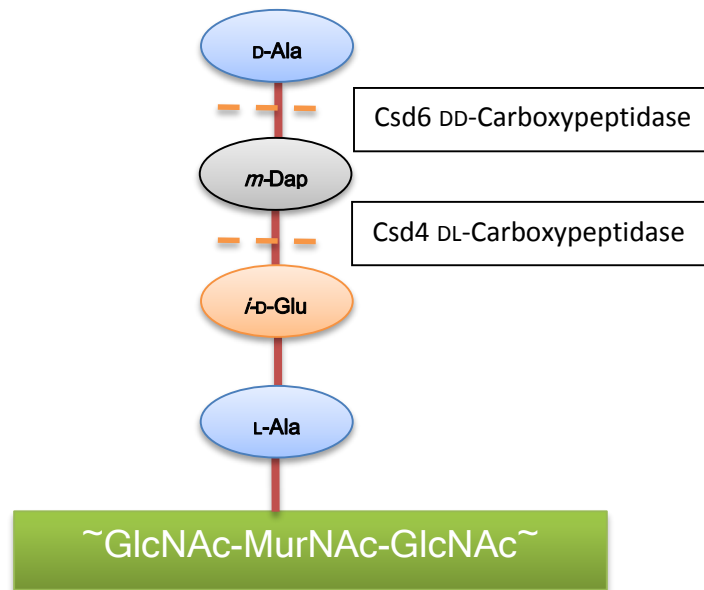


Figure 1.30. PG trimming by Csd6 and Csd4.

1.2.3.3 Mechanism of the zinc-dependent carboxypeptidases

The work described in this thesis focuses on studies with the enzyme Csd4. Sequence homologies indicate that this enzyme is a member of the zinc-dependent M14 family of carboxypeptidases that include the well-studied example carboxypeptidase A (CPA).

CPA is an exoprotease that selectively catalyzes the cleavage of a peptide bond with a hydrophobic amino acid at the C-terminal position. Bovine CPA was the first well-characterized protease and its high-resolution crystal structure has been solved for decades. Structural analysis

revealed that His69, Glu72 and His196 are the three key residues in zinc binding domain. The catalytic H₂O is also bound to the zinc ion. Glu270 also plays an essential role in deprotonation of the catalytic H₂O to a nucleophilic hydroxide. Then the metal-bound hydroxide attacks the carbonyl to form a tetrahedral intermediate. These two steps may occur in concert or stepwise. Structural studies of a CPA-inhibitor complex also indicated the tetrahedral intermediate is stabilized by the Zn (II), Glu270 and Asp127 (96). Then the proton donor Glu270 protonates the amino group of the scissile bond, and the tetrahedral structure collapses to give the shortened peptide and the free C-terminus AA (Figure 1.31).

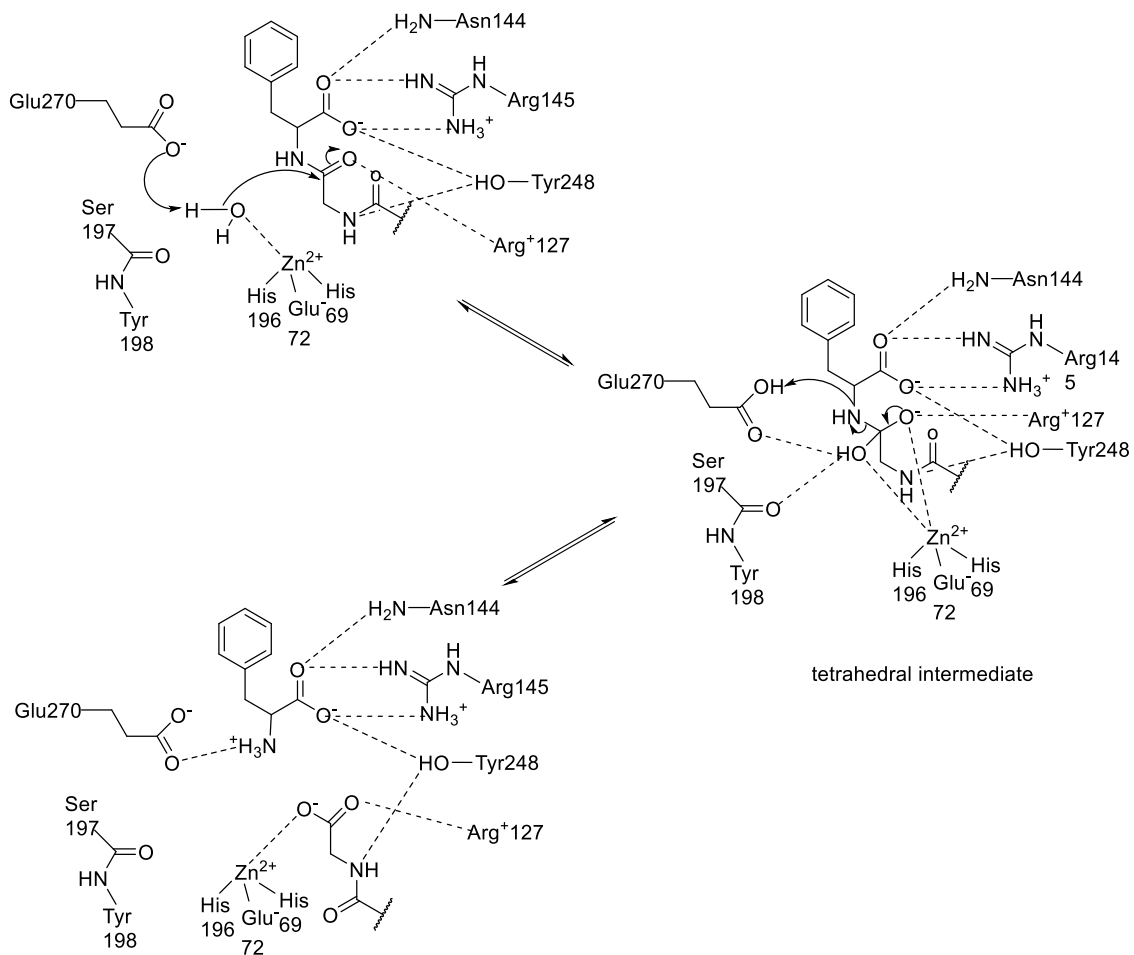


Figure 1.31. The mechanism of carboxypeptidase A.

1.3 Phosphinate Based Inhibitor System and Design

A major goal of this thesis is to prepare inhibitors of the enzymes involved in both the tubulin glutamylation cycle and the peptidoglycan carboxypeptidase Csd4. An inhibition strategy that has been successful with both ligases and proteases is the use of phosphinic acids. Chapter 2 will describe our work on the synthesis and testing of phosphinic acid based inhibitors of TTL7. These inhibitors may also inhibit the corresponding deglutamylases (CCPs). Chapter 3 will describe the synthesis and testing of an inhibitor of the peptidoglycan carboxypeptidase Csd4. The following section will provide background on the development of the phosphinic acid-based inhibitors.

The mechanisms employed by both peptide ligases and peptidases involve the formation of a tetrahedral intermediate, which is generated by the nucleophilic attack of either an amino acid or H_2O onto either an acyl phosphate or amide (Figure 1.32). The phosphinic pseudo-peptide is a structural analogue of the tetrahedral intermediate that can be obtained by replacement of the normal peptide bond $-\text{C}(\text{O})-\text{NH}-$ with a phosphinic acid moiety $-\text{P}(\text{O}_2)-\text{CH}_2-$ (Figure 1.33) (97). The high structural similarity between the catalytic intermediate and the phosphinic pseudo-peptide based inhibitors has been widely studied in the past decades. Potent inhibitors have been reported with a number of enzymes including D-Ala-D-Ala ligase, MurD ligase, and 24-15 zinc endopeptidase (Figure 1.34) (98-101).

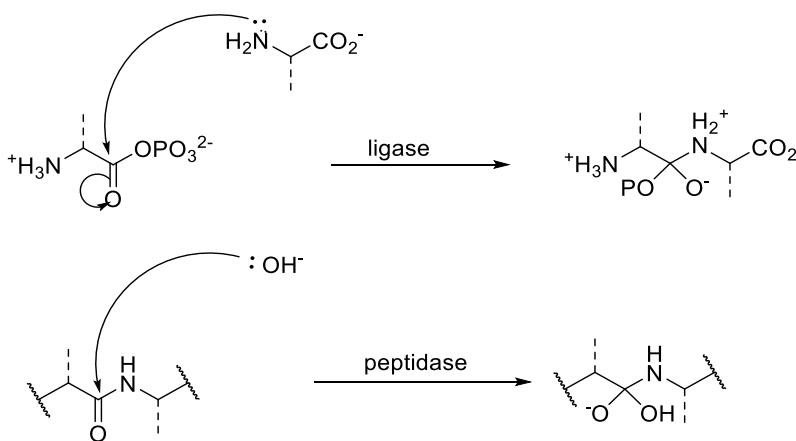


Figure 1.32. Tetrahedral intermediate formation in ligase and carboxypeptidase catalysis.

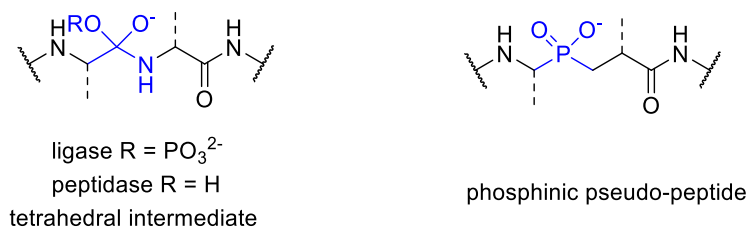


Figure 1.33. The structure of a tetrahedral intermediate and a phosphinic pseudo-peptide.

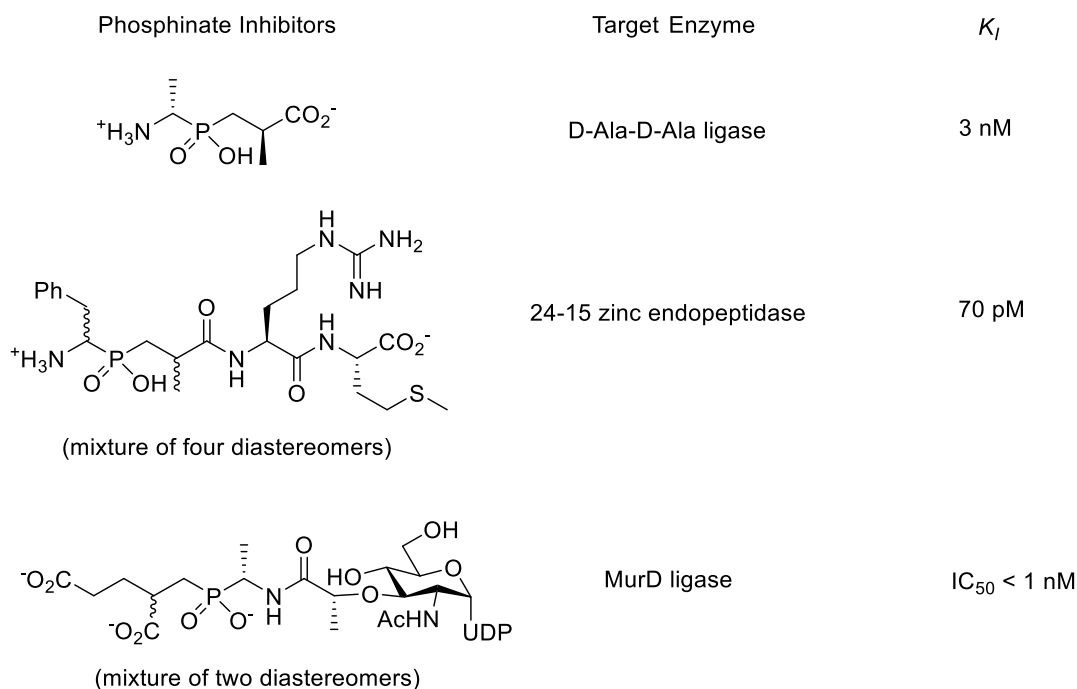


Figure 1.34. The potent inhibitors of various ligases and peptidases.

The potency of phosphinate inhibitors suggests that they mimic the structure of the transition state formed during catalysis. This hypothesis has been supported by structural studies with both ligases and metallopeptidases. In a resolved structure of the metalloprotease astacin in complex with a phosphinate inhibitor (Figure 1.35) (102), it was shown that the phosphoryl group ligated the divalent zinc ion and was held by favorable electrostatic interactions. Moreover, the Glu93 that acted as the base to deprotonate the H₂O molecule during normal catalysis, also had interaction with the phosphoryl group. The Cys64 and Tyr149 residues were located within H-bonding distance of the methylene and phosphinate group, respectively. Mutation of Glu93 and

Tyr149 revealed a significant drop in the activity of astacin, consistent with the hypothesis of transition state mimicry.

Another high-resolution structural study of D-Ala-D-Ala ligase gave similar results. In this work, D-Ala-D-Ala ligase was co-crystallized with a *1S, 3R*-methylphosphinate (Figure 1.34, 1st Entry). This ATP-dependent ligase can phosphorylate the inhibitor to form a phosphorylated phosphinate structure (PPI, Figure 1.36 Left) (52). The crystal structure showed the binding between Mg^{2+} and the PPI as well as ADP in the active site, proving the phosphorylated phosphinate has structural similarity with the tetrahedral intermediate formed in this mechanism. (Figure 1.36 Right). Moreover, the phosphorylated species was found to bind tightly to the ligase (although this was not an irreversible process, the inhibitor off rate was extremely low) due to its similarity to the tetrahedral intermediate.

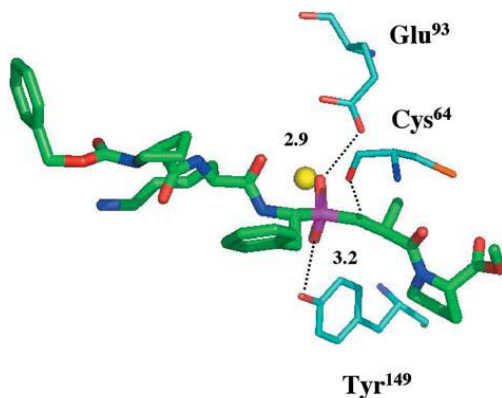


Figure 1.35. Partial structure of the active site of astacin.

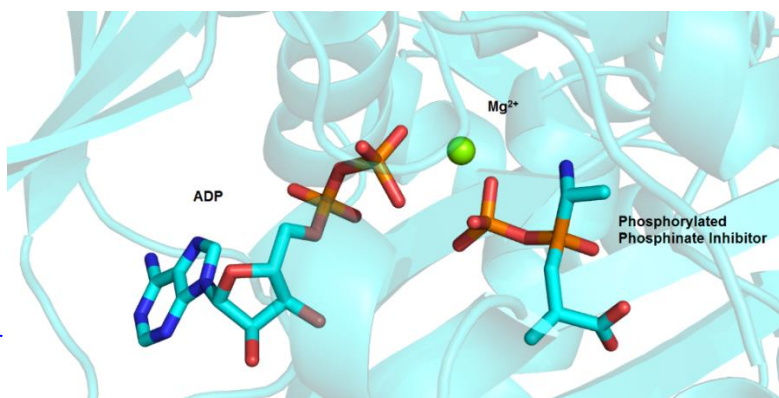
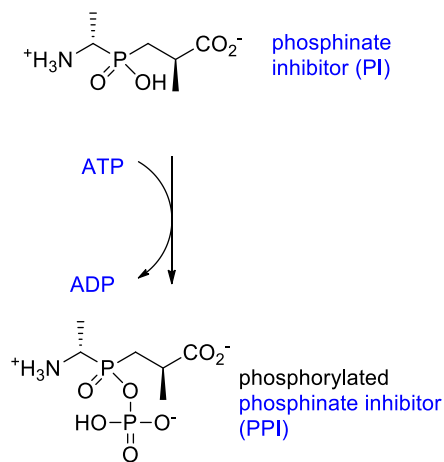


Figure 1.36. Left: The phosphorylation of the phosphinate inhibitor. Right: The active site of the D-Ala-D-Ala ligase, with phosphorylated inhibitor and ADP bound to the Mg^{2+} .

The challenges of inhibitor selectivity that result from the complexity of the intracellular environment fall primarily into two categories. One problem is that enzymes encoded in the same genome or even different genomes may have similar substrates, cofactors, metal ions or active site structures. Thus, mechanism-based inhibitors could block the function of completely irrelevant enzymes, and this may cause severe side effects in clinical trials. The other is that in a multi-subunit or multi-domain enzyme system, the designed inhibitor may not show good selectivity if these subunits or domains share similar structures. For instance, the inhibitors of matrix metalloproteinase-2 (MMP-2) were found to have weaker, but still good, potency to other MMP family members (103). These inhibitors incorporated thiol or hydroxamate groups that were designed to increase the zinc binding affinity (Figure 1.37, top left). However, these types of compounds also turned out to be highly potent inhibitors of TACE (tumor necrosis factor- α -converting enzyme) (104). To overcome these problems, phosphinic pseudo-peptides were investigated and a modified inhibitor with excellent selectivity (Figure 1.37, Top right), was discovered (105). Another example is the anticancer drug RXP03, which is also a peptidyl phosphinic acid inhibitor. RXP03 was designed to target MMP-11 of breast cancer, and the dosing assay showed it had potent inhibitory activity against MMP-11 and 13, but relative low activity towards other MMP enzymes.

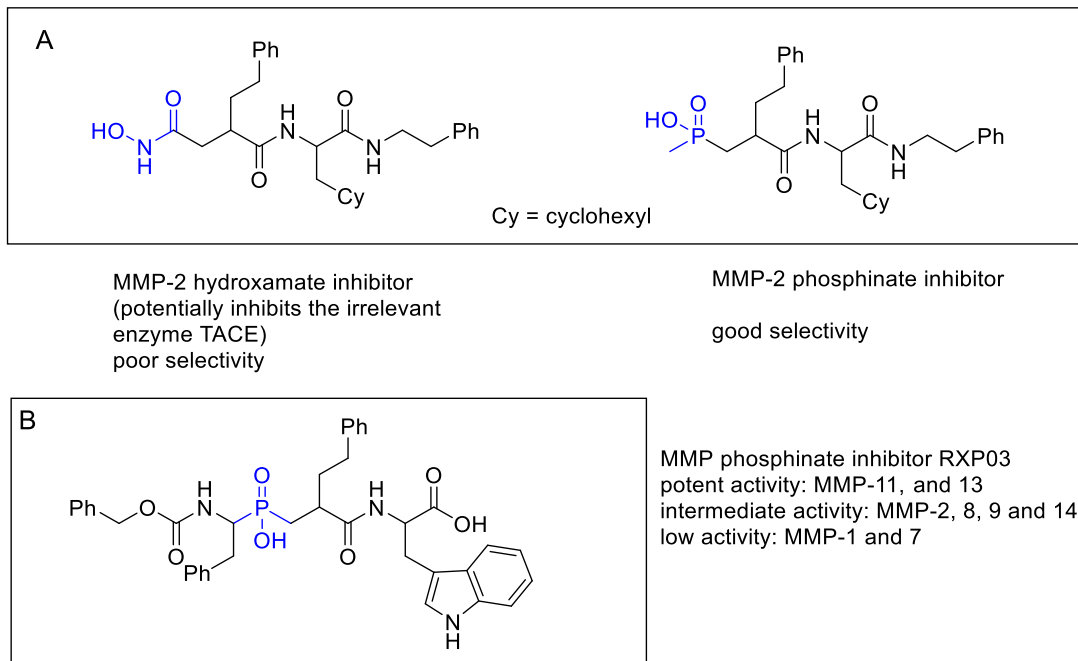
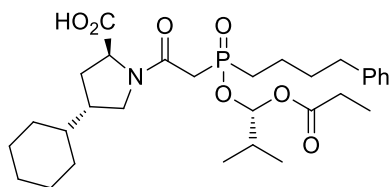
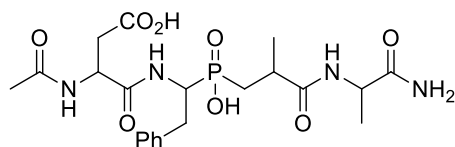


Figure 1.37. A(top): The phosphinate and hydroxamate inhibitor of MMP-2. B(bottom): The MMP-9 phosphinate inhibitor RXP03.

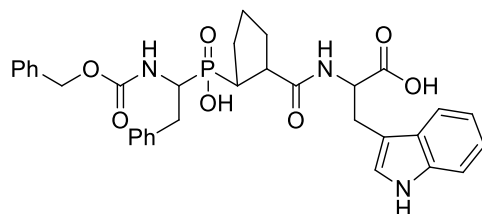
Another example demonstrating the potential selectivity of phosphinate inhibitors is the development of domain-selective inhibitors of angiotensin converting enzyme (ACE). ACE is a zinc endopeptidase that hydrolyzes the decapeptide angiotensin I (DRVTIHPFHL) to the octapeptide angiotensin II (DRVTIHPF) (106). The latter is a vasopressor factor that causes enhanced angiostasis and results in hypertension. The somatic ACE (sACE) has an *N*-domain and a *C*-domain, and in the resolved structures both domains contain substrate binding sites and have similar activity. Fosinopril (Figure 1.38) is the first clinically used phosphinic pseudo-peptide inhibitor of ACE, however, this compound does not show domain selectivity (106). To study the functions of the separated *N*- or *C*-domains of ACE, the *N*-domain inhibitor RXP407 and *C*-domain inhibitor RXPA380 were developed, and both of the compounds showed high domain binding selectivity (Figure 1.38) (107,108).



Fosinopril
 K_i (ACE) = 0.37 nM



RXP407
 K_i (ACE, N-domain) = 7 nM
 K_i (ACE, C-domain) = 7500 nM



RXPA380
 K_i (ACE, N-domain) = 10000 nM
 K_i (ACE, C-domain) = 3 nM

Figure 1.38. The clinical drug fosinopril, *N*-domain inhibitor RXP407, and *C*-domain inhibitor RXPA380.

1.4 Project Goals

1.4.1 Inhibition studies of the tubulin polyglutamylase TTLL7 (Tubulin Tyrosine Ligase-Like 7)

TTLL7 is a β tubulin polyglutamylase involved in PTM. It is generally thought to be an initiation glutamylase, although some research has suggested TTLL7 can catalyze both initiation and elongation. Moreover, the elongation linkage pattern (α - vs. γ -) has not been determined yet. Therefore, three mechanism-based phosphinate inhibitors are designed in order to mimic the tetrahedral intermediate formed during three possible modes of catalysis (Figure 1.39).

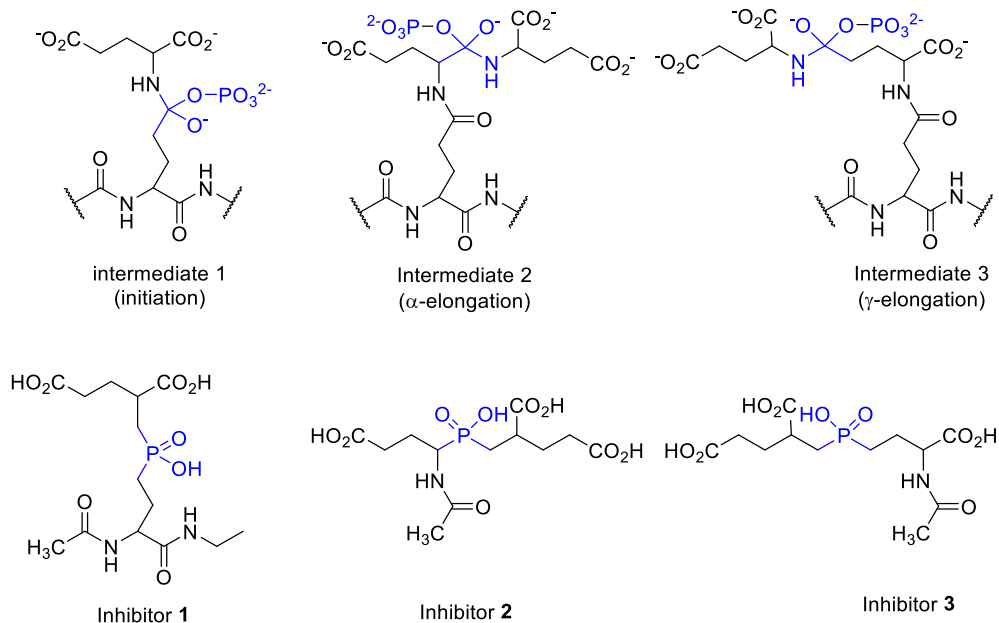


Figure 1.39. Top: the tetrahedral intermediates formed during tubulin initiation and elongation (α - and γ -). Bottom: the designed phosphinate inhibitors mimicking these intermediates.

In order to test if a peptide could serve as a TTL7 substrate, a 15AA *N*-acetyl peptide (Peptide 1) with an identical sequence to β II tubulin CTT, and a 19 AA *N*-acetyl peptide (Peptide 2) with an identical sequence to β VI tubulin CTT was also targeted for synthesis (Figure 1.40).

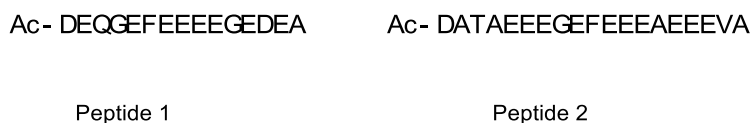


Figure 1.40. The sequence of linear peptide1 and peptide2.

Chapter 2 will describe our synthesis of the inhibitor and peptides. Kinetics and inhibition tests with the peptide substrates and inhibitors **1** – **3** will be completed by our collaborators in the Roll-Mecak Lab at the Cell Biology and Biophysics Unit, National Institute of Neurological Disorders in Maryland, USA. The phosphinate inhibitors will be assayed against both the peptide substrate and full length tubulin substrate, respectively.

1.4.2 Inhibition and structural studies on the peptidoglycan modifying carboxypeptidase Csd4 from *Helicobacter pylori*

The DL-carboxypeptidase Csd4 catalyzes the hydrolysis of the peptide bond between *iso*-D-Glu and *meso*-Dap. The natural substrate of Csd4 is the uncrosslinked tripeptide strand in the PG meshwork (Figure 1.41, Left). Thus we design and plan to synthesize the *N*-acetyl L-Ala-*iso*-D-Glu-*meso*-Dap tripeptide, to examine its feasibility as a Csd4 substrate and the necessity of the glycan chain in catalysis (Figure 1.41, Right). Moreover, a phosphinate inhibitor mimicking the tetrahedral intermediate formed during the hydrolysis of the *iso*-D-Glu-*meso*-Dap bond will also be prepared for inhibition studies (Figure 1.41, Right).

The tripeptide and inhibitor will be evaluated using a continuous coupled kinetic assay with *H. pylori* Csd4 and the coupling enzyme *m*-Dap dehydrogenase (DAPDH). These synthetic and kinetic studies are the subject of Chapter 3. The optimization of pH/buffer conditions as well as Csd4 mutation studies will be completed by Dr. Anson Chan in our collaborator Dr. Michael Murphy's Lab at the Department of Microbiology and Immunology, University of British Columbia. The peptide substrate and phosphinate inhibitor will also be co-crystallized with Csd4 for structural studies in Prof. Murphy's lab. Finally our inhibitor will be used in *in vivo* studies with the live bacteria in the labs of Prof. Erin Gaynor (UBC Microbiology) and Prof. Nina Salama (University of Washington, Seattle, WA, US).

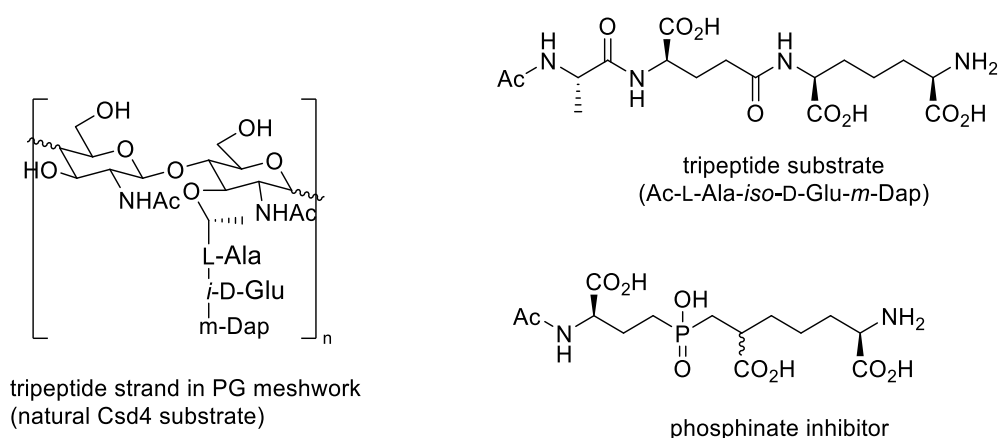


Figure 1.41. Left: the natural substrate of Csd4. Right: the tripeptide substrate and phosphinate inhibitor of Csd4.

2. Substrate and Inhibitor Design for the Enzyme TTLL7

As discussed in Section 1.1.2 and 1.1.3, tubulin polyglutamylation regulates the activity of structural MAPs and motor proteins. Although several tubulin polyglutamylases were identified, their exact biological and physiological function remains still elusive. Ikegami *et al* studied different cell lines in which TTLL1 (α tubulin favored) or TTLL7 (β tubulin favored) genes were knocked out. They found that the cell lines lacking TTLL1 displayed abnormal neuronal processes and low level synaptic transmission (109), and that cell lines lacking TTLL7 were repressed in neurite growth (110). However, it is still unclear how the length of the glutamate side chain and the mode of linkage affect the interaction between MTs and MAPs. Even the catalytic function (initiation only or both initiation/ elongation) is controversial. Van Dijk *et al* concluded TTLL7 is a β tubulin initiase based on *in vivo* assay results (111), but Mukai *et al* found TTLL7 performed both initiation and elongation by using *in vitro* assay (50).

To further understand these issues, more detailed information about the TTLL reaction needs to be gathered, for instance, what are the lengths, structures and sites of glutamate side chains? Although no structural model of a TTLL is available to date, Mukai *et al* tested TTLL7's substrate preference to understand its binding site specificity. It was reported the activity with intact MTs is 2.5 fold higher than that with free β tubulin, indicating that TTLL7 preferentially binds to polymerized MTs (50). Moreover, they found a small polypeptide with the same sequence as the tubulin CTT competitively inhibited the reaction when present at high concentration. These results suggested that TTLL7 does bind to truncated substrate and supports the possibility of using a peptide as a TTLL7 substrate.

In this chapter, we describe the design and synthesis of two peptide substrates bearing the sequence of the tubulin C-terminal tail (CTT). We predicted these peptides would serve as alternate substrates of TTLL7. We also describe the design and synthesis of three mechanism based phosphinate inhibitors mimicking tubulin initiation and α -/ γ - elongations. Finally, the testing of these compounds with TTLL7 carried out by our collaborator Dr. Antonina Roll-Mecak is also included. These kinetic results confirm TTLL7's activity on polypeptide substrates with a CTT sequence. Moreover, the synthesis and testing of potential pseudopeptide inhibitors is presented, and a discussion regarding the future design of TTLL7-targeted drugs is also provided.

2.1 Previous Advances at Assaying TTLL7 activity

It was initially reported that TTLL7 is an initiase based on western blot assay with antipolyglutamate antibodies GT335 and polyE (111). However, by utilizing MALDI mass spectrometry and tandem mass spectrometry, Mukai *et al* did *in vitro* assays with newborn mice tubulin (β II and β III) as substrates and found TTLL7 can perform both initiation and elongation. The polyglutamylation incorporated up to 16 glutamates into the tubulin (Figure 2.1). Moreover, a new modification site E440 in the CTT of β II was identified in addition to the previous discovered site E435 (Figure 2.2) (50,112).

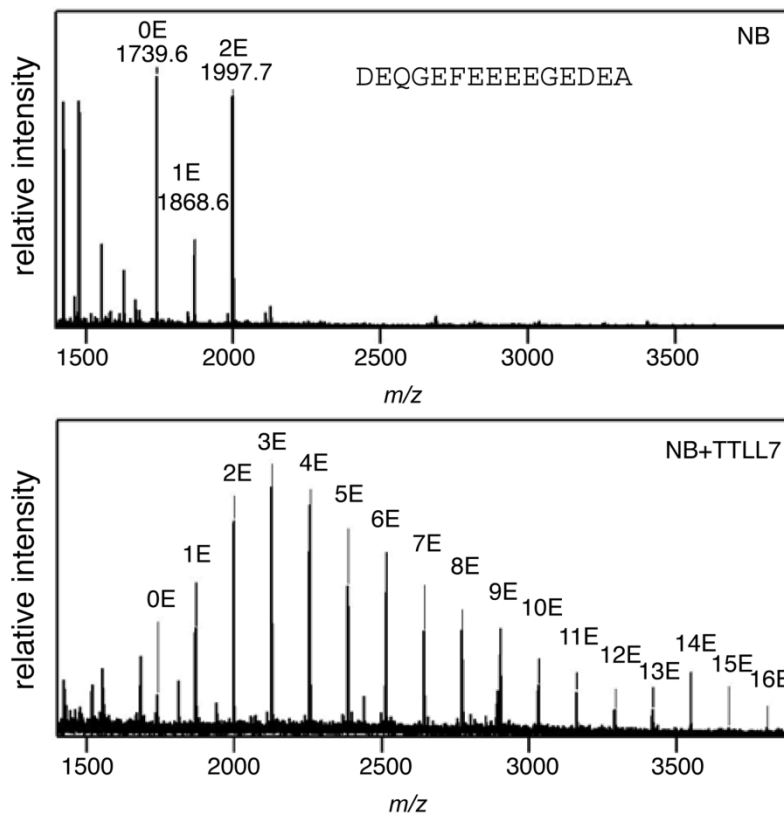


Figure 2.1. MALDI of CTT peptides of newborn β II Tubulin (Top) and those peptides after incubation with TTLL7 (Bottom).

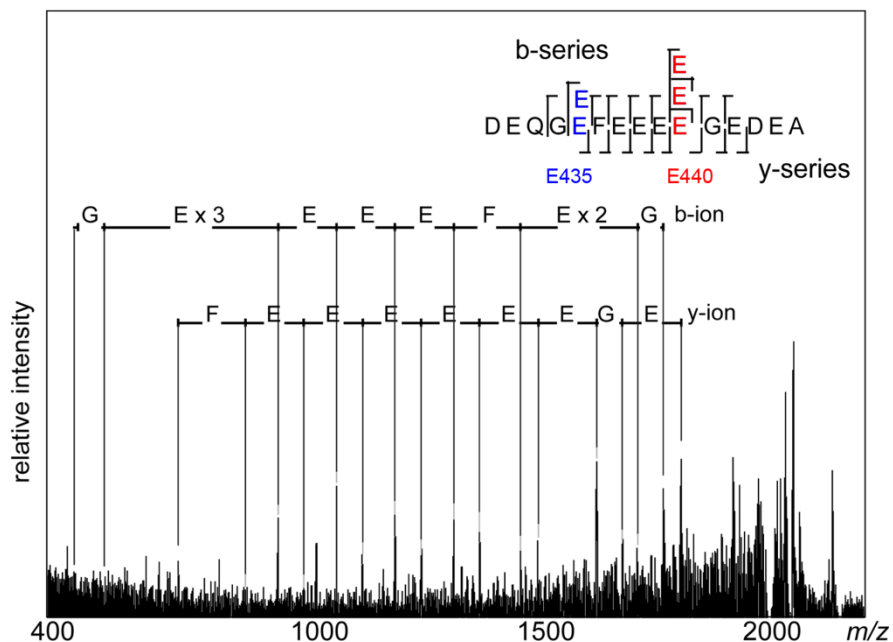


Figure 2.2. Tandem mass spectrometry of CTT peptide with 3E incorporated after TTL7 incubation.

The Michaelis constants (K_M) of these three substrates (tubulin, ATP and glutamate) were also examined with both adult and newborn mouse MTs: K_M (ATP) = 13.3 or 21.3 μM , K_M (Glu) = 12.8 or 12.0 μM , K_M (tubulin) = 12.5 or 11.3 μM , respectively. The Lineweaver-Burk plots with fixed concentration of any one substrate showed non-parallel linear curves, indicating that a sequential binding mechanism and not a ping-pong mechanism is utilized (113). Moreover, Mukai *et al* also did preliminary inhibitor testing, and they identified βIII and βIV tubulin CTT peptides as competitive inhibitors (Figure 2.3). In particular, the βIII tubulin CTT peptide showed a inhibition constant $K_I = 0.5$ mM. Although the K_I value is ~ 40 fold higher than tubulin's K_M , it supported the hypothesis that a tubulin C- terminal peptide could serve as a substrate of TTL7.

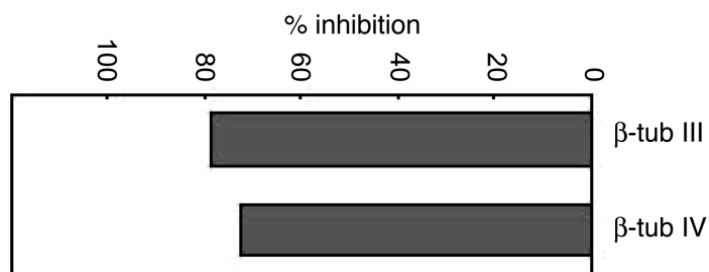


Figure 2.3. Inhibitory efficiency of class III and class IV β tubulin C-terminal peptides (10 mM).

2.2 Design and Synthesis of Phosphinate Inhibitors

Given the precedence for the inhibition of ligases using phosphinic acids, three phosphinic acid inhibitors were designed to target the initiation step and α -/ γ - elongation steps in tubulin polyglutamylation (98,100,114-116). In addition, as the *in vitro* repeats of TTLL7's elongation capability conflicts with those of the *in vivo* assay, the designed elongation inhibitors can be used to test both theories. These inhibitors are structural analogues of the intermediates formed during the ligation reactions. The core component is a dialkyl phosphinic acid bearing a tetrahedral structure (Figure 2.4, blue). The phosphinate ($pK_a \sim 2$) is thought to have a strong binding affinity to ATP-grasping enzymes (52,98,117-119); thus if TTLL7 has elongation capability, either of these two elongation inhibitors **2** and **3** will inhibit of TTLL7 to some extent.

The initiation inhibitor **1** was proposed to mimic the tetrahedral intermediate **I** formed in the initiation step. For this inhibitor, *N*-acetylation and ethyl amide were placed on either end to simulate the linear tubulin sequence. Compared to the elongation activity, the initiation activity of TTLL7 has been characterized by several previous studies. Also the initiation is the prerequisite of the elongation. Thus it is more likely that the catalysis of TTLL7 undergo through intermediate **I** than through intermediate **II** or **III**, and inhibitor **1** was thought to has higher affinity when binding to TTLL7. For these reasons, the inhibitor synthesis started with the initiation inhibitor **1**, in order to maximize the probability for observing a potent inhibition of TTLL7. The elongation inhibitors **2** and **3** were proposed to mimic the tetrahedral intermediate **II** and **III** when a second glutamate was added to the α -carboxylate or γ -carboxylate, respectively. For these two inhibitors, their structures simulated the Glu-Glu dipeptide moiety generated by addition of a glutamate to the polyglutamate side chain. For ease of synthesis no attempts were made to control stereochemistry and inhibitors were proposed as diastereomic mixture.

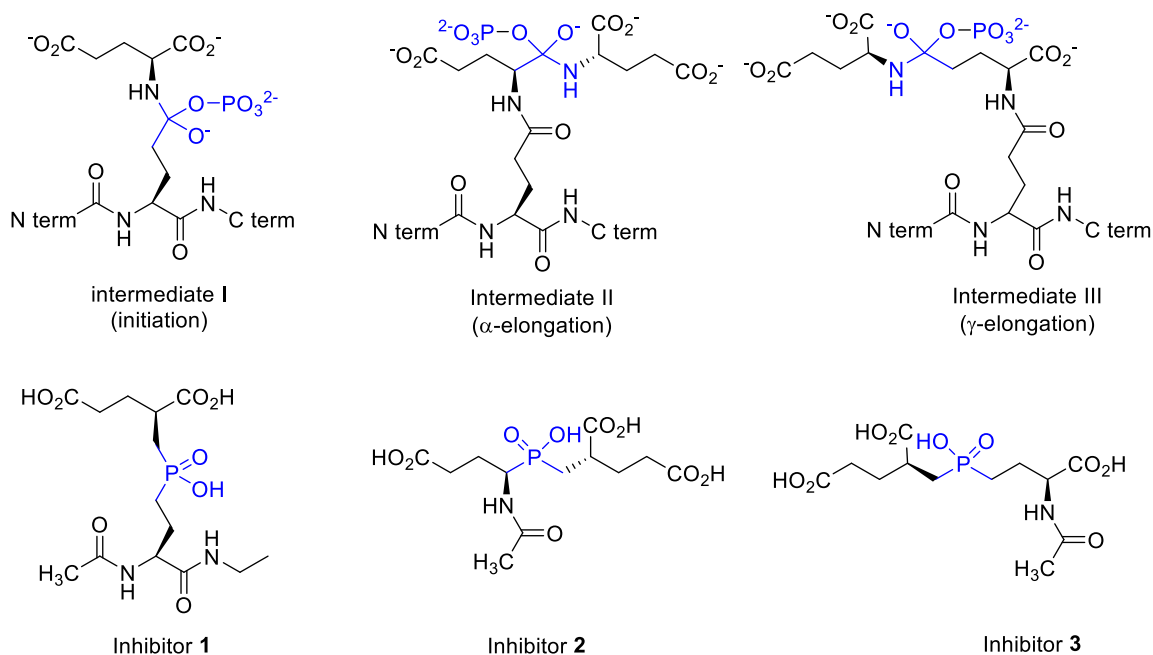


Figure 2.4. The structure of the potential TLL7 intermediates (top) and the structure of the corresponding inhibitors (bottom).

2.2.1 Synthesis of initiation inhibitor 1 and elongation inhibitor 3

The synthesis of inhibitor **1** and **3** followed the route used to prepare phosphinic compounds that were designed as inhibitors of folic poly- γ -glutamate handling-enzymes (Figure 2.5) (114,120). Inhibitor **1** started with a literature known (*S*)-alkene (compound **5**), which was prepared using a one-step reaction from a *N*-carboxybenzyl (Cbz-) and benzyl ester protected L-glutamic acid (compound **4**) with lead (IV) acetate and cupric acetate. Treatment of compound **5** with ammonium hypophosphite ($\text{NH}_4^+\text{H}_2\text{PO}_4^-$) and triethylborane (Et_3B) gave the alkylphosphinic acid (compound **6**) (120,121). The addition mechanism starts with an electrophilic addition of the Lewis acid Et_3B onto the alkene compound **5** to give intermediate **5a** (Figure 2.6). The ring structure is opened by the nucleophilic attack of the hypophosphite. Finally, the intermediate **6a** is protonated by the ammonium to give the *mono*-alkylphosphinic acid **6**.

The subsequent coupling reaction was the key step of the synthesis since all three inhibitors were prepared through coupling reactions with the same acceptor molecule dimethyl α -methylene pentanedioate **13** (122,123). This alkene compound was prepared according to a literature known method, by dimerization of methyl acrylate using *tri-n*-butyl phosphine (120).

The coupling step converted a *mono*-alkylphosphinic acid into a *di*-alkylphosphinic acid that gives the backbone structure of the Glu-Glu analogue. The mechanism of this reaction is similar to a Michael addition reaction (Figure 2.7). Hexamethyldisilazane (HMDS) is a trimethylsilylate reagent which first forms a bis(ditrimethylsilyl)phosphine compound **6c**. Then the donor couples with α -methylene pentanedioate by attacking the alkene moiety. Finally, the resulting carbanion **7a** is hydrolyzed by MeOH to give the coupled compound **7** as a mixture of two diastereomers.

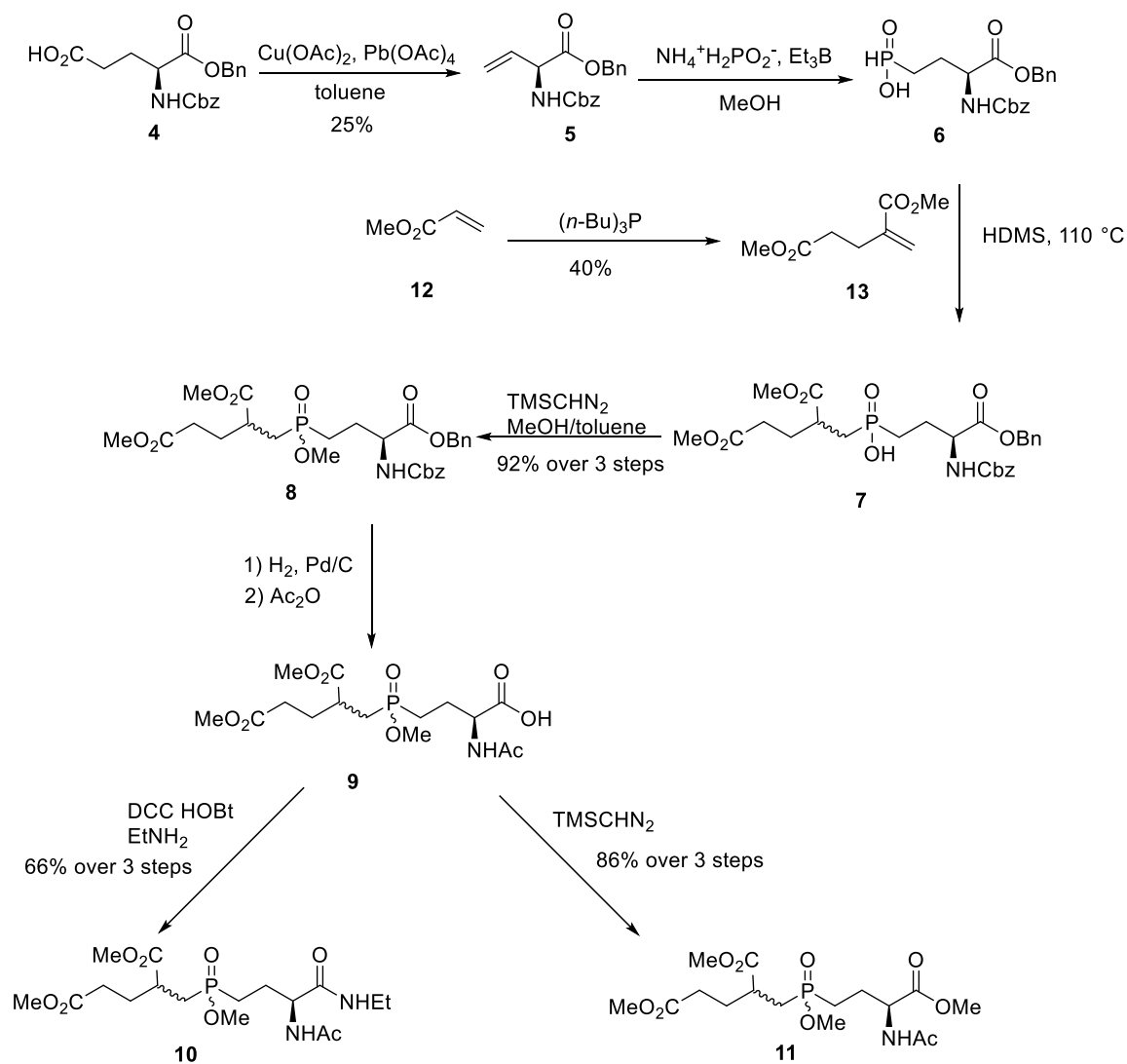


Figure 2.5. Synthesis of inhibitor **1** and **3**.

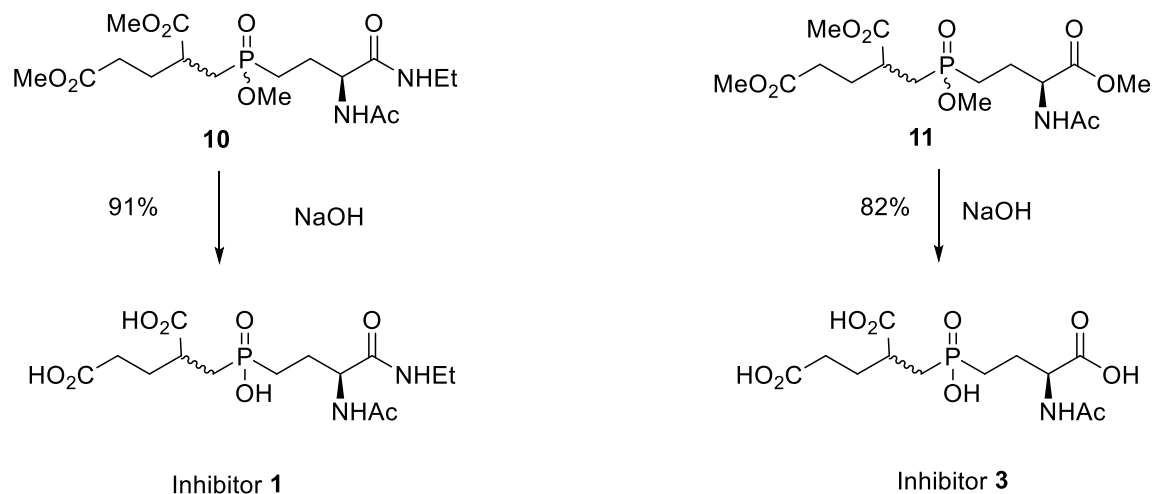


Figure 2.5 Synthesis of inhibitor **1** and **3** (continued)

The *di*-alkylphosphinic acid **7** was methylated by trimethylsilyl diazomethane to give compound **8** as a mixture of four diastereomers. Removal of the Cbz- group by hydrogenolysis and *N*-acetylation with acetic anhydride gave compound **9**. In the pathway to inhibitor **1**, the free carboxylic acid generated by hydrogenolysis was coupled with ethyl amine to give compound **10**. In the pathway to inhibitor **3**, the carboxylic acid is simply methylated to give compound **11**. Compounds **10** and **11** were demethylated using hydrolyzed by NaOH and then purified by an ion exchange column to give the final inhibitors **1** and **3**. Both of these inhibitors were prepared as a mixture of two diastereomers.

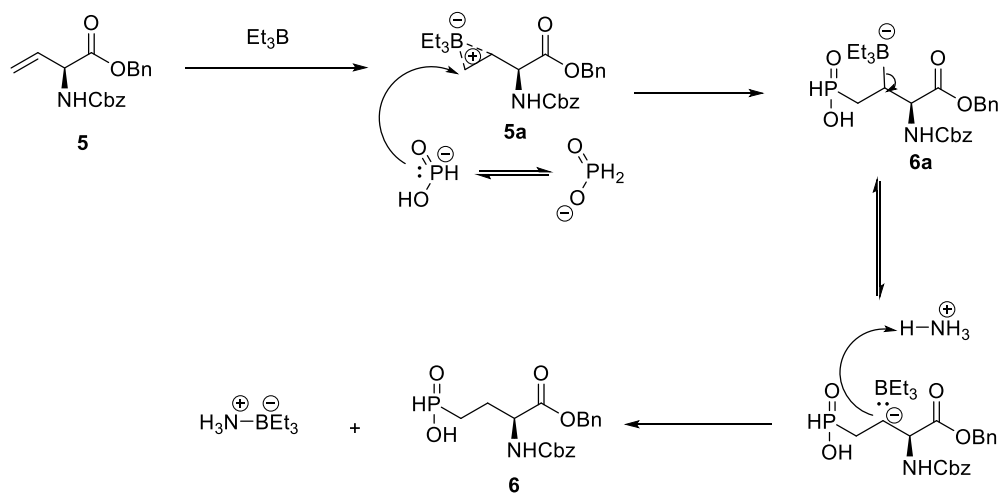


Figure 2.6. Mechanism of the reaction to synthesize *mono*-alkylphosphinic acid **6**.

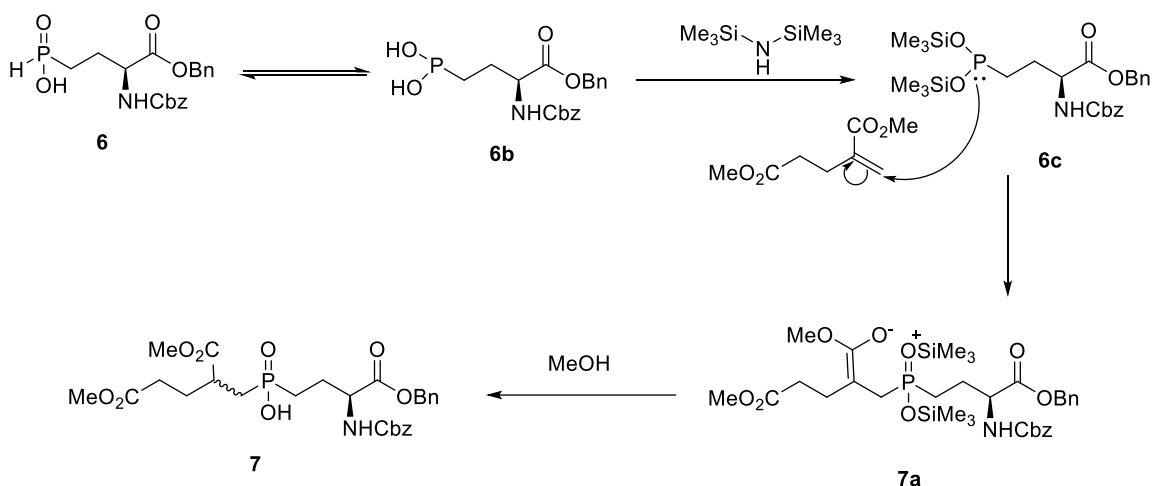


Figure 2.7 The mechanism of the coupling reaction to synthesize compound 7.

2.2.2 Synthesis of elongation inhibitor 2

Compared to the synthesis of inhibitor **1** and **3**, the synthetic route for inhibitor **2** was more circuitous. As reported in previous studies, the synthesis of peptidyl-like phosphinic acids using Michael additions is problematic, when the Michael donor bears a γ -acyl C-O ester in its side chain. Georgiadis *et al* reported that the reaction between an aspartic acid-like phosphinic donor bearing a variety of different protecting groups and an α -methylene pentanoate was unsuccessful (Figure 2.8.A) (123). We also attempted the same type of reaction as used in the synthesis of inhibitor **1** and **3**, and did not observe the formation of the proper coupled product (Figure 2.8.B). Georgiadis *et al* attributed the failure of the coupling reaction to the existence of a carboxyl group at the γ or δ position, and they managed to synthesize the desired phosphinic acid by using a phenyl group as a masked carboxylic acid. The γ -phenyl phosphinic donor successfully coupled with the alkene acceptor and was subsequently oxidized to give a carboxylic acid (Figure 2.8.C).

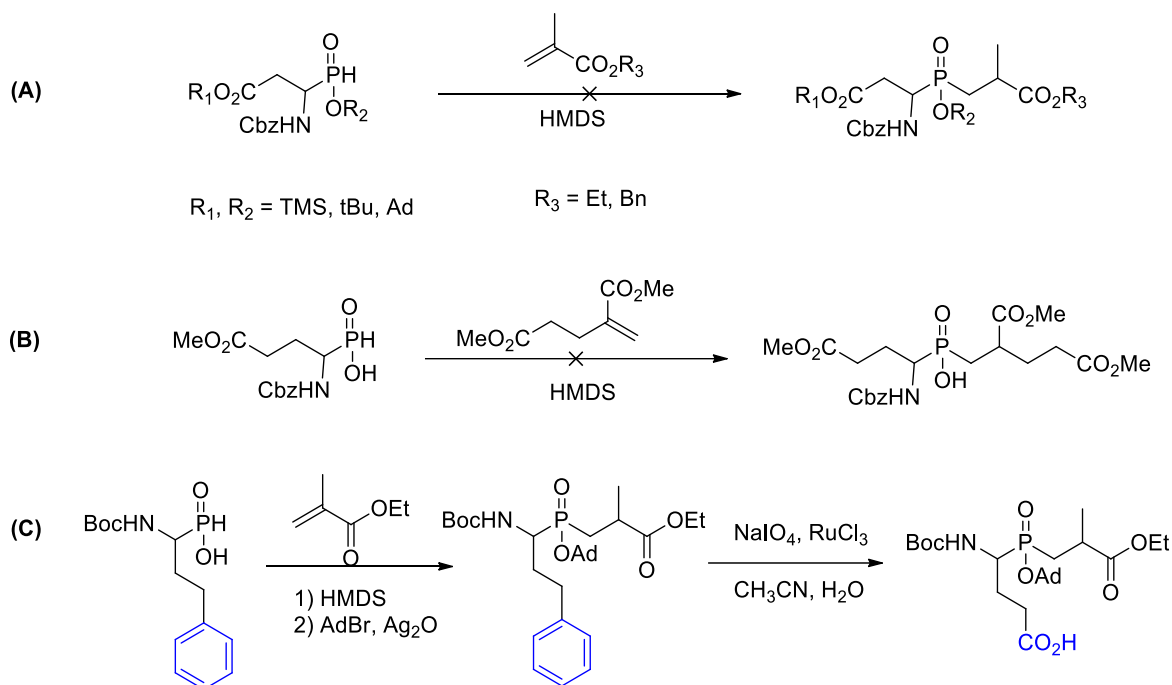


Figure 2.8. A – B) The normal Michael addition reactions are unsuccessful for preparing α -amino phosphinic acid inhibitor. C) Georgiadis's strategy is using a phosphinic acid with phenyl group to complete the coupling reaction first, and followed by oxidation of the phenyl to a carboxylic acid.

We started the synthesis of inhibitor **2** with the preparation of the phenyl phosphinic acid donor **17** (Figure 2.9). This compound was synthesized using a literature known method that requires three steps from 3-phenylpropanal (compound **14**). Compound **18** was obtained after dimethyl α -methylenepentanedioate was coupled with the donor **17**, and this was methylated using TMSCHN_2 to give compound **19** as a mixture of eight stereoisomers. The key step of inhibitor **2** synthesis is the oxidation that converts the phenyl group to a carboxylic acid. This step was achieved by treating compound **19** with a large excess of NaIO_4 and catalytic amount of RuCl_3 . The carboxyl compound **20** was then methylated to give compound **21**, and the Boc- group was selectively removed substituted by an acetyl group (compound **22**). Finally, inhibitor **2** was obtained as a mixture of four stereoisomers (unknown relative amounts) by global demethylation using NaOH . With all three inhibitors, no attempts were made to separate or purify the desired diastereomer and the mixture of diastereomers was directly used in the inhibition studies.

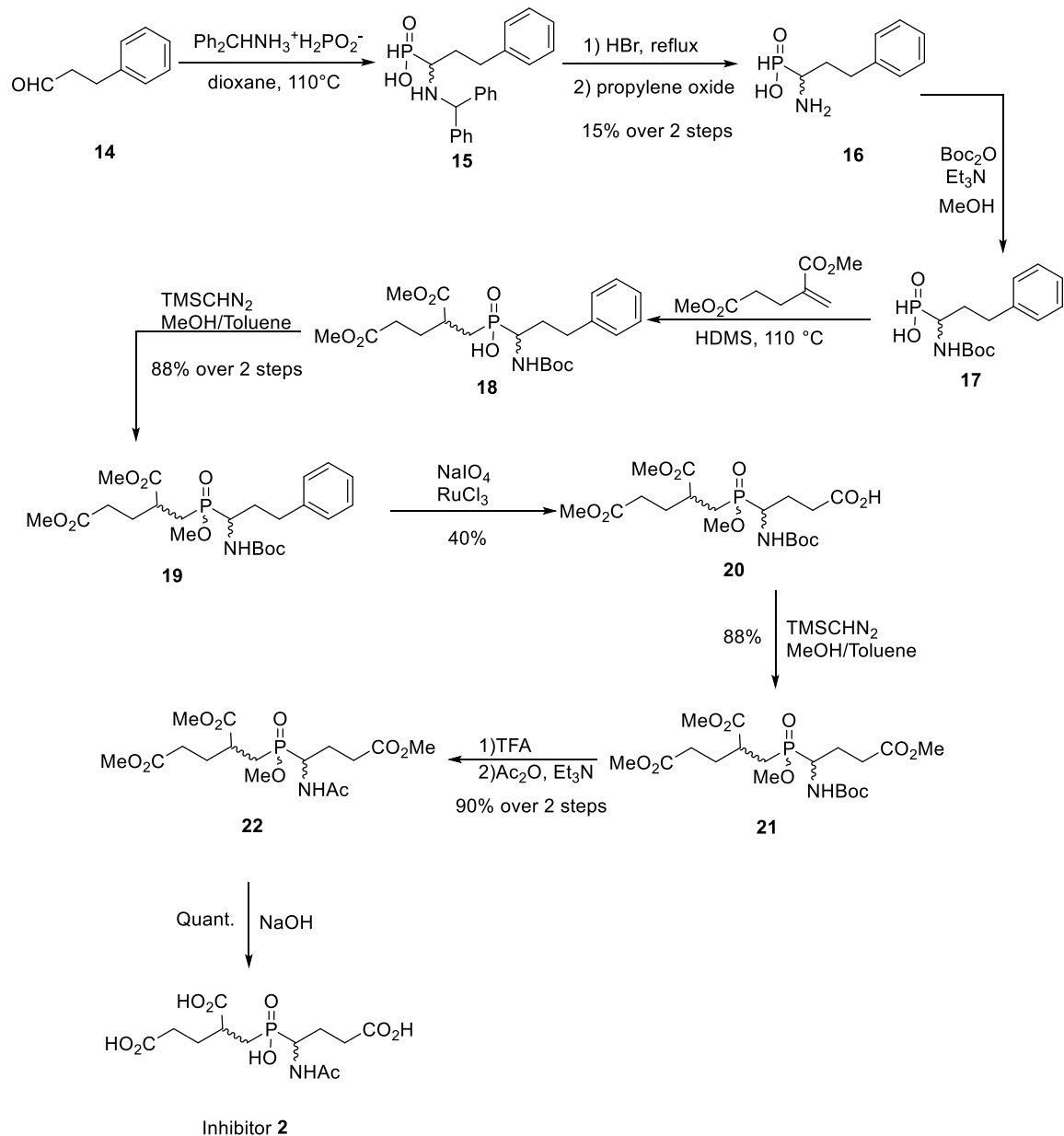


Figure 2.9. Synthesis of inhibitor 2.

2.3 Testing Inhibitors with TTLL7

The activity of polyglutamylase TTLL7 was measured using a synthetic *N*-acetylated β IVb-tubulin CTT peptide (Figure 2.10) as substrate. The unacetylated peptide was firstly prepared via a solid phase peptide synthesis and was left linked to the resin. The resin-linked peptide was then acetylated at the *N*-terminus with acetic anhydride and was then cleaved off the resin using

trifluoroacetic acid (TFA). It was then purified using HPLC. In the lab of our collaborator Dr. Antonina Roll-Mecak, the peptide (100 μM) was incubated with recombinant mouse TTLL7 in a buffered solution of glutamate, Mg^{2+} and ATP. The reaction was run at multiple concentration levels of inhibitor **1-3** (0 μM – 1000 μM , Figure 2.12). Two control reactions lacking ATP and Glu respectively were also monitored. The quantitative measurement of the reaction extent was monitored using ESI-TOF LC-MS (Figure 2.11). Progress was assessed by following the decrease in the intensity of the signal due to the substrate peptide as well as the increase in that due to the glutamylated product. It was shown that under the given conditions, the principle reaction is initiation and the major product is mono-glutamylated peptide (Figure 2.11, 2nd Entry). Meanwhile a minor peak of di-glutamylated product was also observed, but its peak intensity was much lower (10% -15% of the major product peak). Amongst all three inhibitors, inhibitor **2** showed the highest potency for TTLL7, with an IC_{50} of 150 μM . The other two inhibitors showed only weak inhibition and displayed IC_{50} values in the mM level. All three inhibitors were also tested against the related tubulin tyrosine ligase (TTL). However, none of these compounds displayed significant inhibition with this enzyme, suggesting they were specific to the TTLL enzyme (124).

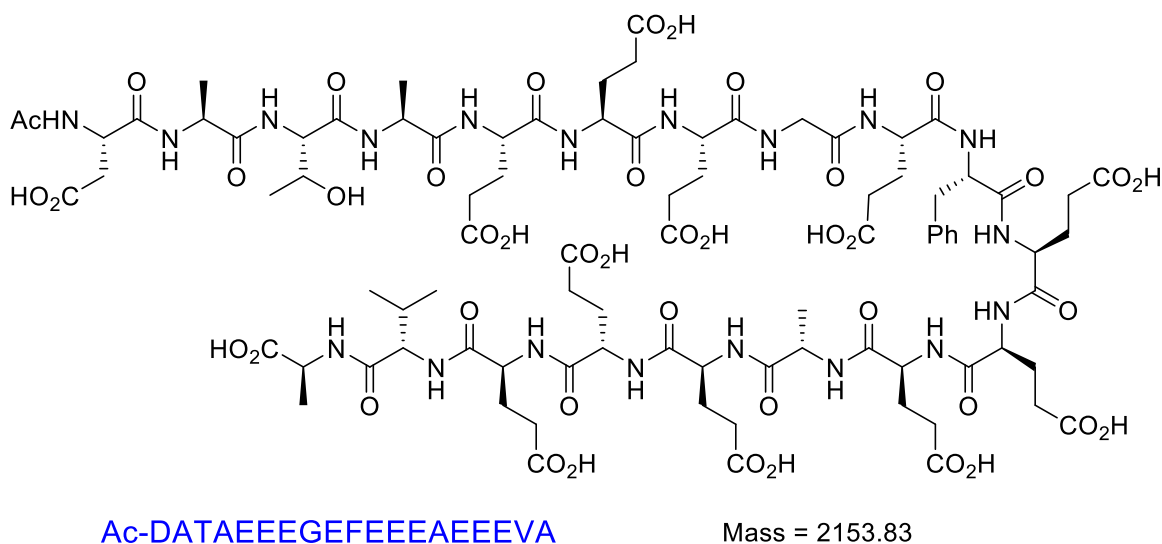


Figure 2.10. Structure of the βIVb -tubulin CTT peptide.

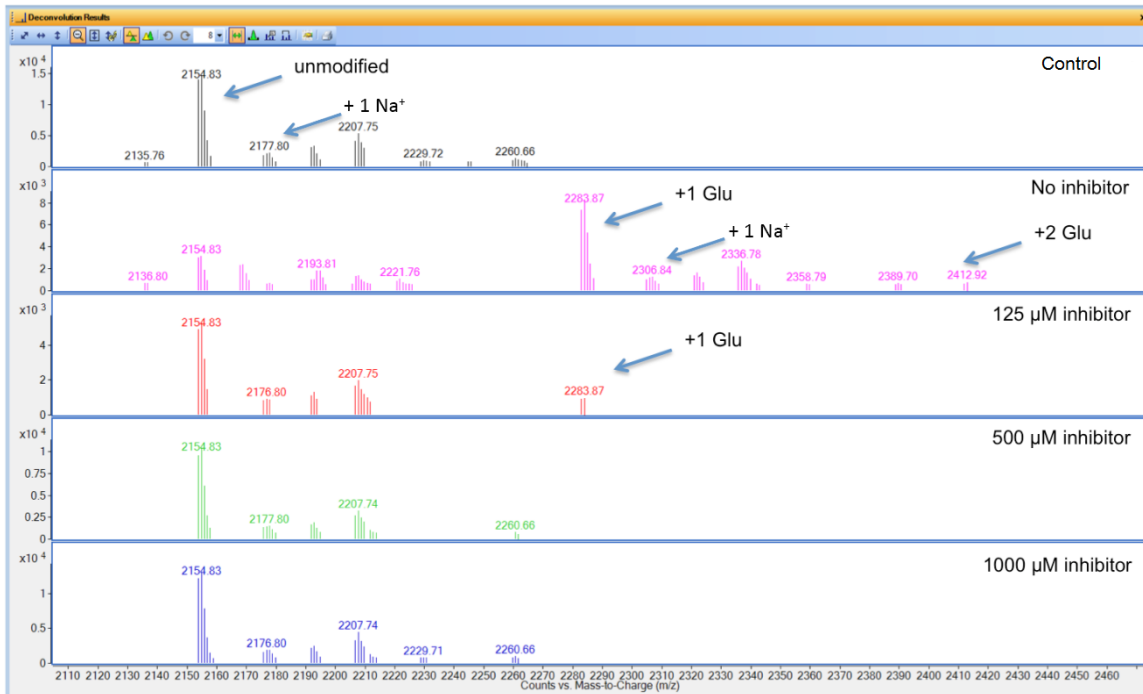


Figure 2.11. A series of mass spectra monitoring changes in the mass of The CTT peptide after enzymatic incubations in the presence of varying amounts of inhibitor 2.

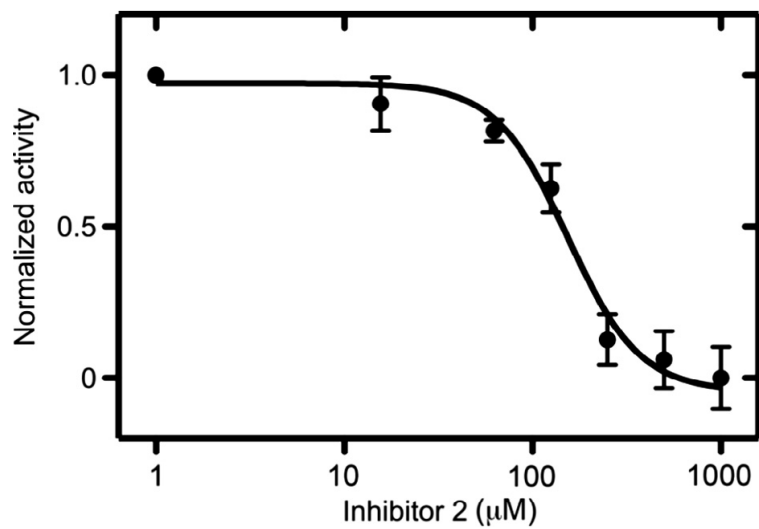


Figure 2.12. A plot of normalized activity versus the concentration of inhibitor 2 for the inhibition of tubulin C-terminal peptide (100 μM) glutamylation by TTL7.

2.4 Discussion

Although the three inhibitors were designed to act on different steps of tubulin polyglutamylation, they are all structural analogues of a Glu-Glu dipeptide. The main difference between inhibitor **2** and inhibitors **1** & **3** is that inhibitor **2** mimics an α -linked peptide bond while inhibitors **1/3** mimic an γ -linked one. As the extent of reaction was very low, we could not tell whether α -elongation or γ -elongation was involved. The higher potency of inhibitor **2** was consistent with the previously reported western blot results using the antibody GT335 that recognizes α -linked side chains (125,126). Thus, our results support the notion that α addition is involved in the TLL7 elongation steps.

The kinetic data also reflected that all three inhibitors have the ability to inhibit the initiation step, as it was the predominant reaction monitored in our assay. The results are not exactly consistent with our prediction as we expected that inhibitor **1** showed higher potency to TLL7 than inhibitors **2** and **3**. The fact that inhibitor **2** bound most tightly to TLL7 cannot be fully understood until more structural information is available. A published structure of a related enzyme, tubulin tyrosine ligase (TTL), showed a conserved subdomain with a long groove containing many positive charged residues (Arg and Lys) (124). This subdomain is the tubulin/CTT peptide binding site and is thought to recognize the highly negatively-charged CTT residues. The significance of these charge-charge interactions has been supported by studies on peptide substrate specificity. It has been shown that TTL activity dropped dramatically when the peptide length was decreased to 10 amino acids (127). In the case of TLL7, it is likely that a similar subdomain may exist and that could help to explain the higher potency of more negatively charged inhibitor **2**.

The effects of neighboring or remote groups on inhibitor have also been observed in other ATP dependent ligases (100,128). In the case of MurD which (adds a D-Glu to the UDP-MurNAc-L-Ala, see Section 1.2.2.1), the phosphinic inhibitor **4** lacking a UDP-MurNAc moiety showed very poor activity ($IC_{50} > 1$ mM) (Figure 2.13). When a UDP group was connected to the pseudodipeptide via a non-sugar linker (inhibitor **5**), the potency dramatically increased to a micromolar level. Finally the closest analogue **6**, bearing both a UDP and a GlcNAc moiety, showed the greatest potency and was active at the nanomolar level. Thus groups remote to the actual phosphinic acid can have large effects on potency, and help to explain why even our best inhibitor was only active at the 150 μ M range.

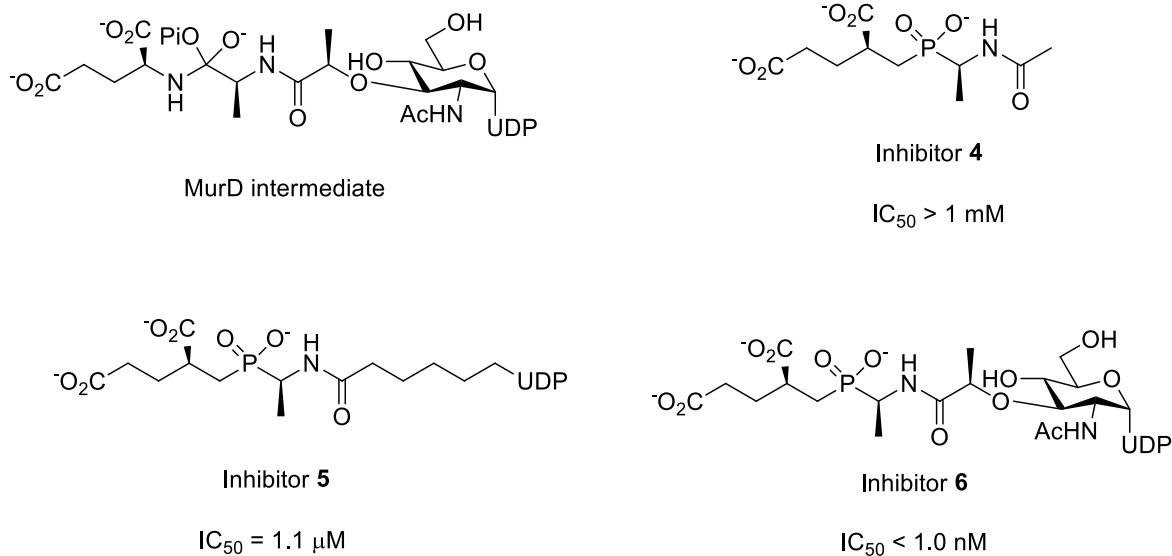


Figure 2.13. MurD inhibitors showed different potency depending on the presence of the sugar and UDP group.

2.5 Summary

In this chapter, we have tested a synthetic β IVb tubulin CTT peptide as a substrate analogue of tubulin polyglutamylase TTLL7. We have also detailed the design, synthesis and testing of three dipeptyl phosphinic acid inhibitors **1**, **2** and **3** targeted against TTLL7 initiation and elongation reactions. The synthetic peptide served as substrate of TTLL7, and the reaction gave the mono-glutamyl peptide as the principal product and di-glutamyl peptide as a minor product. The enzymatic reactions with peptide supported the notion that small molecules could productively bind to TTLL7. In the inhibitors testing, we found inhibitor **2** showed the highest inhibition activity with an IC_{50} at 150 μM , whereas inhibitors **1** and **3** were only active at the millimolar level. These inhibition results were consistent with the observation that α linkages were present in tubulin isolated from mouse brain. The limited potency of the inhibitors suggested that occupation of the extended positively charged groove was important for binding.

Most of the TTLL family enzymes have only been discovered recently, and studies on these enzymes, including their cellular function and regulatory roles in biological pathways are in the very early stages. It is possible that the discovery of the well-characterized polyglutamylase

inhibitors with decent potency would be a breakthrough in the research of this unexplored area. The three inhibitors we made are the first known compounds that show activity against this family of enzymes. Given the potency observed with phosphinic acid inhibitors of other ligases such as D-Ala-D-Ala ligase or MurD, it should be possible to improve these values and design more potent inhibitors.

2.6 Future Directions

Future efforts regarding TTL7 will focus on improving the current inhibitors to obtain higher potency and testing the inhibitors with other tubulin polyglutamylases and deglutamylases. Based on the importance of “remote” binding feature, our strategy is to incorporate the phosphinic acid into the synthetic CTT peptide (129). The peptidyl phosphinic inhibitor with an extended peptide chain will provide the required negatively charged side chains to occupy the conserved strip and increase the binding affinity. To generate that phosphinic peptide, an initial target is to make the suitable phosphinic monomer for solid phase peptide synthesis. The phosphinate pseudopeptide fits the requirements of a monomer that can be used in solid phase synthesis and can be synthesized in a similar style as inhibitor **1** (Figure 2.14). With this compound, the peptide inhibitor **7** will be obtained and tested in the same fashion as previous inhibitors to see if it has marked improvement in activity.

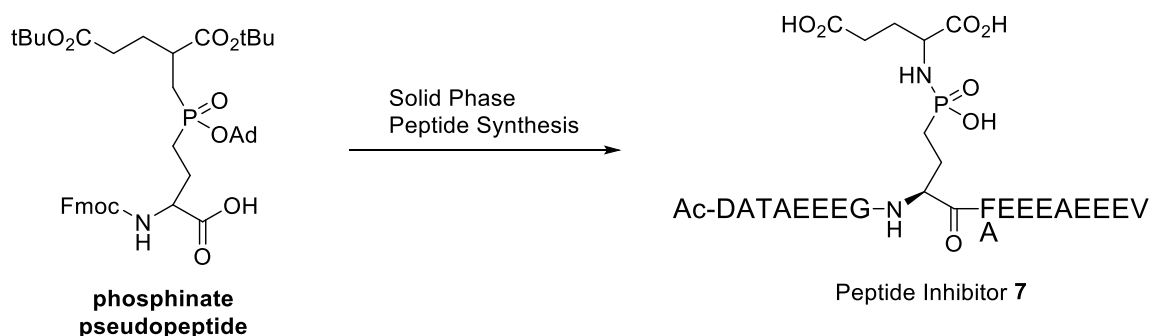


Figure 2.14. Peptide inhibitor synthesis.

Another direction is to test the current inhibitors with other TTL enzyme family members, as well as the cytosolic carboxypeptidases (CCPs) that act as tubulin deglutamylases. The CPP

enzymes hydrolyze peptide bonds (mechanism see Section 1.2.3.2), and these inhibitors are also structural analogues to the tetrahedral intermediate formed during hydrolysis. Therefore, the phosphinic acid-based inhibitors may show inhibition potency against tubulin deglutamylases.

2.7 Experimental

2.7.1 Materials and general procedures

Chemicals were purchased from Aldrich Chemical Co., Alfa Aesar Co. or Fisher Scientific and used without further purification unless otherwise noted. The TLC silica gel (aluminum sheets) was from EMD Chemical Inc. Silica gel chromatography was prepared using Silica Gel SiliaFlash F60 (Silicycle, 230-400 mesh). Ion exchange resin AG-1X8 was purchased from Bio-Rad Laboratories and resin Amberlite IR-120H was purchased from Aldrich Co.. CH_2Cl_2 , MeOH and TEA were distilled under Ar from CaH_2 .

^1H NMR spectra and proton-decoupled ^{31}P NMR spectra was recorded on a Bruker AV400dir spectrometer or a Bruker AV400inv spectrometer at field strength of 400 MHz and 162 MHz, respectively. High resolution mass spectrometry was performed by electrospray ionization (ESI-MS) using an Esquire LC mass spectrometer. Mass spectrometry of high MW molecules was performed by Matrix-assisted laser dispersion ionization (MALDI-MS) using a Bruker Autoflex MALDI-TOF. All mass spectrometry was obtained at the UBC Mass Spectrometry Facility. Neutral compounds were detected as positive ions, and negatively charged compounds were detected as negative ions.

2.7.2 Synthesis of inhibitor 1

2.7.2.1 Compound 8

To compound **4** (160 mg, 0.5 mmol) in MeOH (20 mL) were added ammonium hypophosphite (204 mg, 2.5 mmol) and triethylborane (1.0 M in THF, 1.2 mL). The solution was stirred for 3h, then evaporated to dryness under reduced pressure. The resulting residue was dissolved in aqueous KHSO_4 (1.0 M, 10 mL), and was extracted with EtOAc (3 x 50 mL). The combined

organic phases were dried over anhydrous Na₂SO₄. Removal of the solvent in vacuo gave a colorless oil (189 mg), which was used in the next step without further purification.

A mixture of the colorless oil (189 mg, crude) and hexamethyldisilazane (395 mg, 2.4 mmol) was heated for 1 h at 110 °C under argon. Dimethyl 2-methylenepentanedioate (110 mg, 0.66 mmol) was then added. The resulting mixture was heated for 3 h at 90 °C. After cooling to 70 °C, the reaction was quenched with MeOH (10 mL). The resulting solution was evaporated to dryness in vacuo, then extracted with a NaHCO₃ solution (10%, 15 mL) and diethyl ether (10 mL). The aqueous phase was separated, and extracted with EtOAc (3 x 50 mL). The combined organic phases were dried over anhydrous Na₂SO₄, filtered, and the solvent was removed under reduced pressure to give a yellow oil (215 mg). This oil was used in the next step without further purification.

To a solution of the oil prepared above (215 mg, compound **7**, crude) in MeOH/toluene (4:1, 20 mL) was added trimethylsilyldiazomethane (1.0 M in Et₂O, 1.5 mL) dropwise, until the yellow color stopped fading. The reaction mixture was stirred for 40 min, followed by quenching with the addition of acetic acid (1 mL). The resulting solution was evaporated to dryness in vacuo to give a yellow oil, and the resulting residue was purified by chromatography on silica gel (2% MeOH in CH₂Cl₂) to give compound **5** as a colorless oil (261 mg, 92 % over 3 steps). ¹H NMR (400 MHz, CDCl₃) δ 7.35 – 7.34 (m, 10H), 5.72 – 5.65 (m, 1H), 5.18 (s, 2H), 5.10 (s, 2H), 4.43 (brs, 1H), 3.71 – 3.48 (m, 9H), 2.80 – 2.77 (m, 1H), 2.35 – 2.31 (m, 2H), 2.19 – 2.13 (m, 2H), 1.98 – 1.92 (m, 3H), 1.78 – 1.67 (m, 3H). ³¹P NMR (CDCl₃) δ 56.47, 55.93. MS (ESI) (m/z) 578.4 [M+H]⁺, 600.3 [M+Na]⁺.

2.7.2.2 Compound **10**

To a solution of compound **8** (710 mg, 1.2 mmol) in MeOH (20 mL) was added Pd/C (10% , 50 mg). The resulting mixture was stirred under hydrogen gas (1 atm) for 5 h, and then filtered through celite. The filtrate was evaporated in vacuo and dried under reduced pressure to give a colorless oil (387 mg).

The oil (387 mg, 1.1 mmol) was dissolved in an aqueous solution of acetic acid (0.1 M, 20 mL). Acetic anhydride (560 mg, 5.5 mmol) was added dropwise, and the pH was adjusted to 6 by the addition of triethylamine. The resulting solution was acidified to pH 2 by the addition of Amberlite IR-120H ion exchange resin. Filtration and removal of the solvent in vacuo gave a colorless oil as crude (523 mg).

To a portion of this oil (278 mg) in dry CH₂Cl₂ (20 mL) was added hydroxybenzotriazole (357 mg, 2.3 mmol) at -15 °C under Ar. The mixture was stirred for 30 min, followed by addition of 1-ethyl-3-(3-dimethylaminopropyl)carbodiimide hydrochloride (EDC•HCl) (447 mg, 2.3 mmol). A solution of ethylamine (70% wt. in water, 0.1 mL, 1.4 mmol) in CH₂Cl₂ (10 mL) was precooled in an ice bath, and then added into the reaction mixture at -15 °C. The reaction was stirred for 1 h at -15 °C, and another 2h at rt. The reaction was diluted with water (10 mL) and extracted with CH₂Cl₂ (3 x 100 mL). The combined organic phase was washed by citric acid (10%), NaHCO₃ (5%), and brine. The resulting solution was dried over Na₂SO₄, filtered, and evaporated to dryness in vacuo. The residue was purified by chromatography on silica gel (5% MeOH in CH₂Cl₂) to give compound **6** as a colorless oil (220 mg, 66% over 3 steps). ¹H NMR (400 MHz, CDCl₃) δ 7.24 – 7.18 (m, 1H), 7.08-7.03 (m, 1H), 4.56-4.49 (m, 1H), 3.77 – 3.63 (m, 9H), 3.31 – 3.20 (m, 2H), 2.90 – 2.76 (m, 1H), 2.38 – 2.31 (m, 2H), 2.29 – 2.17 (m, 1H), 2.12-2.02 (m, 1H), 2.02 (s, 3H), 1.98 – 1.90 (m, 3H), 1.89 – 1.69 (m, 3H), 1.13 (t, J = 7.2 Hz, 3H). ³¹P NMR (162 MHz, CDCl₃) δ 59.36, 58.94, 58.72, 58.33. MS (ESI) (*m/z*) 423.4 [M+H]⁺, 445.4 [M+Na]⁺.

2.7.2.3 Inhibitor **1**

Compound **10** (90 mg, 0.2 mmol) was dissolved in a solution of NaOH (0.5 M, 10 mL) and stirred for 1h at rt. The solution was neutralized with Amberlite IR-120H ion exchange resin and then was filtered. The pH of the filtrate was readjusted to 10 using NaOH (2.0 M), and the solution was loaded onto a column of AG 1-X8 resin (formate form, 100-200 mesh, 10 mL). The column was washed with water (50 mL) and formic acid (0.5 M, 50 mL) and was then eluted with formic acid (4.0 M, 100 mL). The fractions containing the compound were combined and evaporated to dryness in vacuo to give inhibitor **1** as a glassy solid (76 mg, 91%). ¹H NMR (400 MHz, MeOD) δ 4.35 – 4.28 (m, 1H), 3.22 (q, J = 7.1 Hz, 2H), 2.84 – 2.72 (s, 1H), 2.38 (dd, J = 14.1, 7.1 Hz, 2H), 2.23 (m, 1H), 2.01 (s, 3H), 1.99 – 1.92 (m, 2H), 1.92 – 1.84 (m, 2H), 1.84 – 1.70 (m, 3H), 1.12 (t, J = 7.2 Hz, 3H). ³¹P NMR (162 MHz, CD₃OD) δ 52.45. MS (ESI) (*m/z*) 379.4 [M-H].

2.7.3 Synthesis of inhibitor **2**

2.7.3.1 Compound **19**

A mixture of (1-((tert-butoxycarbonyl)amino)-3-phenylpropyl)phosphinic acid **17** (1.45 g, 4.8 mmol) and hexamethyldisilazane (3.9 g, 24.2 mmol) was stirred for 1 h at 110 °C under argon, and dimethyl 2-methylenepentanedioate (**8**) (1.1 g, 6.3 mmol) was then added dropwise. The

resulting mixture was stirred for 3 h at 110 °C under argon, and was quenched by slowly adding MeOH (10 mL). The resulting solution was evaporated to dryness in vacuo, then extracted with NaHCO₃ solution (10%, 30 mL) and diethyl ether (15 mL). The aqueous phase was separated, and was extracted with EtOAc (3 x 100 mL). The combined organic phase was dried over anhydrous Na₂SO₄, filtered and evaporated to dryness, to give a yellow oil (2.1 g). The resulting oil was used in the next step without further purification.

To a solution of the above oil (2.1 g, crude) in MeOH/toluene (4:1, 20 mL) was added trimethylsilyldiazomethane (1.0 M in Et₂O, 4.8 mL) dropwise, until the yellow color stopped fading. The reaction mixture was stirred for 40 min, followed by quenching with acetic acid (1 mL). The resulting solution was evaporated to dryness in vacuo to give a yellow oil that was purified by chromatography on silica gel (2% MeOH in CH₂Cl₂) to give compound **9** as a colorless oil (2.07 g, 88% over 2 steps). ¹H NMR (400 MHz, CDCl₃) δ 7.31 (m, 2H), 7.25 – 7.16 (m, 3H), 5.05 – 4.99, 4.73 – 4.79 (2m, 1H), 4.09 – 3.88 (m, 1H), 3.80 – 3.64 (m, 9H), 2.92 – 2.76 (m, 2H), 2.74 – 2.59 (m, 1H), 2.34 (t, J = 7.8 Hz, 2H), 2.29 – 2.16 (m, 1H), 2.02 – 1.92 (m, 2H), 1.92 – 1.80 (m, 3H), 1.48 (s, 9H). ³¹P NMR (162 MHz, CDCl₃) δ 53.86, 53.04, 52.95, 52.89. MS (ESI) (*m/z*) 508.5 [M+Na]⁺.

2.7.3.2 Compound **20**

Compound **19** (765 mg, 1.6 mmol) and sodium periodate (11.9 g, 39 mmol) were dissolved into a mixture of EtOAc (5 mL) and water (50 mL), and then ruthenium (III) trichloride hydrate (10 mg) was added. The resulting mixture was stirred vigorously for 3 h, and EtOAc (10 mL) with H₂O (20 mL) were added. The organic phase was separated, and the aqueous phase was extracted with EtOAc (2 x 50 mL). The combined organic phase was washed with water (20 mL), dried over anhydrous Na₂SO₄, and filtered. Removal of the solvent in vacuo gave a yellow oil, which was purified by chromatography on silica gel (4% MeOH in CH₂Cl₂) to give compound **10** as a colorless oil (365 mg, 40%). ¹H NMR (400 MHz, CDCl₃) δ 5.79, 5.74 (2d, J = 10.4, 10.3 Hz, 1H), 4.09 – 3.90 (m, 1H), 3.83 – 3.62 (m, 9H), 2.92 – 2.78 (m, 1H), 2.53 – 2.38 (m, 2H), 2.38 – 2.21 (m, 3H), 2.07 (d, J = 4.4 Hz, 1H), 2.01 – 1.81 (m, 4H), 1.44 (s, 9H). ³¹P NMR (162 MHz, CDCl₃) δ 54.98, 53.98, 53.53, 53.42. MS (ESI) (*m/z*) 476.2 [M+Na]⁺.

2.7.3.3 Compound **21**

To a solution of compound **20** (1.0 g, 2.2 mmol) in MeOH/toluene (4:1, 20 mL) was added trimethylsilyldiazomethane (1.0 M in Et₂O, 2.2 mL) dropwise, until the yellow color persisted. The reaction mixture was stirred for 40 min, and was quenched by the addition of acetic acid (1

mL). The resulting solution was evaporated to dryness in vacuo to give a yellow oil that was purified by chromatography on silica gel (4% MeOH in CH₂Cl₂) to give the title compound as a colorless oil (0.9 g, 88%). ¹H NMR (400 MHz, CDCl₃) δ 5.20 – 5.14, 4.87 – 4.82 (2m, 1H), 4.18 – 3.87 (m, 1H), 3.85 – 3.45 (m, 12H), 2.89 – 2.75 (s, 1H), 2.54 – 2.40 (m, 2H), 2.39 – 2.29 (m, 2H), 2.29 – 2.18 (m, 1H), 2.18 – 2.07 (m, 1H), 2.03 – 1.76 (m, 4H), 1.43 (s, 9H). ³¹P NMR (162 MHz, CDCl₃) δ 53.65, 52.67, 52.57. MS (ESI) (m/z) 468.3 [M+H]⁺, 490.3 [M+Na]⁺.

2.7.3.4 Compound **22**

To a solution of compound **21** (830 mg, 1.8 mmol) in TFA (10 mL) and CH₂Cl₂ (7 mL) was added water (0.5 mL). The resulting solution was stirred for 3 h, and then was evaporated in vacuo to give a red oil as crude (650 mg), which was used in the next step without further purification.

The above oil (650 mg) was dissolved in an aqueous solution of acetic acid (0.1 M, 15 mL). Acetic anhydride (9.1 g, 8.9 mmol) was added dropwise into the solution, and the pH was maintained at 6 by addition of triethylamine. After stirring for 10 min, the resulting solution was acidified with Amberlite IR-120H ion exchange resin to pH~2 and filtered. Removal of the solvent in vacuo gave a red oil, which was purified by chromatography on silica gel (3% MeOH in CH₂Cl₂) to give compound **12** as a colorless oil (636 mg, 90% over 2 steps). ¹H NMR (400 MHz, CDCl₃) δ 6.98 – 6.93 (m, 1H), 4.42 – 4.29 (m, 1H), 3.78 – 3.65 (m, 12H), 2.89 – 2.75 (m, 1H), 2.42 (t, J = 7.3 Hz, 2H), 2.33 (t, J = 7.7 Hz, 2H), 2.29-2.18 (m, 1H), 2.18 – 2.08 (m, 1H), 2.04 (s, 3H), 1.99 – 1.82 (m, 4H). ³¹P NMR (162 MHz, CDCl₃) δ 56.26, 56.23, 56.20, 55.72. MS (ESI) (m/z) 432.2 [M+Na]⁺.

2.7.3.5 Inhibitor **2**

Compound **22** (210 mg, 0.5 mmol) was dissolved into a NaOH solution (0.5 M, 10 mL), and stirred for 1h. The solution was neutralized by Amberlite IR-120H ion exchange resin to pH~7, then was filtered. The pH of the filtrate was readjusted by NaOH (2.0 M) to 10, then loaded to a column of AG 1-X8 resin (formate form, 100-200 mesh, 10 mL). The column was washed with water (50 mL) and formic acid (0.5 M, 50 mL), and then was eluted by formic acid (4.0 M, 100 mL). The fractions containing the compound were combined and evaporated to dryness in vacuo to give inhibitor **2** as a colorless oil (188 mg, 99 %). ¹H NMR (400 MHz, CD₃OD) δ 4.39 – 4.21 (m, 1H), 2.89 – 2.76 (m, 1H), 2.50 – 2.32 (m, 4H), 2.25 – 2.18 (m, 2H), 2.05 (s, 3H), 2.03 – 1.91 (m, 2H), 1.91 – 1.78 (m, 2H). ³¹P NMR (162 MHz, CD₃OD) δ 49.03. MS (ESI) (m/z) 352.4 [M-H]⁻.

2.7.4 Synthesis of inhibitor 3

2.7.4.1 Compound 11

To a solution of compound **9** (710 mg, 1.2 mmol) in MeOH (20 mL) was added Pd/C (10% , 50 mg). The resulting mixture was stirred under hydrogen gas (1 atm) for 5 h, and then filtered through celite. The filtrate was evaporated in vacuo and dried under reduced pressure to give a colorless oil (387 mg).

The oil (387 mg, 1.1 mmol) was dissolved in an aqueous solution of acetic acid (0.1 M, 20 mL). Acetic anhydride (560 mg, 5.5 mmol) was added dropwise into the solution, and the pH was adjusted to 6 by addition of triethylamine. The resulting solution was acidified to pH 2 by addition of Amberlite IR-120H ion exchange resin. Filtration and removal of the solvent in vacuo gave a colorless oil (523 mg) that was used in the next step.

To a portion of the colorless oil (238 mg, 0.6 mmol) in MeOH/toluene (4:1, 20 mL) was added trimethylsilyldiazomethane (1.0 M in Et₂O, 1.0 mL) dropwise, until the yellow color persisted. The reaction mixture was stirred for 40 min, and was then quenched by the acetic acid (1 mL). The resulting solution was evaporated to dryness in vacuo to give a yellow oil that was purified by chromatography on silica gel (4% MeOH in CH₂Cl₂) to give compound **7** as a colorless oil (241 mg, 86% over 3 steps). ¹H NMR (400 MHz, CDCl₃) δ 6.79 – 6.60 (m, 1H), 4.67 – 4.57 (m, 1H), 3.80 – 3.64 (m, 12H), 2.92 – 2.75 (m, 1H), 2.43 – 2.30 (m, 2H), 2.29 – 2.10 (m, 2H), 2.05 (s, 3H), 2.03 – 1.92 (m, 3H), 1.89 – 1.72 (m, 3H). ³¹P NMR (162 MHz, CDCl₃) δ 56.29, 55.80. MS (ESI) (m/z) 410.4 [M+H]⁺, 432.3 [M+Na]⁺.

2.7.4.2 Inhibitor 3

Compound **11** (185 mg, 0.47 mmol) was dissolved in a NaOH solution (0.5 M, 10 mL), and stirred for 1h. The solution was neutralized with Amberlite IR-120H ion exchange resin and then filtered. The pH of the filtrate was readjusted with NaOH (2.0 M) to 10, and was loaded to a column of AG 1-X8 resin (formate form, 100-200 mesh, 10 mL). The column was washed by water (50 mL) and formic acid (0.5 M, 50 mL), and then was eluted by formic acid (4.0 M, 100 mL). The fractions containing the compound were combined and evaporated to dryness in vacuo to give inhibitor **3** as a colorless oil (136 mg, 82%). ¹H NMR (400 MHz, CD₃OD) δ 4.54 – 4.39 (m, 1H), 2.89 – 2.71 (m, 1H), 2.46 – 2.30 (m, 2H), 2.30 – 2.09 (m, 2H), 2.02 (s, 3H), 2.00 – 1.89

(m, 3H), 1.88 – 1.77 (m, 3H). ³¹P NMR (162 MHz, CD₃OD) δ 52.46. MS (ESI) (*m/z*) 352.4 [M-H].

2.7.5 Peptide synthesis

Standard solid-phase methods and the Fmoc/*t*-Bu strategy were used to synthesize the *N*-acetylated peptide Ac-DATAEEEEGEFEEEEAEVEA on a C S Bio (Menlo Park, CA) 136XT peptide synthesizer. Fmoc-Ala-Wang resin was used on a 0.25 mmol scale. Standard Fmoc protected amino acids were used during the synthesis with acid labile protecting groups for glutamate and aspartate side chains. The following amino acid were used: Fmoc-L-Glu(OtBu)-OH, Fmoc-Gly-OH, Fmoc-L-Asp(OtBu)-OH, Foc-Thr(*t*Bu)-OH, Fmoc-Val-OH and Fmoc-Ala-OH(H₂O). All chemicals were purchased from Advanced Chemtech (Louisville, KY) and C S Bio, except for DMF and activating reagents, which were purchased from Aldrich.

The free *N*-terminus of the amino acid peptide resin (~0.05 mmol peptide) was reacted with acetic anhydride (2 mL, 25 mmol) and for 1h at room temperature. Following acetylation, the peptide resin was washed with methanol. It was then cleaved from the resin using a 2h treatment of 95% trifluoroacetic acid (TFA): 5% H₂O solution (5 mL), precipitated with cold diethyl ether, and purified by reverse-phase HPLC using a linear gradient of acetonitrile and water on a Waters C-18 Delta Pak column (300 x 19 mm², 300 Å, 15 cm) at a flow rate of 10 mL min⁻¹. Peptides eluted between 80% - 75% H₂O. Purification by HPLC afforded peptide as a white solid (~ 30 mg).

2.7.6 Inhibition assay

Mouse TTLL7 was expressed in *E. coli* Rosetta2 DE3 pLysS (Novagen) as an *N*-terminal GST fusion. Expression was induced with 0.5 mM isopropylthiogalactoside for 16 hours at 16 °C. Cells were lysed using a microfluidizer and centrifuged at 31,000 xg for 45 minutes to pellet cellular debris. The fusion protein was purified *via* GST affinity chromatography and the GST tag was subsequently removed *via* TEV protease cleavage. TTLL7 was further purified to homogeneity *via* ion exchange and gel permeation chromatography. To determine the IC₅₀ value for inhibitor **2**, 10 μM TTLL7 was incubated with 100 μM of a synthetic *N*-acetylated βIVb-tubulin tail peptide (Ac-DATAEEEEGEFEEEEAEVEA) in the presence of increasing concentrations of inhibitor **2** (0 μM, 15 μM, 62.5 μM, 125 μM, 250 μM, 500 μM, and 1000 μM) in 20 mM HEPES (pH 7.0), 100 mM NaCl, 5 mM MgCl₂, 1 mM ATP, 1 mM glutamate, and 0.5 mM TCEP. Reactions were incubated at 23 °C for 16 hours. All reactions were performed in

triplicate. The control reaction lacked ATP and glutamate and was also performed in triplicate. Reactions were terminated by the addition of an equal volume of 0.1% TFA supplemented with 10 mM EDTA. 10 μ l of each reaction was then separated on a Zorbax 300SB-C18 column (Agilent) using a 0-70% acetonitrile gradient in 0.05% TFA. The column was attached in line with a 6224 ESI TOF LC-MS (Agilent). The average MS signal intensity of the unmodified peptide at each inhibitor **2** concentration was determined using the Masshunter Workstation platform (Agilent) and normalized to the average signal intensity of the unmodified peptide in the control reaction. The data were fit using non-linear regression in the program Prism. The linearity of the signal for the peptide concentrations in the assay was verified using serial dilutions of the substrate peptide.

3. Inhibition and Structural Studies on the Peptidoglycan-Modifying Carboxypeptidase Csd4 from *Helicobacter pylori*

The peptidoglycan (PG) sacculus is continuously remodeled during the bacterial life cycle by a series of PG-modifying enzymes. One effect of this PG modification is the development of diverse cellular shapes in different species. Control over morphology is essential for bacterial survival in many biological environments. In particular, *Helicobacter pylori*, the ϵ proteobacterium harbored by half the world's population, has a helical rod shape that is thought to be closely related to its virulence (89,130). The helical rod cell shape may contribute to its ability to bore into the epithelial mucus layer through a cork-screwing mechanism (90). When *H. pylori* settle in the intestinal tract, they will start colonization and can cause gastritis or peptic ulcers. To date, the models to understand cell shape determination have been built for some species, such as cocci and vibrioids. However, for helical shaped bacteria, there is not much known about the shape remodeling process.

The function of many enzymes involved in PG remodeling have been introduced in Section 1.2. For most Gram-negative bacteria, the pentapeptide covalently attached to the GlcNAc-MurNAc sugar chain is L-Ala-*iso*-D-Glu-*meso*-Dap-D-Ala-D-Ala. After the nascent PG is synthesized, peptide crosslinks are formed by the DD-transpeptidase PBP1 (131). Meanwhile, some crosslinked and uncrosslinked peptides are cleaved or truncated (trimmed) by DD, DL, LD-endopeptidases (EPases) or carboxypeptidases (CPases), including Csd3, 4 and 6 (93-95). All these Csd enzymes play roles in *H. pylori*'s cell shape determination. Deletion of *csd1* or *csd3* will result in mutants with curved rod shape, and deletion of *csd4* or *csd6* will give mutants with a straight rod shape. None of the mutants maintain the helical morphology, thus their pathogenicity is markedly reduced due to a diminished ability to colonize.

Csd4 and 6 were identified as a DL- and a DD-carboxypeptidase, which hydrolyze the peptide bonds between *iso*-D-Glu and *meso*-Dap, and *meso*-Dap and D-Ala, respectively, in an uncrosslinked peptide strand (95). DL-carboxypeptidases, such as Csd4, are relatively rare and little is known about this family of enzymes. Sequence alignments showed that Csd4 contains a zinc-binding domain that belongs to the M14 peptidase superfamily. This M14 family contains a well-studied member carboxypeptidase A (an LL-CPase) that bears the hallmark zinc binding motif HXXE+H (+H₂O). The divalent zinc serves to acidify the bound water molecule and to

stabilize the resulting tetrahedral intermediate. A conserved glutamate acts as the catalytic base residue that deprotonates the nucleophilic water and protonates the leaving amine. The combined benefits lead to efficient hydrolysis of the peptide bond.

This chapter details our studies on the reaction catalyzed by Csd4 and the design and the testing of a Csd4 inhibitor. In addition, *in vivo* inhibition assays are presented. We first briefly summarize the previous advances that have been made towards the identification and characterization of Csd4. Based on the natural muramyl peptide substrate of Csd4, a tripeptide substrate is designed and its synthesis is reported. A structural model of Csd4 bound to the tripeptide is obtained and used to identify potential acid/base residues involved in catalysis. Site-directed mutagenesis is employed to study the structural and morphological roles of specific residues. Moreover, a phosphinate inhibitor of Csd4 that is an intermediate analogue is also designed and synthesized. Comparison of the structural models with substrate bound and inhibitor bound clearly shows the conformational change that occurs during catalysis. A continuous coupled assay is developed to measure the rate of reaction and the kinetic constants k_{cat} , and K_M are determined. The inhibition constant K_I is also measured and a comparison between K_I and K_M demonstrate the effectiveness of the phosphinate inhibitor. Finally, we report the results of the *in vivo* assays of cell shape and toxicity with *C. jejuni* and *H. pylori*. The chapter is concluded with a discussion regarding potential improvements to the current inhibitor, and potential applications in pharmaceutical development.

3.1 Previous Characterization of Csd4 from *H. pylori*

3.1.1 Deletion of the *csd4* gene leads to lack of helical shape in *H. pylori* mutants

Recently Sycuro *et al* reported their discovery of the first three cell shape determinant genes (*csd1 – 3*), through a visual screening of a library of *H. pylori* mutants (93). This library was created using random transposon insertions into various loci and produced over 2000 mutation strains. Mutants lacking *csd1*, 2 or 3 display either slightly curved rod shape or strongly curved shape (letter “C” shape) phenotypes, and are clearly distinguished from the helical wild-type *H. pylori*. Aside from these mutant strains, another with a straight rod shape was recently identified from the same library and was named *csd4* (Figure 3.1).

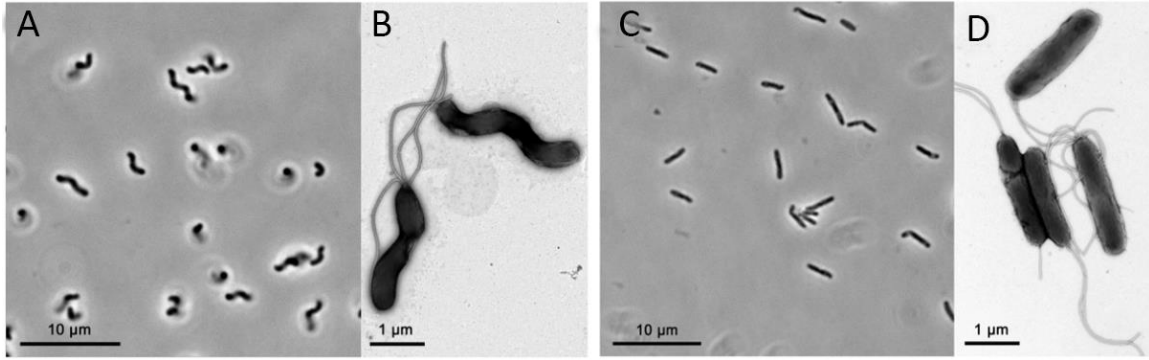


Figure 3.1. A, C) Wild-type and $\Delta csd4$ mutant phase contrast images. B, D) Wild-type and $\Delta csd4$ mutant transmission electron microscopy images.

Deletion of *csd4* results in a drastic shape change, however it does not seem to affect normal physiological properties of the mutants (93). When monitored by transmission electron microscopy (TEM), the $\Delta csd4$ strain did not show any growth deficiency either in a separate culture or in a co-culture with wild-type *H. pylori*. Different stages of cellular division such as cell pole formation and flagella growth were scanned, and no deformity in the mutants was observed. The average length of the rod shape mutants is slightly increased, however the difference is within 10%. Additionally, in the later stationary phase, the mutant strains showed a similar kinetic progress of coccoid transformation.

3.1.2 Csd4 is a DL-carboxypeptidase that hydrolyzes uncrosslinked tripeptides

Sequence analysis revealed that the Csd4 enzyme conserves an *N*-terminal peptidase domain belonging to the M14 peptidase superfamily (132). This enzyme family includes a well-characterized archetype protein *Bacillus sphaericus* endopeptidase I (EPase I). In fact, the so-called *B.sphaericus* EPase I functions as both an endopeptidase and a carboxypeptidase, as it catalyzes the cleavage of the peptide bond between *iso*-D-Glu and *m*-Dap in both muramyl tripeptide (glycan-L-Ala-*iso*-D-Glu-*m*-Dap-D-Ala) and muramyl tetrapeptide (glycan-L-Ala-*iso*-D-Glu-*m*-Dap-D-Ala-D-Ala) (133).

To examine if Csd4 has similar peptidase activity, Sycuro *et al* purified the Csd4 fused with a His Tag by affinity chromatography and incubated the enzyme with the PG sacculi extracted from a $\Delta csd4$ mutant strain. The reaction was monitored by HPLC in the presence of either zinc or EDTA as a negative control. Following treatment with a muramidase, the analysis clearly showed

that in the presence of zinc ion, muropeptide was absent and the amount of muropeptide peak increased. No activity was detected in the batch with EDTA. This observation suggested that Csd4 functions as a zinc-dependent DL-CPase rather than DD-EPase. To verify the result, the muropeptide (GlcNAc-MurNAc-L-Ala-*iso*-D-Glu-*m*-Dap) was isolated and tested as a substrate for Csd4. A similar disappearance of the muramyl tripeptide was observed, along with the formation of the muropeptide. In addition, a control reaction with the murotetrapeptide (GlcNAc-MurNAc-L-Ala-*iso*-D-Glu-*m*-Dap-D-Ala) did not show any reaction. Taken together with the *in vitro* results, Csd4 was confirmed to be a DL-carboxypeptidase that cleaved the isopeptide bond between D-Glu and *m*-Dap (Figure 3.2).

Aside from the functional similarity, structural modelling of the Csd4 protein using M14 family members with known crystal structures revealed several matches in conserved domains including the zinc binding site (134). Sycuro *et al* deduced that position E222 was likely to be key catalytic residue. To test the hypothesis, a strain bearing a point mutant *E222A* was generated. This *H. pylori* variant strain displayed a straight rod morphology, indicating that Csd4 is functioning as a zinc-dependent carboxypeptidase.

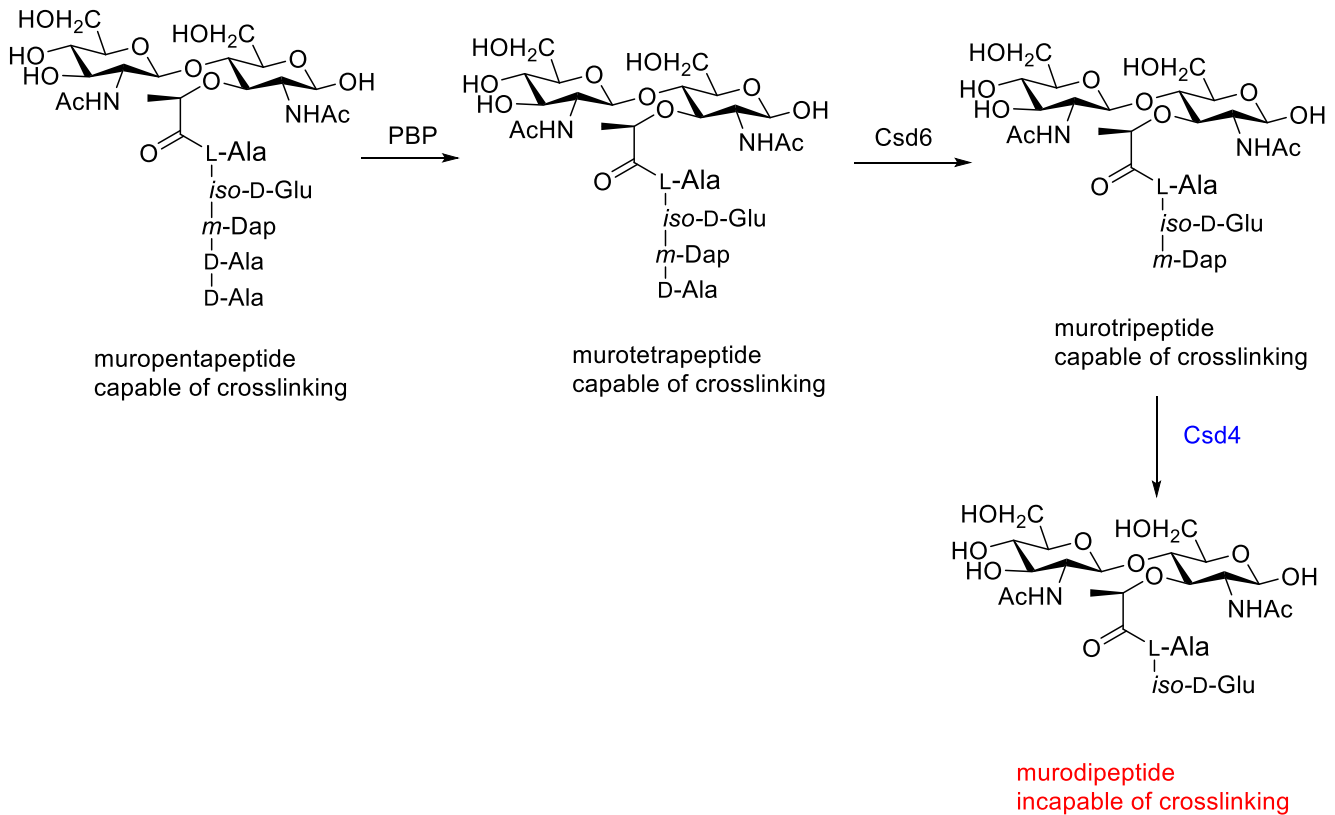


Figure 3.2. The trimming process of single strand muropeptide in *H. pylori*.

3.1.3 Muropeptide composition analysis and genetic mutation results indicate two distinct PG modification pathways control the helical rod shape

To further investigate the Csd4 function *in vivo* and its effect on cell morphology, Sycuro *et al* analyzed the PG sacculi muropeptide composition of several *H. pylori* mutant species (Table 3.1) (95). As expected, both the point mutant *E222A* and the null mutant $\Delta csd4$ showed identical percentage composition. Compared to the wild-type species, the tripeptide component in these two mutants is increased by over 400% (4% to 17%), providing *in vivo* evidence of Csd4 CPase activity. Another interesting difference is that the tetrapeptide component decreases by 80% in these two variants (10% to 2%). The drastic drop of tetrapeptide may also be related to the cell shape phenotypic change.

Table 3.1. Muropeptide composition of PG in mutant strains.

Strains	Wild-type (Avg \pm Sd)	$\Delta csd1$	$\Delta csd3$	$\Delta csd4$	<i>csd4-E222A</i>
Monomers (Total)	58.7 \pm 1.7	54.7	54.8	60.9	60.0
Dipeptide	2.8 \pm 0.4	<u>1.7</u>	<u>2.3</u>	0.0	0.0
Tripeptide	4.0 \pm 0.4	<u>4.7</u>	<u>3.6</u>	17.3	16.1
Tetrapeptide	10.0 \pm 0.6	<u>7.4</u>	<u>6.9</u>	2.3	2.1
Pentapeptide	41.8 \pm 1.1	40.9	42.0	41.3	41.8
Dimers (Total)	41.3 \pm 1.7	45.3	45.2	39.1	40.0

The earlier mutation studies with *csd1 – 3* deletions showed that mutants $\Delta csd1$ and $\Delta csd2$ have a curved rod cell shape while $\Delta csd3$ strain have a highly curved cell shape (135). The double mutation species $\Delta csd1csd2$ displayed a morphology similar to single null mutants $\Delta csd1$ and $\Delta csd2$, suggesting these two genes are allelic. However, the combined mutation products $\Delta csd1csd3$ and $\Delta csd2csd3$ gave a morphology profile with population of highly curved shape, more similar to the single mutant $\Delta csd3$. These results indicate *csd3* is an epistatic gene to both *csd1* and *csd2*. To explore if *csd3* is epistatic to *csd4*, they generated another double mutation strain $\Delta csd3csd4$, but this strain did not resulted in a highly curved phenotype. In fact, the double mutant $\Delta csd3csd4$ showed a curved rod shape distinct from either $\Delta csd3$ or $\Delta csd4$. Thus, it seems that *H. pylori* morphology is controlled independently by both *csd3* and *csd4*.

3.1.4 Csd4 mutant shows weaker gastric stomach colonization but normal PG integrity

Previously, it was reported that $\Delta csd1$ and $\Delta csd3$ *H. pylori* mutant strains showed an impaired ability to colonize in the stomach (95). To examine the effect of $\Delta csd4$ mutation biological function, the $\Delta csd4$ strain was co-cultured with wild type *H. pylori* in mouse stomach. Analysis of the competitive index value showed that the colonization capability of the $\Delta csd4$ strain is markedly weaker than wild-type. Further studies revealed that $\Delta csd4$'s cell wall was intact. Despite the fact that chemical content of its PG layer has been modified, the cell wall resistance to various environments including acidic solution, antibiotics and high osmotic pressure remain at the same level as wild-type.

3.1.5 Reduced motility with shape-dependent phenotypes were observed in gel-like media

To further investigate the possible factors that contribute to reduced colonization ability, the motility of *H. pylori* mutants in a viscous environment was inspected (95). Initially, tests in three different viscous polymer solutions showed that the $\Delta csd4$ mutant moved with the same velocity as the wild-type. However, these polymer solutions are not the close analogues to stomach mucus as their viscoelasticity is not comparable to the gastric environment. Thus, the mutants were assayed in a gel-like agarose media to further explore the relationship between motility and their cellular morphology. In this assay, a significant reduction in halo size was observed for all the mutants when compared to wild-type, which indicates a decrease in cell movement velocity occurred in such a media. Since the agarose is a better mimic of gastric mucus, it is likely that the reduced motility in gel-like media is a key factor accounting for the weakened colonization of the mutants.

3.1.6 Csd4 homologue Pgp1 determines the helical cell shape of *C. jejuni*

Recently, the first PG metalloprotease in *Campylobacter jejuni* Pgp1 (peptidoglycan peptidase 1), was identified from a transposon mutant library (136). This *pgp1* gene is highly conserved in most helical and vibroid bacterial species belonging to ϵ - and δ -Proteobacteria and thus is considered to be a key gene for *C. jejuni*'s morphology. This was demonstrated using a *pgp1* target deletion mutant. The $\Delta pgp1$ strain displayed a striking straight-rod shape distinct from the wild-type helical shape (Figure 3.3). Interestingly, most other physiological properties of

$\Delta pgp1$, including motility, flagellar structure and biofilm level were not obviously altered. Sequence alignment of the Pgp1 enzyme revealed that it has a conserved *N*-terminal domain and zinc binding site shared with the M14 carboxypeptidase family. Taken together, Pgp1 is identified as a homologue of Csd4 in *H. pylori*.

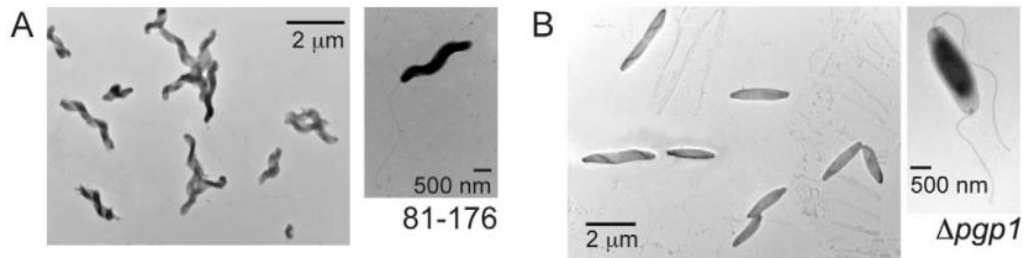


Figure 3.3. Negatively stained TEM images of *C. jejuni* strains. A) 81-176, the wild-type. B) $\Delta pgp1$, the deletion mutant.

Further examination of the muropeptide composition of the $\Delta pgp1$ strain indicates that Pgp1 enzyme has DL-carboxypeptidase activity *in vivo* (Table 3.2). The muropeptide profile of $\Delta pgp1$ peptidoglycan showed a 190% increase (18.4% to 34.4%) in disaccharide tripeptide and a 60% drop (14.5% to 5.9%) in dipeptide. Based on the muropeptide composition data, Pgp1 is likely to function as a carboxypeptidase cleaving the D-Glu-*m*-Dap peptide bond. The same *in vitro* activity assay used with Csd4 supported this notion, and also verified that the activity is dependent on divalent zinc.

Table 3.2. Summary of muropeptide percentage composition of *C. jejuni* strains.

Muropeptide Species	In <i>C. jejuni</i> species		
	wild-type	$\Delta Pgp1$	$\Delta Pgp1c$
Monomers (Total)	43.3	43.4	43.1
Di	<u>14.5</u>	<u>5.9</u>	20.6
Tri	<u>18.4</u>	34.4	3.3
Tetra	<u>18.4</u>	<u>3.1</u>	19.2
Dimers(Total)	49.7	52.5	49.3
Trimers(Total)	6.9	4.2	7.6

3.2 Design and Synthesis of the Ac-L-Ala-*iso*-D-Glu-*m*-Dap Tripeptide

As previous research has identified Csd4 to be a zinc-bound DL-carboxypeptidase, our first target was to obtain a useful substrate. This would allow us to perform kinetic analyses that would ultimately be required for any analysis of Csd4 mutants or inhibitors. Although the monomeric murotripeptide (GlcNAc-MurNAc-L-Ala-*iso*-D-Glu-*m*-Dap) had been shown to be a substrate, the difficulty of its synthesis was prohibitive. Instead we chose to prepare a simplified *N*-acetylated tripeptide (Ac-L-Ala-*iso*-D-Glu-*m*-Dap, Figure 3.4). This compound lacks the sugar residues present in PG, but retains all of the peptide structure.

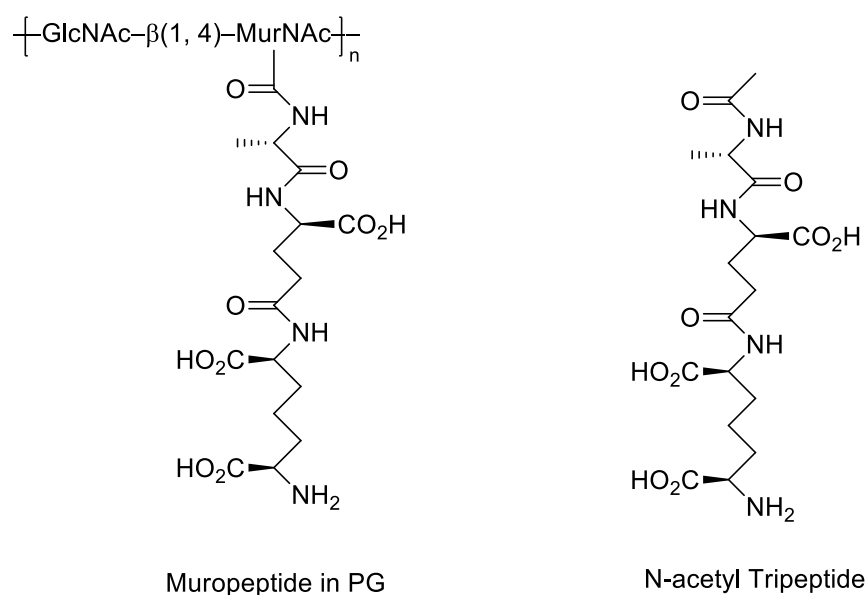


Figure 3.4. The natural substrate muropeptide (left) of Csd4 and the designed tripeptide substrate (right).

The synthesis of the *N*-acetyl tripeptide started from the commercial available *N*-acetyl L-alanine, and an α -*tert*-butyl ester protected D-glutamic acid was introduced at the carboxylate position of the alanine using literature known methodology (Figure 3.5) (137). This generated the dipeptide Ac-L-Ala-D-Glu(OtBu)-OH (Compound **23**). Both of the carboxylates and one of amino groups in *meso*-diaminopimelic acid (*m*-Dap) were protected using benzyl esters and a *tert*-butyloxycarbonyl (Boc-) group, respectively, as described previously in the literature (138). The protection scheme produces an enantiomeric mixture of compound **24**. A second coupling reaction was performed between the dipeptide **23** and the protected *m*-Dap mixture, to give the fully protected tripeptide **25**. After that, deprotection using palladium catalyst and hydrogen gas

followed by 95% trifluoroacetic acid removed the benzyl, Boc- and *tert*-butyl groups. The fully deprotected tripeptide was obtained as a 50/50 mixture of two diastereomers, and no attempts were made to separate or purify the desired diastereomer with the correct absolute configuration.

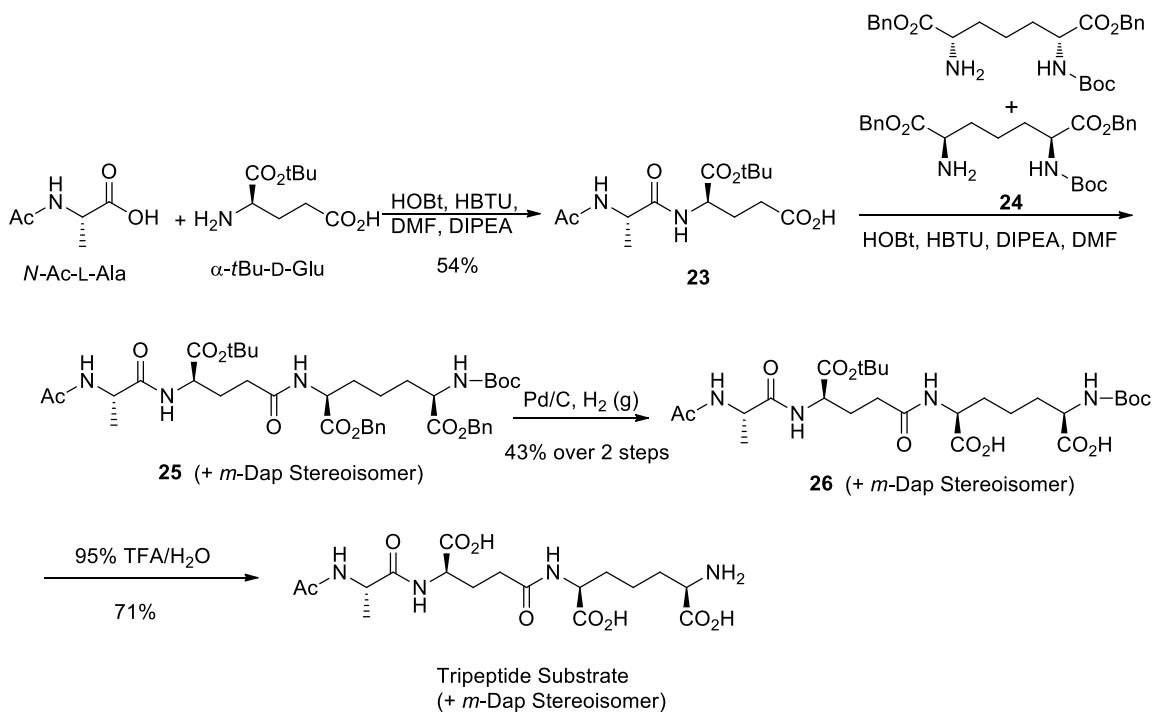


Figure 3.5. The synthetic scheme for the tripeptide substrate.

3.3 Kinetic Studies of Csd4 with the Tripeptide Substrate

After the synthesis of the tripeptide, we examined if this synthetic compound serves as a substrate of Csd4. The kinetics of the Csd4 reaction were monitored using a continuous enzyme-coupled assay in which the absorbance of generated NADPH is measured. When Csd4 hydrolyzes the tripeptide substrate, it releases free *m*-Dap and an *N*-acetyl dipeptide. The released *m*-Dap is then immediately oxidized by the enzyme diaminopimelic acid dehydrogenase (DAPDH), and the cofactor nicotinamide adenine dinucleotide phosphate (NADP⁺) is converted to its reduced form NADPH (Figure 3.6). As NADPH has a characteristic absorbance at 340 nm ($\epsilon = 6220 \text{ M}^{-1} \text{ cm}^{-1}$) (Figure 3.7), the rate of the tripeptide cleavage by Csd4 can be quantified (Figure 3.8).

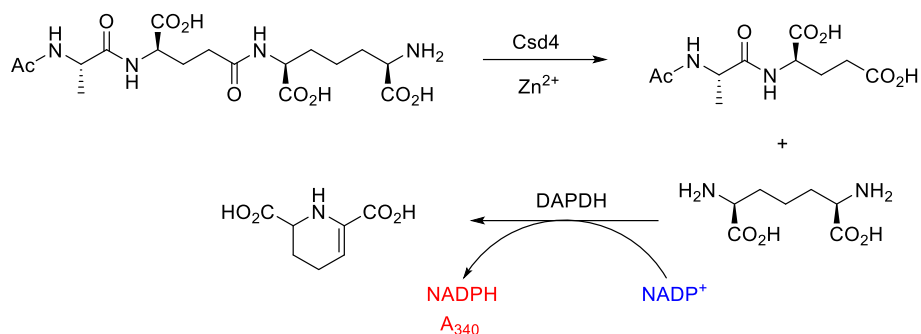


Figure 3.6. The continuous enzyme-coupled assay used in the kinetic analysis.

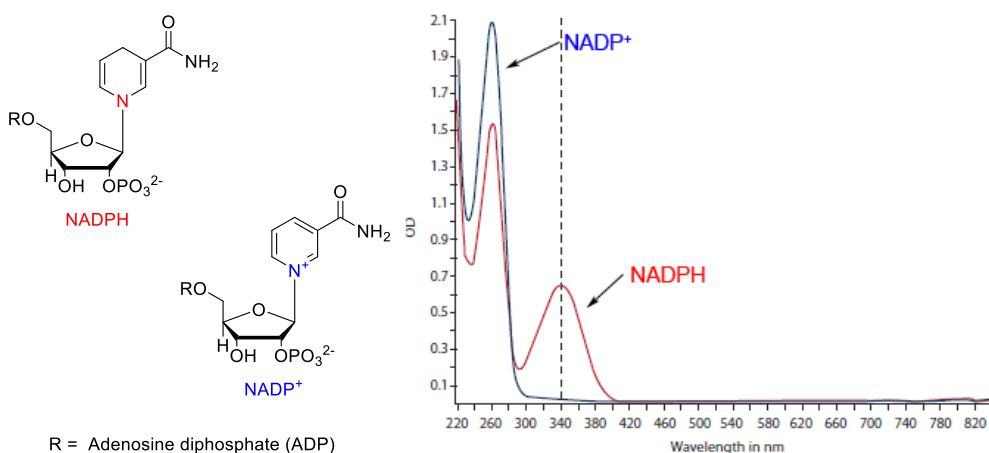


Figure 3.7. Left: the structures of NADP⁺/NADPH. Right: the absorbance of NADP⁺ and NADPH.

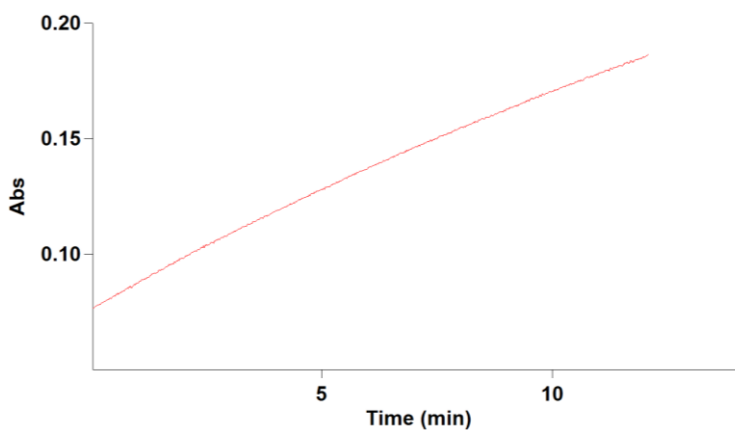


Figure 3.8. Absorbance versus time plot as monitored by UV spectroscopy. The initial slope of the curve represents the initial velocity of Csd4.

The initial velocity data were collected at a series of substrate concentrations varying from 25 μ M to 1.0 mM and were fitted to the Michaelis-Menten equation by using GraphPad® Software

(Figure 3.9). The substrate concentration vs. velocity curve gave the following kinetic parameters: $K_M = 112 \pm 5 \mu\text{M}$, $k_{\text{cat}} = 0.0149 \pm 0.0002 \text{ s}^{-1}$, and $k_{\text{cat}}/K_M = 132 \pm 5 \text{ M}^{-1} \text{ s}^{-1}$. The reported error range was calculated from the non-linear least square fitting on results of kinetic trials carried out on the same day, with enzymes and substrates from the same batch. However, systematic error can occur due to factors such as use of different batches of enzymes and substrates, errors in concentration measurements, as well as temperature fluctuation. These typically lead to an additional 15% error when measurements were performed on different days. The specificity constant (k_{cat}/K_M) is relatively low compared to that of other M14 family members such as CPA, which has a reported k_{cat}/K_M of $9 \times 10^4 \text{ M}^{-1} \text{ s}^{-1}$ with the synthetic tripeptide substrate *N*-dansyl Ala-Ala-Phe. The low specificity constant may reflect that the synthetic tripeptide is not the true substrate of Csd4. In addition, it may reflect the fact that Csd4 is not a basic metabolic enzyme and may simply not have evolved for fast hydrolysis. We also note the exceptionally low activity (k_{cat}) of Csd4 hydrolysis. In the muropeptide profile of wild-type *H. pylori*, the low abundance of trimmed tripeptide (4.0%) and trimmed dipeptide (2.8%, see section 3.1.3) suggests that the amount of Csd4 is low and a highly active carboxypeptidase is not required. To further understand our current results, it would be useful to obtain kinetic data with the GluNAc-MurNAc tripeptide substrate and analyze the importance of the carbohydrate residues.

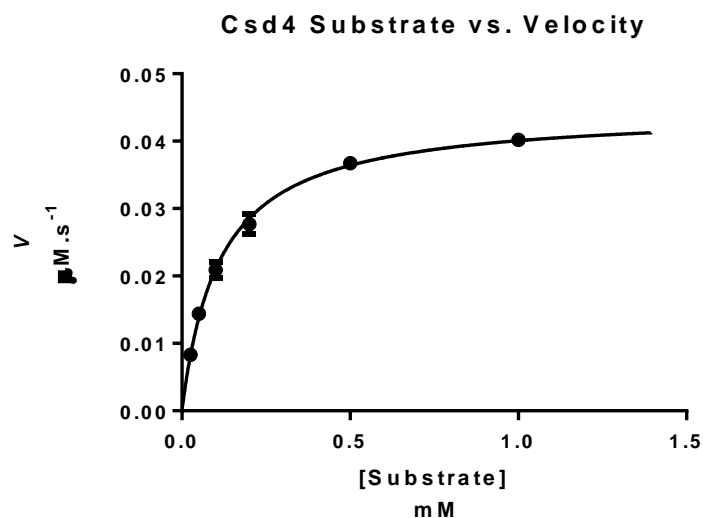


Figure 3.9. Plots of initial velocity vs. substrate concentration for Csd4 catalysis.

Table 3.3. Kinetic constants for the Csd4 catalyzed reaction.

Michaelis-Menten Best-fit values	
K_M (mM)	0.112 ± 0.005
k_{cat} (s^{-1})	0.0149 ± 0.0002
k_{cat}/K_M ($s^{-1} M^{-1}$)	132 ± 5

3.4 Structural Studies of *H. pylori* Csd4 with the Tripeptide Substrate

3.4.1 Crystallization conditions of Apo-Csd4, zinc bound-Csd4 and tripeptide bound-Csd4

Dr. Anson Chan in the Murphy Lab (UBC Microbiology) performed the following crystallography experiments on Csd4. The wild-type apo-Csd4 (Csd4-Initial) was crystallized using reservoir solution containing PEG 3350, Tris pH 8 and NaI by hanging drop vapor diffusion. Crystals appear within a few days at room temperature but were allowed to grow to a sufficient size for approximately 2 weeks.

Zinc-containing crystal structures of wild-type (Csd4-Zn) were obtained by sequentially soaking the crystals in freshly prepared increments of PEG 3350 followed by the addition of an equal volume of the soaking solution supplemented with $ZnCl_2$, respectively. Similarly, the tripeptide containing crystals were prepared by sequential soaking up to 1mM PEG 3350 with each soaking solution also supplemented with $ZnCl_2$, followed by another soak in the solution supplemented with tripeptide and $ZnCl_2$ solution.

3.4.2 Csd4 domain structure

The Csd4 structure with zinc (II) ion (Csd4-Zn) was resolved to 1.4 Å. This Csd4-Zn structure revealed three domains: Domain 1 is the main and larger domain, which has been identified as an *N*-terminal carboxypeptidase domain (CPase domain), and includes zinc (II) and the substrate tripeptide (or natural PG) binding sites. Domain 2 and 3 are two secondary and smaller domains with unknown biological functions. The CPase domain has a globular shape, which is constructed by a nine-stranded antiparallel β sheet core with two clusters of 4 or 5 α helices covering each side (Figure 3.10.A). Similarity screening based on the CPase domain structure identified a funnelin-type CPase family with high structural similarity (139), but low sequence similarity

(under 20%). The minor domains 2 and 3 were not found to be conserved in any related CPase family. The top screening hits for domains 2 and 3 are likely irrelevant proteins, such as human RhoGDI (a down regulator of GTPases) and heparin-sensing system BT4663 (from the human gut symbiont *Bacteroides thetaiotaomicron*). However, even these hits did not share significant similarity with these two domains. As a result, we do not think domains 2 and 3 share similar biological functions with these proteins.

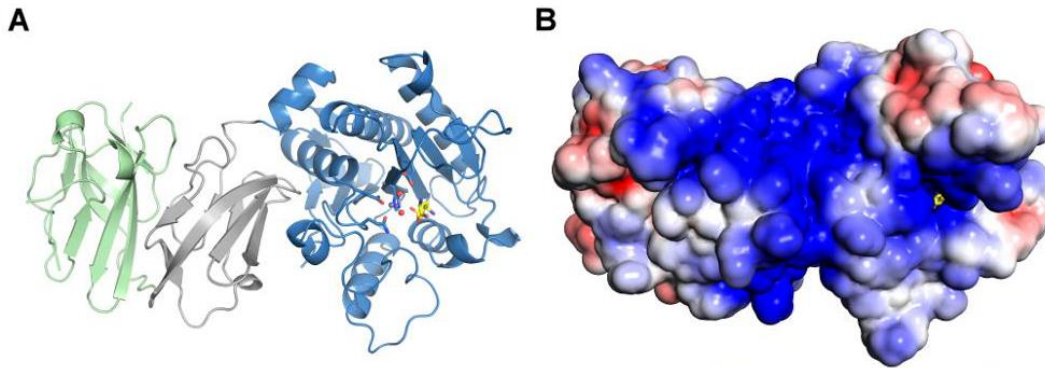


Figure 3.10. A) The overall monomeric structure of Csd4 with Zn (II) and *m*-Dap bound. Domains 1 (CPase domain), 2 and 3 are displayed in color blue, gray and green. B) Overall electrostatic surface potential of Csd4 (Contoured at ± 3 k_BT/e_c).

Although the functions of these two subsidiary domains remain unclear, work in the Salama Lab (U. Washington) showed that Csd4 mutants with domain 3 truncated (Csd4_T1, sequence 1-343, domains 1 and 2 retained) or both domain 2 and domain 3 truncated (Csd4_T2, sequence 1- 251, domain 1 retained) cannot be functionally expressed in *E. coli*. Moreover, the resultant *H. pylori* mutants Csd4_T1 or Csd4_T2 showed slightly curved rod morphology similar to the *Δcsd4* mutant (Figure 3.11). Structural examination of the interfaces between domain 1|2 and 2|3 revealed both of them to be highly hydrophobic, thus they are likely involved in interacting with the natural PG substrate. Such hydrophobic interaction may help localize Csd4 and enhance its activity.

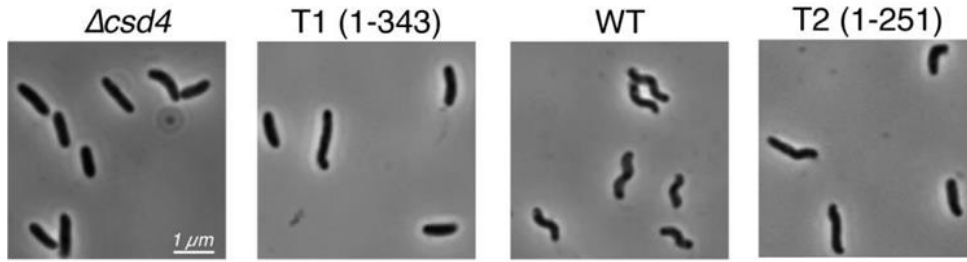


Figure 3.11. 1000X phase contrast images of wild-type and *csd4* mutant *H. pylori* strains.

3.4.3 Zinc and the tripeptide binding Site

Unlike other characterized members of the M14 CPase family that utilize two His residues and one Glu residue in zinc binding, the zinc binding site of Csd4 is constituted by Glu49, His128 and Gln46. From the Csd4-Zn crystal structure, the zinc binding site is a small positively-charged pocket located on the surface of the CPase domain (Figure 3.10.B). The zinc is bound as a hexa-coordinate complex by His128 (monodenate), Glu49 (bidenate) and Gln 46 (monodenate) (Figure 3.12 Left). In addition, two more ligands have been observed and resolved as either water molecules or hydroxide ions.

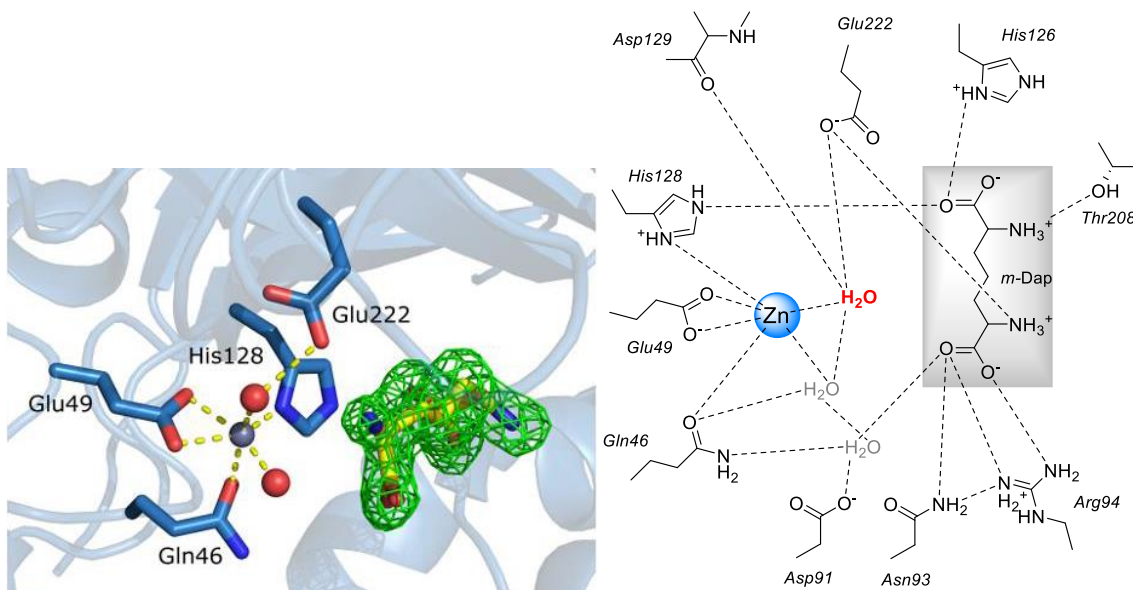


Figure 3.12. Left: the zinc binding pocket with key ligands and a density map for the density of the bound *m*-Dap molecule (contoured at 3 σ). Right: two-dimensional interaction map between Csd4, zinc and *m*-Dap in Csd4 active site.

In the Csd4-Zn structure, a *m*-Dap molecule was found to be included in the substrate binding site. As *m*-Dap is the product of tripeptide substrate cleavage, and was not added into the crystallization buffer, this observation suggests a strong binding affinity sufficient to survive purification. The bound *m*-Dap has direct interactions with several residues, including Asn93, Arg94, His126, His128, Thr208 and Glu222 (Figure 3.12 Right). Moreover, a third water molecule H-bonding with both the zinc ligand Gln46 and the oxygen of the *m*-Dap carboxylate has been also identified.

To further explore the interactions between the tripeptide substrate and Csd4, protein crystals were soaked in a solution containing zinc ion and tripeptide (Figure 3.13.A). While the tripeptide consisted of a mixture of two stereoisomers, we expected that the isomer with the correct stereochemistry (identical to natural mucopeptide) would preferentially bind to the enzyme active site. The Csd4 crystal structure with both Zn (II) and tripeptide bound (Csd4-Tripeptide) was obtained at a resolution of 1.75 Å. Although the zinc occupancy was lower due to the presence of the tripeptide molecule, the coordination sphere of Zn (II) with His128, Glu49 and Gln46 was almost superimposable with the Csd4-Zn counterpart (Figure 3.13.B). In addition, a water molecule coordinated to the metal ion was modeled by its electron density. This water was also observed to form an H-bond with the neighboring Asp129 (carbonyl backbone, monodenate, 2.8 Å) and Glu222 (carboxyl residue, bidentate, 2.9/3.1 Å). Moreover, the water molecule is located at a reasonable distance (3.3 Å) from the carbonyl of the scissile *iso*-D-Glu-(*S*)-*m*-Dap bond (Figure 3.14). Based on its position in the active site, this water is thought to be the catalytic nucleophile for cleavage of the tripeptide substrate.

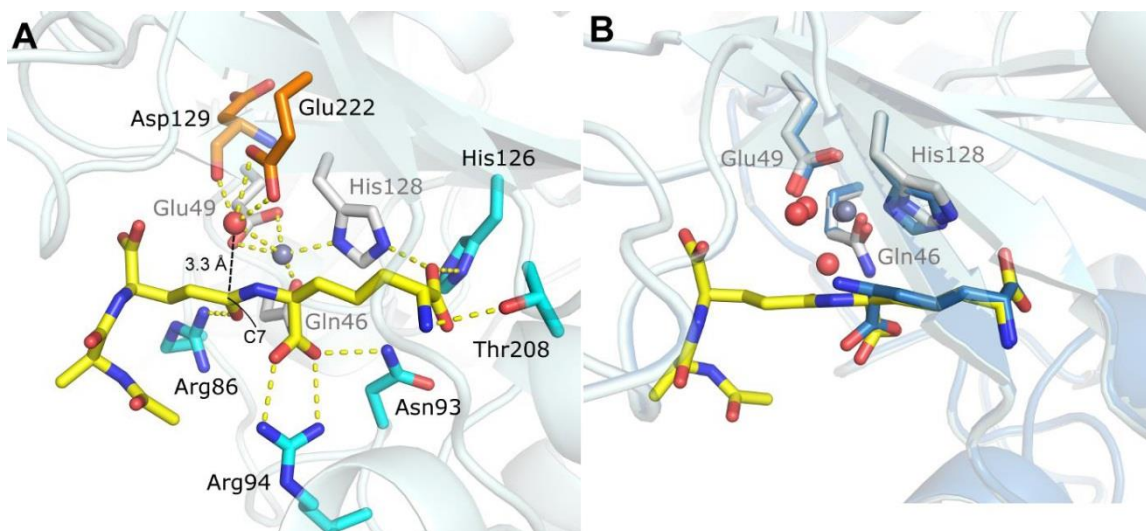


Figure 3.13. Tripeptide binding in Csd4 active site. A) Zinc (purple) and substrate (yellow) interactions with Csd4. Zinc ligands are colored gray; tripeptide ligands are colored cyan; catalytic water and its ligands are red and orange. B) Structural alignments between Csd4-Zn and Csd4-Tripeptide. View is of the active site in panel A with a 30° rotation about the X-axis.

The Csd4-Tripeptide structure clearly revealed that tripeptide substrate has full occupancy in the active site, indicating that the enzymatic reaction was efficiently suspended at the Michaelis complex stage. The lack of reactivity is likely due to the low value of k_{cat} for the tripeptide and the non-optimal pH for catalysis used during crystallization. The structure also shows that the Ac-L-Ala moiety of tripeptide orients outside of the zinc binding pocket. In addition, one Zn (II) coordinated water was displaced by the substrate *N*-terminal amine, and the zinc binding was altered to a penta-coordination state. As we predicted, only the substrate stereoisomer with an *iso*-D-Glu-*m*-Dap with (*S*)-configuration moiety connecting to the peptide bond was observed, suggesting the enzyme selectively bound to the chirality-correct substrate under the soaking conditions. Compared to the Csd4-Zn model, binding contacts with the *m*-Dap moiety of the tripeptide were largely conserved. The only additional interaction occurred between the D-Glu γ -carbonyl oxygen and Arg86.

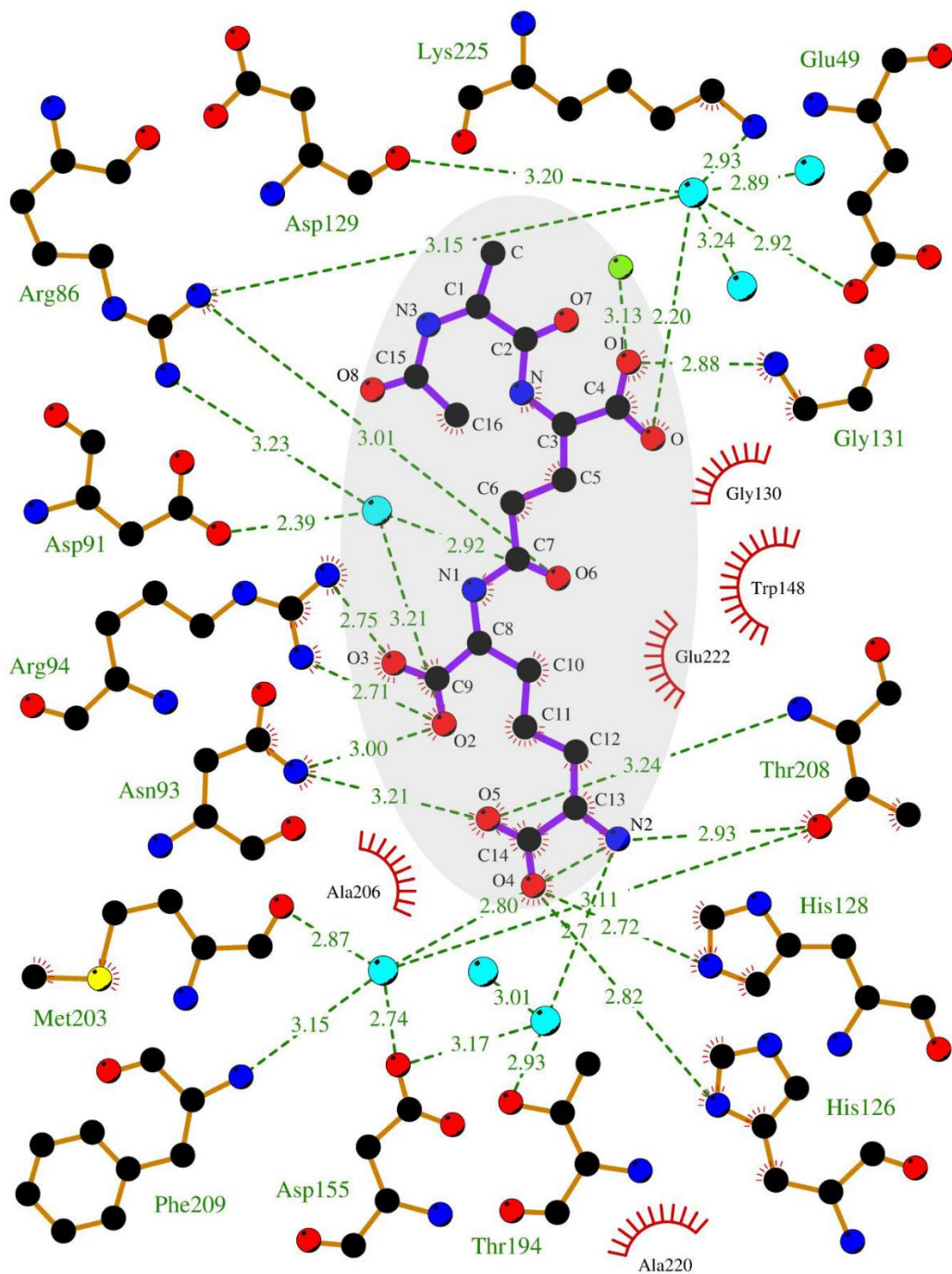


Figure 3.14. Two-dimensional Csd4-Tripeptide interaction map. Tripeptide substrate is highlighted in grey; H₂O molecules are colored cyan; zinc and its ligands are not shown.

3.5 Mutation Studies of *H. pylori* Csd4

3.5.1 Q46 is required for full Csd4 activity

As discussed in section 3.4.3, Gln46 is an atypical zinc binding residue and is not found in other M14 CPase family members. To further study the role of this glutamine residue, Dr. Anson Chan prepared three point mutants (Q46H, Q46E and Q46A) for an *in vitro* activity assay. Q46H and Q46E contain the imidazole and γ -carboxylate moieties commonly observed in CPase zinc binding motif, while Q46A abrogates metal binding at this position. Dr. Anson Chan carried out the following studies using the synthetic tripeptide prepared in this thesis.

Two buffer systems – phosphate and Bis-tris were employed in an activity assay of each mutant. As expected, wild-type Csd4 (Csd4-WT) showed the highest activity at pH 6.5 in both buffers, with a similar activity in each. The mutants' activity had a much bigger variance in the different buffers (Figure 3.15.A). In Bis-tris buffer, mutant Q46H maintained 60% of the activity of Csd4-WT; while in phosphate buffer it lost more than 90% of the wild-type activity. Q46A did not show significant activity in Bis-tris, but it conserved 20% of the activity in the presence of phosphate. No enzymatic reaction is observed for Q46E in either buffer, suggesting a disruption of its active site. Additionally, the pH influence on enzyme activity was also examined (Figure 3.16.B). The results showed Csd4-WT reached its maximum activity at pH 6 and gradually decreased under more basic conditions. However, the Q46H mutant showed optimal activity at pH 5.5.

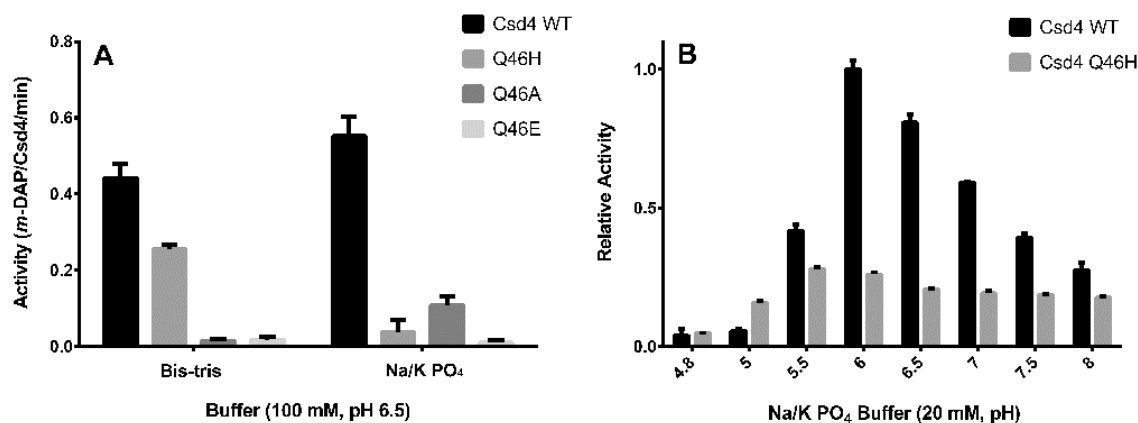


Figure 3.15. Activity tests for wild-type Csd4 and its active site mutants Q46H, Q46A and Q46E. A) Activity difference between wild-type Csd4 and its mutants in two buffer systems: Bis-tris and phosphate. The

enzyme activity is continuously coupled with *m*-Dap dehydrogenase and monitored. B) pH-based differences between wild-type Csd4 and its mutants. The assay was examined by measuring the amount of product after 20 min reaction.

To rationalize the results from the activity test, the crystal structure of the Q46H variant has been inspected. The Zn-bound Q46H structure was obtained at a resolution of 1.75 Å (Figure 3.16). When comparing the Zn-ligand bond lengths and overlaying the binding pockets (Csd4-Zn vs. Csd4-Q46H), structural alternations of the His-Glu-His residues were observed (Table 3.4). A tetragonal-shaped electron density close to the zinc was present and was modeled as phosphate with 90% occupancy. In Csd4-Q46H, this anion occupied the position of the water in Csd4-Zn and coordinated with the zinc. No catalytic water was observed in the mutant crystal structure, which is consistent with the bulky phosphate occupation. In addition, residues Glu222 and Arg86 that normally bind the catalytic water and carbonyl oxygen of the scissile bond, respectively, were rotated to coordinate with the phosphate. The observed binding of phosphate in the Q46H mutant helps to explain why the activity of this mutant was much lower in phosphate buffer than in Bis-tris buffer.

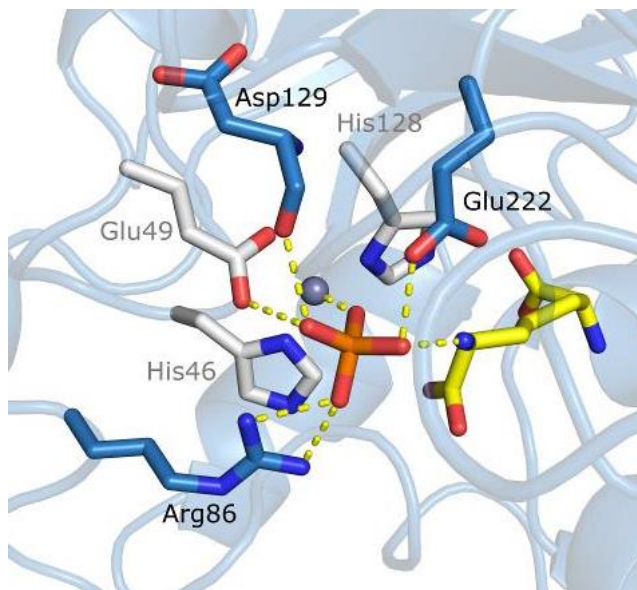


Figure 3.16. Three-dimensional Csd4-Q46H interaction map in the active site with zinc bound. Zinc and binding ligands are colored grey and white; Phosphate and binding ligands are colored orange and blue; *m*-Dap is colored yellow.

Table 3.4. Zinc ligand bond lengths (Å) in the crystal structures.

	Csd4-Zn	Csd4-Tripeptide	Csd4-Q46H
Gln46/His46	2.2	2.0	2.1
Glu49	2.3/2.3	2.4/2.9	2.1/2.5
His128	2.0	2.5	2.1
H ₂ O (nucleophilic)	2.3	2.9	-
H ₂ O (other)	2.2	-	-
Phosphate	-	-	1.9

3.5.2 Csd4 suggests a new family of CPases

After our *in vitro* tests, the Salama group explored the effect of Q46 mutation on *H. pylori*'s morphology. Thus, the variant strains *Q46H* (Figure 3.17, 1H) and *Q46A* (Figure 3.17, 1A) are cultivated. Each mutant has a *3x-Flag* tag fused to its C-terminus. Instead of retaining the helical curved shape of wild-type *H. pylori*, both strains display straight rod or slightly curved rod morphology, which is similar to the strain Δ *csd4*. The protein expression level was also analyzed using immunoblotting analysis with anti-Flag monoclonal antibodies, but no significant change in expression between wild-type and variants was observed.

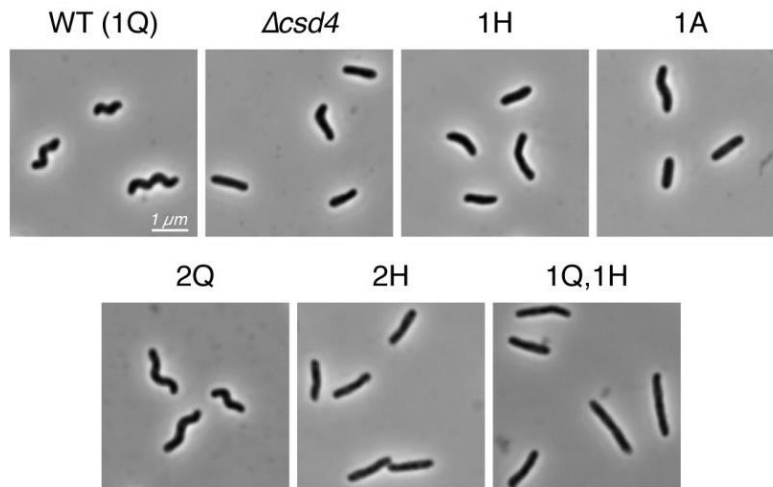


Figure 3.17. 1000X phase contrast images of wild-type and *csd4* variants *H. pylori*. (1H) is *csd4*-Q46H; (1A) is *csd4*-Q46A; (2Q) is *csd4*-WT, *rdxA*:: *csd4*-WT; (2H) is *csd4*-Q46H, *rdxA*:: *csd4*-Q46H; (1Q, 1H) is *csd4*-WT, *rdxA*:: *Csd4*-Q46H.

The *in vivo* results demonstrated the essential role of Gln46 in maintaining the *H. pylori* helical morphology. In addition, by using sequence analysis of Csd4 homologues, the conserved features of the three domains have been identified. From the phylogenetic tree generated based on Csd4 sequence similarity, it was found that most *csd4* homologues were found in δ and ϵ proteobacteria. These species are primarily helical or curved rod-shape bacteria, and based on the conserved residues for zinc binding, they are divided into two branches. Both of them have conserved Glu49 and His128, but the residues at position 46 are distinct. The first branch includes *H. pylori* and other ϵ proteobacteria, which has a Gln residue as a zinc binding ligand and occupies three quarters of the whole category. The second branch are ϵ Proteobacteria that contain His instead of Gln for zinc binding and occupies approximately one quarter of the whole category. Whether all Csd4 homologues play an essential role in determining their cell shape is not known, but the fact that almost all helical ϵ proteobacteria contain Csd4 homologues suggests that they represent a new family of CPases required for control of morphology.

3.6 Design and Synthesis of a Pseudodipeptyl Phosphinate Inhibitor

According to the Csd4-Tripeptide crystal structure, the *iso*-D-Glu-*m*-Dap dipeptide moiety was located in the center of the active site, adjacent to the zinc binding pocket and the catalytic water. However, the Ac-L-Ala moiety was extended outwards from direction of the active site, which indicates that it makes little contribution to the total interaction between the tripeptide and the residues in the binding pocket. Thus, we decided to synthesize a phosphinic acid inhibitor that mimics a dipeptidyl tetrahedral intermediate resembling a truncated *N*-acetyl *iso*-D-Glu-*m*-Dap dipeptide (Figure 3.18). Phosphinic and phosphonic acid pseudopeptides have been shown to act as potent inhibitor of carboxypeptidase A (140). Moreover, linear free energy relationship have demonstrated that they act as transition state analogs (141,142). The dipeptidyl phosphinate is more convenient to synthesize than a tripeptidyl analogue molecule, and it retains the core structure that is stabilized by the zinc ion as well as the key active site residues (Gln46, Glu222 and Arg86).

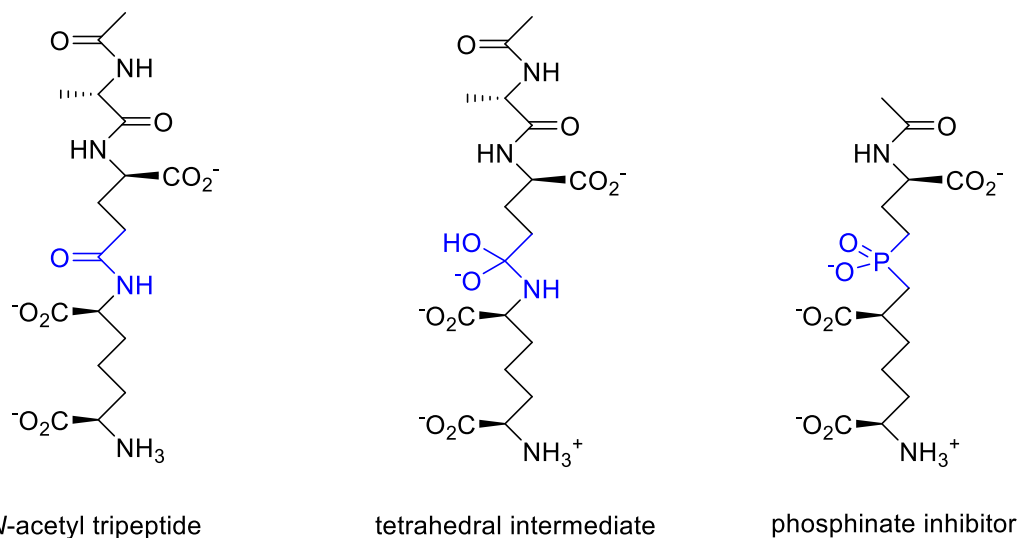


Figure 3.18. Comparison between tripeptide substrate (left), tetrahedral intermediate (middle) and dipeptidyl phosphinate inhibitor (right). The scissile peptide bond is colored to blue.

To synthesize the designed inhibitor, we first prepared two building blocks (compound **29** and **32**) that mimic the *m*-Dap and the D-Glu, respectively (Figure 3.19). The literature known synthesis of compound **29** started with a Boc- and *t*Bu protected D-glutamic acid **27** (143). The coupling between **27** and Meldrum's acid (2,2-dimethyl-1,3-dioxane-4,6-dione) first forms a ketone (**27a**), which is subsequently reduced to a methylene by NaBH₄ (Figure 3.20). The resultant compound **28** was then treated with a dimethyl methylene imine salt in the presence of BnOH, which produced the alkene compound **29**. Compound **32** contains the phosphinic acid moiety, and its synthesis started with a Cbz- and *t*Bu- protected D-glutamic acid **30**. The first step generates alkene **31** via reflux with lead (IV) acetate and Cu (II) acetate (121). The acid **30** initially undergoes a radical decarboxylation promoted by lead (IV) acetate, and the resulting radical is dehydrogenated with a catalytic amount of Cu (II) acetate (Figure 3.21). The alkene **31** was then treated with ammonium hypophosphite and triethylborane to form the hypophosphite **32**. A coupling reaction of compounds **29** and **32** in the presence of hexamethyldisilazane (HMDS) generated phosphinic acid **33**, which was protected by adamantylation to give a fully protected phosphinate **34** as a mixture of four diastereomers. The Cbz- group was selectively removed by hydrogenolysis and the resulting amine was acetylated by acetic anhydride to give compound **35**. Finally, compound **35** was fully deprotected by treatment with 95% trifluoroacetic

acid to give inhibitor **8** as a mixture of two diastereomers. Inhibitor **8** was purified using ion-exchange chromatography and no attempts were made to separate the diastereomers.

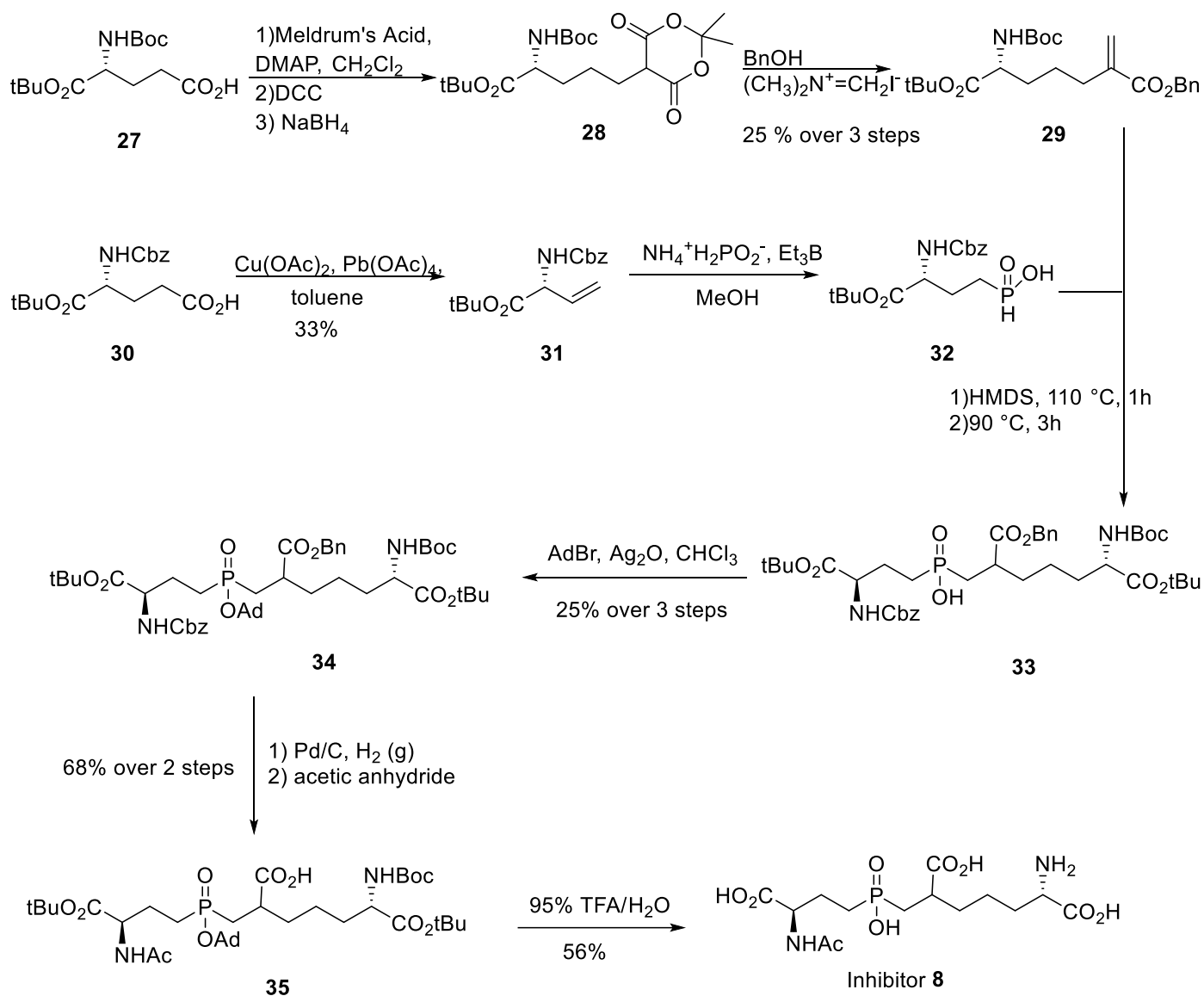


Figure 3.19. Synthesis of the inhibitor **8**.

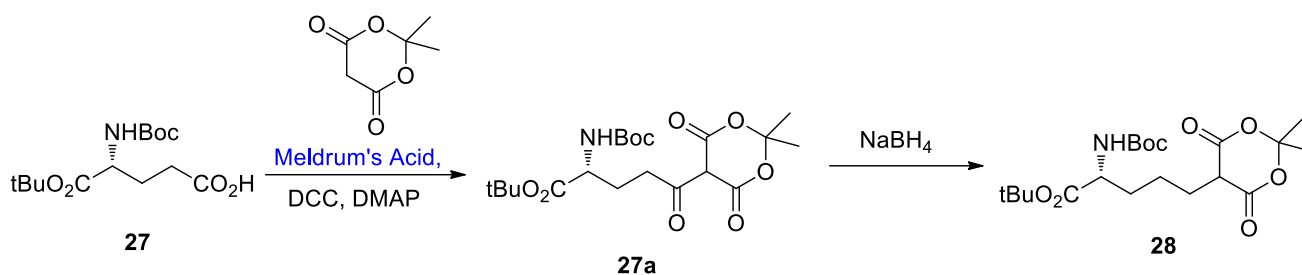


Figure 3.20. Stepwise reactions from compound **27** to compound **28**.

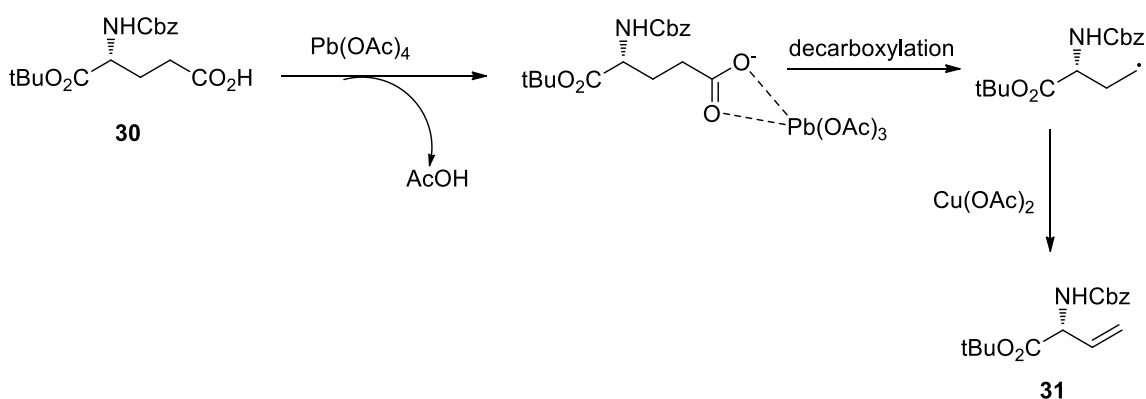


Figure 3.21. Proposed formation of compound **31**.

3.7 Kinetic Studies with Inhibitor **8**

The potency of inhibitor **8** against *H. pylori* Csd4 was tested using the same continuous DAPDH coupled-assay that was employed to monitor the consumption of the tripeptide substrate. A pre-incubation of the inhibitor and the Csd4 enzyme was required as a slow binding process was observed. At a fixed concentration of the inhibitor, the initial velocity data were collected at a series of substrate concentrations ranging from 50 μM to 1.0 mM. The initial velocity data sets were measured at inhibitor concentrations of 0.0 μM , 2.0 μM , 5.0 μM and 10.0 μM . Slow binding of the inhibitor was observed in the assay, and it was preincubated with the enzyme for 20 min at 30 $^\circ\text{C}$ in each measurement.

Considering the enzyme concentration ($[\text{E}]_t = 3 \mu\text{M}$) is comparable with the inhibitor apparent concentration $[\text{I}]$, a significant amount of the inhibitor was competitively bound to the enzyme

active site. As a result, we calibrated the actual concentration of the inhibitor $[I]'$ using methods reported by *Singh et al* (144) (Equation 3.1). Since the calibrated inhibitor concentration is distinct in each measurement with different substrate concentration, we decided to use Dixon plot ($1/V$ vs. $[I]'$) to process the kinetic data (Equation 3.2). From the plotted diagram, the inhibitor binding constant K_I was calculated as $1.4 \pm 0.2 \mu\text{M}$. The error values represent the standard deviation associated with the rate measurement at each specific concentration in all data sets, and were determined by fitting the initial velocity data to a linear regression method included in Microsoft Excel®.

$$I' = I - (1 - V_0'/V_0) * E_t \quad (\text{Equation 3.1})$$

$$\frac{1}{V} = \frac{K_M}{V_{\max} [S] K_i} [I]' + \frac{1}{V_{\max}} \left(1 + \frac{K_M}{[S]}\right) \quad (\text{Equation 3.2})$$

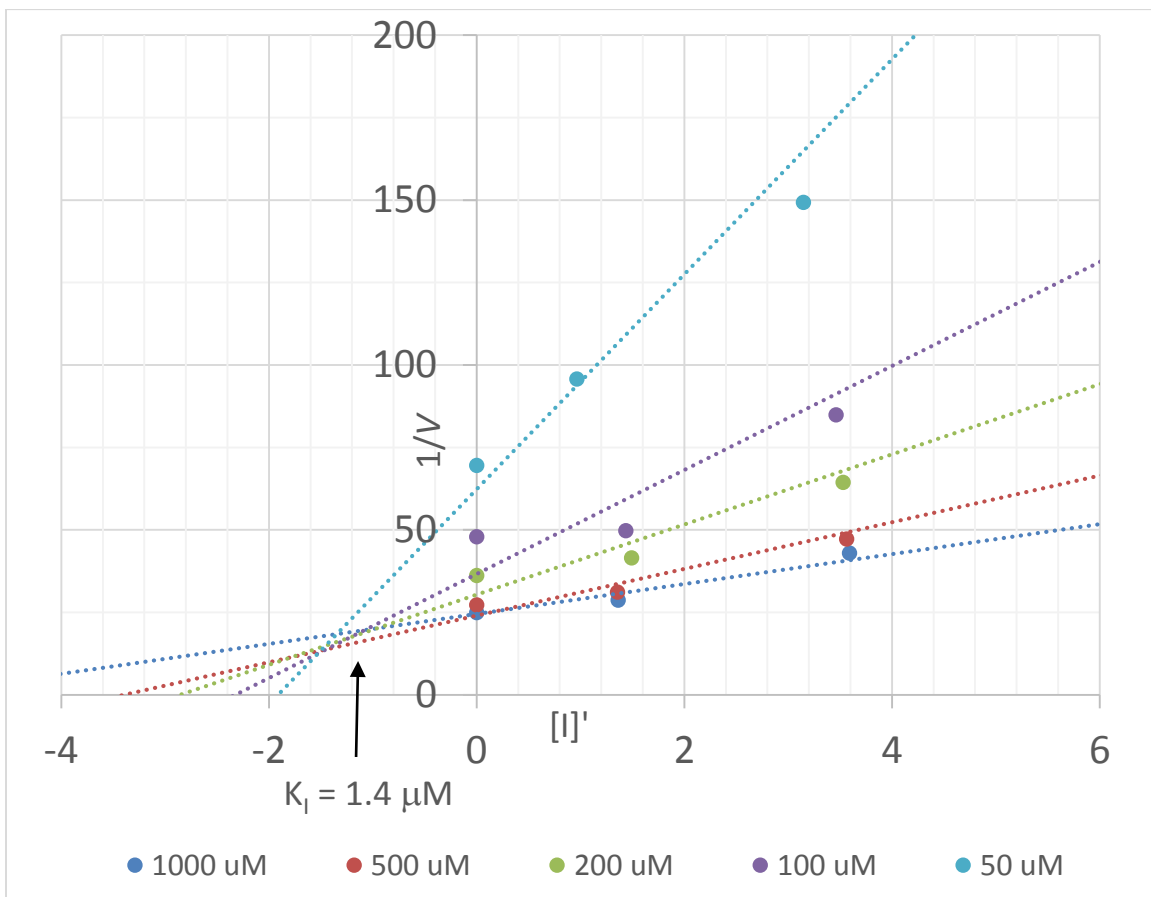


Figure 3.22. Dixon plot for determination of competitive inhibitor kinetic constants.

Table 3.5. The inhibitory constant and the α value of the inhibitor **8**.

K_i (μM)	1.4 ± 0.2
-------------------------	---------------

Compared to the Michaelis constant (K_M , 112.2 μM), the inhibitory constant (K_I) is decreased 99%, which indicates that the inhibitor binds more tightly than the tripeptide substrate. This is expected for a compound that mimics a high energy intermediate. Previous studies on phosphinate inhibitors against CPA indicates that this type of inhibitor is a transition state analogue of CPA hydrolysis (141), which is consistent with our kinetic measurement. Additionally, the solved crystal structure of Csd4 with the inhibitor also clearly displayed that the phosphinate bound in the enzyme active site in a similar manner as the substrate. We did not observe any additional inhibitor molecular bound in the Csd4-Inhibitor structure (*vide infra*). Thus, we conclude that the phosphinate inhibitor **8** is a competitive inhibitor against Csd4 with excellent potency.

3.8 Structural Studies of *H. pylori* Csd4 with the Phosphinate Inhibitor **8**

Crystallization studies on the Csd4-Inhibitor complex were completed by Dr. Anson Chan in the Murphy Lab. Similar to the crystallization conditions used with Csd4-Tripeptide, Apo-Csd4 crystals were soaked with 33% PEG 3350 supplemented with 1.0 mM ZnCl_2 , followed by a solution supplemented with 2.5 mM inhibitor **8** and 1.0 mM ZnCl_2 . After flash freezing the inhibitor containing crystals (Csd4-Inhibitor) were obtained.

The electron density map showed a dipeptidyl structure was clearly present in the active site and was modelled as the phosphinate inhibitor (Figure 3.23.A). The corresponding structure showed that the stereocenter of the inhibitor closest to the phosphinate has an (*S*) configuration, which is consistent with the stereochemistry of the normal substrate. This indicates that Csd4 selectively bound to the inhibitor isomer with the (*S*) stereocenter when incubated with a diastereomeric mixture (approx. 50:50).

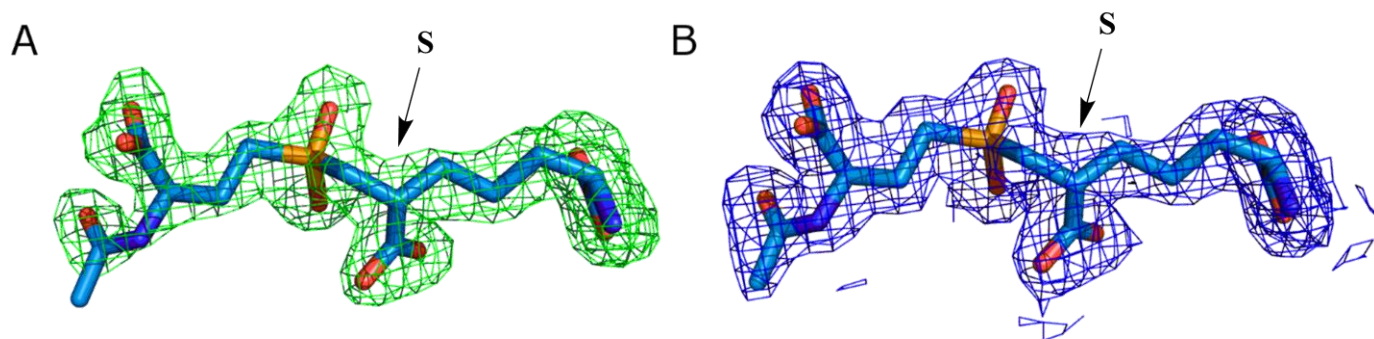


Figure 3.23. Electron density map of inhibitor **8** in the Csd4-Inhibitor complex. The observed electron density of the Csd4 bound inhibitor in A) The initial F_o-F_c map contoured at 3.5σ and B) the refined $2F_o-F_c$ map contoured at 1.5σ . The (S) configuration of the inhibitor stereocenter that is closed to the phosphinate is shown. Carbon atoms are colored blue, oxygen atoms red, and phosphorus atoms orange.

The overall structure of the Csd4-Inhibitor complex was similar to that of the Csd4-Tripeptide complex (Figure 3.24.A). The two structures can be superimposed with a small standard deviation in the active site. The amino and carboxylate groups of the inhibitor were held in positions and orientations by hydrogen bonds and electrostatic interactions which are analogous to those previously described in the Csd4-Tripeptide structure (Figure 3.24.B). The two oxygen atoms of the phosphinic acid are hydrogen bonded to the conserved residues Glu222 and Arg86. Compared to the Csd4-Tripeptide, both of the phosphinic acid oxygen are found to rotate towards the Zn (II) and coordinate with the metal. The electron density of the zinc ion was found in a similar position to that observed previously in the Csd4-Tripeptide. The metal was also coordinated with Glu49, His128 and Gln46, but the position of these three residues were slightly altered. The catalytic water observed in Csd4-Tripeptide was not seen in Csd4-Inhibitor, as the phosphinate mimics the tetrahedral intermediate formed after nucleophilic attack and thus occupies this position. As a result, the water binding residue Asp129 was also found to be positioned at a different angle. The carboxylates of the inhibitor interacted with residues Gly131, Arg94, Asn93, His126 and Thr208, which is very similar to that described previously in Csd4-Tripeptide. The residue Lys225 did not interact with the substrate in the Csd4-Substrate complex, but in Csd4-Inhibitor, it was seen to coordinate with the carboxylate of the D-Glu moiety.

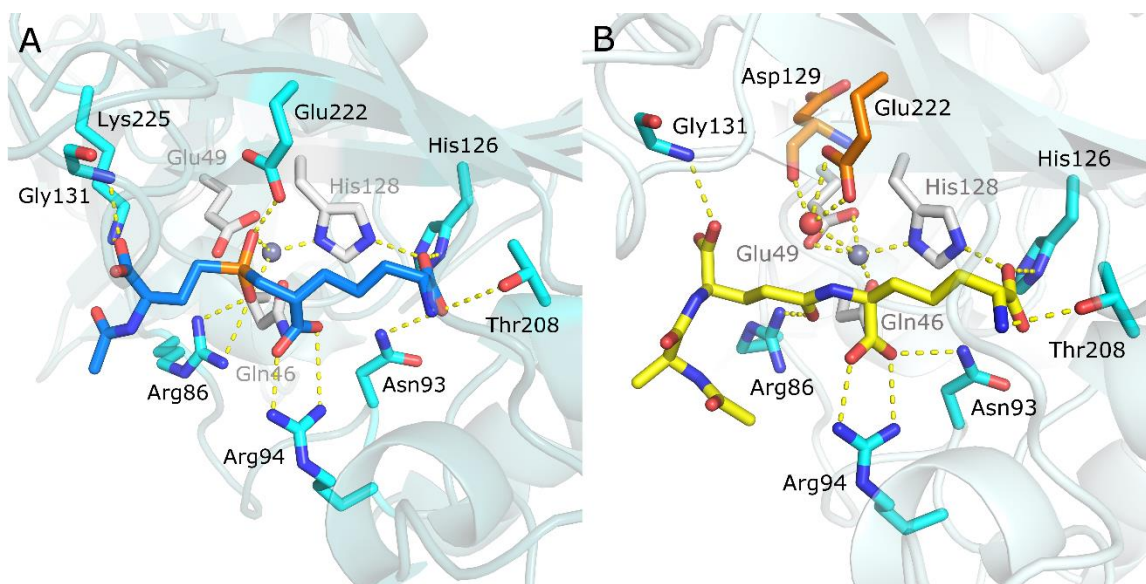


Figure 3.24. Comparison of the active sites of (A) Csd4-Inhibitor complex and (B) Csd4-Tripeptide complex. Zinc ion is colored to grey in both structures. The catalytic water is shown as a red sphere. Interacting amino acid residues are shown in CPK coloring with carbon in cyan, grey and orange. Carbon atoms in the inhibitor and the tripeptide substrate are colored light blue and yellow, respectively. Oxygen, nitrogen and phosphorus atoms are shown in red, blue and orange, respectively.

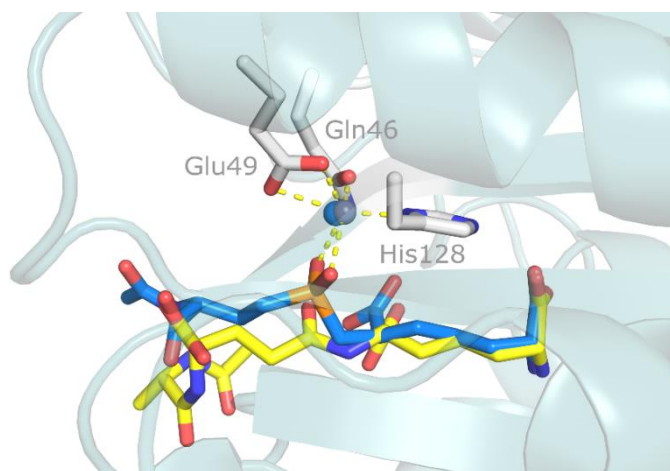


Figure 3.25. Structural alignment of the active site of the Csd4-Inhibitor and the Csd4-Tripeptide complex. The Zn (II) binding motif Glu49, His128 and Gln46 are shown with carbons in grey. The zinc ion is colored as grey sphere for Csd4-Tripeptide and as a blue sphere for Csd4-Inhibitor, respectively. Carbon atoms of the tripeptide are colored yellow, and those of the inhibitor are blue. Oxygen, nitrogen and phosphorus atoms are shown in red, blue and orange respectively.

The Csd4-Inhibitor structure effectively supports the proposed catalytic mechanism for a zinc metalloprotease, and indicates that inhibitor **8** is acting as a mimic of the tetrahedral intermediate. As mentioned previously in this section, the enzyme selectively bound the stereoisomer of inhibitor **8** that had similar stereochemistry as the substrate. Structural alignment of the active sites indicates that the Zn (II) is positioned in nearly identical places in the two structures. (Figure 3.25). However, the phosphinate of the inhibitor has twisted in order to coordinate with the zinc atom. Additionally, the phosphinate oxygen that displaced the nucleophilic water was found to be coordinated with residue Glu222. This conformational change could explain the slow binding phenomenon observed in the inhibition kinetics. Based on this structural information, we proposed the catalytic mechanism of Csd4 as follows (Figure 3.26): The zinc-bound catalytic water is initially deprotonated by residue Glu222. The hydroxide then attacks the carbonyl group in the scissile peptide bond and forms a tetrahedral intermediate. The process occurs with a twisting of the peptide backbone so that the tetrahedral oxyanion intermediate is stabilized by Zn (II), residue Arg86 and Glu222. Finally, the same Glu222 protonates the Dap amino group, causing peptide bond breaking and release of a free *m*-Dap.

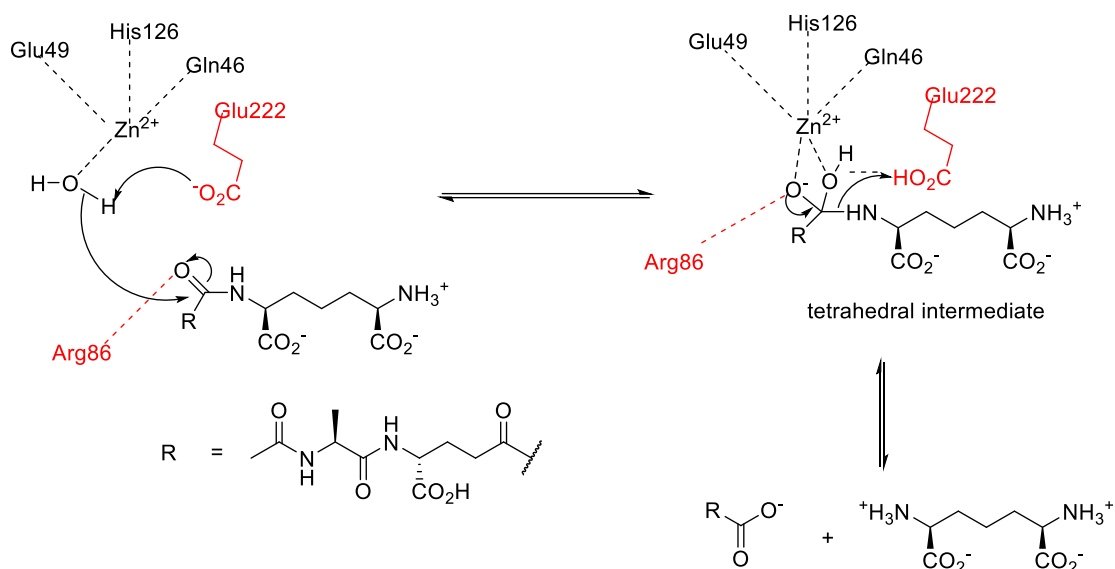


Figure 3.26. Proposed mechanism of Csd4 catalyzed hydrolysis of the tripeptide substrate.

3.9 *In vivo* Assays of Inhibitor 8 with *H. pylori* and *C. jejuni*

All the *in vivo* experiments were performed in either Dr. Erin Gaynor's laboratory at the UBC Department of Microbiology or in Dr. Nina Salama's laboratory at the Fred Hutchinson Cancer Research Center. The strains of *C. jejuni*, *H. pylori* and their mutants used for the morphology assays were first incubated in the lysogeny broth (LB) media for 18 h. Then the cultured bacteria were diluted to a specific optical density (OD, for *C. jejuni*, 0.0002; for *H. pylori*, 0.0006) to control the colony-forming unit (CFU, an estimate of the number of viable and fissile bacteria in each unit volume of the culture) to approximately 1.0×10^6 / mL. The cultures were transferred to a 96 well microtitre plate followed by the addition of inhibitor 8 at varying concentrations (from 70 μ M to 4.5 mM). The same amount of water was added to the control. The cellular morphology was examined by differential interference contrast (DIC) microscopy. The assayed cultures were monitored for a maximum of 48 h.

3.9.1 Assay with *C. jejuni*

The morphological effects of inhibitor 8 on *C. jejuni* cell shape were explored in the laboratory of our collaborator Dr. Erin Gaynor at the Microbiology Department of UBC. In the *in vivo* assay with *C. jejuni*, two strains of the bacterium were cultured: the wild-type *C. jejuni* 81-176 and the acapsular mutant *C. jejuni* $\Delta kpsM$. The difference between these two strains is that the wild-type *C. jejuni* contains the bacterial capsule, which is a polysaccharide barrier exterior to the cell wall. The gene *kpsM* is an ATP-binding cassette transporter protein involved in the transport of the capsular polysaccharide across the inner membrane (145). Thus, the knockout mutant $\Delta kpsM$ does not contain the capsule layer and inhibitor 8 may have improved access to the periplasm. The contrast of these two strains was used to examine whether the acapsular mutant showed an increased sensitivity to the inhibitor.

Based on the microscopic observation of *C. jejuni* cellular morphology at several time points ($t = 6\text{h}$, 24h and 48h), it was found that maximal cell straightening for both wild-type and $\Delta kpsM$ occurred at 24 h after the incubation with inhibitor concentrations greater than 0.3 mM (Table 3.6). This time point corresponds to the middle or late stage of the logarithmic phase of the bacterial growth curve. Additionally, more curved bacteria than straight ones were observed with 0.3 mM and 0.6 mM inhibitor, but the straightened cells started dominating when the inhibitor concentration was over 1.1 mM. No straightened *C. jejuni* cells were observed in the first 6 h, corresponding to the lag phase or early stage of the logarithmic phase. Interestingly, as the

inhibitor concentration increased, both a toxicity effect and a morphology effect was observed. When the concentration of the inhibitor was over 0.1 mM, a drop in cell density were resulted. This indicates that bacterial growth was inhibited, and both strains are more sensitive to the toxicity than to the cell straightening activity. With the inhibitor concentration above 2.3 mM, the bacterial growth for both strains completely ceased and only cellular debris was observed. There is no direct evidence showing that inhibitor **8** binds any essential enzyme in addition to Csd4, but based on the structure of this inhibitor, we think it is possible that inhibitor **8** could potentially inhibit the activity of the *m*-Dap ligase MurE. Under high inhibitor concentrations, inhibitor **8** may permeate the inner membrane and show lethal effects. As a result, our measured minimal inhibitory concentration (MIC) against *C. jejuni* wild-type and $\Delta kpsM$ was found to be 2.3 mM.

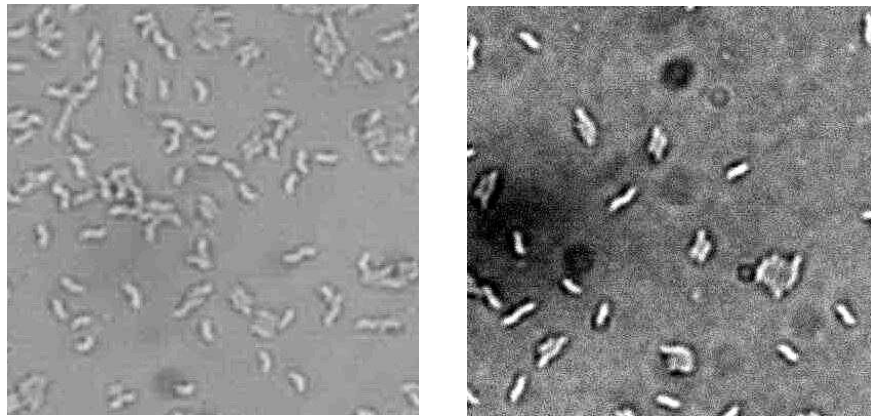


Figure 3.27. DIC microscopy images of the *C. jejuni* wild-type (left) (natural growth, control) and *C. jejuni* wild-type treated with 2.3 mM inhibitor (right) for 24h.

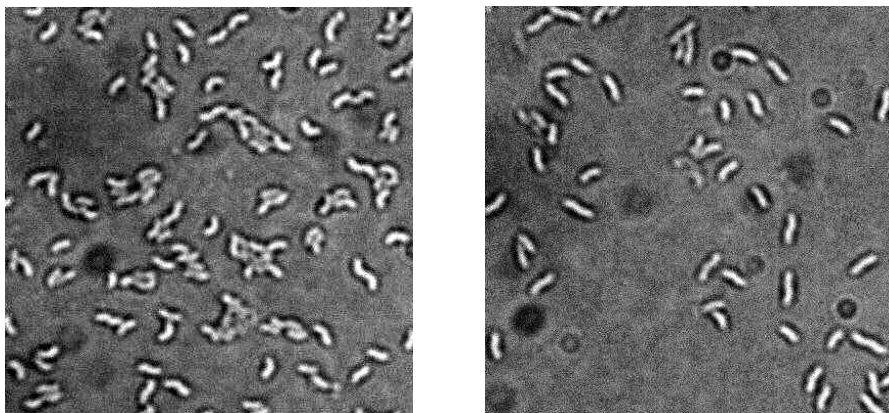


Figure 3.28. DIC microscopy images of the *C. jejuni* $\Delta kpsM$ (left) (natural growth, control) and *C. jejuni* $\Delta kpsM$ treated with 2.3 mM inhibitor (right) for 24h.

Table 3.6. Summary of microscopic observations of cellular morphology (*C. jejuni*).

Strain	[Inhibitor] (mM)	Summary of Microscopic observations of cellular morphology		
		6 h	24 h	48 h
<i>C. jejuni</i> wild type	4.5	Very few helical cells. Cellular debris.	No cells observed. Cellular debris	No cells observed Cellular debris.
	2.3	Very few helical cells. Cellular debris.	No cells observed. Cellular debris.	No cells observed. Cellular debris.
	1.1	Very few helical cells. Cellular debris.	Cell straightening.	Mainly coccoid, a few straightened cells
	0.6	Very few helical cells. Cellular debris.	Cell straightening.	Mainly coccoid, a few straight cells
	0.3	A few helical cells.	Cell straightening,	Coccoid
	0.1	A few helical cells.	Helical, slightly straightened.	Coccoid
	0.07	Helical	Helical	Coccoid
	0	Helical	Helical	Coccoid
<i>C. jejuni</i> $\Delta kpsM$	4.5	Very few helical cells. Cellular debris.	No cells observed. Cellular debris.	No cells observed. Cellular debris.
	2.3	Very few helical cells. Cellular debris.	No cells observed Cellular debris.	No cells observed Cellular debris.
	1.1	Very few helical cells.	Cell straightening.	Mainly coccoid, a few straightened cells
	0.6	Helical cells	Cell straightening, helical cells.	Mainly coccoid, a few straightened cells
	0.3	Helical cells	Cell straightening, helical cells.	Coccoid cells
	0.1	Helical cells	Helical cells	Coccoid cells
	0.07	Helical cells	Helical cells	Coccoid cells
	0	Helical cells	Helical cells	Coccoid cells

An analysis of the DIC microscopic images using the CellTool® Software, was used to establish a geometric model of the bacterial cell shape in the binary dimensions of axis length and side curvature (see experimental section **3.12.9** for definition of these terms). The axis length and side curvature of all the cells in the control and incubated strains were calculated, and these values reflect the degree of the cell curved shape. Based on these measurements, cells of the two batches were plotted in an 2D coordinate system with axis length (horizontal) and side curvature (vertical) (Figure 3.29 and Figure 3.30). The distribution histograms of wild-type vs. wild-type + inhibitor **8** and $\Delta kpsM$ vs. $\Delta kpsM$ + inhibitor **8** were also plotted as a function of their side curvature (Figure 3.31 and Figure 3.32). Both of the batches treated with the inhibitor show a negative shift in side curvature, indicating the cell straightening by the inhibitor is statistically significant.

Additionally, a slight larger shift (absolute value) observed with $\Delta kpsM$ (approximately 0.45) than that observed with wild-type (approximately 0.40) suggested that the acapsular mutant is more permeable to inhibitor **8** than wild-type, but it also showed that the removal of the capsule has limited impact on increasing the permeability. These results indicate that the use of a Csd4 inhibitor may mimic the effects of the deletion of the Csd4 gene. This indicates that inhibitor **8** is able to cross the out membrane and enter the periplasm in *C. jejuni*. It also suggests that inhibitor **8** is active against the *C. jejuni* enzyme Pgp1.

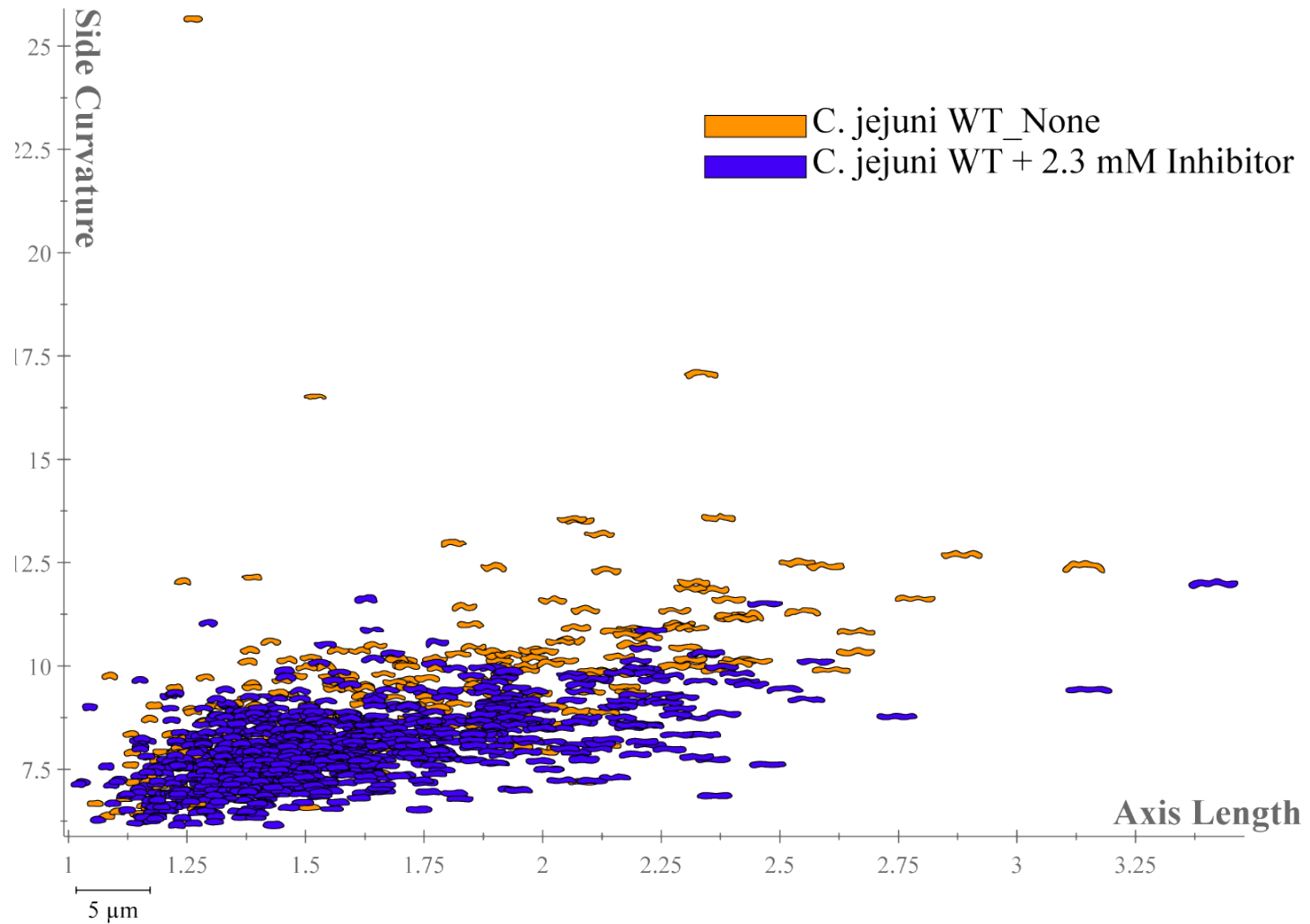


Figure 3.29. Strain shape distribution of *C. jejuni* wild-type (natural growth) and wild-type treated with 2.3 mM inhibitor for 24h.

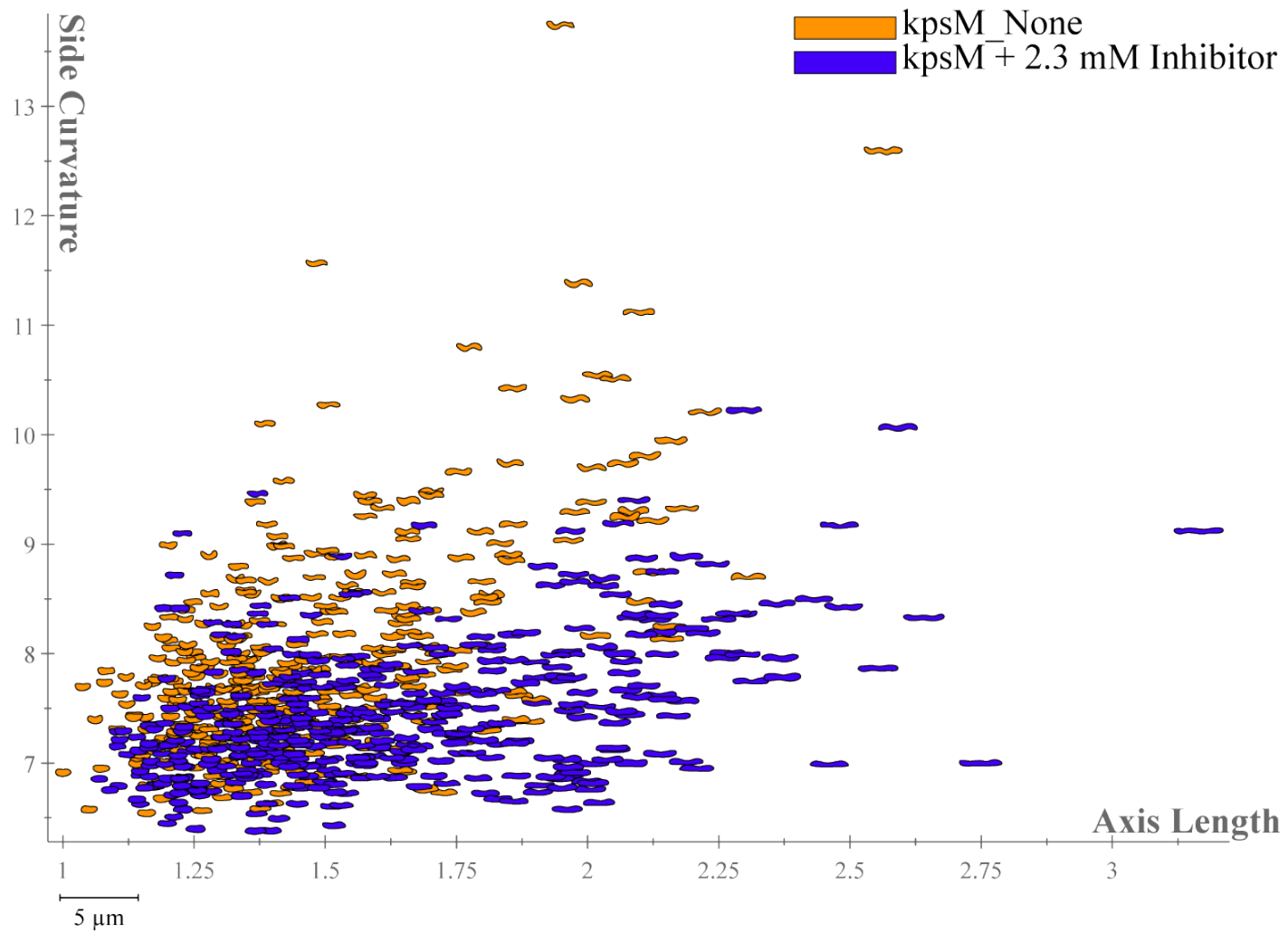


Figure 3.30. Strain shape distribution of *C. jejuni* $\Delta kpsM$ (natural growth) and $\Delta kpsM$ treated with 2.3 mM inhibitor for 24h.

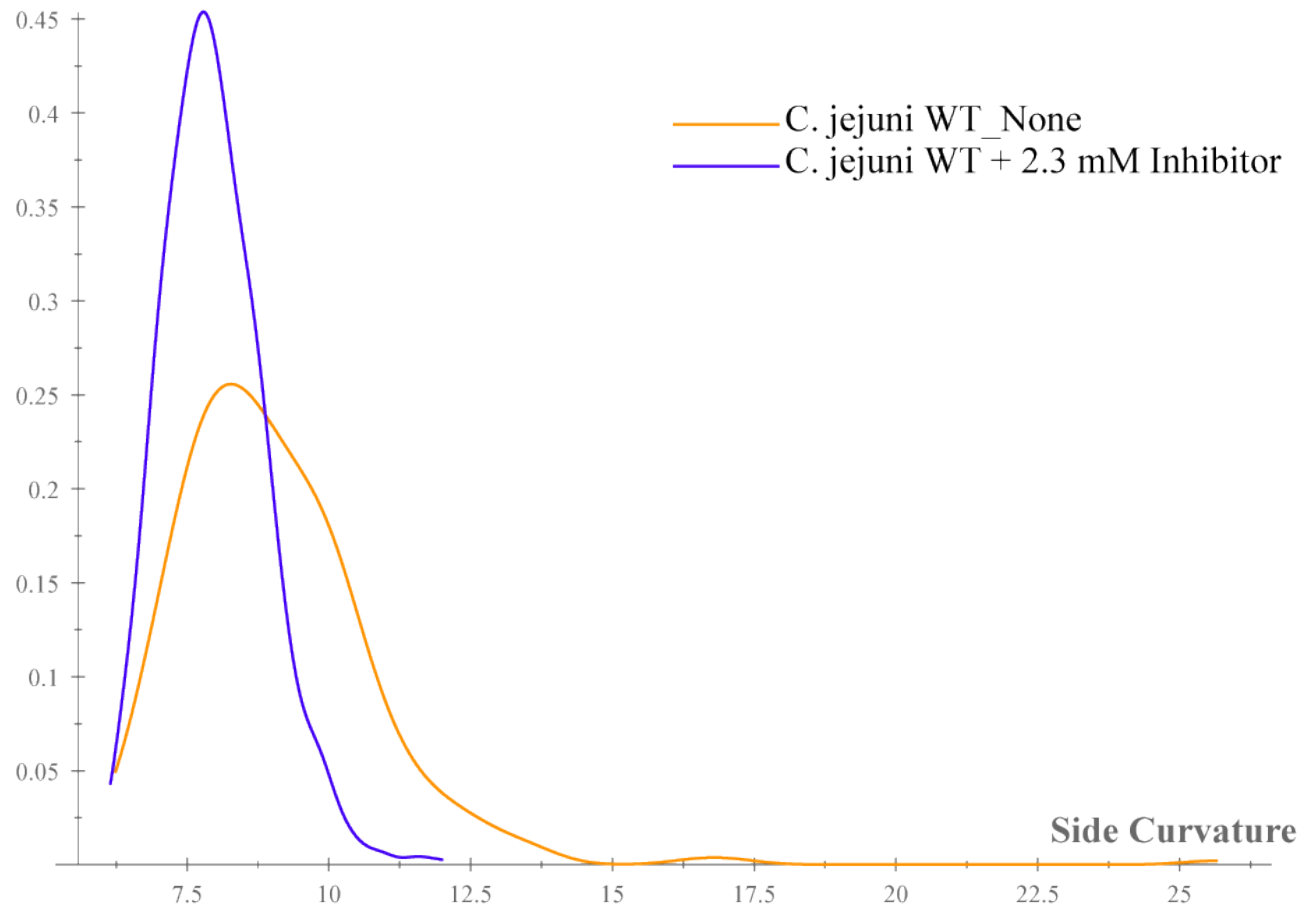


Figure 3.31. Histogram displaying population density of *C. jejuni* wild-type (natural growth, control) and *C. jejuni* wild-type treated with 2.3 mM inhibitor for 24h.

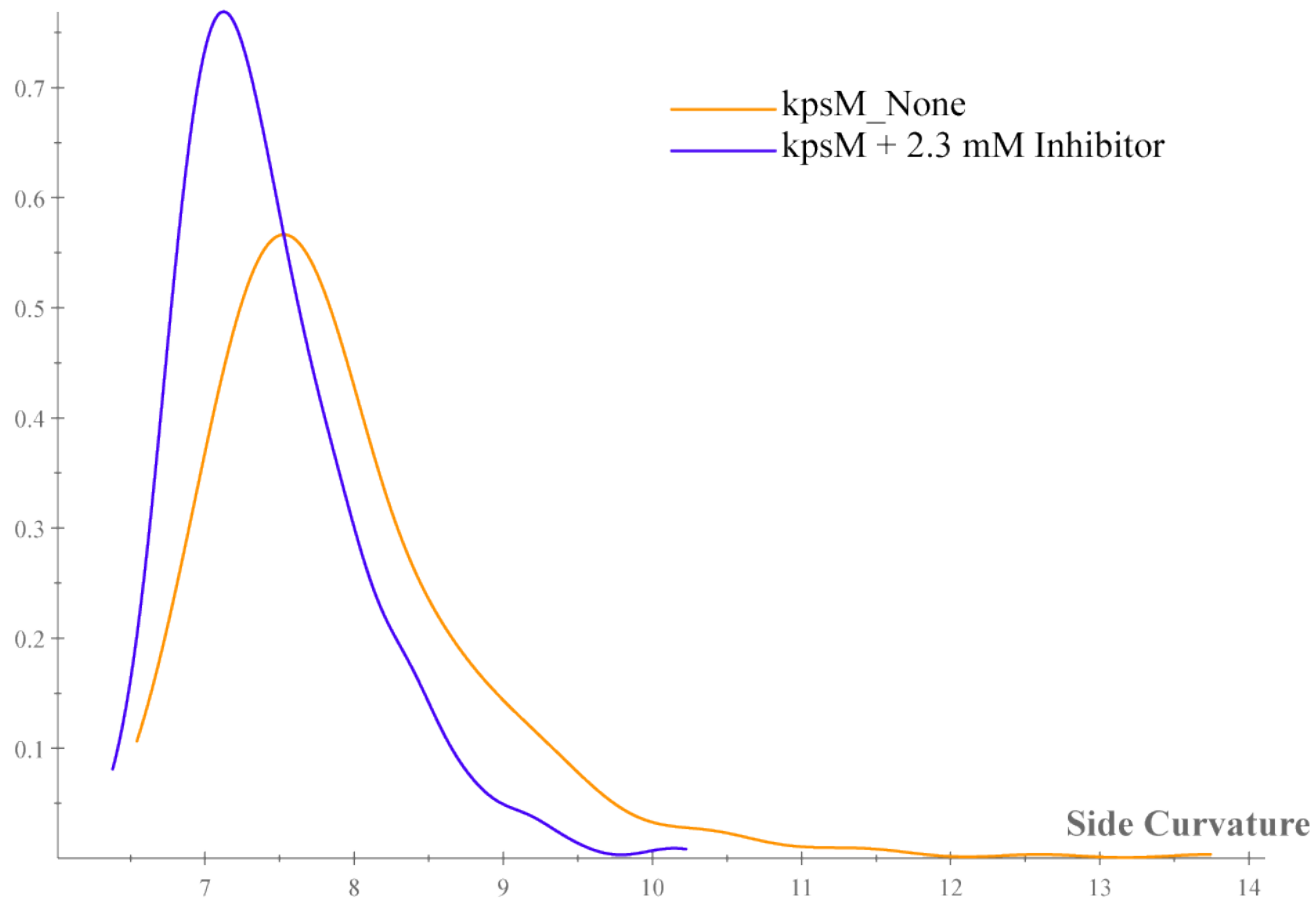


Figure 3.32. Histogram displaying population density of *C. jejuni* $\Delta kpsM$ (natural growth, control) and *C. jejuni* $\Delta kpsM$ treated with 2.3 mM inhibitor for 24h.

3.9.2 Assay with *H. pylori*

The morphological effects of inhibitor **8** on *H. pylori* cell shape were tested in the laboratory of our collaborator Dr. Nina Salama at the Fred Hutchinson Cancer Research Center. As *H. pylori* does not produce a capsular layer, only the wild-type J99 strain was incubated with the inhibitor. Similar to the results with *C. jejuni*, no straight rod cells were observed in the first 6 h, but straightening was observed after 24 h incubation. In addition, high inhibitor concentrations displayed both toxicity and morphological effects. The sensitivity of *H. pylori* was tested at three inhibitor concentrations, and cell straightening was observed when the inhibitor concentration was 2.5 mM or greater (Figure 3.33). The distribution histogram of *H. pylori*_WT vs. *H. pylori*_WT+ 2.5mM inhibitor displayed a peak shift of 1.2 in side curvature between the control and the inhibited bacteria batch (Figure 3.34). Compared to the effect on *C. jejuni*, the shift value observed with *H. pylori* is much larger, indicating the outer membrane of *H. pylori* is more permeable to inhibitor **8**. Alternatively, it could indicate that inhibitor **8** is more potent against Csd4 than the homologue Pgp1. Additionally, the cell shape distribution of *H. pylori* showed a larger separation between the untreated batch and the treated bacteria (Figure 3.35). Therefore, inhibitor **8** displays stronger morphological effects on *H. pylori* than on *C. jejuni*.

Table 3.7. Summary of microscopic observations of cellular morphology (*H. pylori*).

Strain	Inhibitor concentration (mM)	Summary of microscopic observations of cellular morphology		
		6 h	24 h	48 h
<i>H. pylori</i> J99	5.0	Helical, cellular debris	Cell straightening	Straightened cells, a few coccoid cells
	2.5	Helical, cellular debris	Cell straightening	Straightened cells, a few coccoid cells
	0	Helical	Helical	Helical and coccoid cells

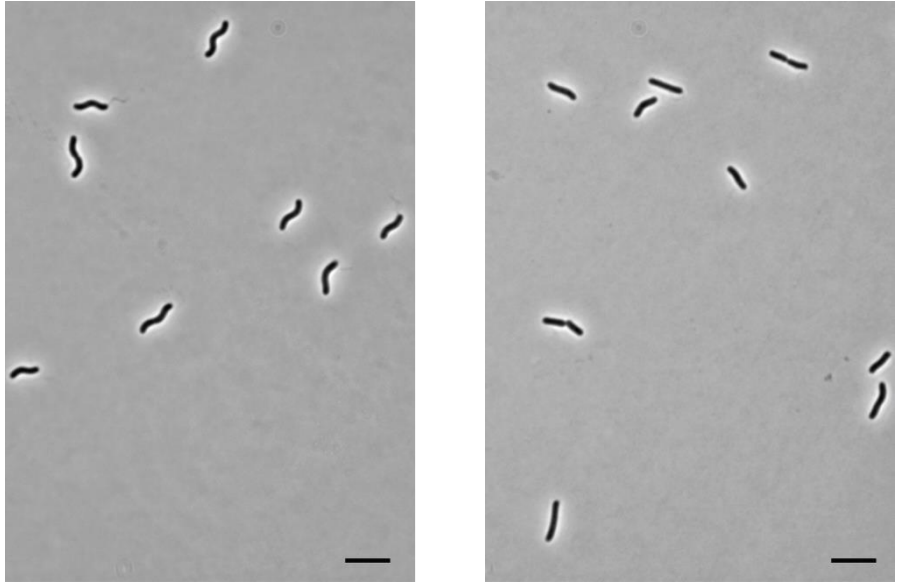


Figure 3.33. DIC microscopy images of the *H. pylori* wild-type (left) (natural growth, control) and wild-type treated with 2.5 mM inhibitor (right) for 24h.

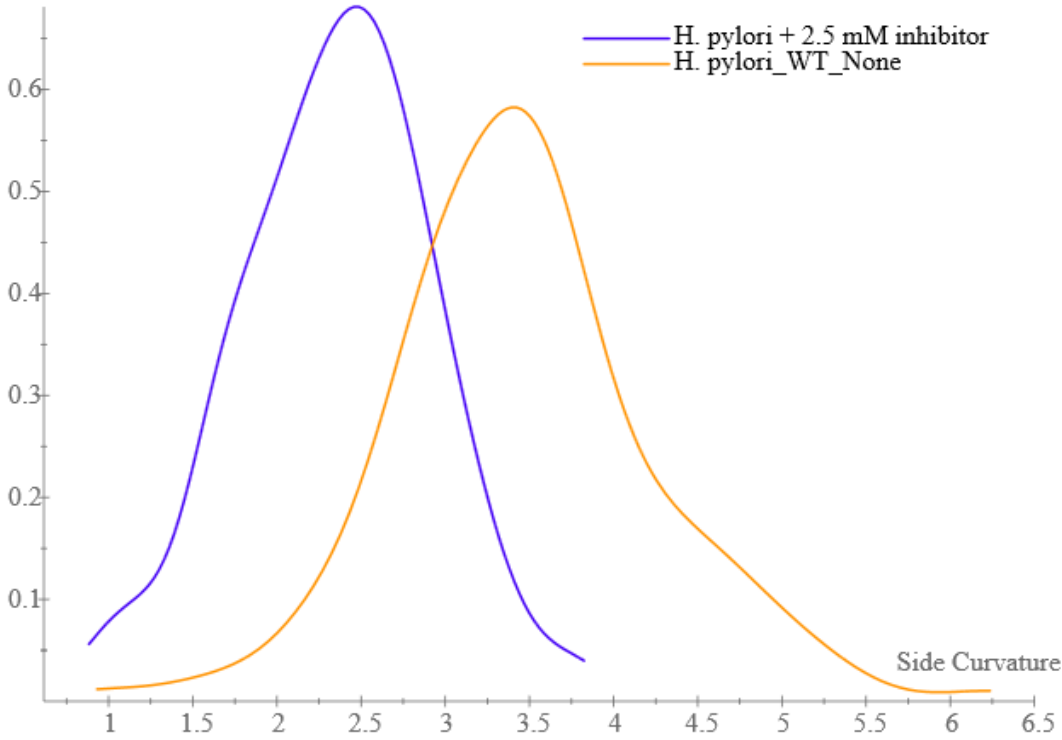


Figure 3.34. Histogram displaying population density of *H. pylori*_WT (natural growth, control) and that treated with 2.5 mM inhibitor for 24h. Horizontal axis indicates the actual side curvature of the cell.

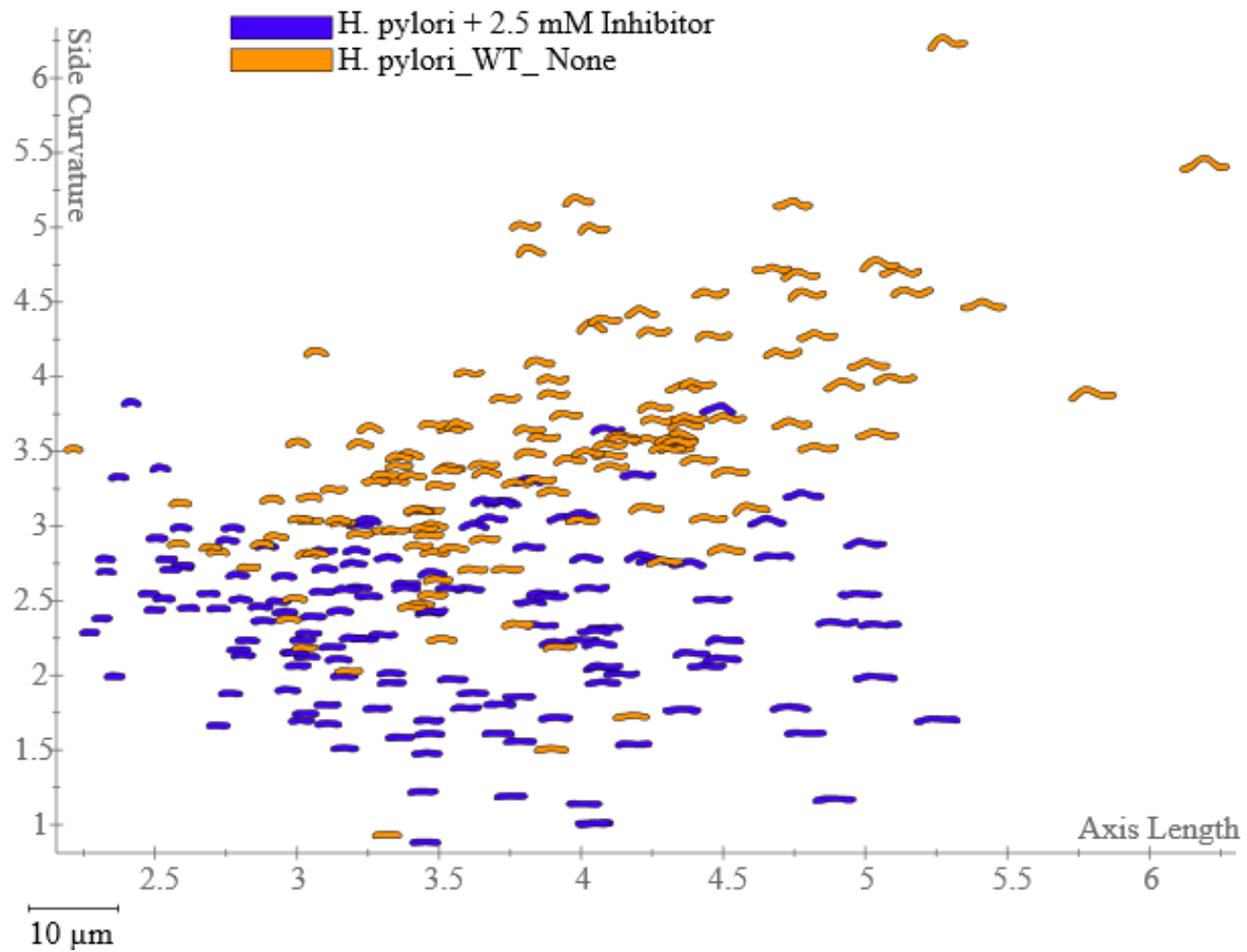


Figure 3.35. Strain shape distribution of wild-type *H. pylori* (natural growth) and that treated with 2.5 mM inhibitor for 24h. The horizontal and vertical axis show the actual length and side curvature of *H. pylori* cells.

3.10 Summary

In this chapter, we have detailed structural and inhibitory studies of the newly discovered *H. pylori* cell shape determinant, Csd4. The results that we have collected are in agreement with the proposed mechanism of zinc metalloproteases based on the well-studied M14 enzyme CPA. We propose that Csd4 represents a new sub-class of M14 proteases that use an uncommon His-Glu-Gln triad in zinc binding.

An alternative substrate of the Csd4 reaction, Ac-L-Ala-iso-D-Glu-*m*-Dap, was prepared via a seven-step synthesis as a mixture of two stereoisomers. This synthetic compound greatly facilitated the detailed analysis of the crystal structure and the reaction kinetics. Through the development of a continuous DAPDH-coupled assay, the kinetic constants including K_M , k_{cat} and k_{cat}/K_M were determined as $112 \pm 5 \mu\text{M}$, $0.0149 \pm 0.0002 \text{ s}^{-1}$, and $132 \pm 5 \text{ M}^{-1} \text{ s}^{-1}$, respectively. The value of k_{cat} and k_{cat}/K_M are smaller by 2 – 3 orders of magnitude than that of carboxypeptidase A. Both the low activity and low specificity indicate that either the peptidoglycan trimming is a slow process or the synthetic tripeptide is a poor substrate for Csd4.

We also synthesized the first intermediate analogue inhibitor of this enzyme via a 10-step synthetic pathway as a mixture of two stereoisomers. The inhibition kinetics were analyzed and to our surprise, inhibitor **8** behaved not as a fully competitive inhibitor but as a mixed-type inhibitor against Csd4 with an apparent K_I value of $3.3 \pm 0.8 \mu\text{M}$. The value of K_I is significantly lower than that of K_M for the tripeptide substrate, indicating that inhibitor **8** closely mimics the actual tetrahedral intermediate and binds to the enzyme much more tightly than the substrate. Thus, the results of the inhibition studies clearly support our proposed mechanism of Csd4. We do not fully understand the reason that the inhibitor displayed mixed inhibition against Csd4. But taken together with the facts that the inhibitor shows slow binding to Csd4 as well as that Csd4 contains two other minor domains of unknown functions, it is possible that the inhibitor has binding affinity to some other domain of Csd4.

We also obtained the crystal structures of Csd4-Tripeptide and Csd4-Inhibitor. The crystallographic studies of both these two complexes showed that Csd4 selectively bound the stereoisomer with an (*S*) stereochemistry at the *m*-Dap α carbon connecting to the scissile peptide bond. Based on the structure of Csd4-Tripeptide, we mapped a series of key residues in the Csd4 active site. The zinc binding motif consists of His128, Glu49 and an unusual Gln46. Additionally, we identified the two key residues typically involved in the carboxypeptidase mechanism: Glu222

and Arg86. Glu222 is the residue responsible for the deprotonation of water and the protonation of the departing amine. Arg86 is the residue responsible for stabilizing the tetrahedral intermediate. Several other residues including Gly131, Arg94, Asn93, His126 and Thr208 that interact with the substrate were also identified. In the structure of Csd4-Inhibitor, we observed structural reorientation of both the bound inhibitor and certain active site residues. Both of the oxygens of the phosphinate inhibitor were positioned within bonding distance to the Zn (II). As the inhibitor is structural analogue of the tetrahedral intermediate, it can be postulated that the intermediate would have a similar bidentate oxygen coordination with the zinc ion.

Taken together, these studies provide support for a catalytic mechanism that proceeds similarly to that of CPA. A zinc-bound water is initially deprotonated by the carboxylate of Glu222, and the derived hydroxide attacks the scissile peptide bond to form a tetrahedral intermediate. This intermediate is stabilized by Zn (II), Arg86 and Glu222. The amino group is then protonated by the carboxylic acid of Glu222, which promotes the collapse of tetrahedral structure, and the peptide bond is finally hydrolyzed to give the dipeptide and *m*-Dap.

We also examined the morphologic effects of inhibitor **8** on the cell shape of *C. jejuni* and *H. pylori*. For *C. jejuni*, our analysis indicated that cell straightening occurred after 24 h incubation with inhibitor **8** at concentrations greater than 0.3 mM, and the MIC was measured as 2.3 mM. Additionally, the acapsular *C. jejuni* strain *ΔkpsM* showed a greater extent of straightening. At high concentrations, the inhibitor showed toxicity and the straightening effect to both of these bacteria. For *H. pylori*, our initial experiments also showed significant cell straightening with inhibitor concentrations at 2.5 mM or higher. The success of the *in vivo* studies implies that Csd4 is a target for small molecule inhibitors as antibiotics and demonstrates that even polar molecules can cross the out membrane and reach the PG layers.

3.11 Future Directions

3.11.1 Develop more potent inhibitors of Csd4

We have demonstrated that the phosphinate-based peptidyl compound could successfully bind to the Csd4 active site acting mainly as a competitive inhibitor. We will follow the same strategy to make improvements on the current inhibitor **8**. It has been shown in several cases that phosphonic and/or phosphonamic acids displayed greater inhibition against metalloproteases than phosphonic acids (Figure 3.36). It is generally thought that the improved potency of such molecules comes from the potential formation of additional hydrogen bonds as compared to phosphonic acids

(146). In studies of metalloproteases including ACE, thermolysin and CPA, the observed potency increased by as much as two orders of magnitude (146-148).

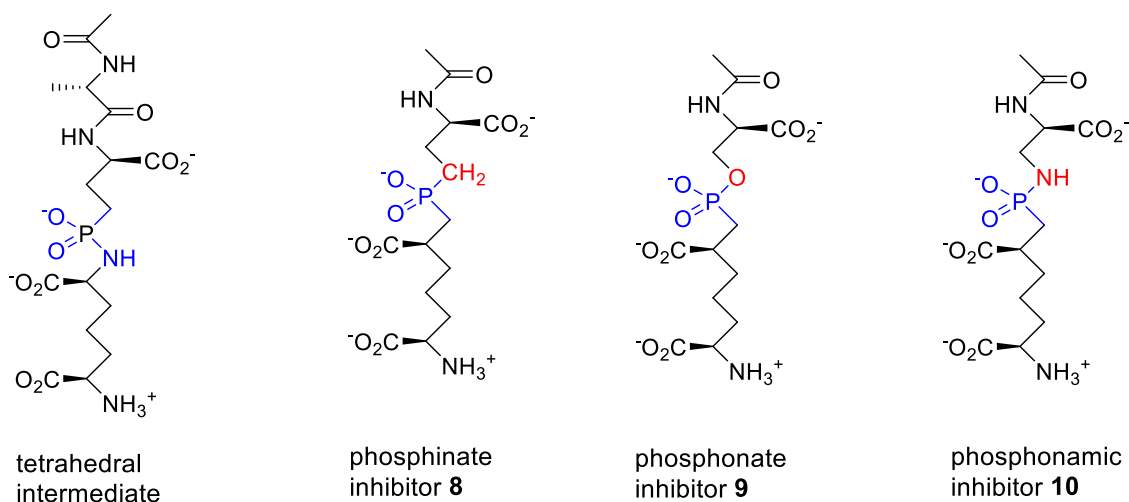


Figure 3.36. Inhibitor design using phosphorus-containing pseudopeptides.

The first targeted compound is the phosphonic acid inhibitor **9** (Figure 3.37). Initially it will be prepared as a mixture of two diastereomers and *in vitro* inhibition tests will be applied to examine its potency. Similar to the synthesis of inhibitor **8**, the preparation of inhibitor **9** will follow the coupling strategy of coupling two small molecules containing a Glu moiety (compound **37**) and a Dap moiety (compound **39**). Using the procedure described by Milewski *et al*, the phosphodiester **36** will be prepared as a racemic mixture, which then will be hydrolyzed to a monoester under mild basic conditions and then activated for coupling using thionyl chloride to give compound **37** (149). Compound **39** is a mono-hydroxyl substitute of *m*-Dap, which will be prepared by the stereoselective reduction of an α -ketodimylester (compound **38**) using a literature known procedure reported by Vederas *et al* (150). Compounds **37** and **39** will be coupled to give the protected inhibitor **40** and a selective demethylation using nucleophilic conditions to produce compound **41** (151). The final steps involve hydrogenolysis as well as global demethylation under basic condition will give inhibitor **9**. Recent inhibition studies on the tubulin-modifying enzyme TTL by Dr. Jenifer Griffith in our lab have successfully prepared phosphonic acid inhibitors using a very similar route (unpublished results). The interaction with inhibitor **9** and Csd4 will also be studied using the continuous DAPDH-coupled assay. Additionally, our second target, the phosphonamic acid analog **10**, could be synthesized using similar synthetic methods.

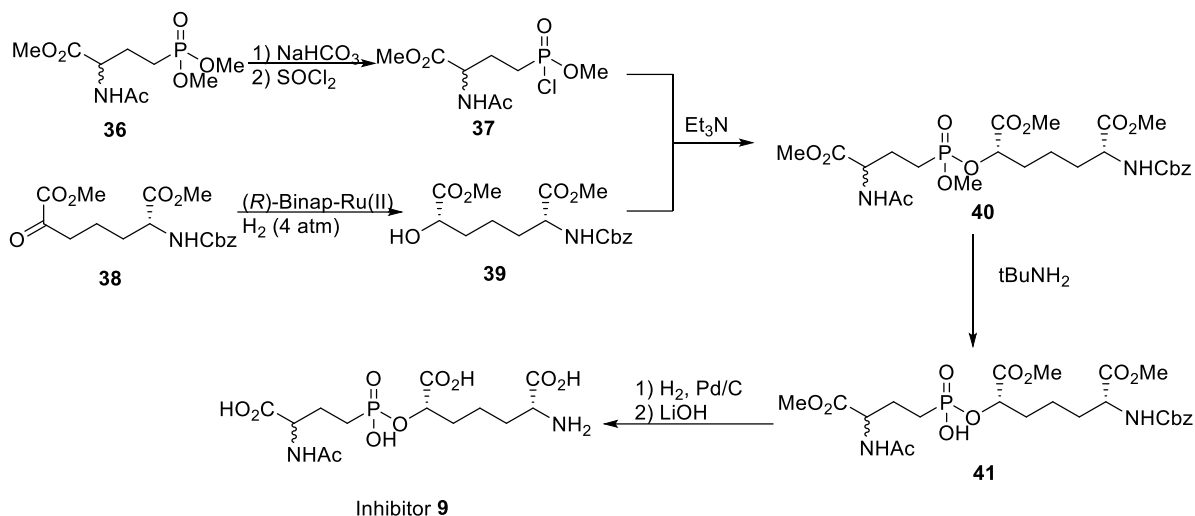


Figure 3.37. Synthetic strategy for Csd4 inhibitor **9**.

3.11.2 Inhibition studies of Csd4 with the new inhibitors

After the synthesis of the phosphonic acid inhibitor **9** and the phosphonamic acid inhibitor **10**, we will examine their *in vitro* inhibition performance using the continuous DAPDH-coupled assay. If a significant potency increase is observed (K_i decreases in 1 – 2 orders of magnitude), we will attempt to isolate the effective diastereomer to further improve its inhibitory potency. In addition, it is interesting to know whether these new inhibitors will show a similar mixed inhibition as inhibitor **8**.

3.11.3 Crystal structure of Csd4-Inhibitor complexes

From our obtained structure of Csd4-Inhibitor **8** complex, we have identified several active site residues that have interactions with the inhibitor and the zinc ion. If the new inhibitors **10** and **11** show greater inhibition effects on Csd4, we will crystallize the complexes of Csd4-Inhibitor **9** and Csd4-Inhibitor **10** using the optimized conditions obtained from Csd4-Inhibitor **8** experiments. By comparing the structural differences between Csd4-Inhibitor **8** and Csd4-Inhibitor **9/10**, we will get additional information of the active site and the importance of different residues. Thus, these crystallographic studies will be extended to examine the interactions of other inhibitors with Csd4.

3.11.4 Morphological effects of inhibitor on cell shape and colonization potential

Our preliminary results from the *in vivo* inhibition assay with both *H. pylori* and *C. jejuni* indicated that the significant cell straightening occurs in both bacterial species in the presence of inhibitor **8**. This phenotypic change strongly suggests that the inhibitor is acting on Csd4. The importance of this finding is that it can be used as a microbiology tool for monitoring cell shape morphology vs. time in live bacteria. (93-95).

Our initial morphological assay also indicates the inhibitor concentration range for cell straightening is in the millimolar level. The reason for this observation is likely to be that the highly polar functional groups (phosphonic acid and the carboxylic acid) of the inhibitor make it difficult to permeate the outer membrane. However, this assay demonstrates the possibility that small polar molecules can cross the outer membrane into the periplasm. Thus, it would be reasonable to speculate that a more potent inhibitor with similar polarity or a less polar inhibitor with similar potency will have improved morphological effects on the bacteria.

As aforementioned, our collaborator Dr. Erin Gaynor from UBC microbiology and Dr. Nina Salama from Fred Hutchison Cancer Research Center will carry the *in vivo* assay to examine the morphological effects on *C. jejuni* and *H. pylori*, respectively. Once we have inhibitors that display a sub-micromolar inhibition activity in cell straightening, these inhibitors can be tested for antibacterial effects on *C. jejuni* and *H. pylori* colonies. Such studies could provide lead compounds for the development of new type antibacterial reagents.

3.12 Experimental

3.12.1 Synthesis of tripeptide substrate

Chemicals were purchased from Aldrich Chemical Co., Alfa Aesar Co. or Fisher Scientific. Ion exchange resin was from Aldrich Co. and Bio-Rad Laboratories. Silica gel (230-400 mesh) was obtained from Silicycle Inc. The TLC silica gel (aluminum sheets) was from EMD Chemical Inc. CH₂Cl₂, MeOH and TEA were distilled under Ar from CaH₂. ¹H NMR spectra and proton-decoupled ³¹P NMR spectra was recorded on a Bruker AV400dir spectrometer or a Bruker AV400inv spectrometer at field strength of 400 MHz and 162 MHz, respectively. Mass Spectra obtained on a Waters 2965 HPLC-MS.

3.12.1.1 Ac-L-Ala-D-Glu(OtBu)-OH (Compound **23**).

To a solution of N-acetyl-L-alanine (131 mg, 1.0 mmol) in DMF (10 ml), was added HOBt (135 mg, 1.0 mmol) and HBTU (380 mg, 1.0 mmol) and the mixture was stirred for 30 min at RT. D-Glu(OtBu)-OH (203 mg, 1.0 mmol) and DIPEA (0.15 ml, 1.0 mmol) were added and the reaction was stirred for another 2h at RT. The solution was evaporated to dryness under reduced pressure, and was extracted with H₂O/EtOAc. The organic layer was dried over Na₂SO₄, and evaporated to dryness under reduced pressure. The resulting residue was purified by chromatography on silica gel (4% MeOH in CH₂Cl₂) to give compound **23** as a colorless oil (256 mg, 54%). ¹H NMR (400 MHz, MeOD) δ 4.46 – 4.25 (m, 2H), 2.52 – 2.30 (m, 2H), 2.23 – 2.10 (m, 1H), 1.99 (s, 3H), 1.96 – 1.87 (m, 1H), 1.48 (s, 9H), 1.35 (d, *J* = 6.8 Hz, 3H). MS (ESI) (*m/z*) 339.4 [M+Na]⁺.

3.12.1.2 Compound **25**.

To a solution of Ac-L-Ala-D-Glu(OtBu)-OH (Compound **23**, 72 mg, 0.23 mmol) in DMF (5 ml), was added HOBt (34 mg, 0.25 mmol) and HBTU (96 mg, 0.25 mmol), and the mixture was stirred for 30 min at RT. Compound **24** (98 mg, 0.21 mmol) and DIPEA (27 mg, 0.21 mmol) were added, the reaction was stirred for another 2h at RT. Compound **24** was prepared as a mixture of two regioisomers according to a literature known method (138). The solution was evaporated to dryness under reduced pressure, and was extracted with H₂O/EtOAc. The organic layer was dried over Na₂SO₄, and evaporated to dryness under reduced pressure. The resulting residue was purified by chromatography on silica gel (4% MeOH in CH₂Cl₂), but the ¹H NMR spectrum showed that the fraction containing compound **25** still included significant amount of impurities. Therefore the impure compound **25** fraction was used for the next step without further purification. MS (ESI) (*m/z*) 791.5 [M+Na]⁺.

3.12.1.3 Compound **26**.

To a solution of compound **25** (70 mg, 0.91 mmol) in MeOH (20 ml) was added Pd/C (10%, 50 mg). The resulting mixture was stirred under hydrogen gas (1 atm) for 5 h, and then filtered through celite. The filtrate was evaporated in vacuo and dried under reduced pressure to give compound **26** as a colorless oil. The crude oil was dissolved in NaHCO₃ solution (10%) and the pH was adjusted to 8.0. This was loaded onto a column of AG 1-X8 resin (formate form, 100-200 mesh, 5 ml). The column was washed with water (50 ml) and formic acid (0.5 M, 100 ml). The fractions containing the product were combined and evaporated to dryness in vacuo to give

compound **26** (mixture of two diastereomers) as a colorless oil (55 mg, 43% over 2 steps). ¹H NMR (400 MHz, MeOD) δ 4.41 – 4.32 (m, 2H), 4.30 – 4.18 (m, 2H), 2.71 (m, 2H), 2.38 – 2.30 (m, 2H), 2.02 (s, 3H), 1.90 – 1.84 (m, 4H), 1.78 – 1.63 (m, 2H), 1.48 (s, 9H), 1.45 (s, 9H), 1.40 – 1.35 (m, 3H). MS (ESI) (m/z) 611.3 [M+Na]⁺.

3.12.1.4 Ac-L-Ala-*iso*-D-Glu(OH)-*meso*-Dap-OH (Tripeptide Substrate).

Compound **26** (55 mg, 0.91 mmol) was dissolved in TFA (9.5 ml)/H₂O (0.5 ml). The resulting solution was stirred for 3h at RT, and then was evaporated in vacuo. The residue was redissolved in H₂O (2.0 ml) and the pH of the solution was adjusted to 8 by adding NaHCO₃ (0.5 M). This was loaded onto a column of AG 1-X8 resin (formate form, 100-200 mesh, 5 ml). The column was washed with water (50 ml) and formic acid (0.5 M, 50 ml), and then was eluted by formic acid (4.0 M, 100 ml). The fractions containing the compound were combined and evaporated to dryness in vacuo to give the tripeptide substrate (mixture of two diastereomers) as a colorless oil (28 mg, 71%). ¹H NMR (400 MHz, MeOD) δ 4.40 (m, 3H), 4.12 – 3.94 (m, 1H), 2.49 – 2.28 (m, 3H), 2.27 – 2.16 (m, 1H), 2.08 – 2.03 (m, 2H), 1.99 (s, 3H), 1.99 – 1.86 (m, 2H), 1.85 – 1.72 (m, 1H), 1.67 – 1.52 (m, 1H), 1.44 – 1.35 (m, 3H). MS (ESI) (m/z) 433.4 [M+H]⁺.

3.12.2 Bacterial strains and growth conditions

Strains used in this work, as well as primers and plasmids used in strain construction are described in Table 1. *H. pylori* were grown in Brucella broth (BB) with 10% fetal bovine serum (Gibco) without antimicrobials or on horse blood (HB) agar plates with antimicrobials as described (93). Bacteria were incubated at 37 °C under microaerobic conditions in a trigas incubator (10% CO₂, 10% O₂, and 80% air). For resistance marker selection HB plates were supplemented with 15 µg ml⁻¹ chloramphenicol (Cm), 25 µg ml⁻¹ kanamycin or 60 mg ml⁻¹ sucrose. For plasmid selection and maintenance in *E. coli*, cultures were routinely grown in Luria-Bertani (LB) broth or agar at 37 °C supplemented with 100 µg ml⁻¹ ampicillin.

3.12.3 Cloning and recombinant expression of Csd4

Wild-type Csd4, consisting of the native *H. pylori* strain G27 sequence (HPG27_353) minus the first 20 N-terminal signal sequence residues, three Csd4 active-site variants (Q46H, Q46A and Q46E) and *Corynebacterium glutamicum meso*-diaminopimelate dehydrogenase (DAPDH) were used in this study. Cloning of *csd4* into pET15 vector for recombinant expression has been described previously (95). Gln46 variants were made in pET15-*csd4* using the Agilent

QuikChange XL kit with primers A1-A6 described in Table 1 and verified by sequencing. All Csd4 variants were overexpressed in *E. coli* strain BL21 (DE3). Each 1 L culture was inoculated with 2 ml of overnight culture and incubated at 37 °C with shaking. When the cell density reached an optical density at 600 nm of ~0.9, the temperature was reduced to 20 °C for 30 min and then induced with 0.25 mM isopropyl- β -D-thiogalactopyranoside (IPTG) and grown overnight. The cells were pelleted, resuspended and lysed at 4 °C in binding buffer (25 mM NaH₂PO₄ pH 8, 600 mM NaCl, 10% glycerol and 5 mM imidazole) with an Emulsi Flex-C5 homogenizer (Avestin). The soluble fraction was loaded onto a ProBond nickel resin affinity column (Invitrogen) and the protein was eluted with increasing imidazole in binding buffer at pH 7.5. Csd4 was then dialyzed into 25 mM NaH₂PO₄ pH 7.5, 500 mM NaCl and digested with thrombin overnight (500:1 w/w Csd4:thrombin ratio) at 4 °C to remove the His-tag. Benzamide beads were used to remove the thrombin and the protein was further purified by gel-filtration chromatography (Superdex 200 16/60 column) equilibrated with 20 mM Tris pH 7.5, 500 mM NaCl. Q46H Csd4 used for crystallization was not additionally purified by gel-filtration but was buffer exchanged by ultrafiltration. The protein concentration was calculated using an extinction coefficient value of 36190 M⁻¹cm⁻¹ for folded Csd4 protein (ϵ_{folded}). ϵ_{folded} was derived using the Beer-Lambert law and UV absorption values of Csd4 denatured in 6M guanidium hydrochloride and predicted extinction coefficient values ($\epsilon_{\text{unfolded}}$) (152). Protein samples were then concentrated to ~15-20 mg ml⁻¹ and flash frozen in liquid nitrogen. Recombinant DAPDH protein was expressed and purified from *E. coli* BL21 (DE3) (vector was a generous gift from Lilian Hor and Matthew Perugini, La Trobe University, Australia) as previously described (153).

3.12.4 Crystallization and structure determination

3.12.4.1 Csd4-Zn and Csd4-Tripeptide

(Anson Chan, ansonch@mail.ubc.ca)

Initial phasing by molecular replacement using available structures of distantly-related carboxypeptidases did not lead to interpretable maps. Instead, a crystallization condition containing iodide was optimized to employ *de novo* phasing. The final structures of wild-type Csd4 and its variants were crystallized in the $P2_12_12_1$ space group using reservoir solution containing 16-20% PEG 3350, 0-100 μ M Tris pH 8 and 0.3-0.4 M sodium iodide by hanging drop vapor diffusion. Crystals appear within a few days at room temperature but were allowed to grow to a sufficient size for approximately 2 weeks. The crystal structure was initially determined

to 2.1 Å by single wavelength iodide phasing using data collected at the UBC Astrid X-ray homesource (1.54 Å wavelength) at 100K. Data was processed and phased using HKL3000 (154) (Csd4-initial in Table 2). The anomalous substructure determined by SHELXD (155) contained 14 iodide sites. A combination of autobuilding with ArpWarp (156) and manual rebuilding using Coot (157) were used to complete the structure. Zinc-containing crystal structures of WT and Q46H Csd4 were obtained by sequentially soaking the crystals in freshly prepared 3% increments of PEG 3350 (all other concentrations remaining the same as the reservoir; ~5 min per step) up to 27% followed by the addition of an equal volume of 27% soaking solution supplemented with 4 mM ZnCl₂ for 30 and 60 min, respectively. These crystals were then soaked in 27% soaking solution with ethylene glycol as a cryoprotectant (25% (v/v)). Similarly, the tripeptide containing crystals were prepared by sequential soaking up to 33% PEG 3350, but with each soaking solution also supplemented with 1 mM ZnCl₂, followed by a 30 min soak in the 33% solution supplemented with 2.5 mM tripeptide and 1 mM ZnCl₂. An equal volume of 33% soaking solution supplemented with 4 mM ZnCl₂ was then added and soaked for another 9 min, followed by a quick soak in the same cryoprotectant and flash frozen. Native (0.98 - 1.00 Å) and zinc-anomalous (1.26 - 1.28 Å) wavelength datasets on derivitized crystals were collected at the Canadian Lightsource beamlines 08B1-1 and 08ID-1 at 100 K and processed using XDS (158). The original Csd4 structure was then used as a starting point for direct refinement using PHENIX and manual rebuilding with Coot. Poor electron density precluded modelling of the following loop region on domain 3: residues 389-394 (Csd4-Tripeptide); residues 389-392 with Lys393 modeled as Ala (Csd4-Q46H and Csd4-Zn). All structures have excellent stereochemistry, with 96.9-97.4% of residues in the favored region of the Ramachandran plots and no outliers.

3.12.4.2 Csd4-Inhibitor

Csd4 was crystallized in the P212121 space group with a reservoir solution containing 13-18% PEG 3350, 15 µM Tris pH 8 and 0.4 M sodium iodide by hanging drop vapor diffusion. Crystals were grown for approximately two weeks to reach a sufficient size. The inhibitor-bound structure was then obtained by sequentially soaking crystals of Csd4 in freshly prepared well solution with 1.6 mM ZnCl₂ and PEG 3350 in increments of 3% up to 28% (~5 min per step) followed by the addition of an equal volume of 28% soaking solution supplemented with 2 mM inhibitor for 80 min. These crystals were then briefly soaked in cryoprotectant consisting of 25% (v/v) ethylene glycol prepared with soaking solution and flash frozen. A native 0.9796 Å wavelength dataset to 1.9 Å resolution was collected at 100 K at the Canadian Light Source CMCF-BM Beamline and processed using XDS (158). The structure factors were directly refined against our apo-Csd4

crystal structure (PDB ID: 4WCK) using PHENIX (159) and manual completed using Coot (157). The structure has excellent stereochemistry with 96.7% of residues in the favored region of the Ramachandran plot and no outliers.

3.12.5 Sequence alignments

Homologs of Csd4 were identified from the non-redundant database at the National Center for Biotechnology Information utilizing BLASTP (<http://blast.ncbi.nlm.nih.gov/Blast.cgi>) and an *E*-value cutoff of 1×10^{-7} . Identical protein sequences derived from different strains of the same species and proteins with short alignment coverage were removed. The sequences were aligned with Clustal Omega (160) and a bootstrapped tree (with 500 replicates, subtree pruning and regrafting and five random starts) was generated using PhyML (161) within Seaview (162). The aligned sequences were also used to generate some figure using Consurf (163) to identify the degree of amino acid conservation.

3.12.6 Stopped kinetic assays

C. glutamicum DAPDH was used to determine the cleavage rates by Csd4 and its variants by consuming the predicted product of the Csd4 reaction, *m*-DAP, and NADP⁺. The consumption of NADP⁺ to produce NADPH is detectable as an increase in absorbance at 340 nm. To determine the activity profile of DAPDH over various pH values, various concentrations of DAPDH was incubated with 100 mM buffer (Bis-tris pH 5.6 and 6.5, MES pH 6, and Tris pH 7.5 and 8), 500 mM NaCl, 0.3 mM NADP⁺ and 1.2 mM *m*-DAP. Due to differing DAPDH activity at varying pH, an uncoupled assay was used to examine the pH effects on Csd4 activity. 5 μM Csd4 was incubated in 20 mM Na/K phosphate (pH 4.8, 5, 5.5, 6, 6.5, 7, 7.5 and 8), 500 mM NaCl and 7 μM EDTA for 5 min at 30 °C, followed by the addition of 17 μM ZnCl₂ and incubating for another 5 min. The reaction was then initiated by the addition of 1 mM tripeptide, incubated for 20 min and stopped by boiling the sample for 10 min at 98 °C. The sample was then centrifuged to remove precipitated protein, mixed with Tris pH 8 (100 mM final concentration), 2.5 mM NADP⁺ and 2.5 μM DAPDH and the relative activity was determined based on final absorption values at 340 nm.

3.12.7 Synthesis of inhibitor 8

Chemicals were purchased from Aldrich Chemical Co., Alfa Aesar Co. or Fisher Scientific and used without further purification unless otherwise noted. The TLC silica gel (aluminum sheets)

was from EMD Chemical Inc. Silica gel chromatography was prepared using Silica Gel SiliaFlash F60 (Silicycle, 230-400 mesh). Ion exchange resin AG-1X8 was purchased from Bio-Rad Laboratories and resin Amberlite IR-120H was purchased from Aldrich Co.. CH₂Cl₂, MeOH and TEA were distilled under Ar from CaH₂.

¹H NMR spectra and proton-decoupled ³¹P NMR spectra was recorded on a Bruker AV400dir spectrometer or a Bruker AV400inv spectrometer at field strength of 400 MHz and 162 MHz, respectively. High resolution mass spectrometry was performed by electrospray ionization (ESI-MS) using an Esquire LC mass spectrometer. Mass spectrometry of high MW molecules was performed by Matrix-assisted laser desorption ionization (MALDI-MS) using a Bruker Autoflex MALDI-TOF. All mass spectrometry was obtained at the UBC Mass Spectrometry Facility. Neutral compounds were detected as positive ions, and negatively charged compounds were detected as negative ions.

3.12.7.1 Compound **31**

Compound **30** (1.54 g, 4.6 mmol) was added to 20 mL anhydrous benzene in a round bottom flask. To the resulted suspension was added cupric acetate monohydrate (208 mg, 1.2 mmol). The mixture was stirred for 1 hr at rt under argon. Then fresh lead (IV) tetraacetate (4.1 g, 9.2 mmol) was added and the reaction was allowed to stir for another 1 hr at room temperature. The reaction was heated to reflux overnight under argon. After filtering through celite, the filtrate was diluted with EtOAc and washed three times with water and one time with brine. Then the organic layer was dried with MgSO₄. After filtration, the filtrate was concentrated under reduced pressure. Further purification with flash chromatography (silica, 10:1 of Hexane:EtOAc) gave 450 mg (33 %) compound **31** as a colorless oil. ¹H NMR (400 MHz, CDCl₃) δ 7.49 – 7.29 (m, 5H), 5.90 (m, 1H), 5.35 (d, *J* = 17.0 Hz, 1H), 5.25 (d, *J* = 10.4 Hz, 1H), 5.13 (s, 2H), 3.45 (m, 1H), 1.47 (s, 9H). MS (ESI) (*m/z*) 314.3 [M+Na]⁺.

3.12.7.2 Compound **34**.

To compound **31** (400 mg, 1.4 mmol) in MeOH (20 mL) was added ammonium hypophosphite (350 mg, 4.2 mmol) and triethylborane (1.0 M in THF, 2.8 mL). The solution was stirred for 3h, then evaporated to dryness under reduced pressure. The resulting residue was dissolved in aqueous KHSO₄ (1.0 M, 10 mL), and was extracted with EtOAc (3 x 50 mL). The combined organic phases were dried over anhydrous Na₂SO₄. Removal of the solvent in vacuo gave a colorless oil, which was used in the next step without further purification.

A mixture of the colorless oil (330 mg, crude) and hexamethyldisilazane (640 mg, 4.0 mmol) was heated for 1 h at 110 °C under argon. Compound **29** (300 mg, 0.70 mmol) was then added. The resulting mixture was heated for 3 h at 90 °C. After cooling to 70 °C, the reaction was quenched with MeOH (10 mL). The resulting solution was evaporated to dryness in vacuo, then extracted with a NaHCO₃ solution (10%, 15 mL) and diethyl ether (10 mL). The aqueous phase was separated, and extracted with EtOAc (3 x 50 mL). The combined organic phases were dried over anhydrous Na₂SO₄, filtered, and the solvent was removed under reduced pressure to give a yellow oil (215 mg). This oil was used in the next step without further purification.

The crude oil (mainly compound **33**, 400 g) and 1-adamantylbromide (235 g, 1.2 mmol) were dissolved in chloroform (20 mL). This solution was heated to reflux. Silver oxide (4 x 140 mg, 2.4 mmol) was added in a quarter portion each time, over 40 min. This solution was refluxed for an additional hour. The solvent was removed in vacuo, and the residue was suspended in diethyl ether and filtered through celite. The filtrates were concentrated. The residue was purified by column chromatography using chloroform/methanol (9.6:0.4) as eluent. Compound **34** was obtained as a colorless foamed gum (mixture of four diastereomers, 265 mg, 0.286 mmol, 25%). ¹H NMR (400 MHz, CDCl₃) δ 7.42 – 7.28 (m, 10H), 5.66 – 5.44 (m, 1H), 5.21 – 4.90 (m, 4H), 4.35 – 4.02 (m, 2H), 2.91 – 2.73 (m, 1H), 2.26 – 1.97 (m, 12H), 1.98 – 1.83 (m, 2H), 1.82 – 1.53 (m, 16H), 1.52 – 1.22 (m, 25H). ³¹P NMR (162 MHz, CDCl₃) δ 50.76, 50.32, 50.19. MS (ESI) (m/z) 947.8 [M+Na]⁺.

3.12.7.3 Compound **35**.

To a solution of compound **34** (260mg, 0.28 mmol) in MeOH (20 mL) was added Pd/C (10%, 50 mg). The resulting mixture was stirred under hydrogen gas (1 atm) for 5 h, and then filtered through celite. The filtrate was evaporated in vacuo and dried under reduced pressure to give a colorless oil (210 mg).

The oil was dissolved in an aqueous solution of acetic acid (0.1 M, 20 mL). Acetic anhydride (285 mg, 2.8 mmol) was added dropwise, and the pH was adjusted to 6 by the addition of triethylamine. The resulting solution was stirred for 10 min and was acidified to pH 2 by the addition of Amberlite IR-120H ion exchange resin. Filtration and removal of the solvent in vacuo gave a colorless oil as crude. The resulted oil was purified by silica gel chromatography (5% MeOH in chloroform) and gave compound **35** as a colorless oil (sets of enantiomers, 114 mg, 0.19 mmol, 68%). ¹H NMR (400 MHz, CDCl₃) δ 6.60 – 6.52 (m, 1H), 4.58 – 4.41 (m, 2H), 2.20 –

2.06 (m, 21H), 2.05 – 2.01 (s, 3H), 2.02 (s, 3H), 1.87 – 1.37 (m, 35H). ³¹P NMR (162 MHz, CDCl₃) δ 54.30, 52.28. MS (ESI) (m/z) 741.6 [M-H]⁻.

3.12.7.4 Inhibitor **8** (Csd4 Inhibitor).

Compound **35** (141 mg, 0.19 mmol) was dissolved in TFA (9.5 ml)/H₂O (0.5 ml). The resulting solution was stirred for 3h at RT, and then the solvent was evaporated in vacuo. The residue was redissolved in H₂O (2.0 ml) and the pH of the solution was adjusted to 8 by adding NaHCO₃ (0.5 M). This was loaded onto a column of AG 1-X8 resin (formate form, 100-200 mesh, 5 ml). The column was washed with water (50 ml) and formic acid (0.1 M, 50 ml; 0.5 M, 50 mL), and then was eluted by formic acid (4.0 M, 100 ml). The fractions containing the compound were combined and evaporated to dryness in vacuo to give the tripeptide substrate (mixture of two diastereomers) as a colorless oil (42 mg, 0.106 mmol, 56%). ¹H NMR (400 MHz, MeOD) δ 4.44 (s, 2H), 2.22 – 2.08 (m, 3H), 2.03 – 2.00 (m, 2H), 2.00 (s, 3H), 2.00 – 1.91 (m, 4H), 1.82 – 1.70 (m, 4H). ³¹P NMR (162 MHz, MeOD) δ 31.14. MS (ESI) (m/z) 395.3 [M-H]⁻.

3.12.8 Testing of Csd4 activity using a continuous coupled assay

Csd4 activity with the tripeptide substrate was monitored using a continuous coupled assay that involves *m*-Dap dehydrogenase (DAPDH) and NADP. The production of NADPH occurred during the oxidation of *m*-Dap by DAPDH, and the rate of tripeptide substrate hydrolysis was followed by monitoring the increase in absorbance at 340 nm using a Cary300 UV-Vis spectrophotometer. All kinetic assays were performed at 30 °C in 100 mM phosphate buffer (pH 6.5) in the presence of 500 mM NaCl and 2.5 mM NADP. The concentration of Csd4 and DAPDH were set to 3.0 μM and 10.0 μM. The concentration of ZnCl₂ was fixed to 30 μM. Assay mixtures were pre-incubated at 30 °C for 10 – 15 min, and then initiated by addition of the substrate at different concentrations. A non-linear lag associated with the coupled assay was observed in the first 5 min, therefore the initial velocity data was measured based on the slope of the linear plot after 5 min (6 – 20 min) using Microsoft Office Excel 2013. Each data point in the Csd4 substrate concentration vs. initial velocity plot was calculated from the average of triplicate assays. The data were fitted by GraphPad® software using a non-linear fit program, and the kinetic parameters were determined based on this fit.

In the inhibition assay, the initial velocity was monitored in the presence of inhibitor **8** at several concentration levels. The concentration of all the components is consistent with the activity assays. The pH and temperature of the solution were also kept identical. The inhibitor was added

to the mixture (without the tripeptide substrate), and pre-incubated for 20 – 30 min due to the phenomenon of slow inhibitor binding, the reaction was initiated by the addition of the tripeptide substrate. The initial velocity values were calculated from the linear slope between 5 – 20 min after initiation using Microsoft Office Excel 2013. The data were collected at apparent inhibitor concentrations of 2.0 μM , 5.0 μM and 10.0 μM . The Dixon plot were generated by Microsoft Office Excel® 2013 and related parameters were calculated based on this fit.

3.12.9 *In vivo* assays of inhibitor 8 with *C. jejuni* and *H. pylori*

Wild-type *C. jejuni* strain 81-176 and the acapsular mutant $\Delta kpsM$ were pulled from frozen stocks onto Mueller-Hinton agar plates supplemented with vancomycin (10 $\mu\text{g/ml}$) and trimethoprim (5 $\mu\text{g/ml}$). *kpsM* is an ABC transporter protein involved in the transport of the capsular polysaccharide across the inner membrane. After overnight growth on these plates, cells were streaked to new plates, allowed to grow for approximately 6-7 hours, and then inoculated to a broth culture and grown overnight with shaking. This results in log phase growth by morning (about 18h after inoculation). The log phase cultures were diluted to an OD of 0.0002 at 600 nm, corresponding to approximately 1×10^6 cells / ml, and 50 μl was added to each well of a microtitre plate. Doubling dilutions of the inhibitor were made in water, and 5 μl added to each well. 5 μl of H_2O was used as a control. The microtitre plate was incubated overnight, and at 24h the OD_{600nm} was measured to determine the MIC (minimal inhibitory concentration) of the inhibitor. 5 μl from each well was spotted onto Mueller-Hinton agar to check for growth and determine the MBC (minimal bactericidal concentration). 1 μl from each well was examined in the microscope to check for cell morphology. The CellTools analysis was done using images from 24h, with either no inhibitor or with 2.3 mM.

Bacterial shapes were derived from manually thresholded phase-contrast images (100x) and mutually aligned as previously described (164,165). Briefly, image contours at the threshold level were extracted and smoothed via spline interpolation to polygons with 50 evenly spaced vertices. Cells were then aligned along their long axes and the point ordering adjusted so as to be consistent across the population, such that any specific range of vertices identifies similar anatomical landmarks (e.g., the poles) across the population. Centerlines running from pole to pole, midway between the two sides of each shape, were modeled as a system of compressed springs repelled from the edges of the shape except at the endpoints, which are allowed to slide along the shape. The spring system is numerically relaxed to define a line that stretches along the entire length of the shape while remaining smooth and equidistant from the sides. The code for

shape extraction, smoothing, and centerline finding is part of the Celltool® software package, made freely available by the authors.

Two measurements of 2D cell shape were employed to characterize bacteria in this study: the length of the central axis (the centerline described above), and side curvature, a measure of the total curvature of bacterial outline excluding the poles. This size-invariant “normalized curvature” measurement has been previously defined (164). Briefly, curvature is the reciprocal of the radius of a circle tangent to a curve at any point; as such, a straight line has zero curvature while a point on a bent line has a curvature proportional to the tightness of the bend. We summed the curvatures at each (non-pole) point on the outline, multiplying by the total length of these portions of the outline to account for the fact that small cells will have higher curvature (smaller radii of tangent circles) due to their size alone. Code for performing these measurements is also part of the Celltool® package.

References

1. Cooper, G. (2000) The Cytoskeleton and Cell Movement. in *The Cell: A Molecular Approach*, 2nd Ed., Sinauer Associates, Sunderland (MA). pp
2. Weber, K., Rathke, P. C., and Osborn, M. (1978) Cytoplasmic microtubular images in glutaraldehyde-fixed tissue culture cells by electron microscopy and by immunofluorescence microscopy. *Proc. Natl. Acad. Sci. USA* **75**, 1820-1824
3. Janke, C., and Chloë Bulinski, J. (2011) Post-translational regulation of the microtubule cytoskeleton: mechanisms and functions. *Nat. Rev. Mol. Cell Biol.* **12**, 773-786
4. Nogales, E., Whittaker, M., Milligan, R. A., and Downing, K. H. (1999) High-resolution model of the microtubule. *Cell* **96**, 79-88
5. Nogales, E., Wolf, S. G., and Downing, K. H. (1998) Structure of the $\alpha\beta$ tubulin dimer by electron crystallography. *Nature* **391**, 199-203
6. Vallee, R. B. (1986) Reversible assembly purification of microtubules without assembly-promoting agents and further purification of tubulin, microtubule-associated proteins, and MAP fragments. *Methods Enzymol.* **134**, 89-104
7. Mitchison, T., and Kirschner, M. (1984) Dynamic instability of microtubule growth. *Nature* **312**, 237-242
8. Verhey, K. J., and Hammond, J. W. (2009) Traffic control: regulation of kinesin motors. *Nature Rev. Mol. Cell Biol.* **10**, 765-777
9. Vallee, R. B., Williams, J. C., Varma, D., and Barnhart, L. E. (2004) Dynein: an ancient motor protein involved in multiple modes of transport. *J. Neurobiol.* **58**, 189-200
10. Duncan, J. E., and Goldstein, L. S. B. (2006) The Genetics of Axonal Transport and Axonal Transport Disorders. *PLoS Genetics* **2**, e124
11. Berg JM, T. J., Stryer L. (2002) Kinesin and Dynein Move Along Microtubules. in *Biochemistry*, 5th Edition Ed., W H Freeman, New York. pp
12. Desai, A., and Mitchison, T. J. (1997) Microtubule polymerization dynamics. *Annu. Rev. Cell Dev. Biol.* **13**, 83-117
13. Garnham, C. P., and Roll-Mecak, A. (2012) The chemical complexity of cellular microtubules: tubulin post-translational modification enzymes and their roles in tuning microtubule functions. *Cytoskeleton (Hoboken, N.J.)* **69**, 442-463
14. Roll-Mecak, A., and McNally, F. J. (2010) Microtubule-severing enzymes. *Curr. Opin. Cell Biol.* **22**, 96-103
15. Akhmanova, A., and Hoogenraad, C. C. (2005) Microtubule plus-end-tracking proteins: mechanisms and functions. *Curr. Opin. Cell Biol.* **17**, 47-54

16. Akhmanova, A., and Steinmetz, M. O. (2008) Tracking the ends: a dynamic protein network controls the fate of microtubule tips. *Nature Rev. Mol. Cell Biol.* **9**, 309-322
17. Conde, C., and Caceres, A. (2009) Microtubule assembly, organization and dynamics in axons and dendrites. *Nat. Rev. Neurosci.* **10**, 319-332
18. Sheetz, M. P., Steuer, E. R., and Schroer, T. A. (1989) The mechanism and regulation of fast axonal transport. *Trends Neurosci.* **12**, 474-478
19. Lindemann, C. B., and Lesich, K. A. (2010) Flagellar and ciliary beating: the proven and the possible. *J. Cell Sci.* **123**, 519-528
20. Surrey, T., Nedelec, F., Leibler, S., and Karsenti, E. (2001) Physical properties determining self-organization of motors and microtubules. *Science* **292**, 1167-1171
21. Jordan, M. A., and Wilson, L. (2004) Microtubules as a target for anticancer drugs. *Nature reviews. Cancer* **4**, 253-265
22. Downing, K. H. (2000) Structural basis for the interaction of tubulin with proteins and drugs that affect microtubule dynamics. *Annual review of cell and developmental biology* **16**, 89-111
23. Janke, C., and Kneussel, M. (2010) Tubulin post-translational modifications: encoding functions on the neuronal microtubule cytoskeleton. *Trends Neurosci.* **33**, 362-372
24. Wloga, D., and Gaertig, J. (2010) Post-translational modifications of microtubules. *J. Cell Sci.* **123**, 3447-3455
25. Westermann, S., and Weber, K. (2003) Post-translational modifications regulate microtubule function. *Nature Rev. Mol. Cell Biol.* **4**, 938-947
26. Verhey, K. J., and Gaertig, J. (2007) The tubulin code. *Cell Cycle* **6**, 2152-2160
27. Caron, J. M. (1997) Posttranslational modification of tubulin by palmitoylation: I. In vivo and cell-free studies. *Molecular Biology of the Cell* **8**, 621-636
28. Zambito, A. M., and Wolff, J. (1997) Palmitoylation of tubulin. *Biochem. Biophys. Res. Commun.* **239**, 650-654
29. Huang, K., Diener, D. R., and Rosenbaum, J. L. (2009) The ubiquitin conjugation system is involved in the disassembly of cilia and flagella. *J. Cell Biol.* **186**, 601-613
30. Conacci-Sorrell, M., Ngouenet, C., and Eisenman, R. N. (2010) Myc-nick: a cytoplasmic cleavage product of Myc that promotes α -tubulin acetylation and cell differentiation. *Cell* **142**, 480-493
31. Magiera, M. M., and Janke, C. (2014) Post-translational modifications of tubulin. *Curr. Biol.* **24**, R351-R354
32. Erck, C. (2005) A vital role of tubulin-tyrosine-ligase for neuronal organization. *Proc. Natl Acad. Sci. USA* **102**, 7853-7858

33. Janke, C. (2005) Tubulin polyglutamylase enzymes are members of the TTL domain protein family. *Science* **308**, 1758-1762
34. Kalinina, E. (2007) A novel subfamily of mouse cytosolic carboxypeptidases. *FASEB J.* **21**, 836-850
35. Paturle-Lafanechere, L. (1991) Characterization of a major brain tubulin variant which cannot be tyrosinated. *Biochemistry* **30**, 10523-10528
36. Peris, L. (2006) Tubulin tyrosination is a major factor affecting the recruitment of CAP-Gly proteins at microtubule plus ends. *J. Cell Biol.* **174**, 839-849
37. Bieling, P. (2008) CLIP-170 tracks growing microtubule ends by dynamically recognizing composite EB1/tubulin-binding sites. *J. Cell Biol.* **183**, 1223-1233
38. Hammond, J. W. (2010) Posttranslational modifications of tubulin and the polarized transport of Kinesin-1 in neurons. *Mol. Biol. Cell* **21**, 572-583
39. Fourest-Lieuvin, A., Peris, L., Gache, V., Garcia-Saez, I., Juillan-Binard, C., Lantez, V., and Job, D. (2006) Microtubule regulation in mitosis: tubulin phosphorylation by the cyclin-dependent kinase Cdk1. *Molecular Biology of the Cell* **17**, 1041-1050
40. Faruki, S., Geahlen, R. L., and Asai, D. J. (2000) Syk-dependent phosphorylation of microtubules in activated B-lymphocytes. *J. Cell Sci.* **113 (Pt 14)**, 2557-2565
41. Akella, J. S. (2010) MEC-17 is an α -tubulin acetyltransferase. *Nature* **467**, 218-222
42. Shida, T., Cueva, J. G., Xu, Z., Goodman, M. B., and Nachury, M. V. (2010) The major α -tubulin K40 acetyltransferase α TAT1 promotes rapid ciliogenesis and efficient mechanosensation. *Proc. Natl Acad. Sci. USA* **107**, 21517-21522
43. Valenzuela-Fernandez, A., Cabrero, J. R., Serrador, J. M., and Sanchez-Madrid, F. (2008) HDAC6: a key regulator of cytoskeleton, cell migration and cell-cell interactions. *Trends Cell Biol.* **18**, 291-297
44. Eddé, B. (1990) Posttranslational glutamylation of α -tubulin. *Science* **247**, 83-85
45. Rogowski, K. (2009) Evolutionary divergence of enzymatic mechanisms for posttranslational polyglycylation. *Cell* **137**, 1076-1087
46. Wloga, D. (2009) TTL3 is a tubulin glycine ligase that regulates the assembly of cilia. *Dev. Cell* **16**, 867-876
47. Redeker, V. (1994) Polyglycylation of tubulin: a posttranslational modification in axonemal microtubules. *Science* **266**, 1688-1691
48. Audebert, S. (1993) Reversible polyglutamylation of α - and β -tubulin and microtubule dynamics in mouse brain neurons. *Mol. Biol. Cell* **4**, 615-626
49. Pathak, N., Austin, C. A., and Drummond, I. A. (2011) Tubulin tyrosine ligase-like genes *ttl3* and *ttl6* maintain zebrafish cilia structure and motility. *J. Biol. Chem.* **286**, 11685-11695

50. Mukai, M., Ikegami, K., Sugiura, Y., Takeshita, K., Nakagawa, A., and Setou, M. (2009) Recombinant mammalian tubulin polyglutamylase TLL7 performs both initiation and elongation of polyglutamylation on beta-tubulin through a random sequential pathway. *Biochemistry* **48**, 1084-1093
51. Dideberg, O., and Bertrand, J. (1998) Tubulin tyrosine ligase: a shared fold with the glutathione synthetase ADP-forming family. *Trends Biochem. Sci.* **23**, 57-58
52. Fan, C., Moews, P., Walsh, C., and Knox. (1994) Vancomycin resistance: structure of D-alanine:D-alanine ligase at 2.3 Å resolution. *Science* **266**, 439-443
53. Lyons, P. J., Sapio, M. R., and Fricker, L. D. (2013) Zebrafish cytosolic carboxypeptidases 1 and 5 are essential for embryonic development. *J. Biol. Chem.* **288**, 30454-30462
54. Berezniuk, I., Lyons, P. J., Sironi, J. J., Xiao, H., Setou, M., Angeletti, R. H., Ikegami, K., and Fricker, L. D. (2013) Cytosolic carboxypeptidase 5 removes alpha- and gamma-linked glutamates from tubulin. *J. Biol. Chem.* **288**, 30445-30453
55. Berezniuk, I., Vu, H. T., Lyons, P. J., Sironi, J. J., Xiao, H., Burd, B., Setou, M., Angeletti, R. H., Ikegami, K., and Fricker, L. D. (2012) Cytosolic carboxypeptidase 1 is involved in processing alpha- and beta-tubulin. *J. Biol. Chem.* **287**, 6503-6517
56. Das, V., Kanakkanthara, A., Chan, A., and Miller, J. H. Potential role of tubulin tyrosine ligase-like enzymes in tumorigenesis and cancer cell resistance. *Cancer Lett.* **350**, 1-4
57. Kashiwaya, K., Nakagawa, H., Hosokawa, M., Mochizuki, Y., Ueda, K., Piao, L., Chung, S., Hamamoto, R., Eguchi, H., Ohigashi, H., Ishikawa, O., Janke, C., Shinomura, Y., and Nakamura, Y. (2010) Involvement of the tubulin tyrosine ligase-like family member 4 polyglutamylase in PELP1 polyglutamylation and chromatin remodeling in pancreatic cancer cells. *Cancer Res.* **70**, 4024-4033
58. van Dijk, J., Miro, J., Strub, J. M., Lacroix, B., van Dorselaer, A., Edde, B., and Janke, C. (2008) Polyglutamylation is a post-translational modification with a broad range of substrates. *J. Biol. Chem.* **283**, 3915-3922
59. Massoner, P., Lueking, A., Goehler, H., Höpfner, A., Kowald, A., Kugler, K. G., Amersdorfer, P., Horninger, W., Bartsch, G., Schulz-Knappe, P., and Klocker, H. (2012) Serum-autoantibodies for discovery of prostate cancer specific biomarkers. *The Prostate* **72**, 427-436
60. Dráberová, E., Vinopal, S., Morfini, G., Liu, P. S., Sládková, V., Sulimenko, T., Burns, M. R., Solowska, J., Kulandaivel, K., de Chadarévian, J.-P., Legido, A., Mörk, S. J., Janáček, J., Baas, P. W., Dráber, P., and Katsetos, C. D. (2011) Microtubule-Severing ATPase Spastin in Glioblastoma: Increased Expression in Human Glioblastoma Cell Lines and Inverse Roles in Cell Motility and Proliferation. *J. Neuropath. Exp. Neur.* **70**, 811-826
61. Westermann, S., Plessmann, U., and Weber, K. (1999) Synthetic peptides identify the minimal substrate requirements of tubulin polyglutamylase in side chain elongation. *FEBS Lett.* **459**, 90-94

62. Golan, E., Tashjian, A., Armstrong, E., and Armstrong, A. (2011) Pharmacology of Bacterial Infections: Cell Wall Synthesis. in *Principles of Pharmacology: The Pathophysiologic Basis of Drug Therapy*, 3rd Ed., Lippincott Williams & Wilkins. pp
63. Lovering, A. L., Safadi, S. S., and Strynadka, N. C. (2012) Structural perspective of peptidoglycan biosynthesis and assembly. *Annu. Rev. Biochem.* **81**, 451-478
64. El Zoeiby, A., Sanschagrín, F., and Levesque, R. C. (2003) Structure and function of the Mur enzymes: development of novel inhibitors. *Mol. Microbiol.* **47**, 1-12
65. Cooper, G. (2000) Cell Walls, the Extracellular Matrix, and Cell Interactions. in *The Cell: A Molecular Approach*, 2nd Ed., Sinauer Associates, Sunderland (MA): . pp
66. Typas, A., Banzhaf, M., Gross, C. A., and Vollmer, W. (2012) From the regulation of peptidoglycan synthesis to bacterial growth and morphology. *Nat. Rev. Micro.* **10**, 123-136
67. Schönbrunn, E., Sack, S., Eschenburg, S., Perrakis, A., and Krekel, F. (1996) Crystal structure of UDP-N-acetylglucosamine enolpyruvyltransferase, the target of the antibiotic fosfomycin. *Structure* **4**, 1065
68. Skarzynski, T., Mistry, A., Wonacott, A., Hutchinson, S., Kelly, V., and Duncan, K. (1996) Structure of UDP-N-acetylglucosamine enolpyruvyl transferase, an enzyme essential for the synthesis of bacterial peptidoglycan, complexed with substrate UDP-N-acetylglucosamine and the drug fosfomycin. *Structure* **4**, 1465
69. Yoon, H., Lee, S., Mikami, B., Park, H., Yoo, J., and Suh, S. (2008) Crystal structure of UDP-N-acetylglucosamine enolpyruvyl transferase from *Haemophilus influenzae* in complex with UDP-N-acetylglucosamine and fosfomycin. *Proteins* **71**, 1032
70. Benson, T., Filman, D., Walsh, C., and Hogle, J. (1995) An enzyme-substrate complex involved in bacterial cell wall biosynthesis. *Nat. Struct. Biol.* **2**, 644
71. Benson, T., Walsh, C., and Hogle, J. (1996) The structure of the substrate-free form of MurB, an essential enzyme for the synthesis of bacterial cell walls. *Structure* **4**, 47
72. Benson, T., Walsh, C., and Hogle, J. (1997) X-ray crystal structures of the S229A mutant and wild-type MurB in the presence of the substrate enolpyruvyl-UDP-N-acetylglucosamine at 1.8-Å resolution. *Biochemistry* **36**, 806
73. Bouhss, A., Mengin-Lecreux, D., Blanot, D., van Heijenoort, J., and Parquet, C. (1997) Invariant amino acids in the Mur peptide synthetases of bacterial peptidoglycan synthesis and their modification by site-directed mutagenesis in the UDP-MurNAc:L-alanine ligase from *Escherichia coli*. *Biochemistry* **36**, 11556
74. Eveland, S., Pompliano, D., and Anderson, M. (1997) Conditionally lethal *Escherichia coli* murein mutants contain point defects that map to regions conserved among murein and folyl poly-γ-glutamate ligases: identification of a ligase superfamily. *Biochemistry* **36**, 6223

75. Deva, T., Baker, E., Squire, C., and Smith, C. (2006) Structure of Escherichia coli UDP-N-acetylmuramoyl:L-alanine ligase (MurC). *Acta Crystallogr. D* **62**, 1466
76. Gordon, E., Flouret, B., Chantalat, L., van Heijenoort, J., Mengin-Lecreulx, D., and Dideberg, O. (2001) Crystal structure of UDP-N-acetylmuramoyl-L-alanyl-D-glutamate: meso-diaminopimelate ligase from Escherichia coli. *J. Biol. Chem.* **276**, 10999
77. Basavannacharya, C., Robertson, G., Munshi, T., Keep, N., and Bhakta, S. (2010) ATP-dependent MurE ligase in Mycobacterium tuberculosis: biochemical and structural characterisation. *Tuberculosis* **90**, 16
78. Heydanek, M., Struve, W., and Neuhaus, F. (1969) On the initial stage in peptidoglycan synthesis. 3. Kinetics and uncoupling of phospho-N-acetylmuramyl-pentapeptide translocase (uridine 5' -phosphate). *Biochemistry* **8**, 1214
79. van Dam, V., Sijbrandi, R., Kol, M., Swiezewska, E., de Kruijff, B., and Breukink, E. (2007) Transmembrane transport of peptidoglycan precursors across model and bacterial membranes. *Mol. Microbiol.* **64**, 1105
80. Goffin, C., and Ghuysen, J. (1998) Multimodular penicillin-binding proteins: an enigmatic family of orthologs and paralogs. *Microbiol. Mol. Biol. Rev.* **62**, 1079
81. Rogers, T., and Birnbaum, J. (1974) Biosynthesis of fosfomycin by Streptomyces fradiae. *Antimicrob. Agents Chemother.* **5**, 121
82. Kahan, F., Kahan, J., Cassidy, P., and Kropp, H. (1974) The mechanism of action of fosfomycin (phosphonomycin). *Ann. N. Y. Acad. Sci.* **235**, 364
83. Marquardt, J., Brown, E., Lane, W., Haley, T., and Ichikawa, Y. (1994) Kinetics, stoichiometry, and identification of the reactive thiolate in the inactivation of UDP-GlcNAc enolpyruvoyl transferase by the antibiotic fosfomycin. *Biochemistry* **33**, 10646
84. Xie, J., Pierce, J., James, R., Okano, A., and Boger, D. (2011) A redesigned vancomycin engineered for dual D-Ala-D-Ala and D-Ala-D-Lac binding exhibits potent antimicrobial activity against vancomycin-resistant bacteria. *J. Am. Chem. Soc.* **133**, 13946
85. Davis, K. M., and Weiser, J. N. (2011) Modifications to the peptidoglycan backbone help bacteria to establish infection. *Infect. Immun.* **79**, 562-570
86. Ibrahim, H. R., Matsuzaki, T., and Aoki, T. (2001) Genetic evidence that antibacterial activity of lysozyme is independent of its catalytic function. *FEBS Letters* **506**, 27-32
87. Opitz, B., Puschel, A., Schmeck, B., Hocke, A. C., Rosseau, S., Hammerschmidt, S., Schumann, R. R., Suttorp, N., and Hippenstiel, S. (2004) Nucleotide-binding oligomerization domain proteins are innate immune receptors for internalized Streptococcus pneumoniae. *J. Biol. Chem.* **279**, 36426-36432
88. Rosenthal, R. S., Blundell, J. K., and Perkins, H. R. (1982) Strain-related differences in lysozyme sensitivity and extent of O-acetylation of gonococcal peptidoglycan. *Infect. Immun.* **37**, 826-829

89. Montecucco, C., and Rappuoli, R. (2001) Living dangerously: how *Helicobacter pylori* survives in the human stomach. *Nat. Rev. Mol. Cell. Biol.* **2**, 457-466
90. Berg, H. C., and Turner, L. (1979) Movement of microorganisms in viscous environments. *Nature* **278**, 349-351
91. Young, K. D. (2006) The selective value of bacterial shape. *Microbiol. Mol. Biol. Rev.* **70**, 660-703
92. Cabeen, M. T., and Jacobs-Wagner, C. (2007) Skin and bones: the bacterial cytoskeleton, cell wall, and cell morphogenesis. *J. Cell Biol.* **179**, 381-387
93. LK, S., Z, P., KD, G., J, B., and CA, S. (2010) Peptidoglycan crosslinking relaxation promotes *Helicobacter pylori*'s helical shape and stomach colonization. *Cell* **141**, 822
94. Sycuro, L. K., Rule, C. S., Petersen, T. W., Wyckoff, T. J., Sessler, T., Nagarkar, D. B., Khalid, F., Pincus, Z., Biboy, J., Vollmer, W., and Salama, N. R. (2013) Flow cytometry-based enrichment for cell shape mutants identifies multiple genes that influence *Helicobacter pylori* morphology. *Mol. Microbiol.* **90**, 869-883
95. Sycuro, L. K., Wyckoff, T. J., Biboy, J., Born, P., Pincus, Z., Vollmer, W., and Salama, N. R. (2012) Multiple Peptidoglycan Modification Networks Modulate *Helicobacter pylori*'s Cell Shape, Motility, and Colonization Potential. *PLoS Pathog.* **8**
96. Lipscomb, W. N., and Sträter, N. (1996) Recent Advances in Zinc Enzymology. *Chem. Rev.* **96**, 2375-2434
97. Dive, V., Georgiadis, D., Matziari, M., Makaritis, A., Beau, F., Cuniasse, P., and Yiotakis, A. (2004) Phosphinic peptides as zinc metalloproteinase inhibitors. *Cell. Mol. Life Sci.* **61**, 2010-2019
98. Ellsworth, B. A., Tom, N. J., and Bartlett, P. A. (1996) Synthesis and evaluation of inhibitors of bacterial d-alanine: d-alanine ligases. *Chem. Biol.* **3**, 37-44
99. Jiracek, J., Yiotakis, A., Vincent, B., Lecoq, A., Nicolaou, A., Checler, F., and Dive, V. (1995) Development of highly potent and selective phosphinic peptide inhibitors of zinc endopeptidase 24-15 using combinatorial chemistry. *J. Biol. Chem.* **270**, 21701-21706
100. Gegnas, L. D., Waddell, S. T., Chabin, R. M., Reddy, S., and Wong, K. K. (1998) Inhibitors of the bacterial cell wall biosynthesis enzyme Mur D. *Bioorg. Med. Chem. Lett.* **8**, 1643-1648
101. Štrancar, K., Blanot, D., and Gobec, S. (2006) Design, synthesis and structure–activity relationships of new phosphinate inhibitors of MurD. *Bioorg. Med. Chem. Lett* **16**, 343-348
102. Grams, F., Dive, V., Yiotakis, A., Yiallourous, I., Vassiliou, S., Zwilling, R., Bode, W., and Stocker, W. (1996) Structure of astacin with a transition-state analogue inhibitor. *Nat. Struct. Mol. Biol.* **3**, 671-675

103. Bianchini, G., Aschi, M., Cavicchio, G., Crucianelli, M., Prezioso, S., Gallina, C., Nastari, A., Gavuzzo, E., and Mazza, F. (2005) Design, modelling, synthesis and biological evaluation of peptidomimetic phosphinates as inhibitors of matrix metalloproteinases MMP-2 and MMP-8. *Bioorg. Med. Chem.* **13**, 4740-4749
104. Amour, A., Hutton, M., Knauper, V., Slocombe, P. M., Webster, A., Butler, M., Knight, C. G., Smith, B. J., Docherty, A. J., and Murphy, G. (1999) Inhibition of the metalloproteinase domain of mouse TACE. *Annals of the New York Academy of Sciences* **878**, 728-731
105. Fisher, J., and Mobashery, S. (2006) Recent advances in MMP inhibitor design. *Cancer Metast. Rev.* **25**, 115-136
106. Cámara-Artigas, A., Jara-Pérez, V., and Andújar-Sánchez, M. (2009) Angiotensin Converting Enzyme (ACE) Inhibitors. in *Drug Design of Zinc-Enzyme Inhibitors*, John Wiley & Sons, Inc. pp 749-787
107. Georgiadis, D., Beau, F., Czarny, B., Cotton, J., Yiotakis, A., and Dive, V. (2003) Roles of the Two Active Sites of Somatic Angiotensin-Converting Enzyme in the Cleavage of Angiotensin I and Bradykinin: Insights From Selective Inhibitors. *Circulation Research* **93**, 148-154
108. Dive, V., Cotton, J., Yiotakis, A., Michaud, A., Vassiliou, S., Jiracek, J., Vazeux, G., Chauvet, M.-T., Cuniasse, P., and Corvol, P. (1999) RXP 407, a phosphinic peptide, is a potent inhibitor of angiotensin I converting enzyme able to differentiate between its two active sites. *Proc. Natl. Acad. Sci. USA* **96**, 4330-4335
109. Ikegami, K., Heier, R. L., Taruishi, M., Takagi, H., Mukai, M., Shimma, S., Taira, S., Hatanaka, K., Morone, N., Yao, I., Campbell, P. K., Yuasa, S., Janke, C., Macgregor, G. R., and Setou, M. (2007) Loss of alpha-tubulin polyglutamylation in ROSA22 mice is associated with abnormal targeting of KIF1A and modulated synaptic function. *Proc. Natl. Acad. Sci. USA* **104**, 3213-3218
110. Ikegami, K., Mukai, M., Tsuchida, J., Heier, R. L., Macgregor, G. R., and Setou, M. (2006) TLL7 is a mammalian beta-tubulin polyglutamylase required for growth of MAP2-positive neurites. *J. Biol. Chem.* **281**, 30707-30716
111. van Dijk, J., Rogowski, K., Miro, J., Lacroix, B., Eddé, B., and Janke, C. (2007) A Targeted Multienzyme Mechanism for Selective Microtubule Polyglutamylation. *Mol. Cell* **26**, 437-448
112. Westermann, S., Schneider, A., Horn, E. K., and Weber, K. (1999) Isolation of tubulin polyglutamylase from Crithidia; binding to microtubules and tubulin, and glutamylation of mammalian brain alpha- and beta-tubulins. *J. Cell Sci.* **112 (Pt 13)**, 2185-2193
113. Cleland, W. W. (1963) The kinetics of enzyme-catalyzed reactions with two or more substrates or products. I. Nomenclature and rate equations. *Biochim. Biophys. Acta* **67**, 104-137
114. Valiaeva, N., Bartley, D., Konno, T., and Coward, J. K. (2001) Phosphinic Acid Pseudopeptides Analogous to Glutamyl- γ -glutamate: Synthesis and Coupling to Pteroyl

- Azides Leads to Potent Inhibitors of Folylpoly- γ -glutamate Synthetase†. *J. Org. Chem.* **66**, 5146-5154
115. Barinka, C., Hlouchova, K., Rovenska, M., Majer, P., Dauter, M., Hin, N., Ko, Y.-S., Tsukamoto, T., Slusher, B. S., Konvalinka, J., and Lubkowski, J. (2008) Structural Basis of Interactions between Human Glutamate Carboxypeptidase II and Its Substrate Analogs. *J. Mol. Biol.* **376**, 1438-1450
 116. Suzuki, K., Muto, Y., Fushihara, K., Kanemoto, K., Iida, H., Sato, E., Kikuchi, C., Matsushima, T., Kato, E., Nomoto, M., Yoshioka, S., and Ishii, H. (2004) Enhancement of fibrinolysis by EF6265 [(S)-7-amino-2-[[[(R)-2-methyl-1-(3-phenylpropanoylamino)propyl]hydroxyphosphinoyl]methyl]heptanoic acid], a specific inhibitor of plasma carboxypeptidase B. *J. Pharmacol. Exp. Ther.* **309**, 607-615
 117. Hiratake, J., Kato, H., and Oda, J. i. (1994) Mechanism-Based Inactivation of Glutathione Synthetase by Phosphinic Acid Transition-State Analog. *J. Am. Chem. Soc.* **116**, 12059-12060
 118. Abell, L. M., and Villafranca, J. J. (1991) Investigation of the mechanism of phosphinothricin inactivation of Escherichia coli glutamine synthetase using rapid quench kinetic techniques. *Biochemistry* **30**, 6135-6141
 119. Duncan, K., and Walsh, C. T. (1988) ATP-dependent inactivation and slow binding inhibition of salmonella typhimurium D-alanine: D-alanine ligase (ADP) by aminoalkylphosphinate and aminophosphonate analogs of D-alanine. *Biochemistry* **27**, 3709-3714
 120. Feng, Y., and Coward, J. K. (2005) Prodrug Forms of N-[(4-Deoxy-4-amino-10-methyl)pteroyl]glutamate- γ -[ψ P(O)(OH)]-glutarate, a Potent Inhibitor of Folylpoly- γ -glutamate Synthetase: Synthesis and Hydrolytic Stability. *J. Med. Chem.* **49**, 770-788
 121. Liu, S., and Ben, R. N. (2005) C-Linked Galactosyl Serine AFGP Analogues as Potent Recrystallization Inhibitors. *Org. Lett.* **7**, 2385-2388
 122. Thottathil, J. K., Ryono, D. E., Przybyla, C. A., Moniot, J. L., and Neubeck, R. (1984) Preparation of phosphinic acids: Michael additions of phosphonous acids/esters to conjugated systems. *Tetrahedron Lett.* **25**, 4741-4744
 123. Georgiadis, D., Matziari, M., Vassiliou, S., Dive, V., and Yiotakis, A. (1999) A convenient method to synthesize phosphinic peptides containing an aspartyl or glutamyl aminophosphinic acid. Use of the phenyl group as the carboxyl synthon. *Tetrahedron* **55**, 14635-14648
 124. Szyk, A., Deaconescu, A. M., Piszczek, G., and Roll-Mecak, A. (2011) Tubulin tyrosine ligase structure reveals adaptation of an ancient fold to bind and modify tubulin. *Nat. Struct. Mol. Biol.* **18**, 1250-1258
 125. Redeker, V., Le Caer, J. P., Rossier, J., and Prome, J. C. (1991) Structure of the polyglutamyl side chain posttranslationally added to alpha-tubulin. *J. Biol. Chem.* **266**, 23461-23466

126. Redeker, V., Rusconi, F., Mary, J., Promé, D., and Rossier, J. (1996) Structure of the C-Terminal Tail of α -Tubulin: Increase of Heterogeneity from Newborn to Adult. *J. Neurochem.* **67**, 2104-2114
127. Rüdiger, M., Wehland, J., and Weber, K. (1994) The carboxy-terminal peptide of deetyrosinated α tubulin provides a minimal system to study the substrate specificity of tubulin–tyrosine ligase. *Eur. J. Biochem.* **220**, 309-320
128. Tanner, M. E., Vaganay, S., van Heijenoort, J., and Blanot, D. (1996) Phosphinate Inhibitors of the d-Glutamic Acid-Adding Enzyme of Peptidoglycan Biosynthesis. *J. Org. Chem.* **61**, 1756-1760
129. Yiotakis, A., Vassiliou, S., Jiráček, J., and Dive, V. (1996) Protection of the Hydroxyphosphinyl Function of Phosphinic Dipeptides by Adamantyl. Application to the Solid-Phase Synthesis of Phosphinic Peptides. *J. Org. Chem.* **61**, 6601-6605
130. Kusters, J. G., van Vliet, A. H., and Kuipers, E. J. (2006) Pathogenesis of Helicobacter pylori infection. *Clin. Microbiol. Rev.* **19**, 449-490
131. Krishnamurthy, P., Parlow, M. H., Schneider, J., Burroughs, S., Wickland, C., Vakil, N. B., Dunn, B. E., and Phadnis, S. H. (1999) Identification of a novel penicillin-binding protein from Helicobacter pylori. *J. Bacteriol.* **181**, 5107-5110
132. Makarova, K. S., and Grishin, N. V. (1999) The Zn-peptidase superfamily: functional convergence after evolutionary divergence. *J. Mol. Biol.* **292**, 11-17
133. Hourdou, M. L., Guinand, M., Vacheron, M. J., Michel, G., Denoroy, L., Duez, C., Englebort, S., Joris, B., Weber, G., and Ghuyssen, J. M. (1993) Characterization of the sporulation-related gamma-D-glutamyl-(L)meso-diaminopimelic-acid-hydrolysing peptidase I of Bacillus sphaericus NCTC 9602 as a member of the metallo(zinc) carboxypeptidase A family. Modular design of the protein. *Biochem. J.* **292 (Pt 2)**, 563-570
134. Kelley, L. A., and Sternberg, M. J. (2009) Protein structure prediction on the Web: a case study using the Phyre server. *Nat. Protoc.* **4**, 363-371
135. Sycuro, L. K., Pincus, Z., Gutierrez, K. D., Biboy, J., Stern, C. A., Vollmer, W., and Salama, N. R. (2010) Relaxation of peptidoglycan cross-linking promotes Helicobacter pylori's helical shape and stomach colonization. *Cell* **141**, 822-833
136. Frirdich, E., Biboy, J., Adams, C., Lee, J., Ellermeier, J., Giolda, L. D., Dirita, V. J., Girardin, S. E., Vollmer, W., and Gaynor, E. C. (2012) Peptidoglycan-modifying enzyme Pgp1 is required for helical cell shape and pathogenicity traits in Campylobacter jejuni. *PLoS Pathogens* **8**, e1002602
137. Montalbetti, C. A. G. N., and Falque, V. (2005) Amide bond formation and peptide coupling. *Tetrahedron* **61**, 10827-10852
138. Agnihotri, G., Ukani, R., Malladi, S. S., Warshakoon, H. J., Balakrishna, R., Wang, X., and David, S. A. (2011) Structure–Activity Relationships in Nucleotide Oligomerization

- Domain 1 (Nod1) Agonistic γ -Glutamyl-diaminopimelic Acid Derivatives. *J. Med. Chem.* **54**, 1490-1510
139. Gomis-Ruth, F. X. (2008) Structure and mechanism of metallo-carboxypeptidases. *Crit. Rev. Biochem. Mol. Biol.* **43**, 319-345
140. Kaplan, A. P., and Bartlett, P. A. (1991) Synthesis and evaluation of an inhibitor of carboxypeptidase A with a K_i value in the femtomolar range. *Biochemistry* **30**, 8165-8170
141. Hanson, J. E., Kaplan, A. P., and Bartlett, P. A. (1989) Phosphonate analogs of carboxypeptidase A substrates are potent transition-state analog inhibitors. *Biochemistry* **28**, 6294-6305
142. Bartlett, P. A., and Marlowe, C. K. (1983) Phosphoramidates as transition-state analog inhibitors of thermolysin. *Biochemistry* **22**, 4618-4624
143. Hin, B., Majer, P., and Tsukamoto, T. (2002) Facile Synthesis of α -Substituted Acrylate Esters. *J. Org. Chem.* **67**, 7365-7368
144. Singh, V., Evans, G. B., Lenz, D. H., Mason, J. M., Clinch, K., Mee, S., Painter, G. F., Tyler, P. C., Furneaux, R. H., Lee, J. E., Howell, P. L., and Schramm, V. L. (2005) Femtomolar transition state analogue inhibitors of 5'-methylthioadenosine/S-adenosylhomocysteine nucleosidase from *Escherichia coli*. *J. Biol. Chem.* **280**, 18265-18273
145. Bacon, D. J., Szymanski, C. M., Burr, D. H., Silver, R. P., Alm, R. A., and Guerry, P. (2001) A phase-variable capsule is involved in virulence of *Campylobacter jejuni* 81-176. *Mol. Microbiol.* **40**, 769-777
146. Bartlett, P., and Marlowe, C. (1987) Evaluation of intrinsic binding energy from a hydrogen bonding group in an enzyme inhibitor. *Science* **235**, 569-571
147. Karanewsky, D. S., Badia, M. C., Cushman, D. W., DeForrest, J. M., Dejneka, T., Loots, M. J., Perri, M. G., Petrillo, E. W., and Powell, J. R. (1988) (Phosphinyloxy)acyl amino acid inhibitors of angiotensin converting enzyme (ACE). 1. Discovery of (S)-1-[6-amino-2-[[hydroxy(4-phenylbutyl)phosphinyl]oxy]-1-oxohexyl]-L-proline, a novel orally active inhibitor of ACE. *J. Med. Chem.* **31**, 204-212
148. Kaplan, A. P., and Bartlett, P. A. (1991) Synthesis and evaluation of an inhibitor of carboxypeptidase A with a K_i value in the femtomolar range. *Biochemistry* **30**, 8165-8170
149. Milewski, S., Hoffmann, M., Andruszkiewicz, R., and Borowski, E. (1997) Investigation of Mechanism of Nitrogen Transfer in Glucosamine 6-Phosphate Synthase with the Use of Transition State Analogs. *Bioorg. Chem.* **25**, 283-296
150. Gao, Y., Lane-Bell, P., and Vederas, J. C. (1998) Stereoselective Synthesis of meso-2,6-Diaminopimelic Acid and Its Selectively Protected Derivatives. *J. Org. Chem.* **63**, 2133-2143

151. Malachowski, W. P., and Coward, J. K. (1994) The Chemistry of Phosphopeptides: Investigations on the Synthesis of Phosphoramidate, Phosphonate, and Phosphinate Analogs of Glutamyl- γ -glutamate. *J. Org. Chem.* **59**, 7625-7634
152. Gasteiger, E., Hoogland, C., Gattiker, A., Duvaud, S., Wilkins, M. R., Appel, R. D., and Bairoch, A. (2005) Protein identification and analysis tools in the ExPASy server. in *The Proteomics Protocols Handbook* (Walker, J. M. ed.), 1999/02/23 Ed., Humana Press. pp 571-607
153. Hor, L., Peverelli, M. G., Perugini, M. A., and Hutton, C. A. (2013) A new robust kinetic assay for DAP epimerase activity. *Biochimie* **95**, 1949-1953
154. Otwinowski, Z., and Minor, W. (1997) Processing of X-ray Diffraction Data Collected in Oscillation Mode. in *Methods Enzymol.* (Carter, C. W. J., and Sweet, R. M. eds.), Academic Press (N.Y.). pp 301-326
155. Sheldrick, G. M. (2010) Experimental phasing with SHELXC/D/E: combining chain tracing with density modification. *Acta Crystallogr D Biol Crystallogr* **66**, 479-485
156. Perrakis, A., Morris, R., and Lamzin, V. S. (1999) Automated protein model building combined with iterative structure refinement. *Nat. Struct. Biol.* **6**, 458-463
157. Emsley, P., Lohkamp, B., Scott, W. G., and Cowtan, K. (2010) Features and development of Coot. *Acta crystallographica. Section D, Biological crystallography* **66**, 486-501
158. Kabsch, W. (2010) XDS. *Acta Crystallogr. D Biol. Crystallogr.* **66**, 125-132
159. Adams, P. D., Afonine, P. V., Bunkoczi, G., Chen, V. B., Davis, I. W., Echols, N., Headd, J. J., Hung, L. W., Kapral, G. J., Grosse-Kunstleve, R. W., McCoy, A. J., Moriarty, N. W., Oeffner, R., Read, R. J., Richardson, D. C., Richardson, J. S., Terwilliger, T. C., and Zwart, P. H. (2010) PHENIX: a comprehensive Python-based system for macromolecular structure solution. *Acta Crystallogr. D Biol. Crystallogr.* **66**, 213-221
160. Sievers, F., Wilm, A., Dineen, D., Gibson, T. J., Karplus, K., Li, W., Lopez, R., McWilliam, H., Remmert, M., Soding, J., Thompson, J. D., and Higgins, D. G. (2011) Fast, scalable generation of high-quality protein multiple sequence alignments using Clustal Omega. *Mol. Syst. Biol.* **7**, 539
161. Guindon, S., Dufayard, J. F., Lefort, V., Anisimova, M., Hordijk, W., and Gascuel, O. (2010) New algorithms and methods to estimate maximum-likelihood phylogenies: assessing the performance of PhyML 3.0. *Syst. Biol.* **59**, 307-321
162. Gouy, M., Guindon, S., and Gascuel, O. (2010) SeaView version 4: A multiplatform graphical user interface for sequence alignment and phylogenetic tree building. *Mol. Biol. Evol.* **27**, 221-224
163. Ashkenazy, H., Erez, E., Martz, E., Pupko, T., and Ben-Tal, N. (2010) ConSurf 2010: calculating evolutionary conservation in sequence and structure of proteins and nucleic acids. *Nucleic Acids Res.* **38**, W529-533

164. Lacayo, C. I., Pincus, Z., VanDuijn, M. M., Wilson, C. A., Fletcher, D. A., Gertler, F. B., Mogilner, A., and Theriot, J. A. (2007) Emergence of large-scale cell morphology and movement from local actin filament growth dynamics. *PLoS Biol.* **5**, e233
165. Pincus, Z., and Theriot, J. A. (2007) Comparison of quantitative methods for cell-shape analysis. *J. Microsc.* **227**, 140-156

Appendix

NMR Spectra of Selected Compounds

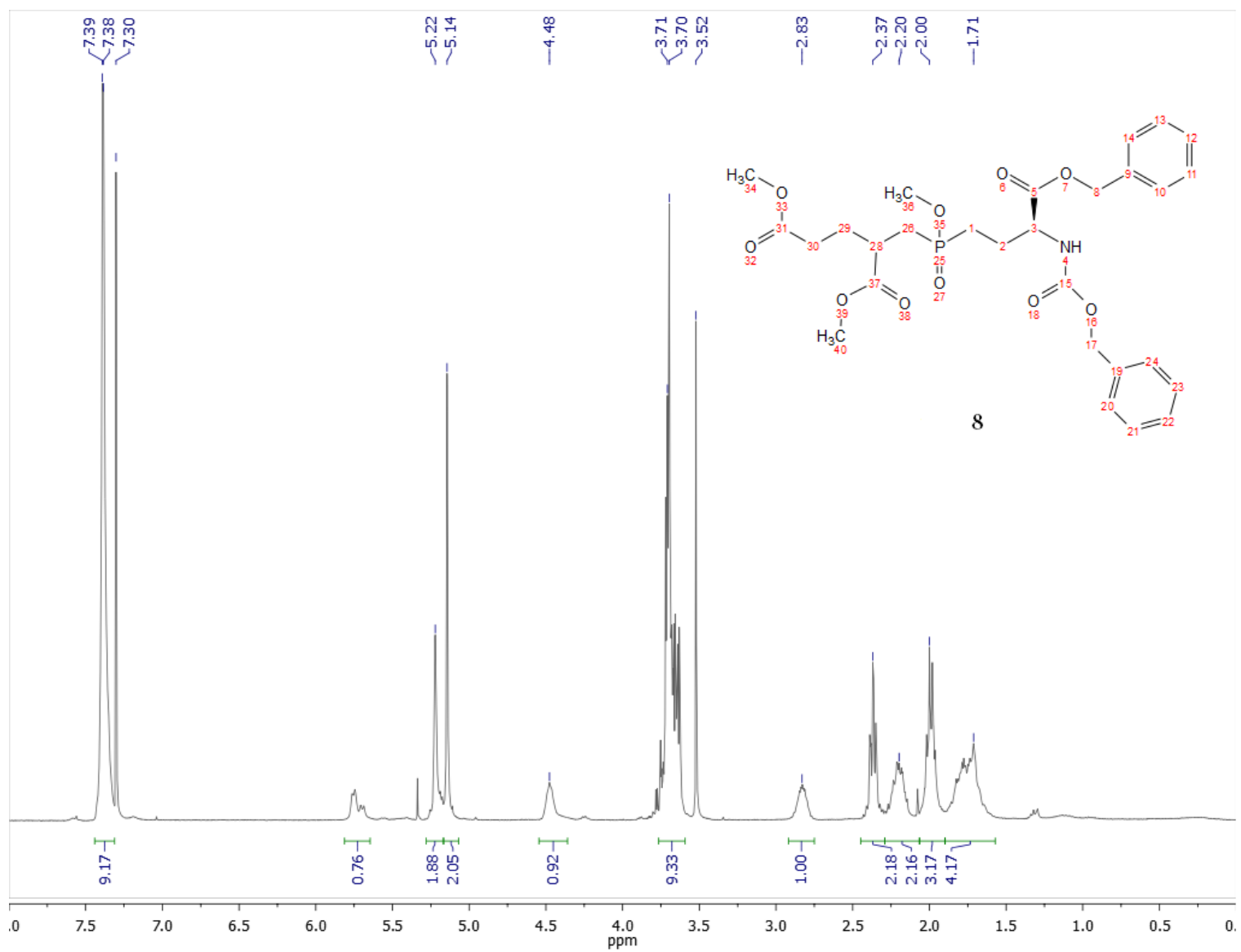


Figure A. 1. ^1H NMR (400 MHz, CDCl_3) spectrum of compound **8**.

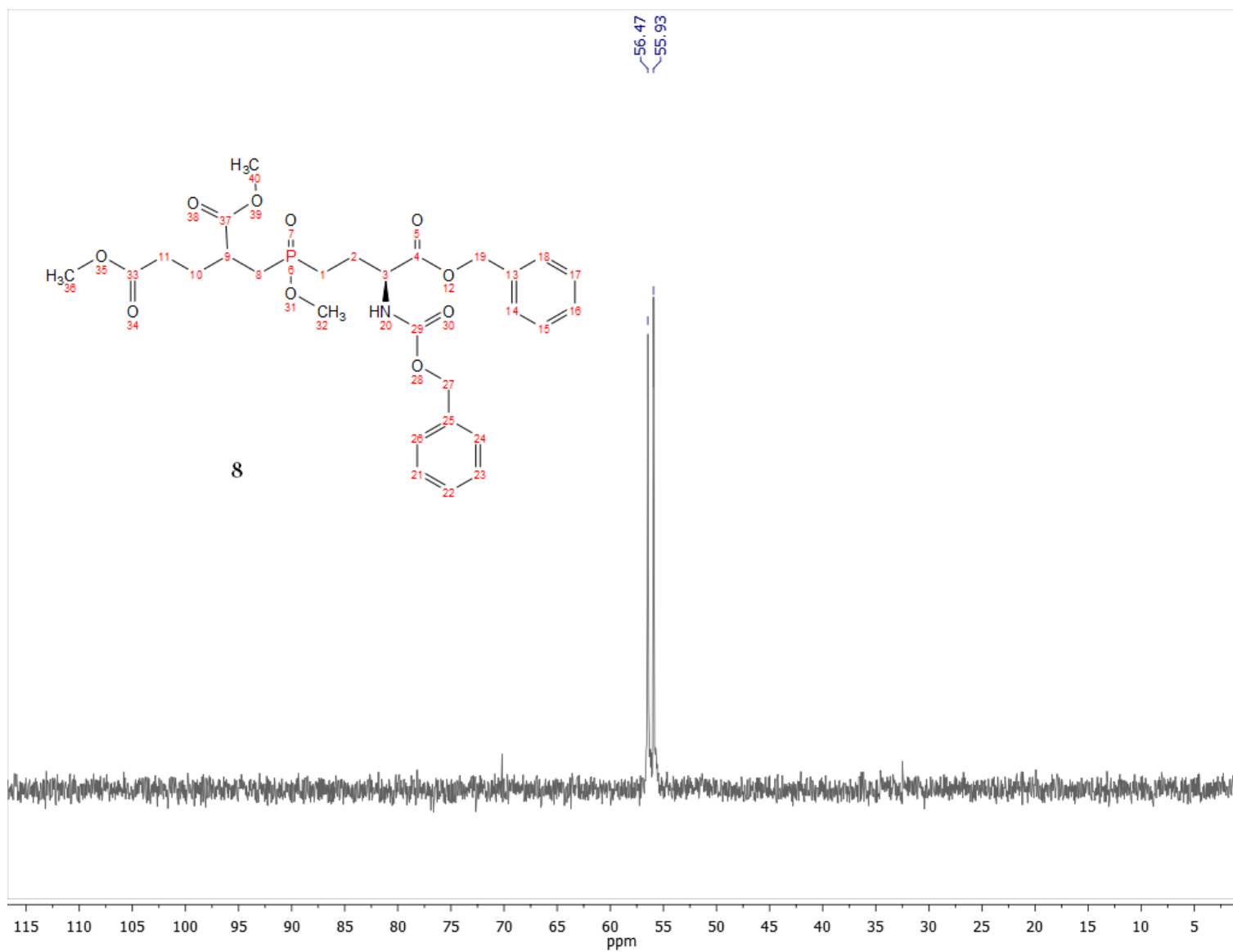


Figure A. 2. ^{31}P (1H) NMR (400 MHz, CDCl_3) spectrum of compound **8**.

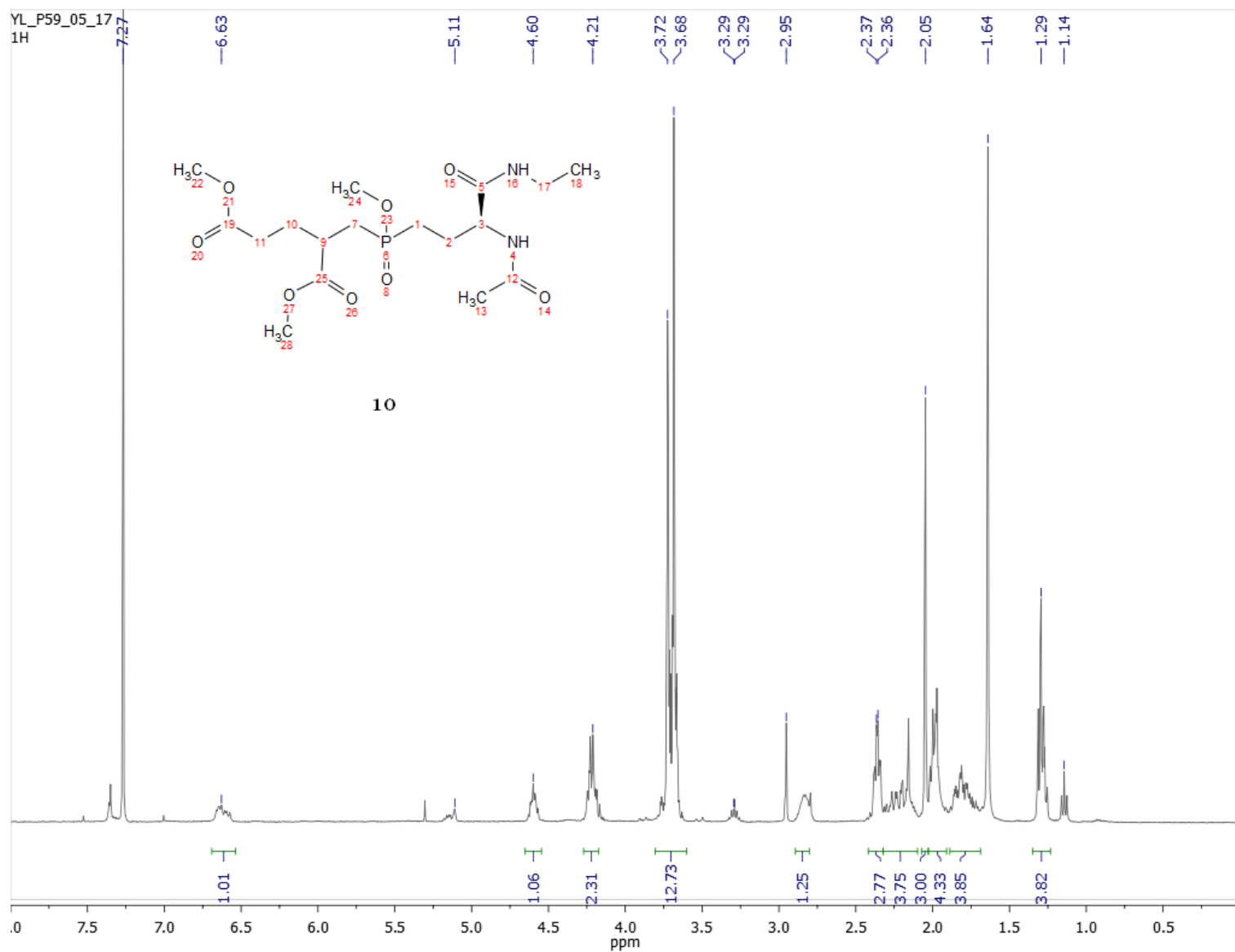


Figure A. 3. ¹H NMR (400 MHz, CDCl₃) spectrum of compound **10**.

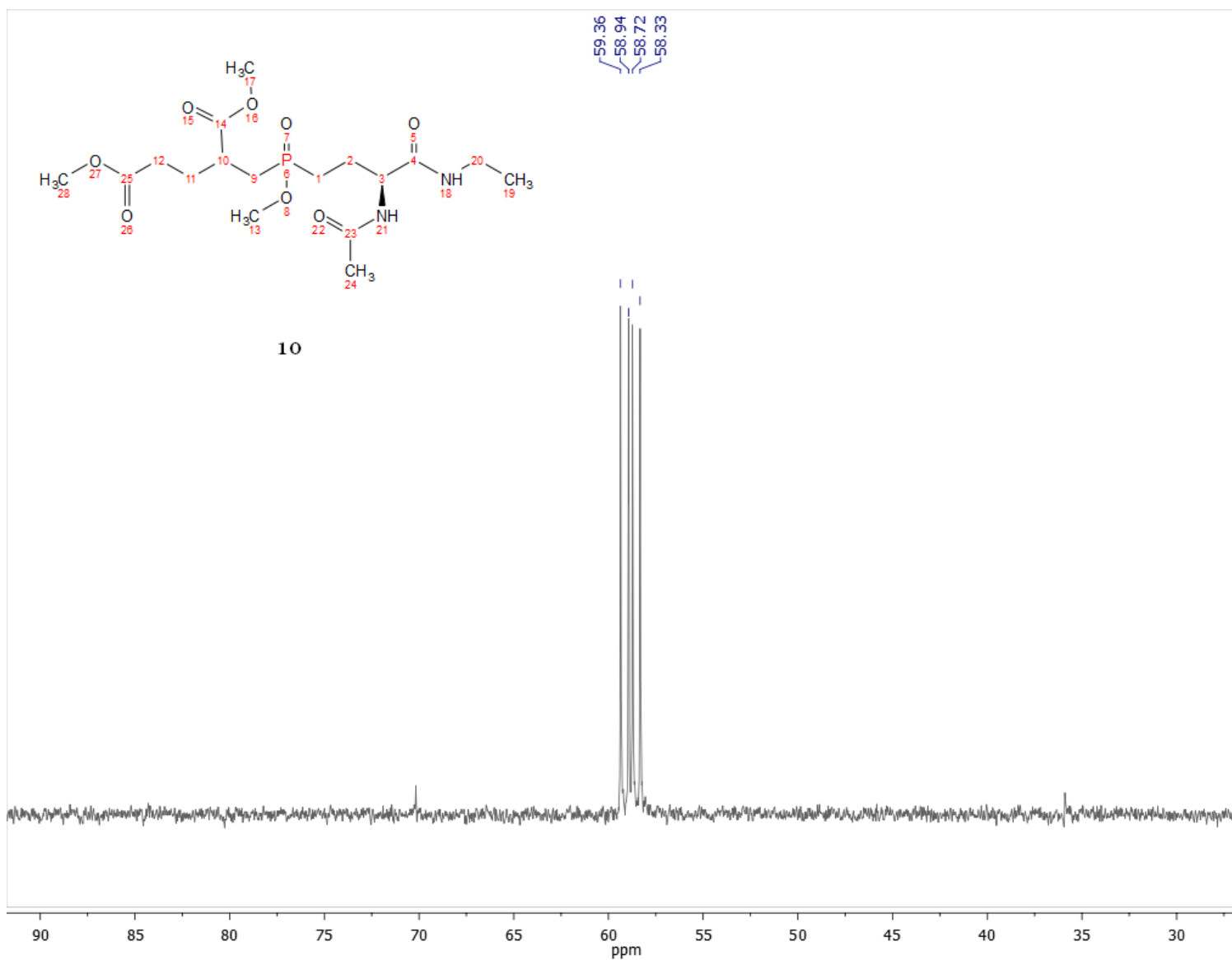


Figure A. 4. ^{31}P (1H) NMR (400 MHz, CDCl_3) spectrum of compound **10**.

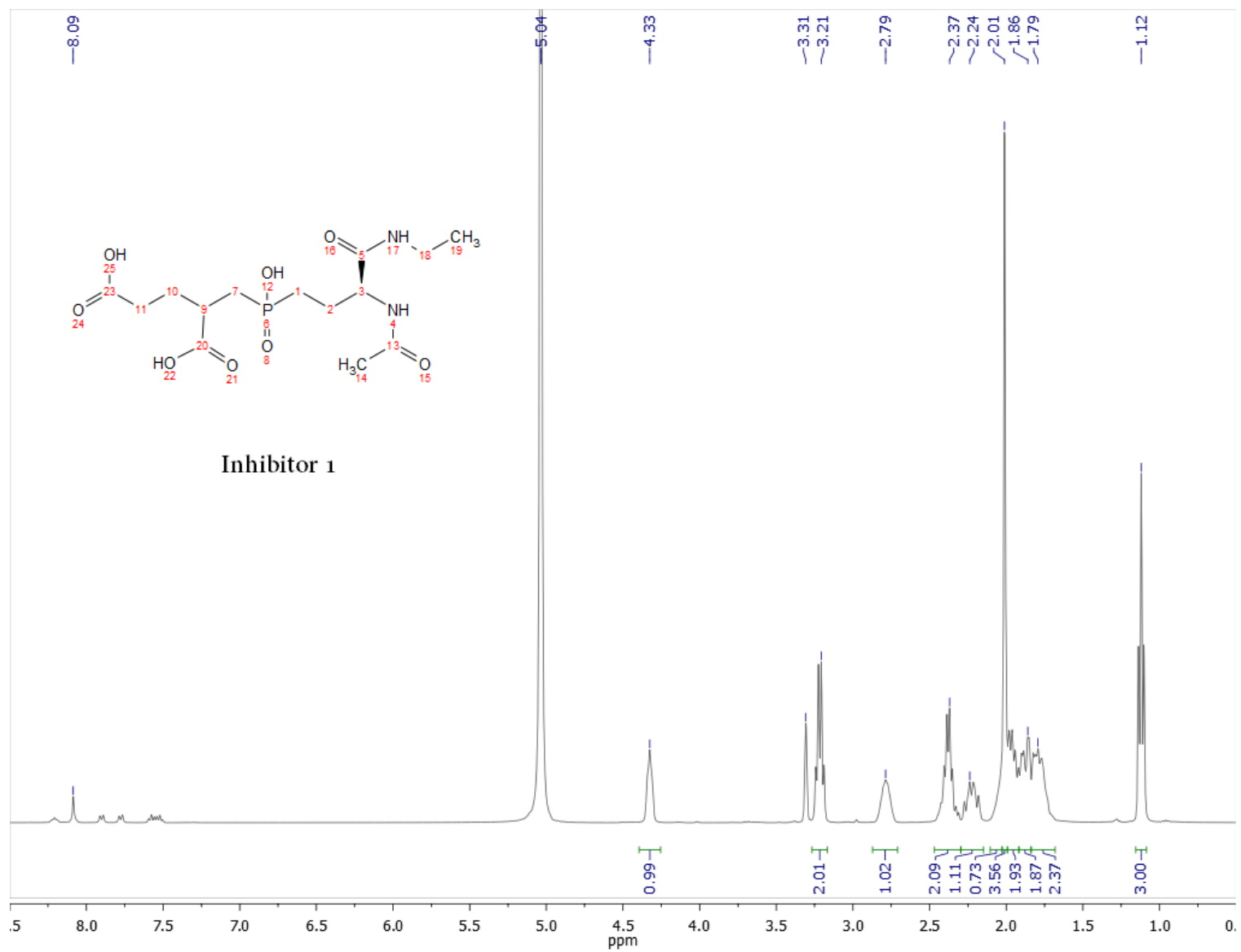


Figure A. 5. ¹H NMR (400 MHz, MeOH) spectrum of inhibitor 1.

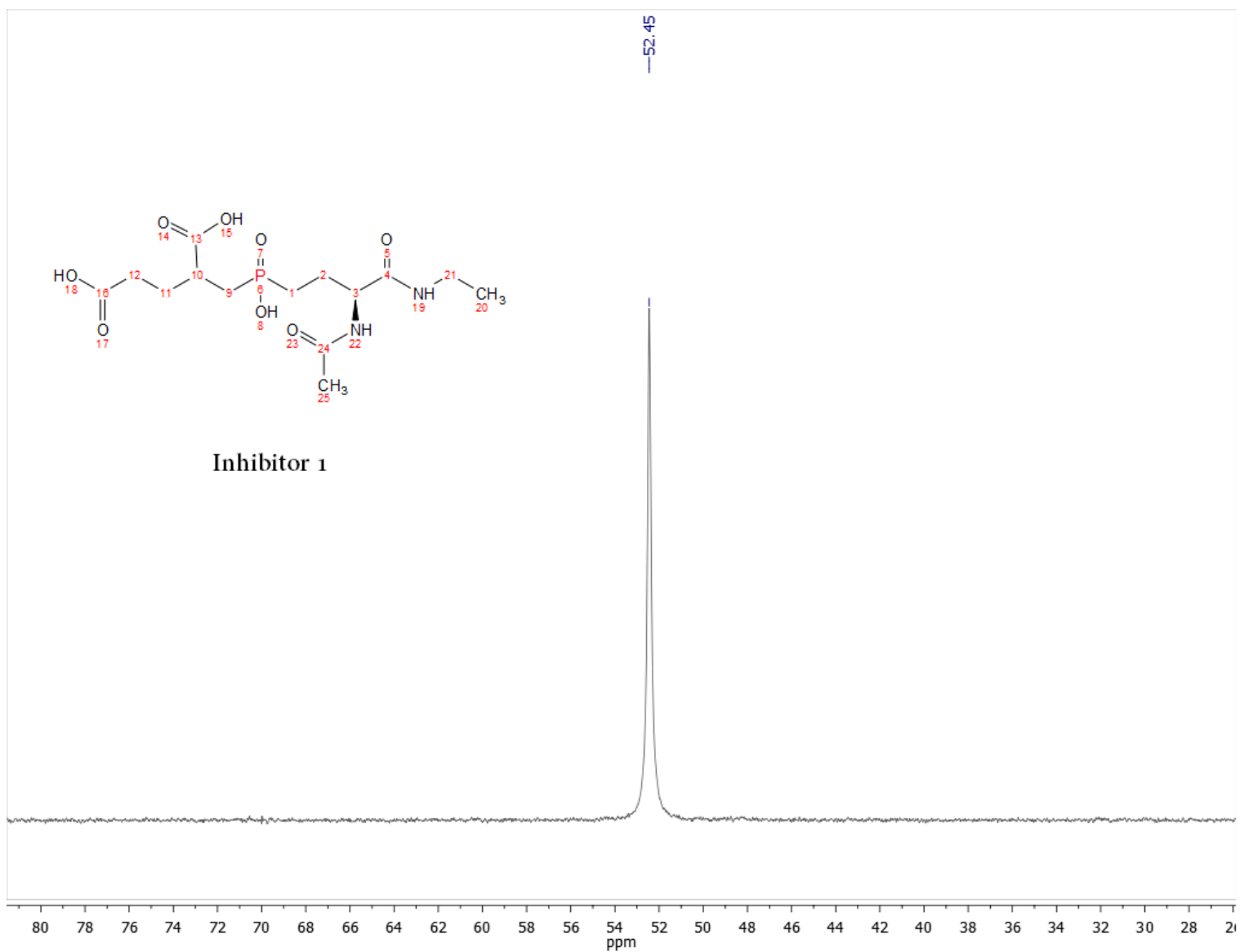


Figure A. 6. ^{31}P (1H) NMR (400 MHz, MeOH) spectrum of inhibitor 1.

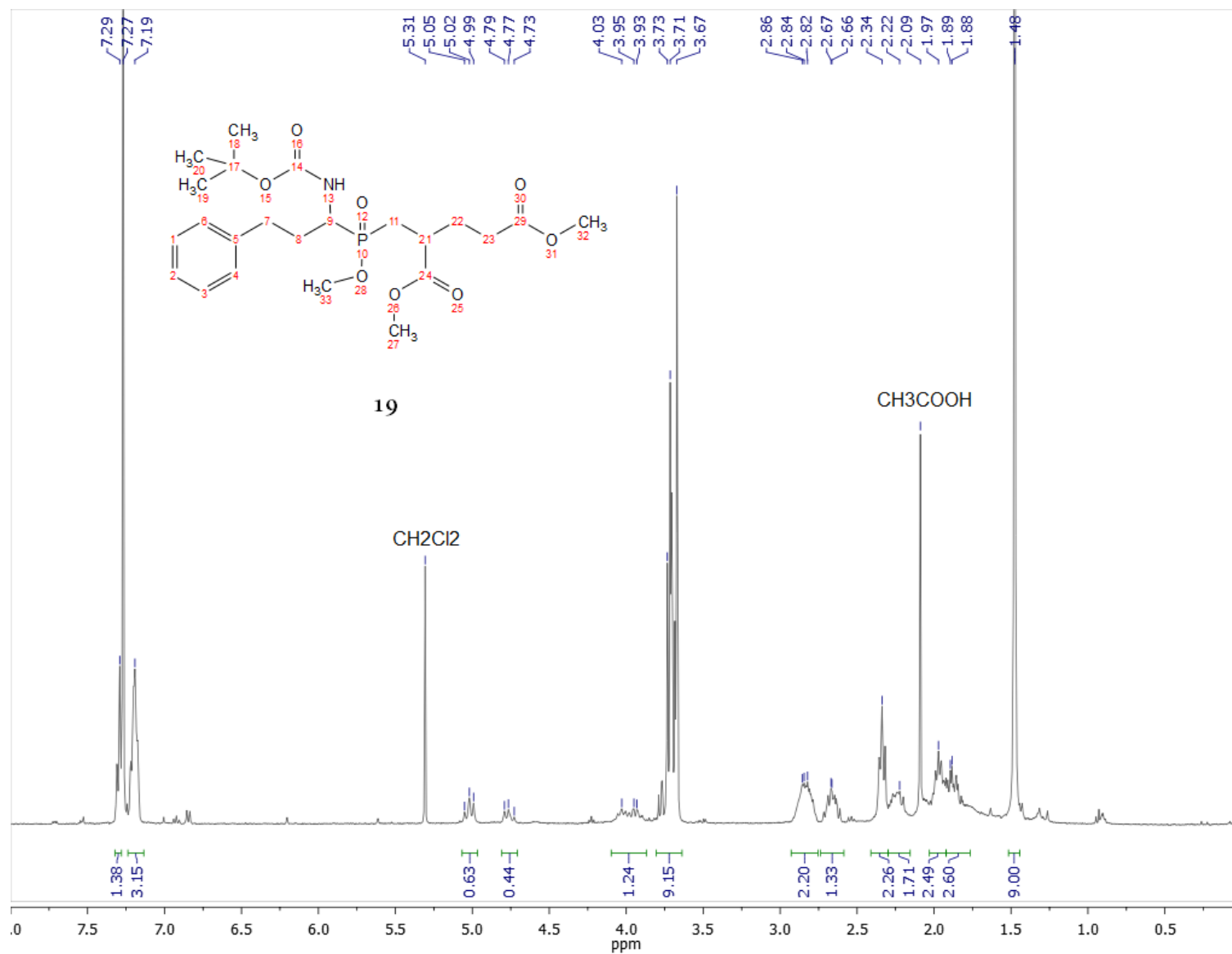


Figure A. 7. ^1H NMR (400 MHz, CDCl_3) spectrum of compound 19.

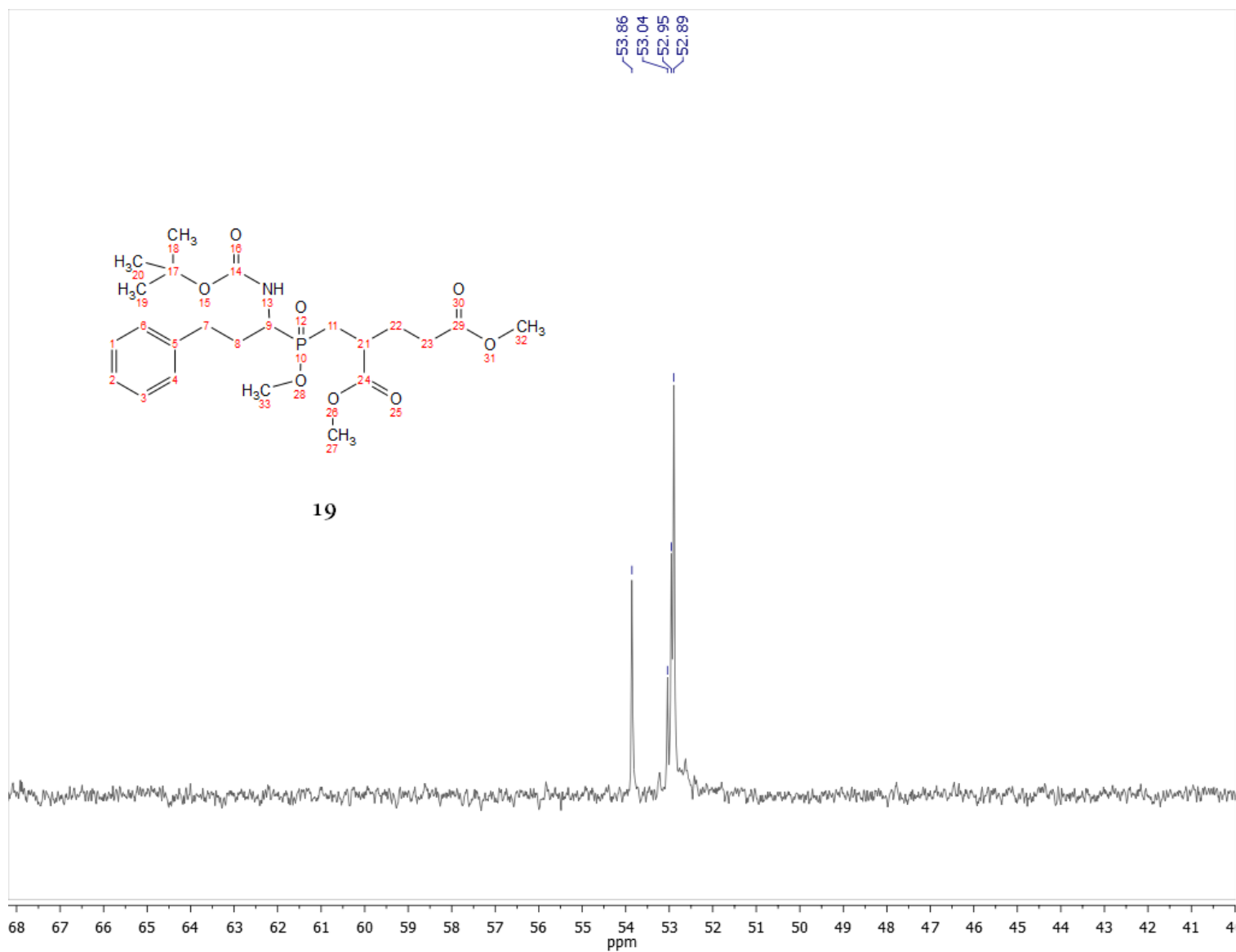


Figure A. 8. ^{31}P (1H) NMR (400 MHz, CDCl_3) spectrum of compound **19**.

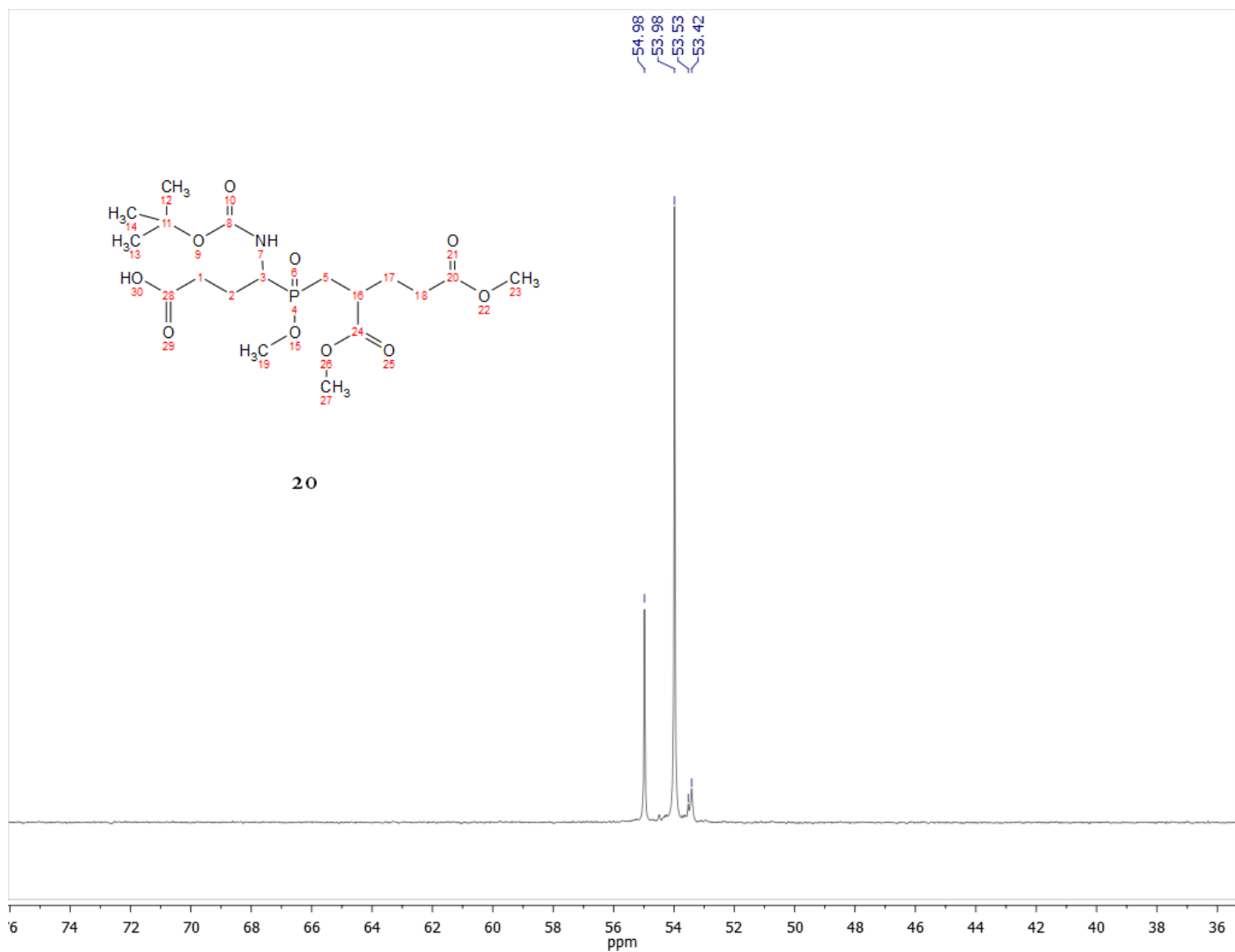


Figure A. 10. ^{31}P (1H) NMR (400 MHz, CDCl_3) spectrum of compound **20**.

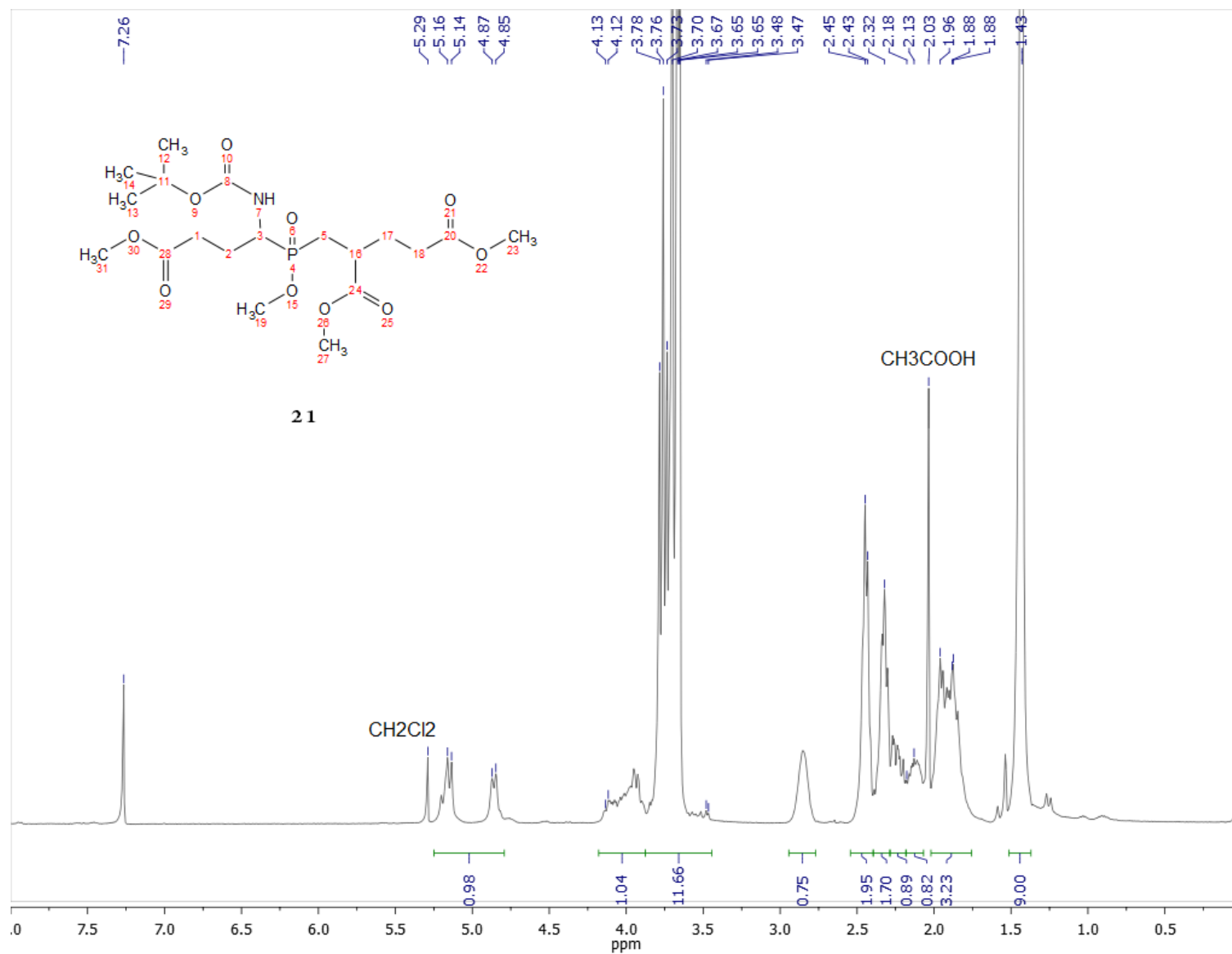


Figure A. 11. ^1H NMR (400 MHz, CDCl_3) spectrum of compound **21**.

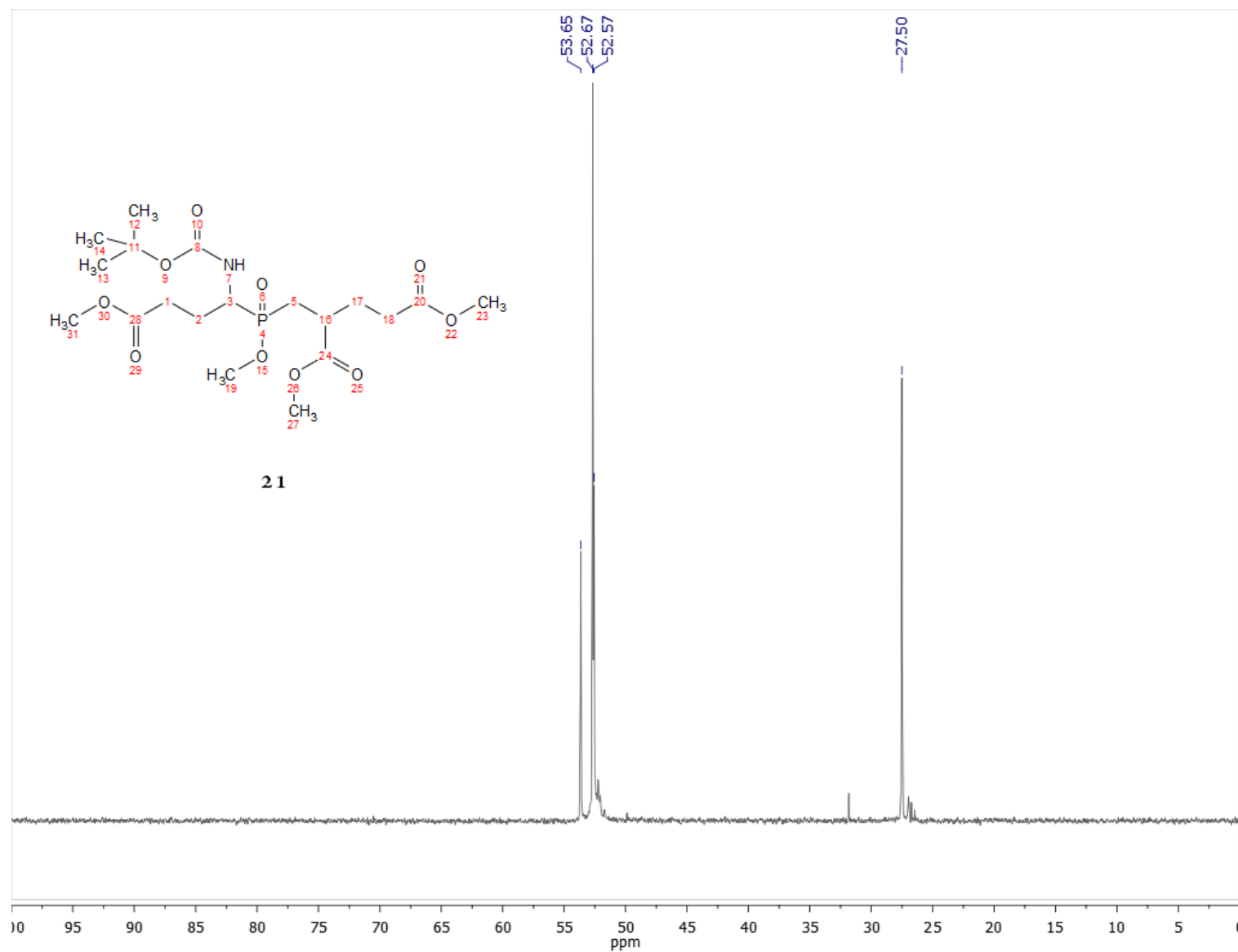


Figure A. 12. ^{31}P (1H) NMR (400 MHz, CDCl_3) spectrum of compound **21**.

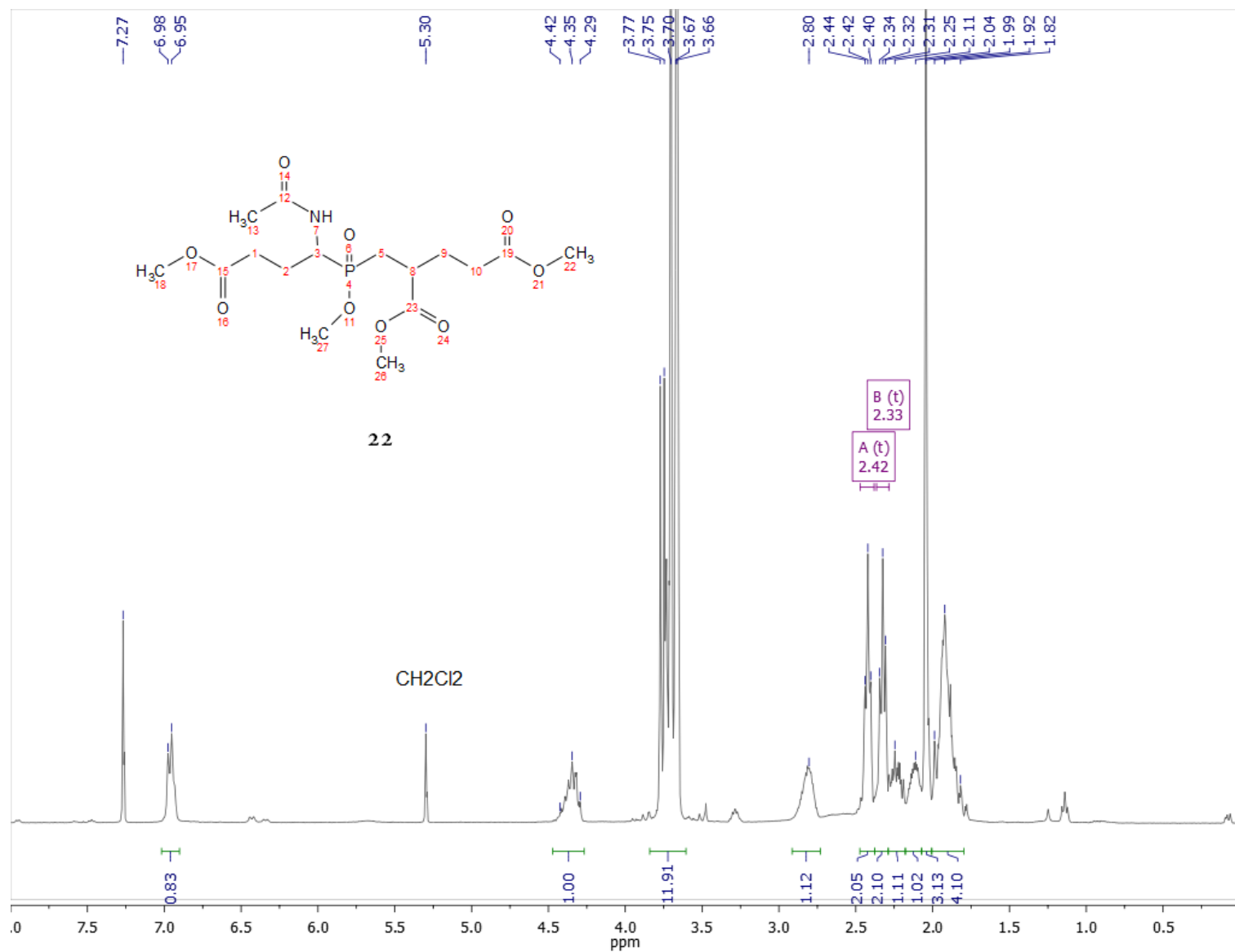


Figure A. 13. ¹H NMR (400 MHz, CDCl₃) spectrum of compound **22**.

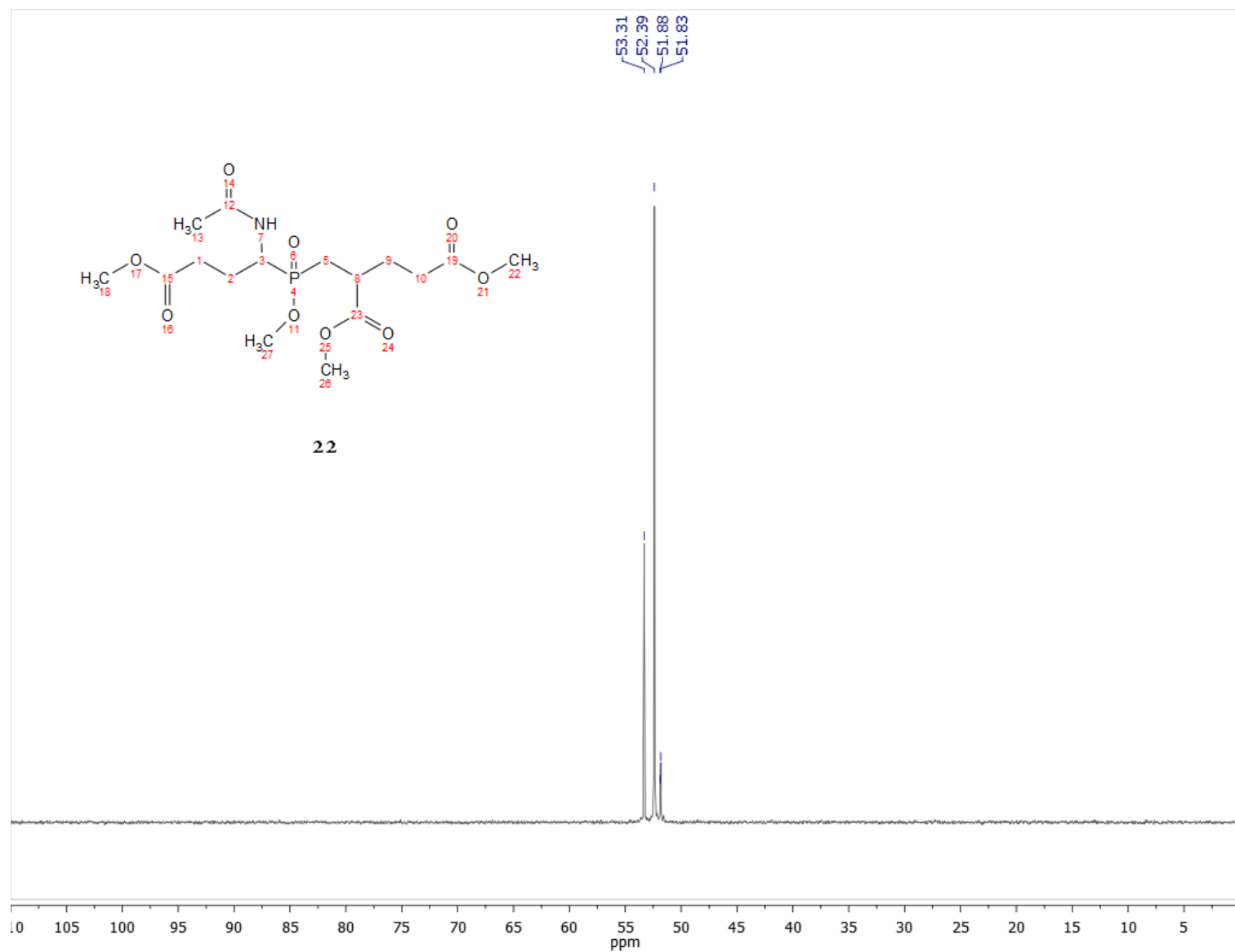


Figure A. 14. ^{31}P (1H) NMR (400 MHz, CDCl_3) spectrum of compound **22**.

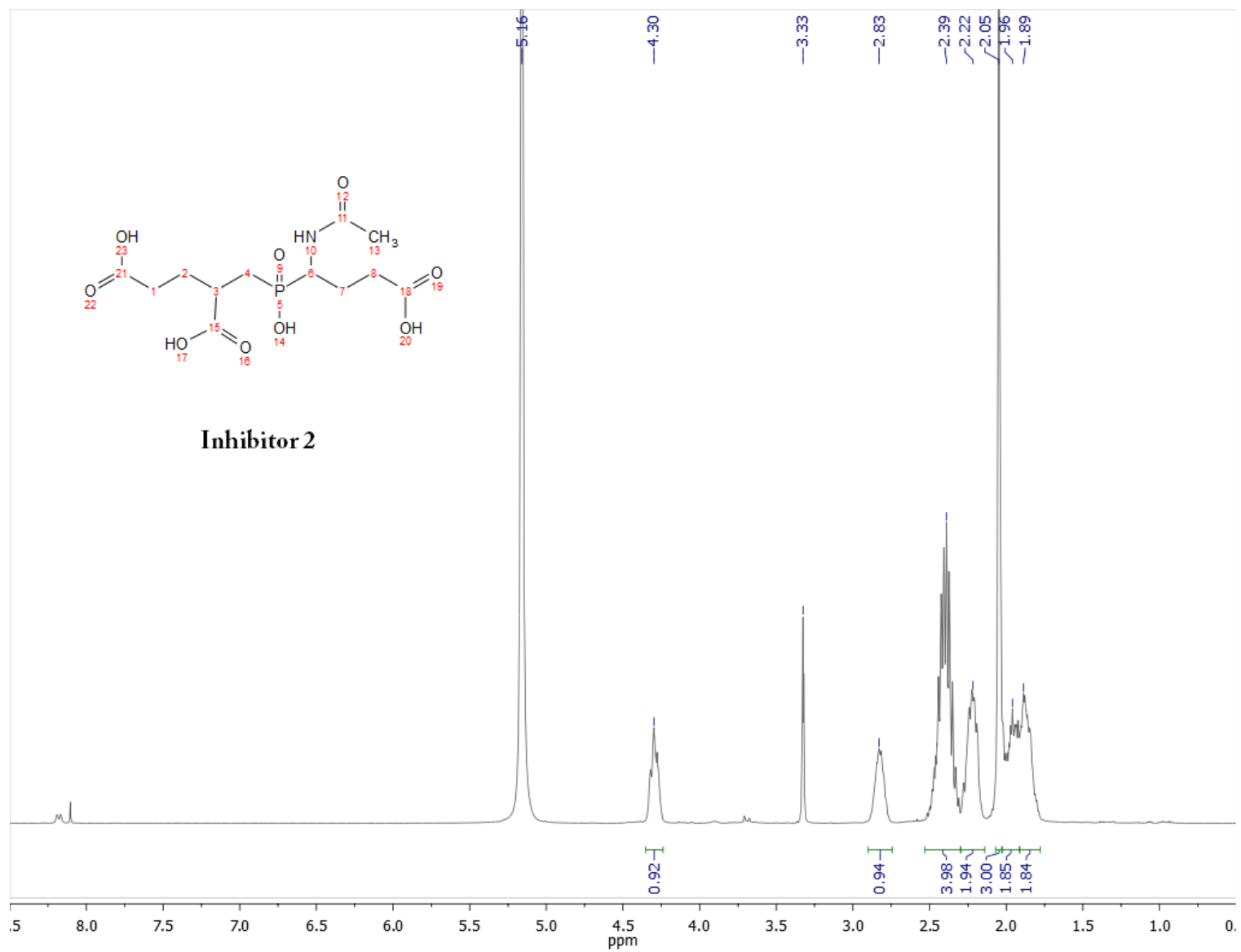


Figure A. 15. ¹H NMR (400 MHz, MeOH) spectrum of inhibitor 2.

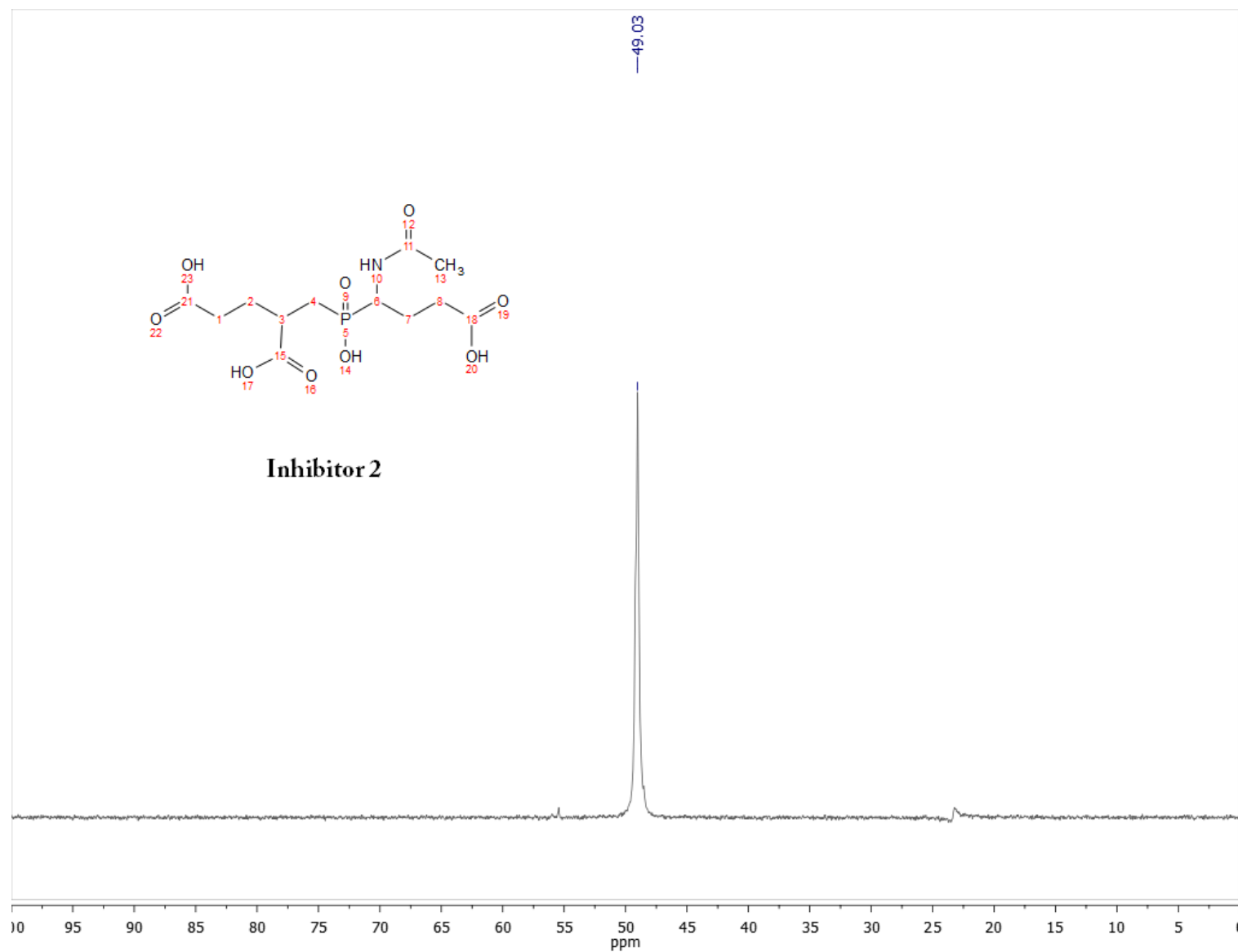


Figure A. 16. ^{31}P (1H) NMR (400 MHz, MeOH) spectrum of inhibitor 2.

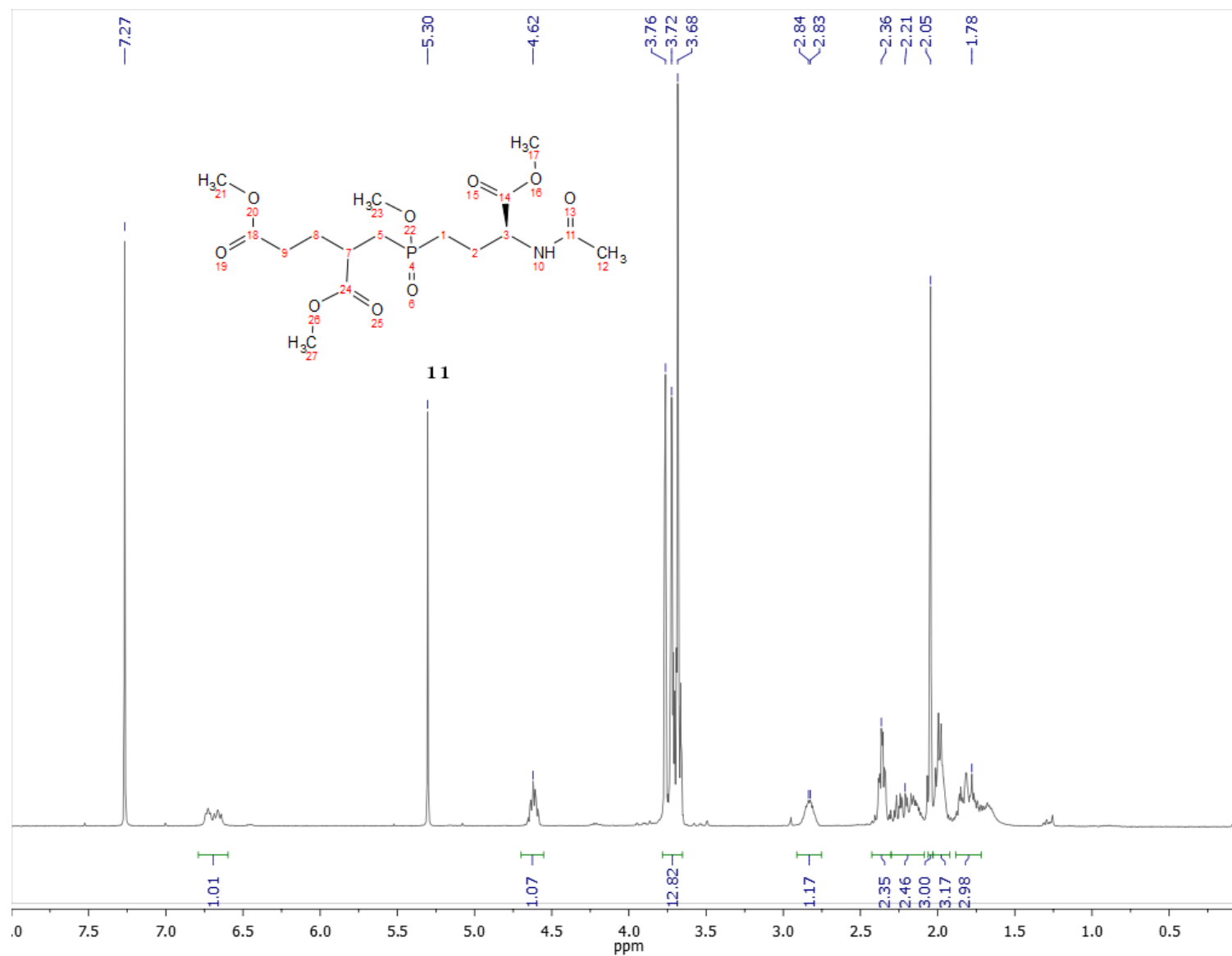


Figure A. 17. ¹H NMR (400 MHz, CDCl₃) spectrum of compound **11**.

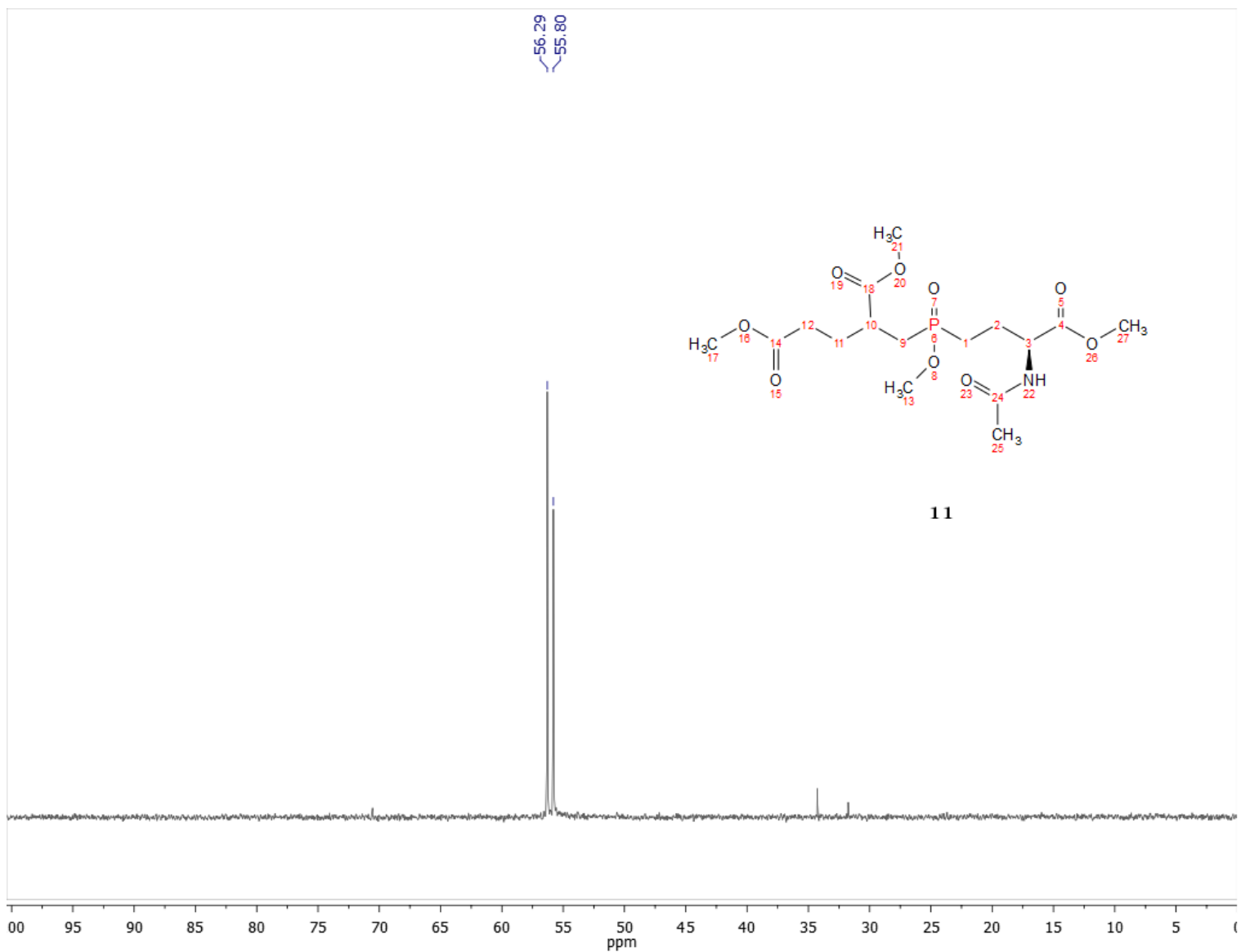


Figure A. 18. ^{31}P (1H) NMR (400 MHz, CDCl_3) spectrum of compound **11**.

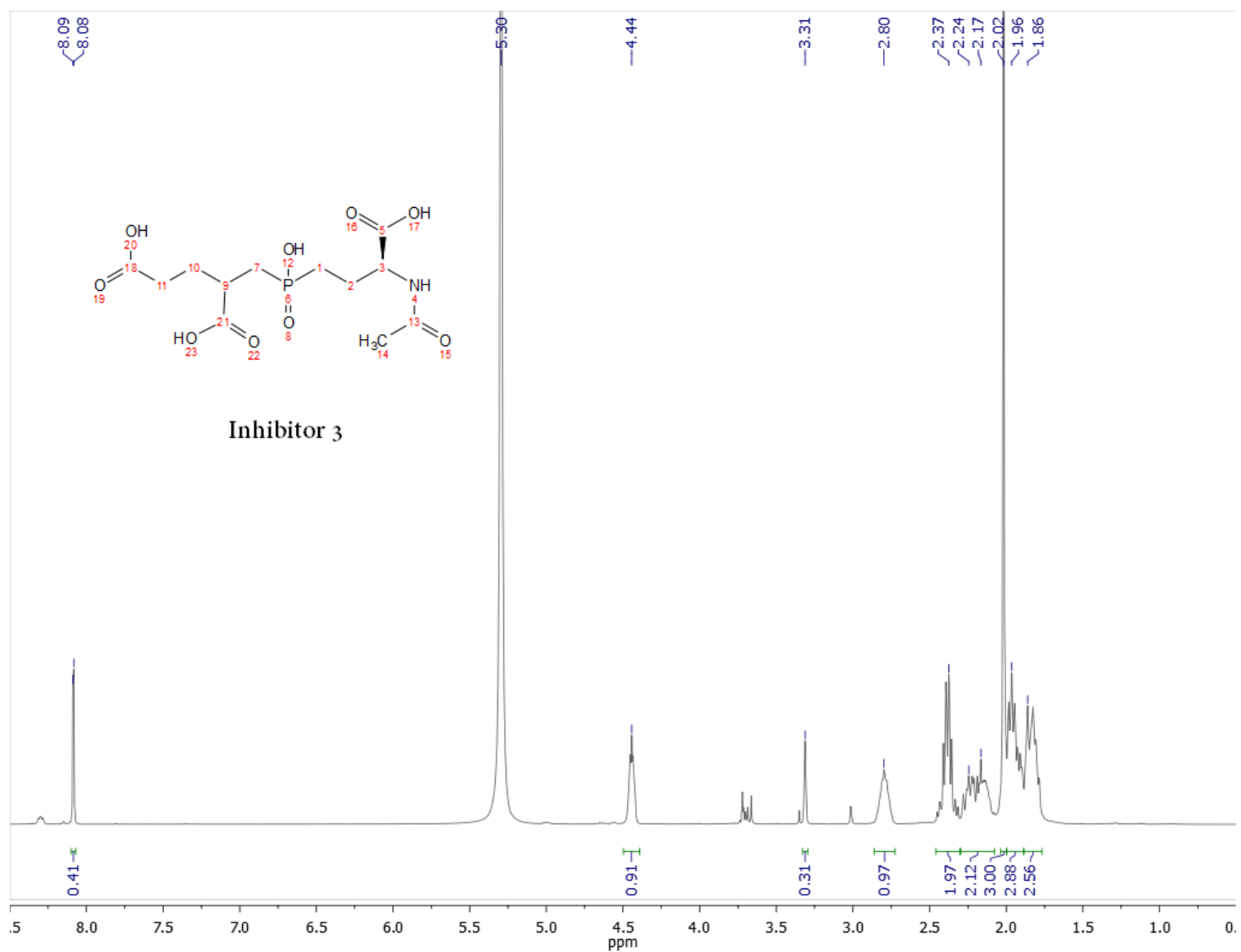


Figure A. 19. ¹H NMR (400 MHz, MeOH) spectrum of inhibitor 3.

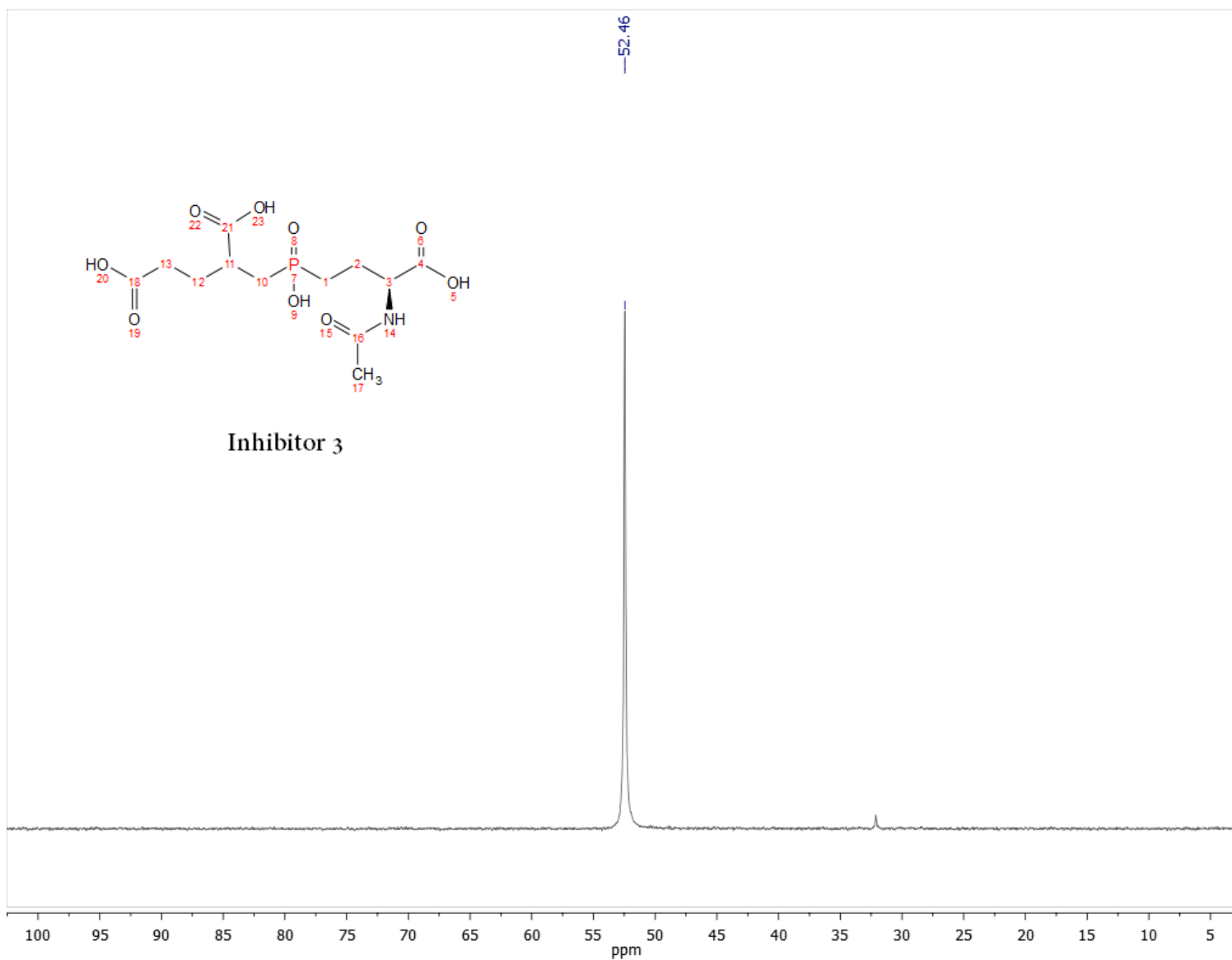


Figure A. 20. ^{31}P (1H) NMR (400 MHz, MeOH) spectrum of inhibitor 3.

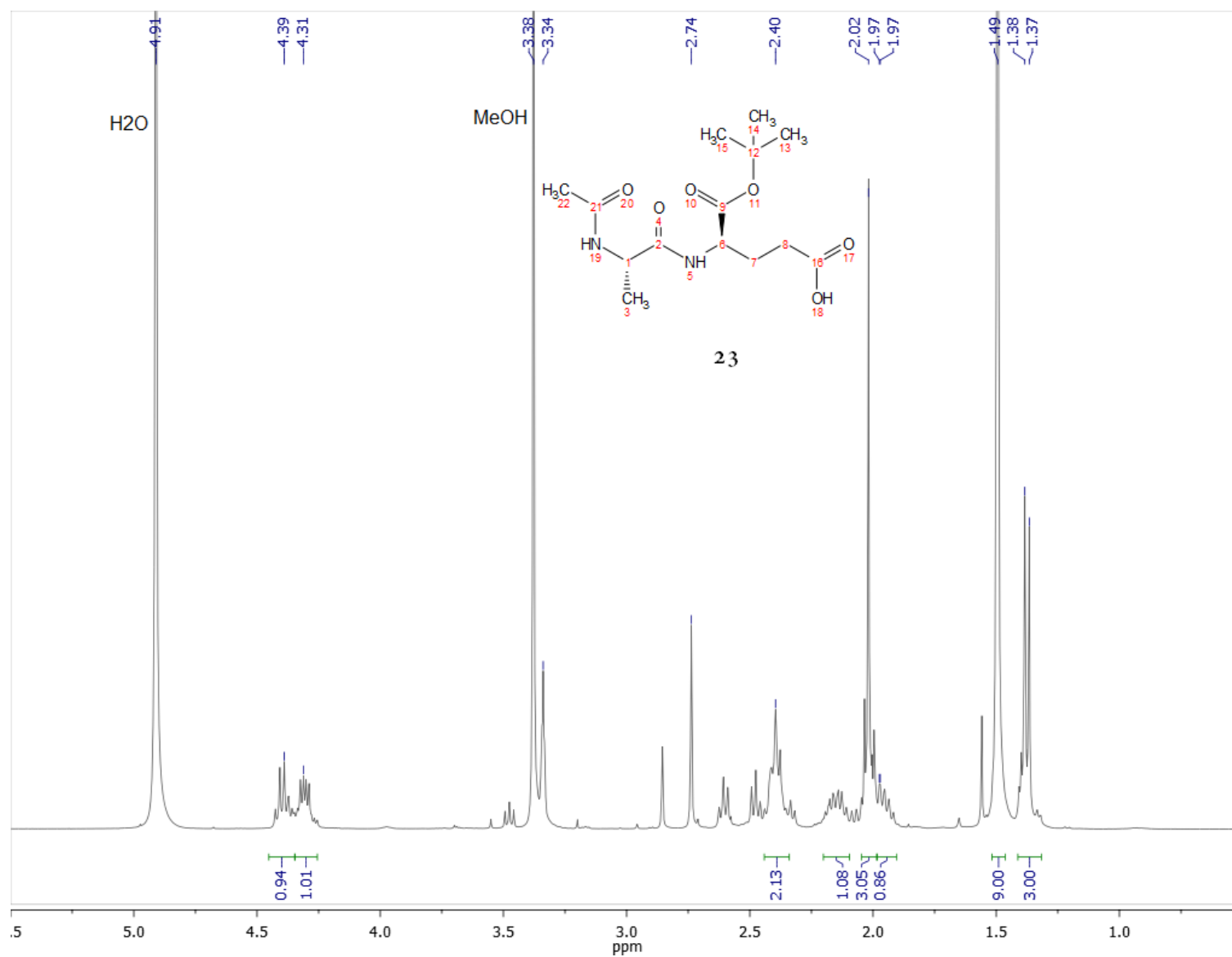


Figure A. 21. ¹H NMR (400 MHz, CDCl₃) spectrum of compound **23**.

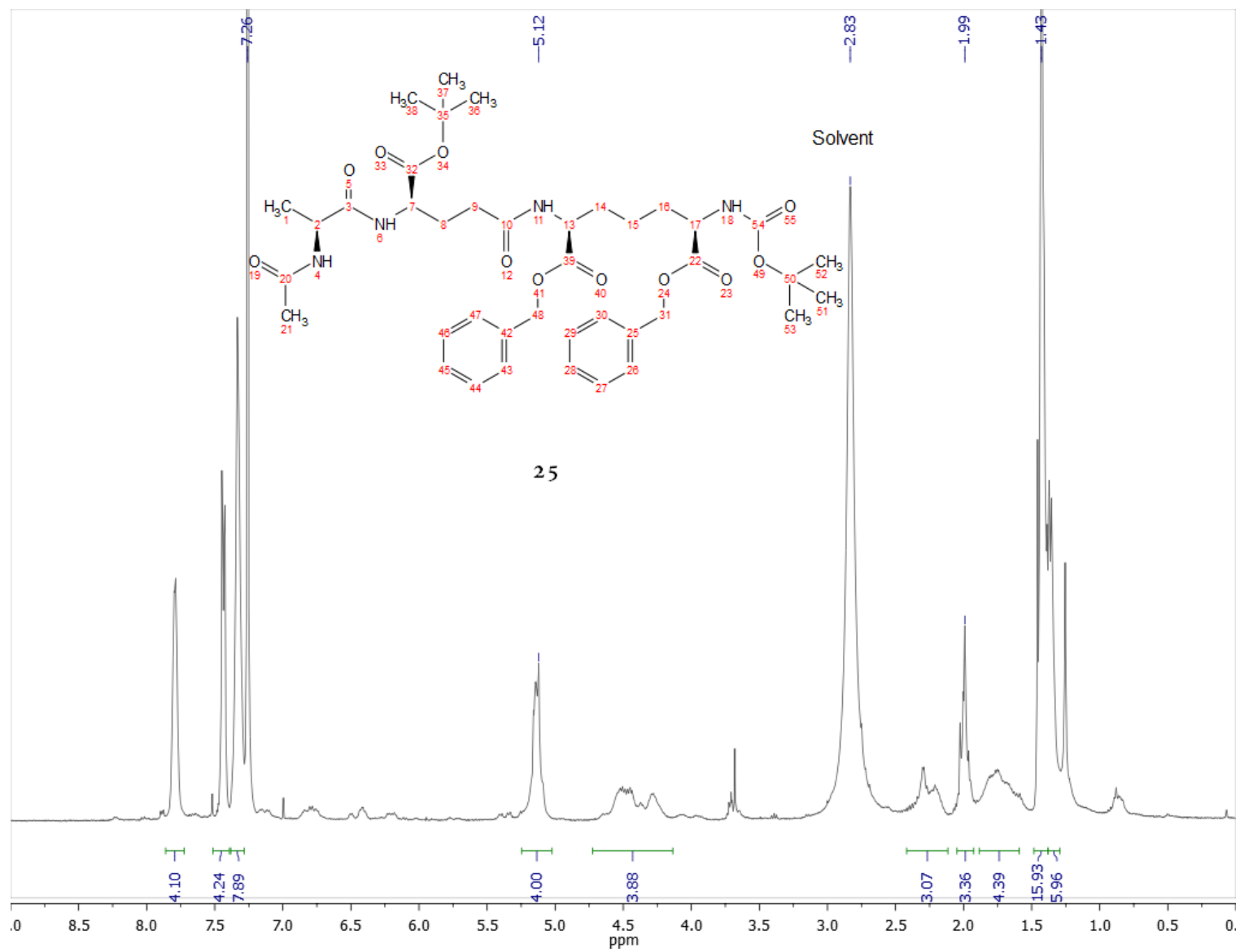


Figure A. 22. ¹H NMR (400 MHz, CDCl₃) spectrum of compound **25**.

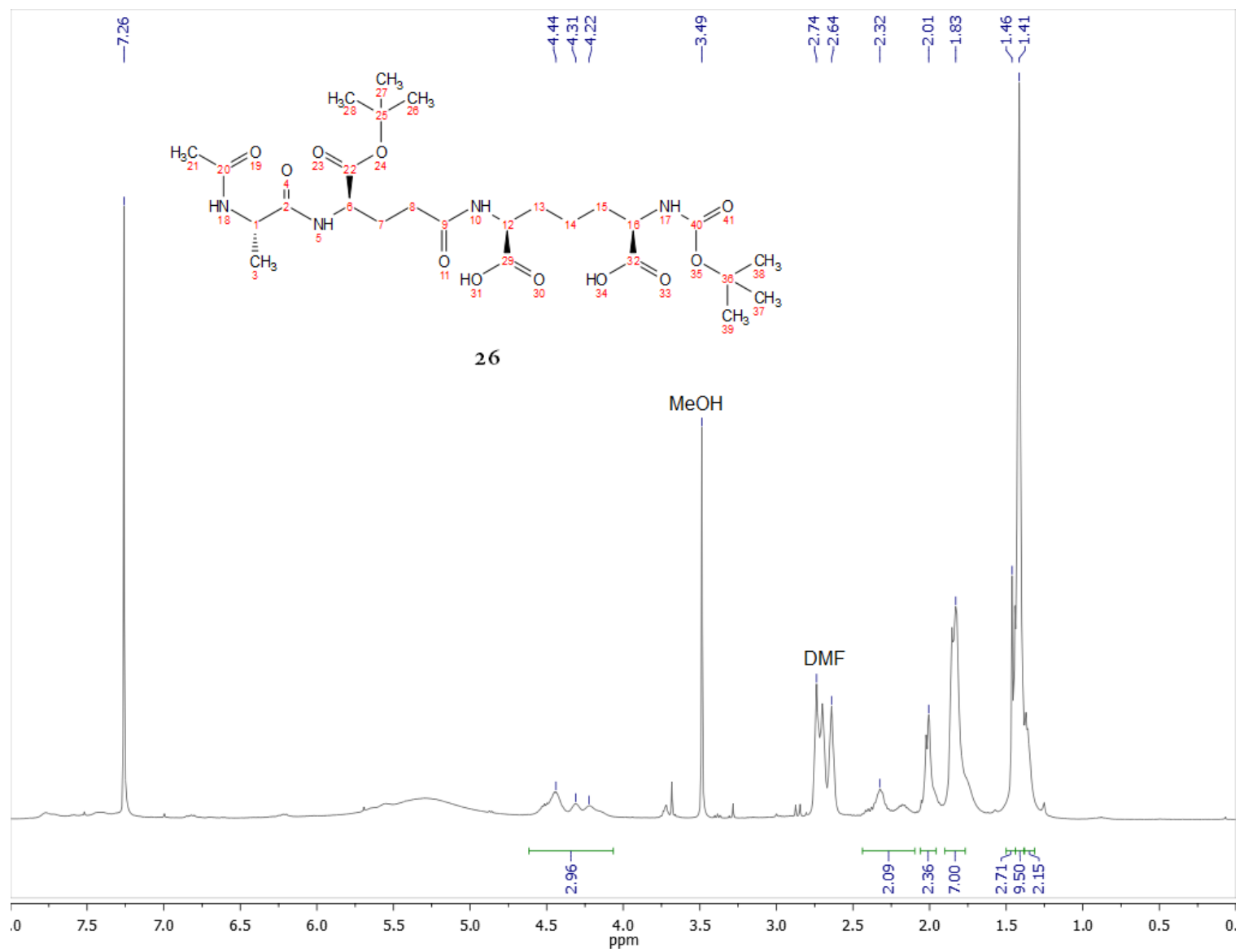


Figure A. 23. $^1\text{H NMR}$ (400 MHz, CDCl_3) spectrum of compound **26**.

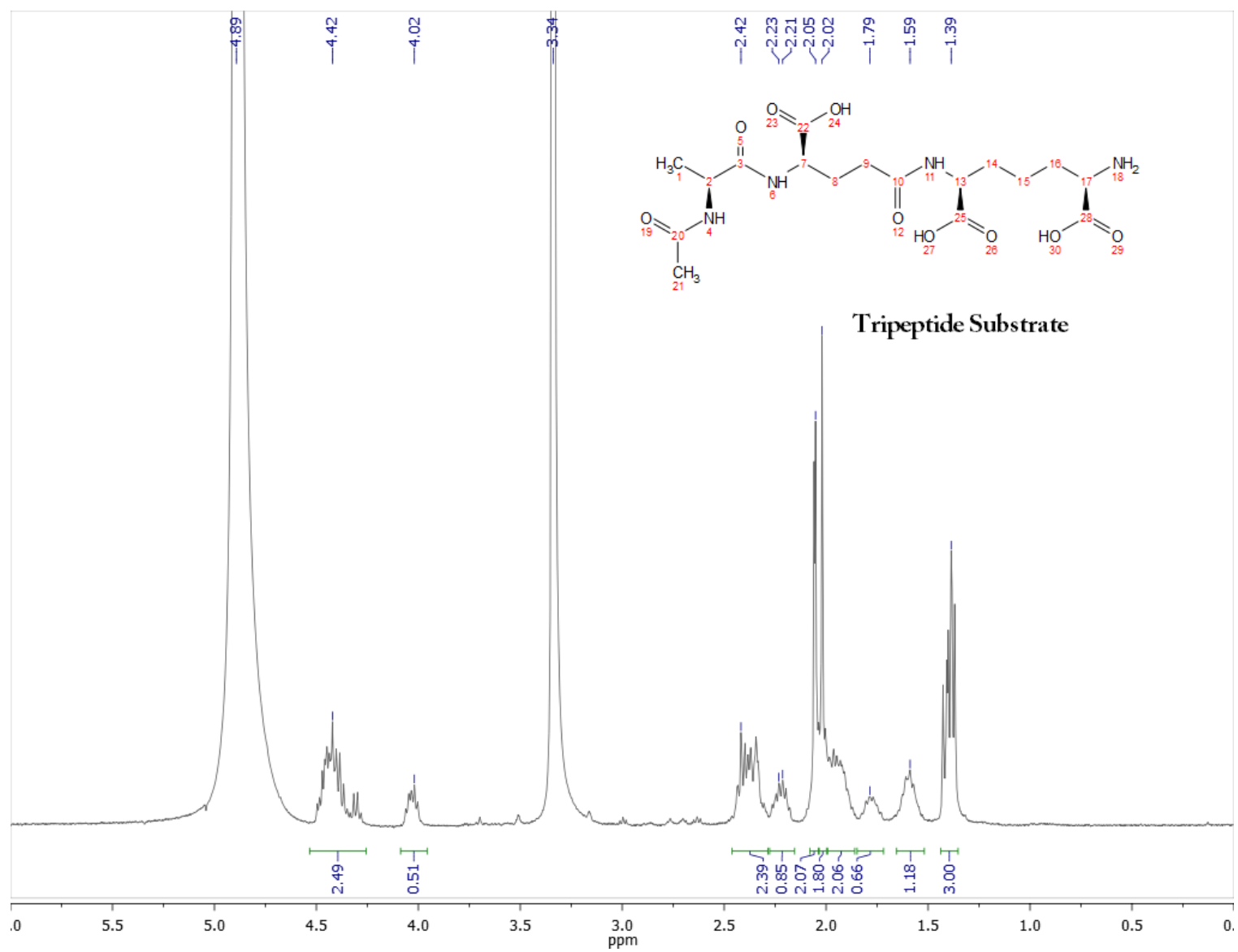


Figure A. 24. ^1H NMR (400 MHz, MeOH) spectrum of tripeptide substrate.

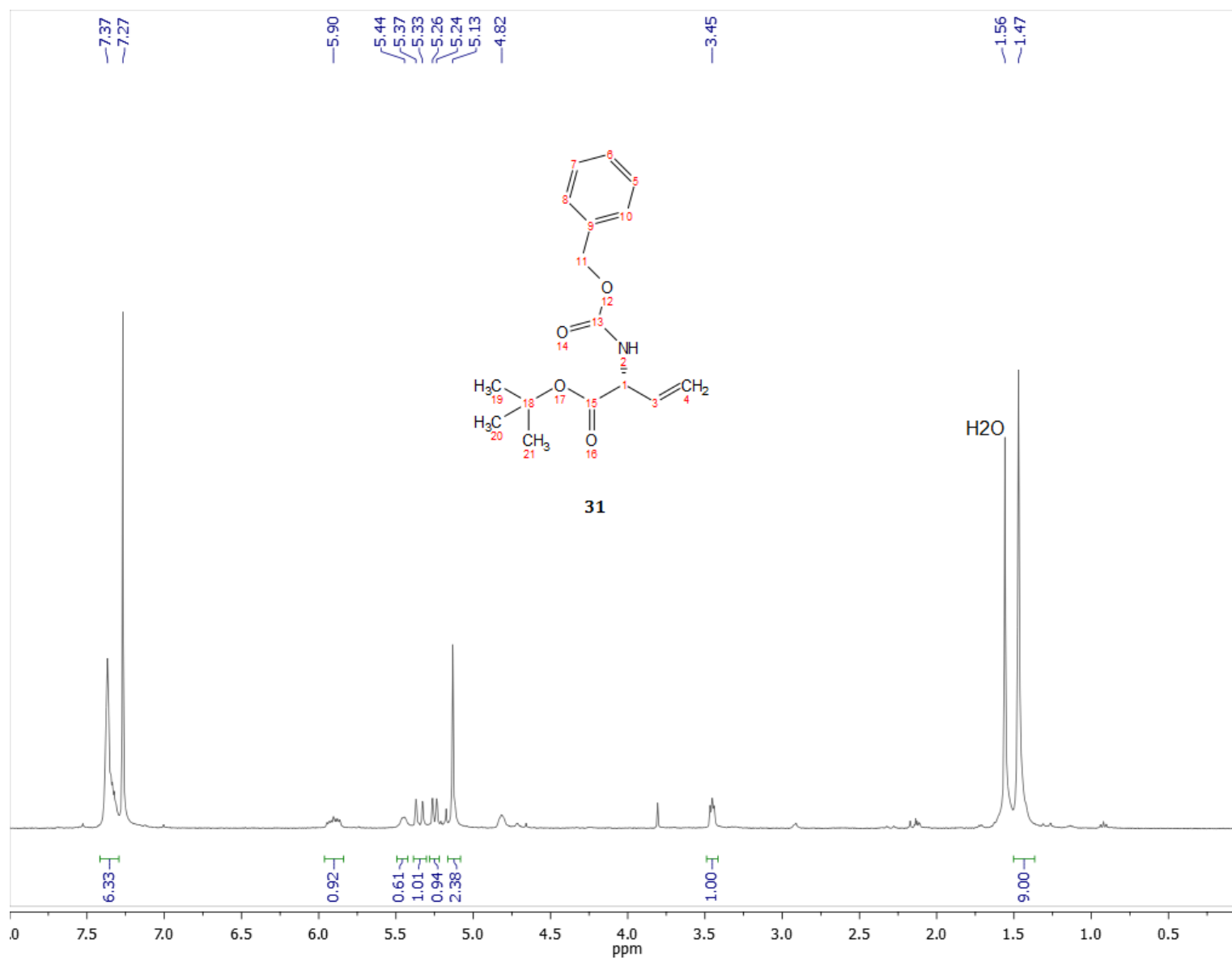


Figure A. 25. ¹H NMR (400 MHz, CDCl₃) spectrum of compound **31**.

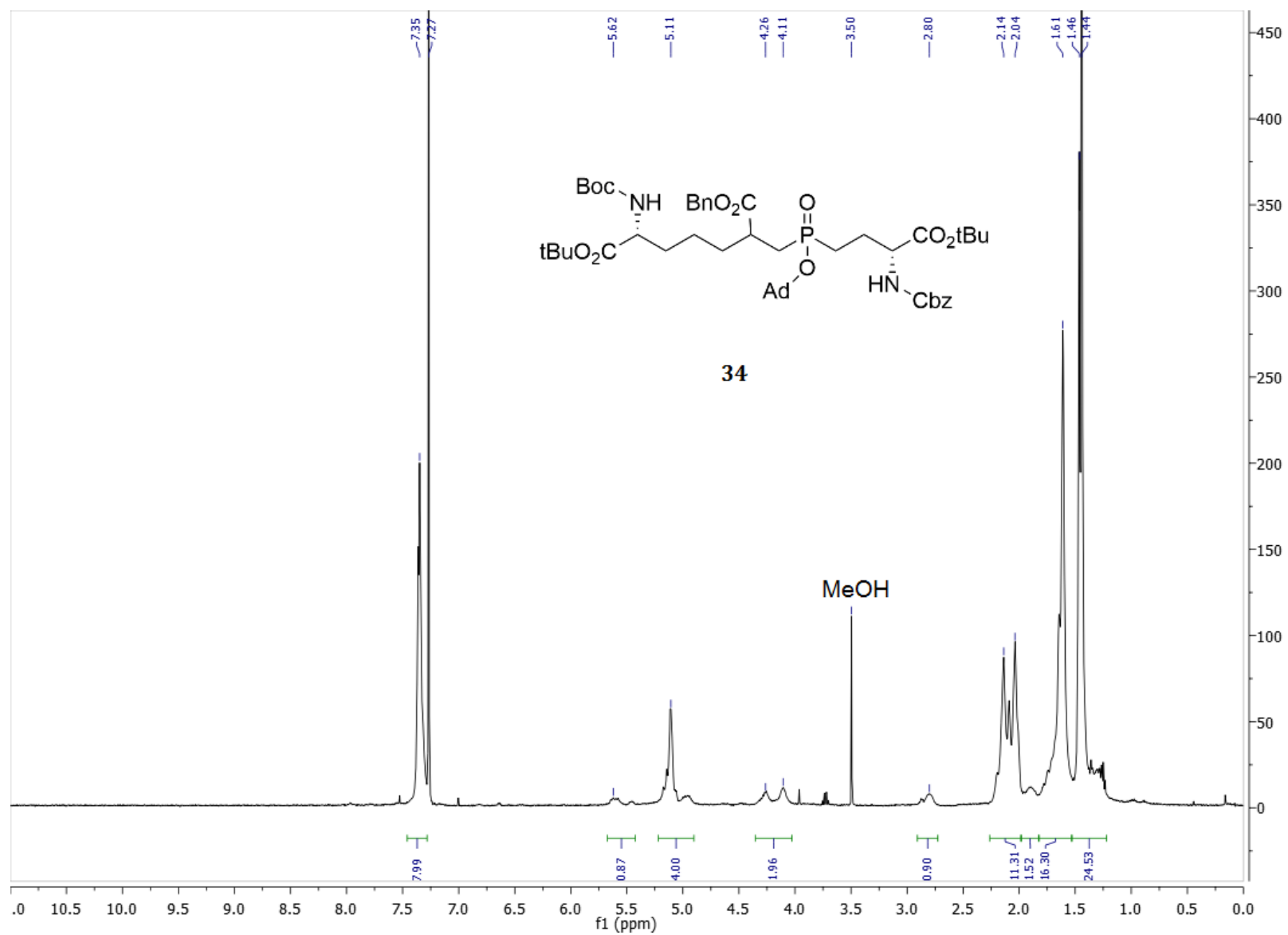


Figure A. 26. ^1H NMR (400 MHz, CDCl_3) spectrum of compound **34**.

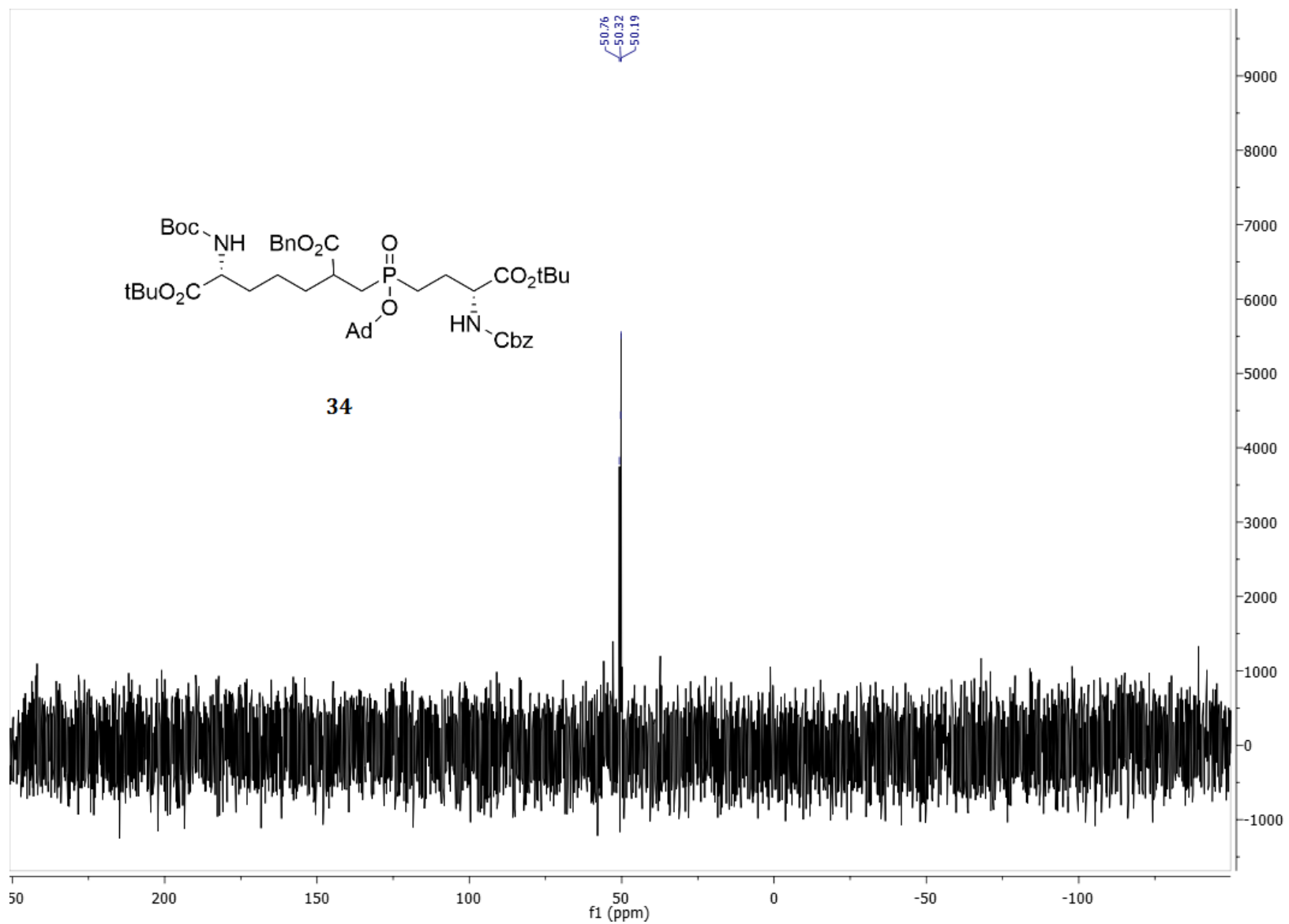


Figure A. 27. ³¹P (1H) NMR (400 MHz, CDCl₃) spectrum of compound **34**.

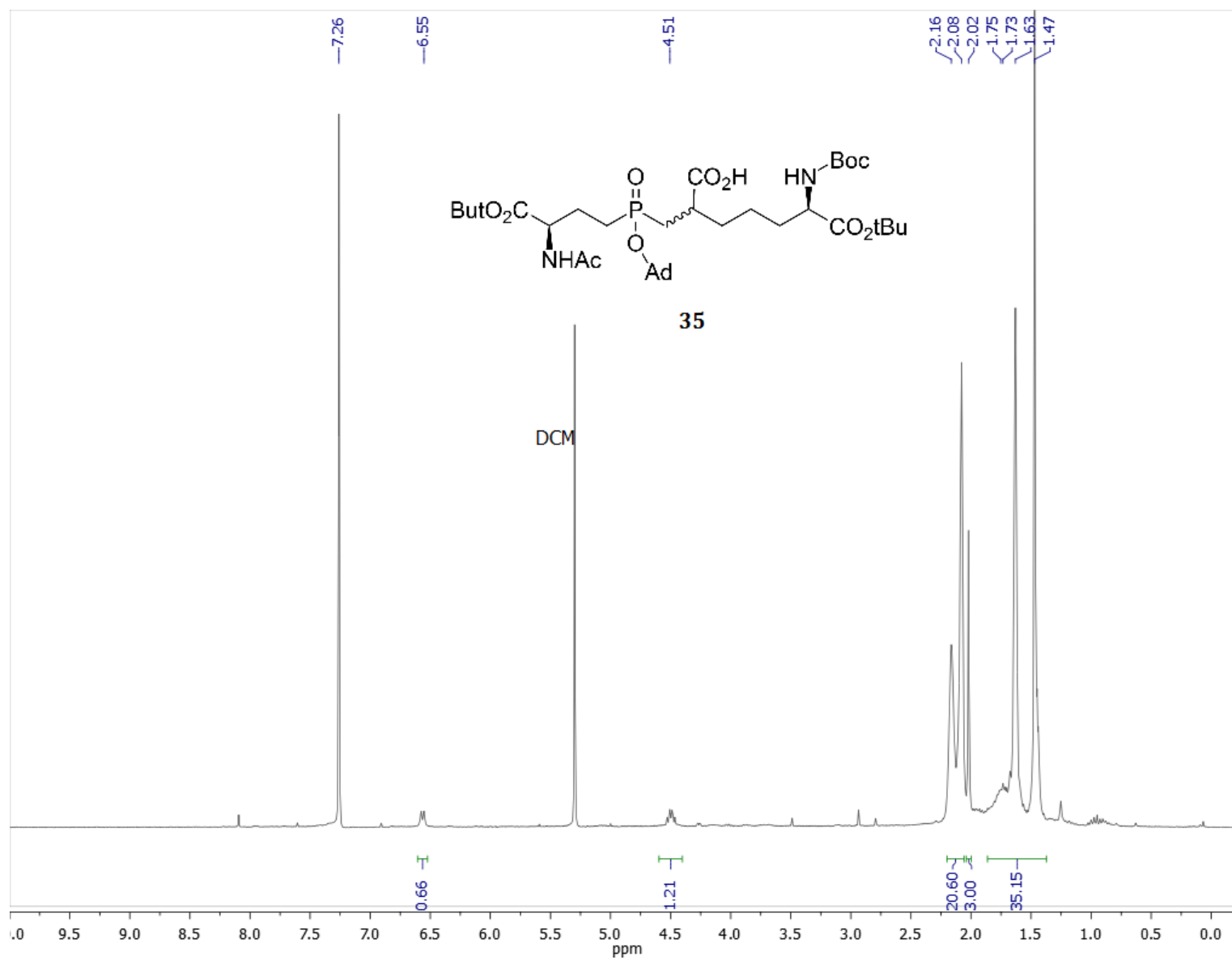


Figure A. 28 ^1H NMR (400 MHz, CDCl_3) spectrum of compound **35**.

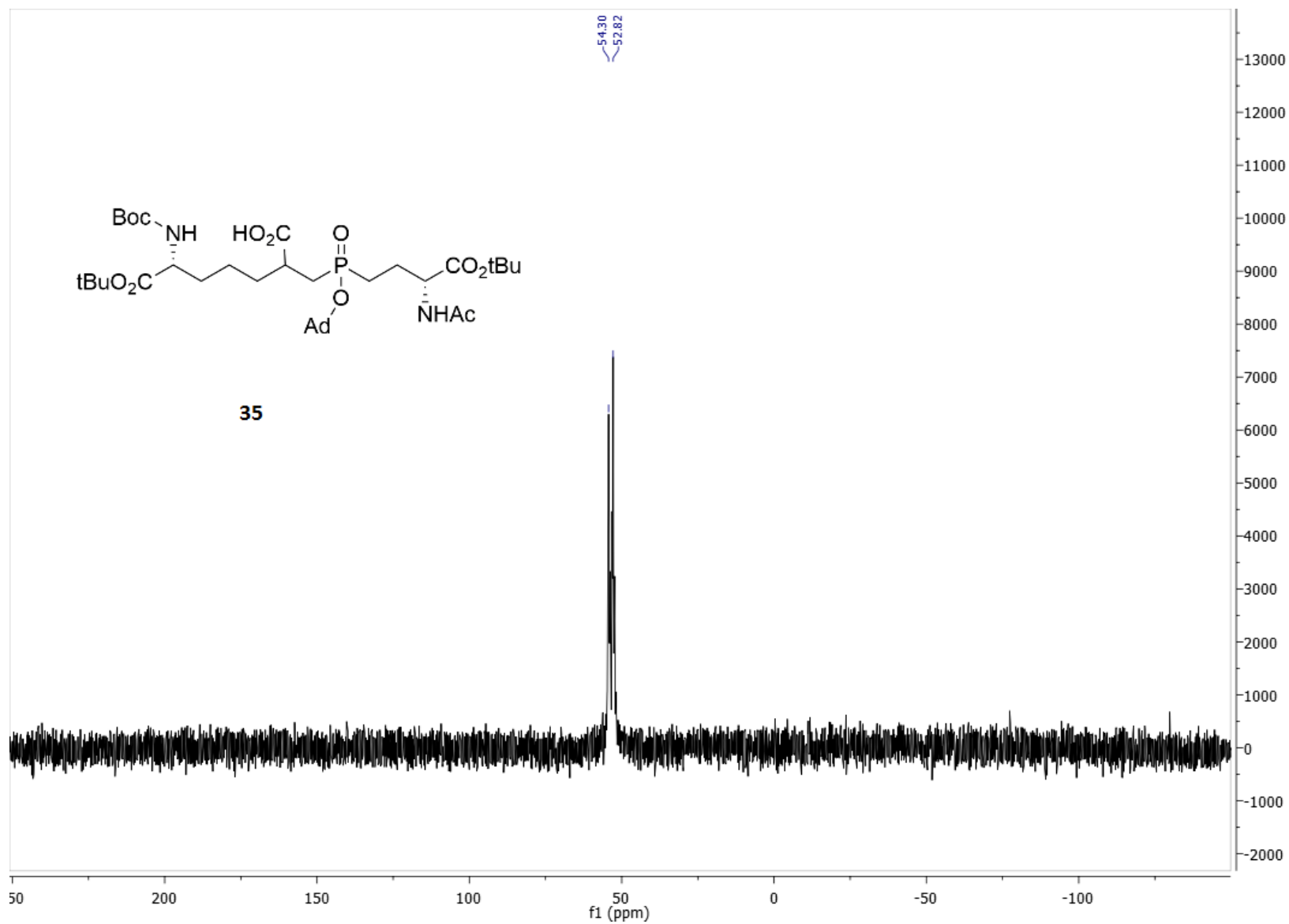


Figure A. 29. ^{31}P (1H) NMR (400 MHz, CDCl_3) spectrum of compound **35**.

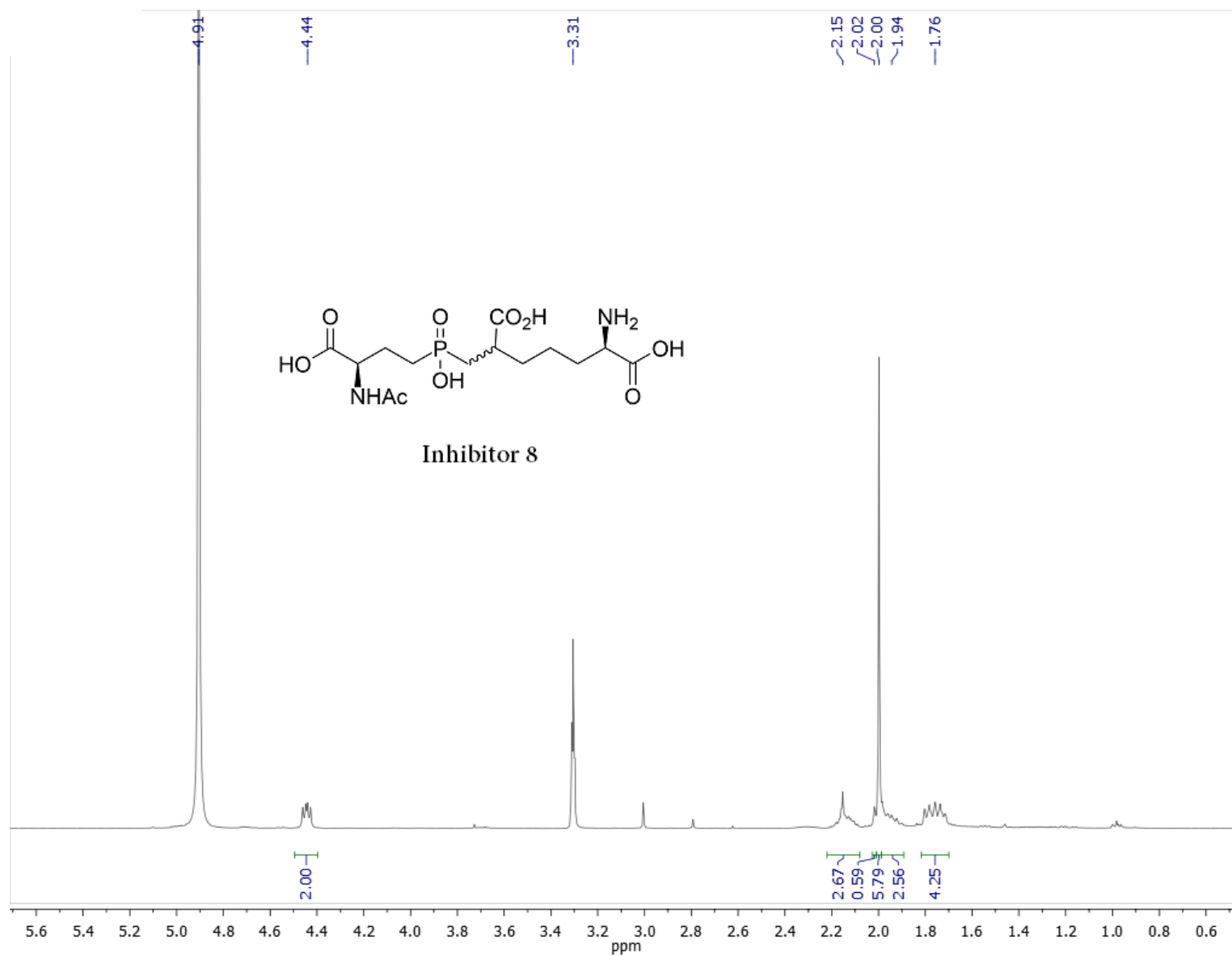


Figure A. 30. ¹H NMR (400 MHz, MeOH) spectrum of inhibitor **8**.

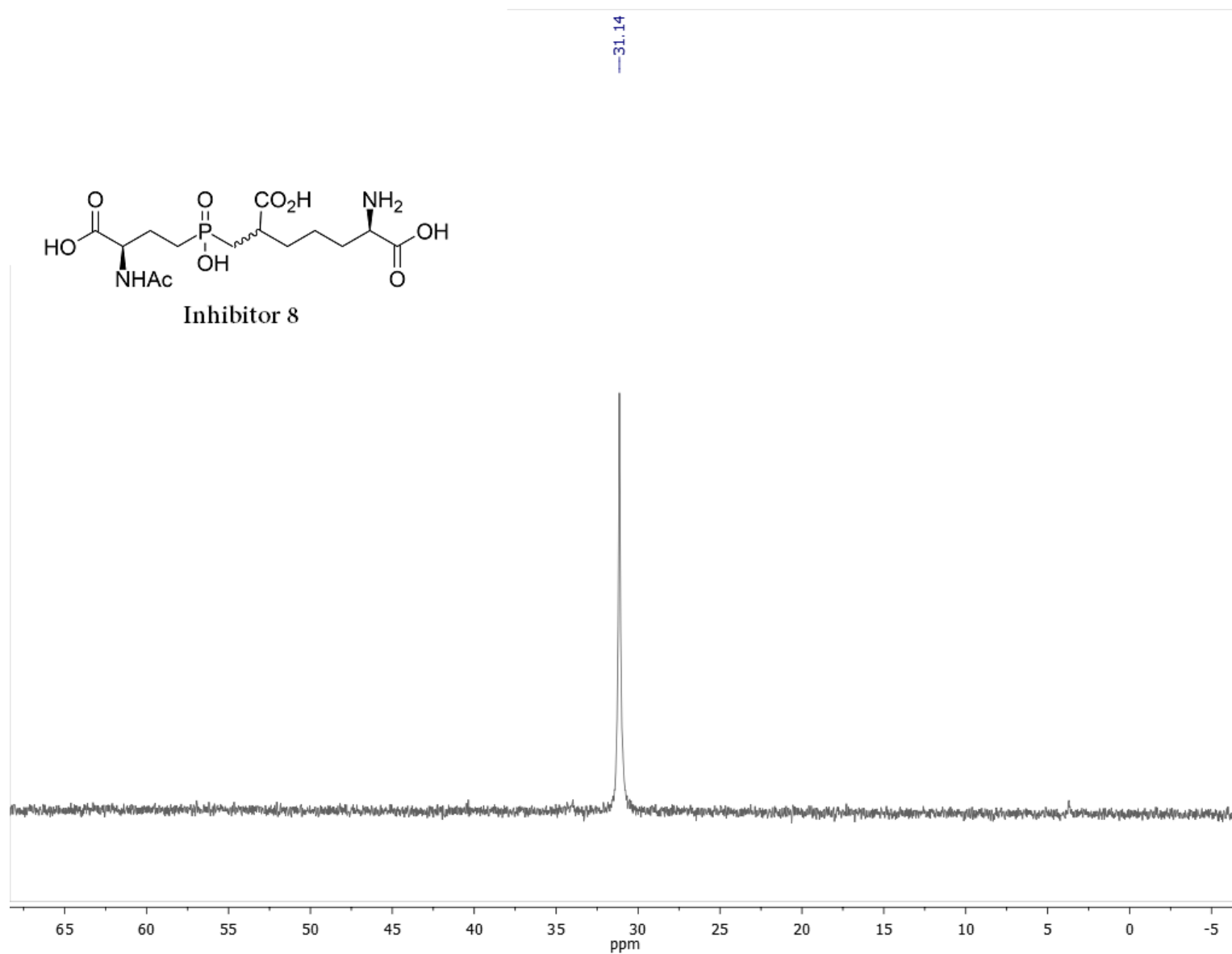


Figure A. 31. ^{31}P (1H) NMR (400 MHz, MeOH) spectrum of inhibitor 8.